Charles University in Prague
Faculty of Mathematics and Physics
The Czech Republic

Université Louis Pasteur Strasbourg
Faculté de Physique
France

Model Calculation of Four–Wave Mixing Polarization and Dynamics in Bulk and Confined Semiconductors

Doctoral Thesis
(Thèse en co–tutelle)

Tomáš Ostatnický

Prague, August 2005

Acknowledgments

The work presented in this thesis was done at Charles University in Prague, the Czech Republic, and Université Louis Pasteur in Strasbourg, France, in the framework of the project "Theèse en co–tutelle" (joint supervision of thesis) of the French government. I spent 18 months at the university in Strasbourg where I've gained a great experience in physics, culture and social life. I would like to express my thanks to both universities which made these studies possible and I thank the French government which supported my stay in France financially.

I thank both my advisors, prof. Petr Malý from Charles University and prof. Bernd Hönerlage from Université Louis Pasteur, for their leadership, support and inspiring discussions. I could always discuss my ideas with other people in the lab which helped me in this way to organize my thoughts and to formulate the theory — I thank Petr Němec, Pierre Gilliot, Mathieu Gallart and Jean–Pierre Likforman for their comments and interest.

I would like to thank in particular my wife Katka for her best personal effort to make my stays in Prague comfortable. She helped me to cope with all my personal problems and she was the source of the spiritual power necessary to finish my studies.

Prague, August 2005

Contents

Chapter 1

Introduction

1.1 Motivation

Solid state physics involves many subjects of interest like transport phenomena, cooling of carrier plasma, nanostructures, etc. Research of electron spin has been one of the most popular fields in solid state physics in the past since it provides a possibility for direct applications. Scaling down dimensions of devices to the sizes of the order of nanometers, one might use the electron spin and its coherence as the carrier of either a classical or a quantum information. Such devices then could be used in new spintronic or quantum computers, opening the new possibilities in future technologies.

Solid state research is connected with various types of materials. Semiconductors are one of the most popular groups of the solids because of their band structure. They remain in the ground state even at nonzero thermodynamic temperatures since thermal fluctuations are too weak to provide enough energy for any excitation. It is then possible to excite a defined number of electrons in well defined states in a crystal. These electrons then may stay excited for long times because of the bottleneck effect what makes them very good candidates as the carriers of informations.

The recent progress in technology allows preparation of semiconductor devices with well defined parameters on the size scales of nanometers. Such objects reveal many interesting phenomena connected with the quantum coherence, therefore we call them *quantum objects* or *nanostructures*. Properties of the nanostructures strongly differ from properties of macroscopic crystals even they were made from a same material. Research in the nanoscale then opens new areas of interest.

Laser physics provides a very powerful tool for experimental investigation of the electron spin as well as for investigation of semiconductors and their nanostructures. Laser spectroscopy is then very well suitable for the experimental research of the spin in semiconductor nanodevices. Since many phenomena take effect on a time scale of several hundreds of femtoseconds (fs), it is necessary to use ultrafast nonlinear spectroscopy besides the usual linear optical spectroscopy. *Four–wave mixing* (FWM) is one of the methods suitable for observation of the dynamics of spins inside the investigated crystal due to its sensitivity to spin of excited carriers.

Semiconductor devices are also widely investigated theoretically. There exist many models for description of various types of semiconductor structures valid under different conditions. Theoretical works, however, are mostly developed in order to describe and simulate selected phenomena with high precision showing the accuracy of the theoretical approach. One usually describes dynamics of electrons and holes in a crystal under assumption of some initial conditions (initial populations of the electron states) and the

optical field, used for excitation and probe of the system's dynamics, is considered to be only some source term in equations. No attention is often paid to transmission of optical field through the crystal boundaries, to strong exciton–photon coupling (resulting in the polariton effect) and the role of optical fields is underestimated.

Dynamical models formulated on the basis of microscopic electron–hole Hamiltonian are usually very precise, however derived equations of motion must be solved numerically. Need of numerical solution might be very inconvenient for experimenters — they often need a tool simple in use in order to evaluate polarization selection rules for FWM response from a system under particular experimental setup. In many cases the FWM response hasn't a definite polarization and this polarization may evolve in time. In such cases, one usually wants only an estimate of the polarization dynamics when building an experiment putting emphasis on fast calculations.

The aim of the theory presented in this thesis is to provide a model usable in nonlinear ultrafast laser spectroscopy of semiconductors and their nanostructures. Unique properties of third–order nonlinear optical processes in systems of a given dimensionality are discussed in order to show which type of model should be chosen for description. The work is focused on polarization of the outgoing signal since it becomes very important in many types of experiments. As an application of a model for bulk materials, a method for measurement of a weak wave vector dependent electron–hole exchange interaction is proposed.

1.2 Subject of the thesis

Four–wave mixing is an experimental technique used for observation of nonlinear coherent processes in materials. Three photons which come from laser sources excite the sample and the fourth photon is radiated and detected, see the sketch in Fig. 1.1. Separation of the photons from the excitation beams transmitted through the sample from the FWM response is done by spatial filtering: if the wave vectors of the excitation beams are $\boldsymbol{K}_1$, $\boldsymbol{K}_2$ and $\boldsymbol{K}_3$, the FWM response can be detected in the directions $-\boldsymbol{K}_1+\boldsymbol{K}_2+\boldsymbol{K}_3$, $\boldsymbol{K}_1-\boldsymbol{K}_2+\boldsymbol{K}_3$ and $\boldsymbol{K}_1+\boldsymbol{K}_2-\boldsymbol{K}_3$ in transmission. In reflection, the diffraction direction are given by the reflection of the three aforementioned directions by the plane of the sample surface. Direction $\boldsymbol{K}_1+\boldsymbol{K}_2-\boldsymbol{K}_3$ is chosen to be the detection direction throughout this thesis. The FWM response in other FWM directions can be calculated simply by permutation of the indices.

The third–order optical response of semiconductors, in particular FWM response, is under experimental and theoretical investigation for a long time. The aim of the four–wave mixing experiments is mainly to detect various channels of the coherence decay or coherent changes in the system. Because of a long history of research in this field, there already exists a big number of models which describe the dynamics of semiconductors under various experimental conditions. Models for bulk semiconductors can be divided into two main groups: on one side, there are phenomenological models based on *Optical Bloch Equations* (OBE) [1, 2], on the other side, one finds *microscopic theories* [3, 4, 5]. A detailed discussion of the two theoretical approaches can be found in chapter 4.

The aforementioned models including phenomenological OBE were successful in explanation and modelling of the basic behaviour of the FWM response without spin. Therefore most of theories are formulated using two bands, one valence and one conduction band. Current research on semiconductors and their nanostructures is, however, focused on spin. It is then interesting to examine which of the models are also able to reproduce polarization properties of the FWM response.

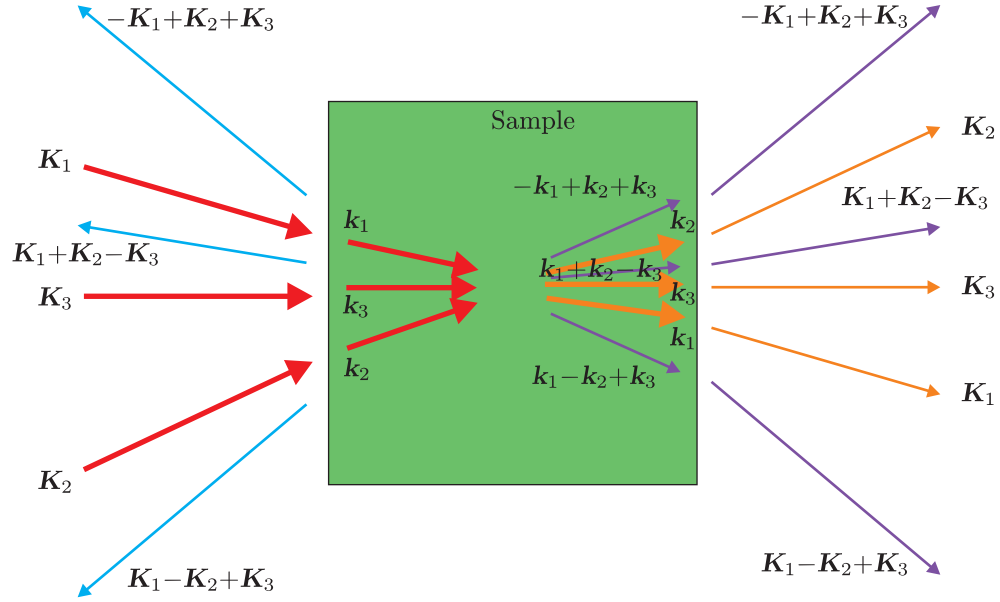

Figure 1.1: Sketch of a general four–wave mixing experiment. Excitation fields (pulsed, red arrows) have wave vectors $\boldsymbol{K}_1$, $\boldsymbol{K}_2$ and $\boldsymbol{K}_3$, the diffracted fields are: transmitted waves (dark blue) $-\boldsymbol{K}_1+\boldsymbol{K}_2+\boldsymbol{K}_3$, $\boldsymbol{K}_1-\boldsymbol{K}_2+\boldsymbol{K}_3$ and $\boldsymbol{K}_1+\boldsymbol{K}_2-\boldsymbol{K}_3$ and reflected waves (light blue). Transmitted excitation fields are sketched by orange arrows. Wave vectors of (polariton) fields inside the sample are denoted as $\boldsymbol{k}_1$, $\boldsymbol{k}_2$, $\boldsymbol{k}_3$ and their combinations according to the diffraction directions.

Although microscopic theories give very precise predictions and one may use them in order to derive results with an arbitrary precision, they are not convenient for use when preparing experiments: calculations are time–consuming and their implementation on computer needs also a long time. One therefore looks for a simpler model which is suitable for the task. In many cases, one applies OBE or their modified form. However, a detailed examination of polarization selection rules of OBE was not published in literature until now and it is not clear whether they can be used in order to predict polarization of the FWM response of semiconductors.

The subject of this thesis is then to examine whether OBE give correct polarization selection rules for FWM on semiconductors and their nanostructures. I show the most striking differences between OBE and other theories and I show under which conditions OBE are applicable. The conclusion is, that OBE may be used in order to describe FWM response of semiconductor nanocrystals since they are similar to atomic systems (they reveal discrete energetical levels of spatially localized states). I examine several level schemes suitable for description of FWM on semiconductor nanocrystals in chapter 5. For every scheme, I show to which type of nanocrystals the model may be applied. OBE are shown to be inappropriate for description of bulk materials or quantum wells, generally systems with translational symmetry. I illustrate this fact using derived polarization selection rules for bulk materials using semiconductor Bloch equations [6] and my calculations of FWM polarization on few level schemes used in literature.

It was stressed before that one needs a model as simple as possible in order to derive polarization of FWM response of an examined system. Microscopic theories are too complex and OBE give wrong predictions. For this reason, a new model suitable for description of intrinsic bulk semiconductors and quantum wells is developed in this thesis.

Using the model, I show that FWM polarization selection rules for a system with an arbitrary symmetry may be derived using only algebraic equations without need of evaluation of system's dynamics and the polarization selection rules may be therefore derived within few seconds. Then I show that this model gives correct predictions of polarization and it also well reproduces other main features of the FWM response (temporal evolution, beating etc.). In order to show how the model may be applied, I propose a FWM experiment in which wave vector–dependent exchange interaction in bulk semiconductor may be measured. Such type of experiment was not established yet and I believe that this work and use of the developed model may help to open new possibilities of FWM spectroscopy because it is possible to easily include influence of symmetry–breaking effects (external fields and forces, crystal orientation etc.).

It is also possible to use the model in an inverse direction. Selection of suitable polarizations of incoming fields and of the detection may allow detection of weak interactions with a given symmetry. The proposal of the measurement of wave vector–dependent exchange interaction is an example of the inversion of the model.

In this thesis, I consider semiconductors with dimensionalities 3D (bulk crystals), 2D (quantum wells) and 0D (quantum dots, nanocrystals). Description of 1D structures (quantum wires) is missing because of a complex interplay of wave vector conservation and localization of the states. Since quantum wires are not of a special attention in polarization–resolved FWM spectroscopy, they are omitted in this work.

1.3 Organization

The thesis may be divided into two main parts, each of them subdivided to chapters. The first part can be labelled as *Overview of theory*. It consists of chapters 2–4. The second part then presents original results which were obtained within the main subject of the thesis — this part includes chapters 5–7. The thesis is introduced by this chapter 1 and the results are summarized in the last chapter 8.

Theoretical introduction gives an overview of many–body physics, atomic systems and their third–order optical response, semiconductors and their response to optical excitation. These subjects are divided to two chapters as follows. In chapter 2, I give an overview of the theory connected with systems of identical particles. First, particle statistics from the point of view of quantum–mechanical operators is briefly introduced. Then the density matrix formalism, which allows description of the system using one–particle states, is developed. Optical response of a system coupled to electromagnetic field is determined by the so–called *coherences* which are described by nondiagonal terms of density matrix. In order to describe the general features of the optical response, I derive and interpret several interesting properties of the density matrix elements in section 2.3. Then I apply the density matrix formalism to atomic systems and I show derivation of optical Bloch equations. Based on the discussion of the density matrix, I show the limitations of the applicability of the derived equations.

Chapter 3 introduces semiconductors. It begins with an overview of the terms *band structure*, *electron spin*, *hole*, *exciton* etc. Then I define exciton spin and I show how an effective one–exciton Hamiltonian may be derived using the method of invariants. Then I define the terms *spin precession* and *spin relaxation*, which are of a big importance in this work. Concerning two–particle Hamiltonian, its structure and consequences are shown: exciton–exciton scattering, biexciton formation and polariton effect. The last part of chapter 3 introduces semiconductor nanostructures.

Chapter 4 shows main properties of the optical third–order response of semiconductors and their nanostructures. I show how the responses of bulk and zero–dimensional structures differ. Then I show which models may be used for description of FWM on these systems (including polarization) and what are the advantages and disadvantages of the various models. Discussion of models for bulk semiconductors is divided according to the two groups of theories to a section which introduces phenomenological modified optical Bloch equations and the second section then introduces microscopic theories. The models are discussed from the point of view of the reproduction of dynamics and polarization of the FWM response.

The second part of the thesis, composed of my original results, contains three chapters. This part may be further divided into chapter 5 which concerns FWM on low–dimensional structures and chapters 6–7 which present the model for bulk semiconductors. In chapter 5, I show that quantum wells may be described by the model for bulk semiconductors with some modifications and quantum dots may be described using OBE. Then I develop polarization selection rules of the FWM response on four basic level schemes which may be used in order to describe quantum dots under various conditions. I show also that the developed polarization selection rules cause fail of OBE in bulk semiconductors [1, 2, 7]. Concerning quantum wells, calculations of spin structure of excitons and biexcitons are presented. I take into account zinc–blende and wurtzite structure of the crystal and three different growth directions. For every type of quantum well, I show the consequences of the biexciton spin structure and exchange interaction on spin conservation and selection polarization rules in FWM.

Chapters 6 and 7 present the model for bulk semiconductors which is the core of this thesis. In chapter 6, basic considerations are summarized and the model is developed step–by–step from microscopic Hamiltonian to the level scheme, Hamiltonian and equations of motion. The particular parts concern linear and nonlinear dipole interaction, polariton–polariton scattering, bipolaritons, relaxation rates and equations of motion.

Discussion of the developed model is present in chapter 7. Using the level scheme, I interpret the wave mixing from the point of view of subsequent particular events which take place in a crystal. Then equations of motion are integrated for two special cases of time order of incoming optical fields under assumption of no spin precession. Based on these equations, one may determine polarization selection rules for nonperturbed semiconductors. Derived polarization selection rules are compared to experimental values. Then I discuss the main characteristics of the model and how it describes various types of experiments (time–resolved, time–integrated and spectrally–resolved). The model is found to be suitable for description of the third–order optical response of semiconductors since the discussed experimentally known phenomena are well reproduced. After this verification of the validity of the model, I show how it may be extended to systems with lower symmetry and dimensionality. Then I compare theoretical calculations with experimental results taken from literature. In the last subsection of chapter 7, I discuss how the spin precession may be measured in four–wave mixing experiments and I propose an experimental setup. Chapter 8 presents conclusions of the thesis.

1.4 Symbol convention

Many different mathematical symbols of various meaning are used in the work so they are summarized in this section for clarity. In the following table, symbols are listed in the left column and their meaning in the right column.

$a, y(x)$	c–number and c–number function .
$\boldsymbol{k}$	Vector .
$\mathbf{M}$	Matrix .
$\vec{\mathbf{\Sigma}}$	Vector of matrices .
$\mathbb{1}$	Identity operator or matrix .
$\hat{a}$	Scalar quantum–mechanical operator .
$\hat{\boldsymbol{L}}$	Vector quantum–mechanical operator .
$\hat{\mathbf{T}}$	Matrix quantum–mechanical operator .
$[\hat{a}, \hat{b}] = \hat{a}\hat{b} - \hat{b}\hat{a}$	Commutator .
$\{\hat{a}, \hat{b}\} = \hat{a}\hat{b} + \hat{b}\hat{a}$	Anticommutator .
δ_{xy} , $\delta(x)$	Kronecker delta, delta function .
$\Theta(x)$	Heaviside step function .
$\sigma^+\sigma^+\sigma^-$, XXY	Polarizations of the excitation fields with respective wave vectors $\boldsymbol{k}_1$, $\boldsymbol{k}_2$, $\boldsymbol{k}_3$.
∂_q^j	$\partial^j / \partial q^j$.
$\boldsymbol{K}_1$, $\boldsymbol{K}_2$, $\boldsymbol{K}_3$	Directions (wave vectors) of excitation fields .
$\boldsymbol{k}_1$, $\boldsymbol{k}_2$, $\boldsymbol{k}_3$	Wave vectors of polaritons which are the excitation optical fields coupled to .

Chapter 2

Systems of identical particles

2.1 Introduction

This thesis is focused on semiconductors which are many–body systems. For this purpose, general properties of such systems are revised in this chapter. A special attention is paid to the symmetry of states of several identical particles with respect to interchange of two particles. The reason for the introduction of basic quantum mechanic is to survey an overview in order to simplify discussions in the following chapters.

The brief introduction of the statistics of the systems of identical particles is given in the section 2.2. Even though excitons are mostly assumed to be bosons, they have a fractional Fermi character [8, 9, 10] and therefore both systems of bosons and fermions are discussed.

Since I deal with the systems of several particles in a mixed state, density matrix formalism is used. It is briefly introduced in the section 2.3 together with the discussion of its connection to the correlation functions expressed by operators. The third–order optical response of semiconductors is driven by the so–called coherences between states of excitons, i.e. by the correlations between their phases (phases of their wavefunctions). There is no classical correspondence so the understanding of the coherences might be difficult. Section 2.3 tries, however, to physically interpret the coherences. Some relations between various density matrix elements are summarized in that section and several important mechanisms of the loose of coherence and population are mentioned.

The discussion of the third–order response is divided to *semiconductors* and *atomic systems* in this thesis since these two basic systems describe two different worlds: highly–correlated and weakly–correlated systems. For the purpose of the following mathematics, it is necessary to introduce atomic systems in section 2.4. Expressions for calculation of the third–order optical response of atomic systems, known as optical Bloch equations, are derived in section 2.5. When polarization of optical field is included to the theory, one gets various model schemes appropriate for particular situations. They are discussed later in chapter 5 with polarization selection rules.

2.2 Systems of identical particles

In the classical physics, one can distinguish macroscopic objects one from the other and, for example, assign a number to each of them. Quantum theory on the contrary deals with the quantum objects which are indistinguishable one from the other and therefore it needs a different formalism which is developed below [11, 12]. The reason is, that quantum

objects have a very small number of degrees of freedom. For example, two photons with equal wave vectors and spins cannot be distinguished one from the other in any type of experiment since they must couple equally to a detection system.

Let's assume in the beginning that there is a possibility of numbering of quantum objects which are of the same nature and their individual states are described by sets of several quantum numbers. If we interchange two particles in the system, no change of the state should be observable. This fact implies that observables must be symmetrical functions of the sets of their variables (i.e. sets of quantum numbers) which describe the system under investigation. The same holds for Hamiltonian thus the energy is invariant under interchange of two particles. In order to give mathematical expressions, we introduce the ket vector of a system of identical particles:

$$|\phi\rangle = \left|c^1_{S_1}\right\rangle \left|c^2_{S_2}\right\rangle \cdots \left|c^N_{S_N}\right\rangle , \tag{2.1}$$

where the c's represent a kind of particles which are distinguished for our purposes by the numbers in the superscript. N gives the total number of the particles and variables S_j represent the sets of quantum numbers appropriate for the particular particles. The basis of the states of the particles is given by the M different sets of quantum numbers $S^{(1)}, S^{(2)}, \ldots, S^{(M)}$. We introduce an operator of interchange of two particles:

$$\hat{P}_{k,\ell}|c^k_{S_k}\rangle|c^\ell_{S_\ell}\rangle = |c^\ell_{S_k}\rangle|c^k_{S_\ell}\rangle , \tag{2.2}$$

which is a special type of an operator of permutation. A general permutation operator $\hat{P}_\alpha$ is then defined as a product of the operators $\hat{P}_{k,\ell}$ defined in (2.2). Depending on the number of interchanges involved in the particular permutation, we distinguish the *even* permutations and *odd* permutations as well as *even* and *odd* permutation operators.

The system of N particles, if described by the sets of quantum numbers $S_1, \ldots, S_N$, is generally in a superposition of the states given by permutations of the state (2.1):

$$|\Psi\rangle = \sum_\alpha F_\alpha \hat{P}_\alpha \left|c^1_{S_1}\right\rangle \left|c^2_{S_2}\right\rangle \cdots \left|c^N_{S_N}\right\rangle , \tag{2.3}$$

where F_α is a c-number. The most important types of states described by the above superposition are the *symmetrical* and the *antisymmetric* state. The symmetrical state $|\Psi_+\rangle$ is the state which doesn't change under any permutation: $\hat{P}_\alpha |\Psi_+\rangle = |\Psi_+\rangle , \ \forall\alpha$. Note that the above equality doesn't follow from the aforementioned assumption that no change of the system is observed after permutation of particles since the phase of the wavefunction is not observable. The antisymmetric state $|\Psi_-\rangle$ is not, on the contrary, invariant under permutation of particles: $\hat{P}_\alpha |\Psi_-\rangle = \pm |\Psi_-\rangle$. The sign on the right hand side depends on whether the permutation is even $(+)$ or odd $(-)$. The types of particles which occur in nature can be classified in terms of the two aforementioned groups of states: particles which occur in symmetrical states are called *bosons* and obey Bose statistics, particles which can be found only in antisymmetrical states are called *fermions* and obey Fermi statistics. The unique properties of fermions and bosons are discussed in the following.

Fermions are the particles determined by the half–integer spin. For example electrons, protons and neutrons have the total spin $\frac{1}{2}$ and they are thus fermions. Since we assumed that every interchange of two fermions changes the sign of the wavefunction, we may write the ket–vector of any state in the form of Slater determinant. Clearly an interchange of two rows or columns changes the sign of the wavefunction. It is known from linear algebra that if there are two equal rows or columns in a determinant, the determinant is equal to

zero. Therefore if two particles in a system of fermions are considered to have the same sets of quantum numbers, the wavefunction is identically zero and therefore the system cannot exist in such state. This fact leads to the well known Pauli exclusion principle, i.e. two fermions cannot occupy the same state. Using an antisymmetrizing operator

$$\hat{A} = N^{-\frac{1}{2}} \sum_{\alpha} (-1)^{\alpha} \hat{P}_{\alpha} \,, \tag{2.4}$$

where N is the number of particles and $(-1)^{\alpha}$ is $+1$ for even permutations and -1 for odd permutations, one can write the Slater determinant in the form:

$$|\Psi_{-}\rangle = \hat{A} \left|c^{1}_{S_1}\right\rangle \left|c^{2}_{S_2}\right\rangle \left|c^{3}_{S_3}\right\rangle \cdots \,. \tag{2.5}$$

It can be shown algebraically that annihilation of the j-th particle transfers the system into the state

$$\left|\Psi'_{-}\right\rangle = (-1)^{(j+1)} \hat{A} |c^{1}_{S_1}\rangle |c^{2}_{S_2}\rangle \cdots |c^{j-1}_{S_{j-1}}\rangle |c^{j+1}_{S_{j+1}}\rangle \cdots \,. \tag{2.6}$$

Let's introduce one–particle annihilation and creation operators in the following way:

$$\begin{aligned} \hat{c}_{S_j}|0\rangle &= 0 \,, \qquad & \hat{c}_{S_j}|S_j\rangle &= |0\rangle \,, \\ \hat{c}^{+}_{S_j}|0\rangle &= |S_j\rangle \,, \qquad & \hat{c}^{+}_{S_j}|S_j\rangle &= 0 \,, \end{aligned} \tag{2.7}$$

where $|0\rangle$ stands for the vacuum state with respect to particles. The last equality follows from the above discussion of the exclusion principle. At this point, I drop the numbering of the particles since they are unambiguously resolved by their quantum numbers . It is possible to prove from the above statements that the following anticommutation relations hold:

$$\{\hat{c}_{S_j}, \hat{c}_{S_\ell}\} = 0 \,, \qquad \{\hat{c}^{+}_{S_j}, \hat{c}^{+}_{S_\ell}\} = 0 \,, \qquad \{\hat{c}_{S_j}, \hat{c}^{+}_{S_\ell}\} = \delta_{S_j S_\ell} \,. \tag{2.8}$$

The anticommutator $\{\hat{a}, \hat{b}\} = \hat{a}\hat{b} + \hat{b}\hat{a}$ was used. Putting $j = \ell$, Pauli exclusion principle can be shown:

$$(\hat{c}_{S_\ell})^2 = 0 \,, \qquad (\hat{c}^{+}_{S_\ell})^2 = 0 \,. \tag{2.9}$$

The operator $\hat{n}_{S_j} = \hat{c}^{+}_{S_j} \hat{c}_{S_j}$, called the population operator, applied on an antisymmetric state, is 0 if the state with quantum numbers given by S_j is not populated, otherwise it is 1. Using the creation operators, the state $|\Psi_{-}\rangle$ can be written in the following way:

$$|\Psi_{-}\rangle = \hat{A}|c_{S_1}\rangle|c_{S_3}\rangle|c_{S_3}\rangle \cdots = \hat{c}^{+}_{S_1} \hat{c}^{+}_{S_2} \hat{c}^{+}_{S_3} \cdots |0\rangle \,. \tag{2.10}$$

The Hamiltonian of the system of particles can be expressed by the creation and annihilation operators. It can be derived following the standard second quantization procedure [13] and for noninteracting fermions, one finds:

$$\hat{H} = \sum_{j=1}^{M} E_{S^{(j)}} \hat{c}^{+}_{S^{(j)}} \hat{c}_{S^{(j)}} \,. \tag{2.11}$$

Particles, which obey the Bose statistics, are those with an integer spin. For example, photons and phonons are exact bosons. Besides these particles, there are also composite bosons made up from several fermions which obey the Bose statistics at low density but reveal more fermion–like character when their density is increased. Since we are interested in the low–density limit throughout the thesis, such complexes will be treated as bosons and

the fermionic nature will be described as a perturbation. Some atoms and excitons are the examples of bosons made up of fermions and thus having the fractional Fermi character. As mentioned above, systems of bosons occur in nature in the symmetrical states, i.e. states which are invariant under permutation of particles. On the contrary to fermions, there is no exclusion principle as will be shown later, i.e. any quantum–mechanical state can be populated by an arbitrary number of particles. According to (2.4), we introduce a symmetrizing operator:

$$\hat{S} = N^{-\frac{1}{2}} \sum_{\alpha} \hat{P}_{\alpha} \,. \tag{2.12}$$

The symmetrical state, on the contrary to fermions, has a different normalization because of no restriction to populations of particular states. It can be written in the form (we use the symbol d for particles in order to discriminate bosons and fermions):

$$|\Psi_+\rangle = (n_{S^{(1)}}! n_{S^{(2)}}! \cdots)^{-\frac{1}{2}} \hat{S} \left|d^1_{S_1}\right\rangle \left|d^2_{S_2}\right\rangle \left|d^3_{S_3}\right\rangle \cdots \,. \tag{2.13}$$

Here, the symbols $n_{S^{(j)}}$ represent the numbers of particles in the quantum–mechanical state defined by the set of quantum numbers $S^{(j)}$. It can be verified that $\langle \Psi_+ | \Psi_+ \rangle = 1$ and that the state (2.13) is invariant under any permutation of particles. For two particles in the same state, we get by the symmetrization procedure:

$$|\Psi_+\rangle = \frac{1}{\sqrt{2}} \hat{S} \left|d^1_s\right\rangle \left|d^2_s\right\rangle = \frac{1}{2} \left(\left|d^1_s\right\rangle \left|d^2_s\right\rangle + \left|d^2_s\right\rangle \left|d^1_s\right\rangle\right) = |d_s\rangle \, |d_s\rangle \neq 0 \,. \tag{2.14}$$

Clearly, the system can exist in such state, i.e. there is no restriction for population of states which comes from the symmetry properties. If no boson–boson interaction is introduced, it is clear that the energy of the system containing n bosons is the sum of energies of contributing particles. This conclusion holds also for the linear harmonic oscillator (LHO), one then might describe bosons as the excitations of LHO, each oscillator then belongs to a particular set of quantum numbers. Populations of the boson levels are expressed by the numbers of excitations of the appropriate oscillators and the multi–particle state $|\Psi_+\rangle$ can be represented by these numbers $n_{S^{(j)}}$. On the contrary to fermions, there is no need for a special order of the one–particle kets (due to invariance under permutation) and therefore one can write:

$$\begin{aligned} |\Psi_+\rangle = |n_{S^{(1)}} n_{S^{(2)}} \cdots n_{S^{(M)}}\rangle = (n_{S^{(1)}}! n_{S^{(2)}}! \cdots)^{-\frac{1}{2}} \cdot \\ \cdot \hat{S} \Big\{ \underbrace{|d^1_{S^{(1)}}\rangle |d^2_{S^{(1)}}\rangle \cdots}_{n_{S^{(1)}} \times} \underbrace{|d^{n_{S^{(1)}}+1}_{S^{(2)}}\rangle |d^{n_{S^{(1)}}+2}_{S^{(2)}}\rangle \cdots}_{n_{S^{(2)}} \times} \cdots \Big\} \,. \end{aligned} \tag{2.15}$$

The basis kets of the system of bosons with the basic sets of spins defined above are:

$$\begin{aligned} &|0\rangle \,, \\ &|1_{S^{(1)}}\rangle \,, \, |1_{S^{(2)}}\rangle \,, \cdots \,, \\ &|2_{S^{(1)}}\rangle \,, \, |2_{S^{(2)}}\rangle \,, \, |1_{S^{(1)}} 1_{S^{(2)}}\rangle \,, \cdots \,, \\ &\quad \vdots \end{aligned} \tag{2.16}$$

The state in the first line is the *vacuum state* (with respect to particles), i.e. all LHOs are in the ground state — no particles are present. The second line represents *one–particle states*, it means that exactly one particle is present. The list continues by *two–particle*

states on the third line (two particles of any quantum numbers are present) and generally m–particle states with m going to infinity. The Hamiltonian in this basis can be generally written in the form:

$$\hat{H} = \sum_j |\Psi_j\rangle\, H_j\, \langle\Psi_j| \;, \tag{2.17}$$

where the summation goes over the basis (2.16) and states $|\Psi_j\rangle$ are eigenstates of the Hamiltonian. According to the discussion of fermions, let's introduce the creation and annihilation operators for bosons. Since the bosons are treated as excitations of LHO, we use their creation and annihilation operators:

$$\begin{aligned} \hat{d}_S\,|0\rangle &= 0\,, & \hat{d}_S\,|n_S\rangle &= \sqrt{n_S}\,|n_S{-}1\rangle \;, \\ \hat{d}_S^+\,|n_S\rangle &= \sqrt{n_S{+}1}\,|n_S{+}1\rangle \;. \end{aligned} \tag{2.18}$$

There is no upper limit for the number of possible excitations. Compared to fermions, the creation and annihilation operators obey *commutation* relations which read:

$$\left[\hat{d}_{S_j}, \hat{d}_{S_\ell}\right] = 0\,, \qquad \left[\hat{d}^+_{S_j}, \hat{d}^+_{S_\ell}\right] = 0\,, \qquad \left[\hat{d}_{S_j}, \hat{d}^+_{S_\ell}\right] = \delta_{j,\ell}\,. \tag{2.19}$$

The operator $\hat{n}_S = \hat{d}_S^+ \hat{d}_S$ is the population operator and its mean value gives the mean number of particles which are in the system in the state S. Using the population operator, it can be shown that:

$$|\psi\rangle = (\hat{d}_S^+)^{n_S}\,|0\rangle \qquad \Rightarrow \qquad \left\langle \psi \left| \hat{n}_S \right| \psi \right\rangle = n_S\,. \tag{2.20}$$

The above equality then justifies us to write the state $|\Psi_+\rangle$ in a more convenient way using the creation operators where no attention must be paid to their order:

$$|\Psi_+\rangle = |n_{S^{(1)}} n_{S^{(2)}} \cdots n_{S^{(M)}}\rangle = \left[\hat{d}^+_{S^{(1)}}\right]^{n_{S^{(1)}}} \left[\hat{d}^+_{S^{(2)}}\right]^{n_{S^{(2)}}} \cdots |0\rangle \;. \tag{2.21}$$

The Hamiltonian can be expressed more conveniently using operators than in Eq. (2.17). Clearly this is the Hamiltonian similar to that of a linear harmonic oscillator:

$$\hat{H} = \sum_{j=1}^{M} E_{S^{(j)}} \left[\hat{d}^+_{S^{(j)}} \hat{d}_{S^{(j)}} + \tfrac{1}{2}\right] + \hat{H}_{\rm int}\,, \tag{2.22}$$

where the first term is the Hamiltonian of noninteracting particles and the term $\hat{H}_{int}$ represents a boson–boson interaction Hamiltonian.

2.3 Density matrix

According to classical statistical physics, mathematical formalism which describes the statistical properties of a system of particles was developed for the purposes of the quantum mechanics. This formalism of *density matrix* is summarized in this section since it will be widely used in the text below.

Let's assume a system which contains a high number of particles. Although it might be generally possible to find a wavefunction describing the state of the system, it is more useful to describe it without the precise knowledge of all (quantum–mechanical) correlations between the wavefunctions of particles, i.e. statistically. We therefore choose a smaller

"representative" subsystem and use the density matrix formalism in order to describe mean values of all correlations which may be found in such representative subsystem (averaging is performed over all small subsystems within the system).

One may use the density matrix formalism also for systems which contain only one particle. Although it would seem useless since one–particle subsystem should always stay in a pure state, it is necessary to realize that the system interacts with its surrounding which may be a heat bath. Every realization of an experiment with the one–particle system then has a unique evolution and the density matrix formalism gives us informations about the mean values of correlations when averaged over all possible realizations of the experiment.

Let $\hat{G}$ be an arbitrary operator and assume an orthonormal basis $|j\rangle\,,\ j = 0 \dots N$. The mean value of $\hat{G}$ in a definite quantum–mechanical state $|\psi\rangle$ can be then expressed as $\langle\hat{G}\rangle = \mathrm{Tr}\,\hat{G}\,|\psi\rangle\langle\psi|$, where $\mathrm{Tr}\hat{M} = \sum_{j=0}^{N}\langle j|\hat{M}|j\rangle$. Now we can perform the averaging over realizations of the wavefunction:

$$\langle\langle\hat{G}\rangle\rangle = \sum_{\psi} p_\psi \mathrm{Tr}\,\hat{G}\,|\psi\rangle\langle\psi|\ , \tag{2.23}$$

where the probability of finding the system in the particular state $|\psi\rangle$ was denoted p_ψ. The density matrix can be therefore defined as:

$$\hat{\varrho} = \sum_{\psi} p_\psi\,|\psi\rangle\langle\psi|\ . \tag{2.24}$$

The above definition is not, however, expressed in a form of a matrix. Inserting the identity operators $\mathbb{1} = \sum_j |j\rangle\langle j|$, we get:

$$\hat{\varrho} = \sum_{\psi}\sum_{j,\ell} |j\rangle\,\langle j|\,\psi\rangle\,p_\psi\,\langle\psi|\,\ell\rangle\,\langle\ell| = \sum_{j,\ell}\varrho_{j\ell}\,|j\rangle\langle\ell|\ , \tag{2.25}$$

$$\varrho_{j\ell} = \sum_{\psi} p_\psi\,\langle\psi|\,\ell\rangle\,\langle j|\,\psi\rangle = \langle j\,|\hat{\varrho}|\,\ell\rangle\ . \tag{2.26}$$

It follows from the definition of $\varrho_{jj} = \sum_\psi p_\psi|\,\langle\psi|\,j\rangle\,|^2$ that the diagonal elements of the density matrix are the probabilities of finding the system in a particular state, i.e. the mean populations of these states. The diagonal elements of the density matrix are then called *populations*. They have not, however, meaning of the number of particles in the system, this property is described by the numbers $\langle j|\hat{n}|j\rangle\varrho_{jj}$. The nondiagonal terms of the density matrix are called *coherences*, their properties are discussed below. It can be shown that the density matrix is hermitian [11]. The mean value of an operator is then, according to (2.23), defined as:

$$\langle\langle\hat{G}\rangle\rangle = \mathrm{Tr}\hat{\varrho}\hat{G}\,. \tag{2.27}$$

From the completeness of the expansion to the states $|\psi\rangle$ in (2.23) it follows that $\mathrm{Tr}\hat{\varrho} = 1$. We know from linear algebra that for a hermitian matrix $\mathrm{Tr}\varrho^2 \le (\mathrm{Tr}\hat{\varrho})^2$ and therefore $\mathrm{Tr}\hat{\varrho}^2 \le 1$. If the system is in a pure state ψ, one finds:

$$\mathrm{Tr}\hat{\varrho}^2 = \mathrm{Tr}\hat{\varrho}\hat{\varrho} = \mathrm{Tr}\,|\psi\rangle\,\langle\psi|\,\psi\rangle\,\langle\psi| = \mathrm{Tr}\hat{\varrho} = 1\,, \tag{2.28}$$

therefore the equality in $\mathrm{Tr}\hat{\varrho}^2 \le 1$ arises only for *pure* states, i.e. states which can be expressed using one wavefunction. Other states are *mixed* and cannot be described by one wavefunction. The equation of motion for the density matrix in Schrödinger picture is:

$$i\hbar\frac{\partial}{\partial t}\hat{\varrho} = [\hat{H}, \hat{\varrho}]\,, \tag{2.29}$$

where $\hat{H}$ is the Hamiltonian of the problem. Density matrix is a constant in Heisenberg picture and operators evolve. We will use an *interaction* picture. The Hamiltonian is separated into a *nonperturbed part* and a *perturbation*: $\hat{H} = \hat{H}_0 + \hat{V}_\mathrm{I}$. The choice of the way how to separate the Hamiltonian is arbitrary with only one requirement that the evolution operator appropriate for $\hat{H}_0$ can be found analytically. The name *interaction* picture comes from the use on systems described by the Hamiltonian $\hat{H}_0$ which are under an influence of a non–stationary perturbation due to e.g. external fields (here optical field). Operators then evolve like in the Heisenberg picture with a nonperturbed Hamiltonian and the temporal evolution of the density matrix is given in the Schrödinger picture according to a transformed interaction Hamiltonian:

$$\hat{U}_0 = \exp\left[-\tfrac{\mathrm{i}}{\hbar}\hat{H}_0\right], \qquad \hat{V}_\mathrm{I} = \hat{U}_0^+ \hat{V} \hat{U}_0\,, \tag{2.30}$$

$$\hat{\varrho} = \hat{U}_0 \hat{\varrho}_\mathrm{I} \hat{U}_0^+\,, \qquad \mathrm{i}\hbar\tfrac{\partial}{\partial t}\hat{U}_\mathrm{I} = \hat{V}_\mathrm{I}\hat{U}_\mathrm{I}\,, \tag{2.31}$$

$$-\mathrm{i}\hbar\frac{\partial}{\partial t}\hat{G}_\mathrm{I} = \left[\hat{V}_\mathrm{I}, \hat{G}_\mathrm{I}\right], \qquad \mathrm{i}\hbar\tfrac{\partial}{\partial t}\hat{\varrho}_\mathrm{I} = \left[\hat{V}_\mathrm{I}, \hat{\varrho}_\mathrm{I}\right], \tag{2.32}$$

where $\hat{G}$ is an arbitrary operator in the Schrödinger picture and transforms to the interaction picture according to (2.30).

It will be shown here how the density matrix elements can be expressed using operators and ensemble averaging. First the density matrix elements are calculated as mean values of some operators. Using the definition (2.24), we can write:

$$\langle j\,|\hat{\varrho}|\,\ell\rangle = \sum_\psi p_\psi \,\langle j|\,\psi\rangle\,\langle\psi|\,\ell\rangle = \sum_\psi p_\psi \,\langle\psi|\,\ell\rangle\,\langle j|\,\psi\rangle = \langle\!\langle |\ell\rangle\langle j| \rangle\!\rangle\,. \tag{2.33}$$

The last average is averaging over the system states and an ensemble. The last equality arises because of invariance of trace operator under cyclic permutation of its argument. The density matrix element $\varrho_{j\ell}$ can be therefore calculated as a mean value of an operator $\hat{\varrho}_{j\ell} = |\ell\rangle\langle j|$. One can use also the creation and annihilation operators in order to calculate density matrix elements. Let's assume now that the system contains identical bosons (including their quantum numbers), therefore the eigenstates are characterized by the number of excited bosons: $|j\rangle = (\hat{d}^+)^j\,|0\rangle$. The point now is to show that for instance $\hat{\varrho}_{11} \neq \hat{d}^+\hat{d}$, therefore to exclude a possible guess $\hat{\varrho}_{j\ell} = (\hat{d}^+)^\ell(\hat{d})^j$. In the following equation, the averages are only in the quantum–mechanical sense:

$$\langle\,|1\rangle\langle 1|\,\rangle = \langle\,\psi|\,1\rangle\,\langle 1|\,\psi\rangle = \langle\psi|\hat{d}^+|0\rangle\langle 0|\hat{d}|\psi\rangle\,, \tag{2.34}$$

$$\langle\hat{d}^+\hat{d}\rangle = \langle\psi|\hat{d}^+\hat{d}|\psi\rangle = \langle\psi|\hat{d}^+|0\rangle\langle 0|\hat{d}|\psi\rangle + \sum_{j=1}^{\infty}|\langle\psi|\hat{d}^+|j\rangle|^2 \geq \langle\,|1\rangle\langle 1|\,\rangle\,. \tag{2.35}$$

It is then clear that one must define:

$$\hat{\varrho}_{j\ell} = |\ell\rangle\langle j| = (\hat{d}^+)^\ell(\hat{d})^j - (\hat{d}^+)^{\ell+1}(\hat{d})^{j+1}\,. \tag{2.36}$$

Considering operators discriminated by some quantum numbers, we can write (2.36) in a more general form (the first number in bra and ket vectors specifies number of particles, the second number stands for other quantum numbers connected with the state):

$$|\ell\lambda\rangle\langle j\mu| = (\hat{d}^+_\lambda)^\ell(\hat{d}_\mu)^j - \sum_\nu (\hat{d}^+_\lambda)^\ell \hat{d}^+_\nu \hat{d}_\nu (\hat{d}_\mu)^j\,. \tag{2.37}$$

Considering the fermion operators, the above formulas can be reasonably simplified with the help of anticommutators (2.8).

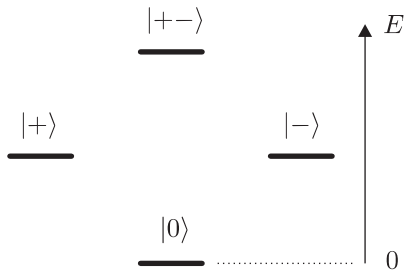

Figure 2.1: Level scheme which represents the states defined in (2.38). For its discussion, see the text below (2.38).

In the following text, I show the connection between populations and coherences in a pure state and the upper limit for the size of coherences according to populations for mixed states. Properties of temporal evolution are outlined at the end of the section.

For an illustration, let's now assume a system which contains two electrons resolved in spin, each of them in either ground or excited state. The electron with the spin $+\frac{1}{2}$ is assumed to couple to the σ^+–polarized light and the electron with its spin $-\frac{1}{2}$ couples to the σ^-–polarized light. The ground state contains both electrons in their ground states and will be denoted $|0\rangle$. The electron creation and annihilation operators will be $\hat{c}^+_{\pm\frac{1}{2}}$ and $\hat{c}_{\pm\frac{1}{2}}$, respectively. Using (2.10), we find the complete basis of the electron states:

$$|0\rangle = \hat{A}|0_{\frac{1}{2}}\rangle|0_{-\frac{1}{2}}\rangle\,, \qquad |+-\rangle = \hat{c}^+_{-\frac{1}{2}}\hat{c}^+_{\frac{1}{2}}\,|0\rangle\ , \tag{2.38}$$

$$|-\rangle = \hat{c}^+_{-\frac{1}{2}}\,|0\rangle\ , \qquad |+\rangle = \hat{c}^+_{\frac{1}{2}}\,|0\rangle\ ,\ . \tag{2.39}$$

This system of states can be schematically drawn using a level scheme, each level representing one of the quantum–mechanical states, see Fig. 2.1. The vertical axis in the sketch represents energy, i.e. the ground state has the lowest (zero) energy and the two–electron state has the highest energy.

The state of the system depicted in Fig. 2.1 can be expressed using the density matrix formalism presented in the section 2.3. We introduce a 4×4 density matrix $\hat{\varrho}$. We assume that the system is in its ground state at $t = 0$, i.e. $\hat{\varrho}(t{=}0) = |0\rangle\langle 0|$ and its temporal evolution is influenced by a resonant and stationary external field, here we assume optical field in the semiclassical approach. The Hamiltonian has the form (in the rotating wave approximation) [1]:

$$\begin{aligned}\hat{H} = {} & \hbar\omega_0[\,|+\rangle\langle +| \,+\, |-\rangle\langle -| \,+\, 2\,|+-\rangle\langle +-|\,] \,+ \\ & + [d_+\mathrm{e}^{-\mathrm{i}\omega_0 t}\,|+\rangle\langle 0| \,+\, d_-\mathrm{e}^{-\mathrm{i}\omega_0 t}\,|-\rangle\langle 0| \,+\, H.c] + \\ & + [d_+\mathrm{e}^{-\mathrm{i}\omega_0 t}\,|+-\rangle\langle -| \,+\, d_-\mathrm{e}^{-\mathrm{i}\omega_0 t}\,|+-\rangle\langle +| \,+\, H.c]\,.\end{aligned} \tag{2.40}$$

The first line stands for the energies of the states and the second and the third line stand for a dipole interaction with the optical field of the strength $d_\pm$ (for two polarizations) and with frequency ω_0. The symbol $H.c.$ denotes the hermitian conjugate terms. The third line immediately follows from the second line or from the Hamiltonian when expressed by operators. Let's assume for instance $d_- = 0$ and therefore the system is in a superposition:

$$|\psi(t>0)\rangle = f_0(t)\,|0\rangle + f_+(t)\,|+\rangle\ , \tag{2.41}$$

where $f_0(t)$ and $f_+(t)$ are generally complex functions which can be determined from the Schrödinger equation. With definition $\omega_R = d_+/\hbar$, the solutions of Schrödinger equation are:

$$f_0(t) = \cos(\omega_R t)\,, \tag{2.42}$$
$$f_+(t) = \sin(\omega_R t)\mathrm{e}^{-\mathrm{i}\omega_0 t}\,. \tag{2.43}$$

The variable ω_R is called the *Rabi frequency* and the oscillations of the wavefunction between the states are the *Rabi oscillations*. There was no need of the density matrix approach so far since the state remains in a pure and normalized ($|f_0|^2 + |f_+|^2 = 1$) state. We get from (2.33) $\varrho_{00} = |f_0|^2$ and $\varrho_{++} = |f_+|^2$, i.e. the population of an ensemble of systems undergo the Rabi oscillations which have the same phase in the respective systems. Coherences can be also calculated by a direct application of (2.33):

$$\varrho_{0+} = \sin(\omega_R t)\cos(\omega_R t)\mathrm{e}^{-\mathrm{i}\omega_0 t} = \varrho_{+0}^*\,. \tag{2.44}$$

The above results can be verified using the density matrix formalism with the Schrödinger equation (2.29). The nondiagonal elements of the density matrix are thus correlations between the quantum–mechanical states. Since the density matrix formalism performs averaging over all possible realizations of an experiment, the correct interpretation of the density matrix elements should be that the diagonal elements are the *mean populations of the appropriate states* and the nondiagonal elements are the *mean correlations* where the word *mean* is used in the sense of the averaging over possible realizations.

According to the above example, let's calculate what are the values of the coherences if a system is in a pure state. Such state can be expressed using the basis functions:

$$|\psi\rangle = \sum f_j\,|j\rangle\ , \tag{2.45}$$

where f_j are arbitrary coefficients. Formula (2.33) shows that

$$\varrho_{j\ell} = \langle\!\langle |\ell\rangle\langle j| \rangle\!\rangle = f_j f_\ell^*\,. \tag{2.46}$$

We can prove that coherences defined by the above formula imply the pure state. By the definition, diagonal elements of the density matrix obey the sum rule:

$$\mathrm{Tr}\hat{\varrho} = 1 = \sum_j \varrho_{jj} = \sum_j S_j^2\,, \tag{2.47}$$

where we defined numbers $S_j = \sqrt{\varrho_{jj}} = |f_j|$. We can therefore write:

$$1 = \left(\sum_j S_{jj}^2\right)^2 = \sum_{j,\ell} S_j^2 S_\ell^2\,. \tag{2.48}$$

Pure states must fulfil the equality $\mathrm{Tr}\hat{\varrho}^2 = 1$. If we set $\varrho_{j\ell} = S_j S_\ell u_{j\ell}$ where $u_{j\ell}$ is a complex unity, we get:

$$\mathrm{Tr}\hat{\varrho}^2 = \sum_{j,\ell} \varrho_{j\ell}\varrho_{\ell j}^* = \sum_{j,\ell} |S_j|^2|S_\ell|^2 = 1\,, \quad \text{q.e.d.} \tag{2.49}$$

We used the equality (2.48) and $S_j = |S_j|$ in the proof because populations are real and positive. In a mixed state, coherences cannot exceed the calculated values for a pure state. This statement doesn't directly follow from (2.49) but it is easy to prove it: assume now

particular realizations of an experiment. The system is then described by its wavefunction (i.e. it is in a pure state). Coherences are then expressed as calculated above: $\varrho_{j\ell} = S_j S_\ell u_{j\ell}^{(1)}$ with an appropriate phase described by the function $u_{j\ell}^{(1)}$, $|u_{j\ell}^{(1)}| = 1$. In a second realization, the coherence would be $\varrho_{j\ell} = S_j S_\ell u_{j\ell}^{(2)}$, i.e. it has the same size but differs in the phase. The average over all realization then gives:

$$|\langle \varrho_{j\ell} \rangle| = \frac{S_j S_\ell}{N} \left| \sum_{m=1}^{N} u_{j\ell}^{(m)} \right| \leq S_j S_\ell = \sqrt{\varrho_{jj}\varrho_{\ell\ell}} = \sqrt{\langle \varrho_{jj} \rangle \langle \varrho_{\ell\ell} \rangle}\,. \tag{2.50}$$

Up to now, a fixed populations in every single realization of the experiment were assumed and the question is, whether the inequality (2.50) remains valid also if the populations vary in particular realizations. We can write:

$$\begin{aligned} |\langle \varrho_{j\ell} \rangle|^2 &= \frac{1}{N} \left| \sum_{m=1}^{N} S_j^{(m)} S_\ell^{(m)} u_{j\ell}^{(m)} \right|^2 \leq \frac{1}{N^2} \left(\sum_{m=1}^{N} S_j^{(m)} S_\ell^{(m)} \right)^2 \leq \\ &\leq \frac{1}{N^2} \left[\sum_{m=1}^{N} \left(S_j^{(m)} \right)^2 \right] \left[\sum_{m=1}^{N} \left(S_\ell^{(m)} \right)^2 \right] = \langle \varrho_{jj} \rangle \langle \varrho_{\ell\ell} \rangle \,. \end{aligned} \tag{2.51}$$

The inequality (2.50) is then general. It follows directly that if the system is e.g. in the pure state $|+\rangle$, the population $\varrho_{++} = 1$ and all other populations are zero. All coherences are then clearly zero, as shown in (2.50) and thus the state of the system is described by one real number ϱ_{++}. This real number does not, however, contain any information about the phase of the system and the system's wavefunction is not described unambiguously. This fact is quite natural since the phase is a variable which is not defined absolutely but relatively. Coherences then correlate phases of the states which are superposed in the wavefunction. Correlations with respect to the system's neighbourhood are missing until we include the surrounding to the system.

For the purpose of discussion of interaction of systems with optical fields, the coherences can be classified to several basic types depending on the nature of states, whose correlations are expressed by the particular coherences. The nature of the states may be discriminated by the number of particles which occupy the level and the coherences are then classified by the difference of these occupation numbers of the correlated states. States $|0\rangle$ and $|\pm\rangle$ in our system differ by one absorbed photon, therefore the coherences $\varrho_{0\pm}$ and $\varrho_{\pm 0}$ will be called *one–photon coherences* in the following text. The reference to photons is due to the fact that the correlations described by these coherences obey correlations between photons if the particles are created by photon absorption. Clearly the coherences $\varrho_{\pm,+-}$ and $\varrho_{+-,\pm}$ are also one–photon coherences. These one–photon coherences represent the macroscopic polarization of the system. Mean value $\langle \hat{P} \rangle = \langle \hat{c}^+ \rangle$ is then the source term in the Maxwell equations. The coherences $\varrho_{0,+-}$ and $\varrho_{+-,0}$ are *two–photon coherences* since they reflect coherence properties of two–photon states. Coherences $\varrho_{+,-}$ and $\varrho_{-,+}$ are of a big interest and they are called *spin coherences*, generally coherences between states with the same number of particles will be called *zero–photon coherences*. These coherences reflect the correlations between two spin states, i.e. what is the correlation between the temporal evolution of one spin with respect to the second one. I discuss the spin coherences in more detail here.

The first thing to be mentioned is, that spin coherences do not describe evolution of the system where both spins are excited and what are the respective correlations of the two

spins. When the system is in a two–particle state, the wavefunction as a whole has some quantum–mechanical phase which is not related to the spin coherence. Spin coherence is a coherence which correlates a one–particle state with respect to another one–particle state, i.e. what is the correlation between the states $|+\rangle$ and $|-\rangle$ superposed in the system's wavefunction.

Assume a repeated experiment: we excite an atom by polarized light and then test the correlation between the states $|+\rangle$ and $|-\rangle$ e.g. by measurement of the polarization of the re–emitted light. The wavefunction (without interaction with a heat bath) in an m–th realization of the experiment is then:

$$|\psi^{(m)}(t)\rangle = f_0^{(m)}(t)\,|0\rangle + f_+^{(m)}(t)\,|+\rangle + f_-^{(m)}(t)\,|-\rangle + f_{+-}^{(m)}(t)\,|+-\rangle\ . \tag{2.52}$$

The spin coherence ϱ_{+-} will be then proportional to the correlation between $f_+(t)$ and $f_-(t)$, i.e. to the number $\left\langle f_+^*(t) f_-(t)\right\rangle$. Since we assumed no interaction which could destroy the phase of the wavefunction, the state of the system is always described by the above formula with $f_j^{(m)}(t) = f_j(t)$ where the functions were the same in all realizations. Now assume there exists for example a random scattering mechanism which is not spin sensitive and does not cause any population changes in the system. The wavefunction then changes and we get:

$$f_0(t)^{(m)} = f_0(t)\mathrm{e}^{\mathrm{i}\phi_0^{(m)}(t)}\,, \tag{2.53}$$

$$f_+(t)^{(m)} = f_+(t)\mathrm{e}^{\mathrm{i}\phi_\pm^{(m)}(t)}\,, \tag{2.54}$$

$$f_-(t)^{(m)} = f_-(t)\mathrm{e}^{\mathrm{i}\phi_\pm^{(m)}(t)}\,, \tag{2.55}$$

$$f_{+-}(t)^{(m)} = f_{+-}(t)\mathrm{e}^{\mathrm{i}\phi_{+-}^{(m)}(t)}\,. \tag{2.56}$$

The functions $f_+^{(m)}(t)$ and $f_-^{(m)}(t)$ have thus the same phases which cancel in the correlation function $\left\langle f_+^*(t) f_-(t)\right\rangle$ and thus the spin coherence prevails although all other coherences decrease in time. Let's now include a new scattering mechanism which is spin–sensitive and doesn't change populations. The random phases of the functions $f_+^{(m)}(t)$ and $f_-^{(m)}(t)$ now differ and thus the coherence decreases in time.

The conclusion of the above discussion is, that the spin coherences prevail for a much longer time than the photon coherences. They can be nonzero as long as the populations of the spins are nonzero due to inequality (2.50). The difference from the value $\sqrt{\varrho_{++}\varrho_{--}}$ is caused by a *spin–sensitive loss of phase*, i.e. if an interaction, which is specific for the particular polarizations, is present. The populations in the density matrix are the special cases of spin coherences and the above calculations give the correct result for their temporal evolution since it is always $\varrho_{\pm\pm} = |f_\pm(t)|^2$.

With the use of (2.50), we can prove one more statement which is important in connection to the optical transitions and correlations between the optical field and the system. Assume that the interaction between the system and the heat bath causes relaxation of population, i.e. transitions from a one–particle state to the ground state. Interaction with a thermalized bath gives the exponential decay of population:

$$\varrho_{++}(t) = \varrho_{++}(t_0)\mathrm{e}^{-(t-t_0)/T_1}\,, \tag{2.57}$$

$$\varrho_{00}(t) = 1 - \varrho_{++}(t_0)\mathrm{e}^{-(t-t_0)/T_1}\,. \tag{2.58}$$

We then directly apply (2.50) and we get the upper limit of the coherence between the ground and the excited state:

$$|\varrho_{0+}(t)| \le \sqrt{\left(1-\varrho_{++}(t_0)\mathrm{e}^{-(t-t_0)/T_1}\right)\varrho_{++}(t_0)\mathrm{e}^{-(t-t_0)/T_1}} \approx \sqrt{\varrho_{++}(t_0)}\mathrm{e}^{-(t-t_0)/2T_1}\,. \tag{2.59}$$

The last step was an assumption of a weak excitation and thus $\varrho_{++}(t_0) \ll 1$. The lower limit of the coherence decay is clearly given by the time constant $T_2 = 2T_1$.

The decrease of coherences and populations was ad–hoc described by a monoexponential decay. One usually assumes that the system interacts with a large thermalized heat bath and thus the dynamics can be in most cases described as monoexponential. The decay of the coherences is then called *dephasing* and the decay of populations *relaxation*. I use the time constant *dephasing time* T_2 and *dephasing rate* $\Gamma_2 = T_2^{-1}$ for the dephasing processes and *relaxation time* T_1 and *relaxation rate* $\Gamma_1 = T_1^{-1}$ for the relaxation processes.

2.4 Atomic systems

Atomic systems are those systems composed of a large number of single atoms. More generally, we can include also systems of molecules or very small crystals under the name "atomic systems". The requirement is, that the particles under consideration do not influence one the other and they are randomly distributed in space. We require in addition the Fermi statistics of optical excitations. Since the collective excitations of atoms in molecules (rotational and vibration modes in molecules, phonons in crystals) obey the Bose statistics, we take into account only excitations of the system of electrons which are energetically well separated from the vibrational and rotational spectra. The boson excitations are then treated as the heat bath. Every particle therefore represents a system with discrete energetical levels which is uncorrelated (in space, phase etc.) with respect to other particles.

I consider a general atomic system in this chapter. In derivation of optical Bloch equations, one usually considers a single two–level system (i.e. a hydrogen atom), however I implicitly consider spin here. It is not explicitly included in OBE (section 2.5) but based on this chapter, polarization selection rules for FWM on atomic systems are derived later in chapter 4.

Interaction of light and matter is treated semiclassically throughout the thesis, i.e. matter is described quantum–mechanically and the optical field (and other external fields) classically. For the optical field, a Slowly Varying Envelope Approximation [14] (SVEA) will be used. It means that the variations of the optical field (its intensity and frequency) in time are assumed to be slow with respect to the oscillations of the vectors of electric and magnetic fields. The vector of the intensity of electric field is then defined using the slowly varying envelope $\mathcal{E}(t)$, central frequency ω_0 and polarization vector $\boldsymbol{e}$ as follows:

$$\boldsymbol{E}(t) = \frac{\boldsymbol{e}}{2}\left[\mathcal{E}(t)\mathrm{e}^{-\mathrm{i}\omega_0 t} + \mathcal{E}^*(t)\mathrm{e}^{\mathrm{i}\omega_0 t}\right] = \boldsymbol{E}^{(-)}(t) + \boldsymbol{E}^{(+)}(t)\,. \tag{2.60}$$

The last equality defines the negative and the positive energy complex parts, respectively. Interaction of the optical field with hydrogen atoms is in the dipole approximation defined by the Hamiltonian:

$$\hat{H}_{\mathrm{int}} = -e\hat{\boldsymbol{r}}\cdot\boldsymbol{E}(t) = -\hat{\boldsymbol{d}}\cdot\boldsymbol{e}E(t)\,, \tag{2.61}$$

where $\hat{\boldsymbol{d}}$ is the dipole moment operator. The Hamiltonian in braket notation reads:

$$\hat{H}_{\mathrm{int}} = -E(t)\boldsymbol{e}\cdot\left[d_+\boldsymbol{e}_+^*\left(|0\rangle\langle+| + |+\rangle\langle 0|\right) + d_-\boldsymbol{e}_-^*\left(|0\rangle\langle-| + |-\rangle\langle 0|\right)\right]\,, \tag{2.62}$$

where I defined $d_+ = \langle 0|\hat{\boldsymbol{d}}|+\rangle$ and $d_- = \langle 0|\hat{\boldsymbol{d}}|-\rangle$ and $\boldsymbol{e}_\pm$ are the polarization vectors for the two respective circular polarizations $\sigma^\pm$ of the optical field. Frequency of the optical

field can, however, vary from the point of view of the particular atoms due to the Doppler effect. The absorption line of the atomic system is thus inhomogeneously broadened.

Before we start development of the theory, let's first identify which processes are responsible for the wave mixing, i.e. creation of the third–order response in a direction which differs from the directions of the incoming fields. We search processes in which interaction of an atom with one photon influences the interaction with the second and the third photon.

The first process to be mentioned is Pauli blocking. The explanation of the wave mixing principle is very simple: assume two optical fields which create an interference pattern in space[1]. The standing waves of the electromagnetic field then interact with atoms and create the population grating. The last photon then feels modulation of refractive index due to saturation effect (caused by Pauli blocking) and thus it diffracts. Diffraction direction is then given by the wave vectors of the incoming photons. If the first two photons have wave vectors $\boldsymbol{K}_1, \boldsymbol{K}_3$ or $\boldsymbol{K}_2, \boldsymbol{K}_3$, the diffraction direction is $\boldsymbol{K}_1+\boldsymbol{K}_2-\boldsymbol{K}_3$ [17].

There exists one more process which forms a diffraction grating, similarly to Pauli blocking. This is the optical Stark effect. The interference pattern created by the first two (strong) optical fields changes periodically the resonance energy of the particular atoms. The last, spectrally narrow, field then feels again a modification of the absorption coefficient. This effect is, however, too weak in comparison to Pauli blocking in atoms. Inhomogeneous broadening in addition causes vanishing of this effect in gases. But it was predicted and measured in semiconductors [18].

There is one more possibility how the optical fields influence one the other. An absorbed photon gives some momentum to the atom. The only effect is, that the absorption spectrum of the atom changes a little. The variations of the resonance energy with the propagation direction of the atom (within the range of the changes caused by photon absorption) are, however, very small and thus this phenomenon is hidden within the spontaneous fluctuations of the gas.

We can conclude that Pauli blocking is the only one interaction which can effectively mix the optical fields in the atomic systems. I will therefore omit all other phenomena in the following.

2.5 Optical Bloch Equations

In an optical experiment, optical field is used for both excitation and detection of the changes which occur inside the material. It means that the optical field is a source term in our description and we are interested in the intensity of the optical field which comes from the medium. This point is important in order to realize which quantity is of our interest in the following calculation. We start the mathematical description by the wave equation for the optical field (in SI units):

$$\left[\nabla^2 - \frac{n^2}{c^2}\frac{\partial^2}{\partial t^2}\right] E(t) = -\mu \frac{\partial^2}{\partial t^2} P(t)\,, \tag{2.63}$$

where ∇^2 is the Laplace operator, n the background refractive index, c the vacuum light velocity and μ is the medium magnetic permeability. $E(t)$ is the magnitude of the intensity

[1] The concept of the diffraction grating works in the systems where the positions of the atoms are fixed. In gases, Pauli blocking works as well but the separation of the third–order response is not done by spatial filtering but by temporal filtering instead. The technique of photon echo [15, 16] is used on gases.

of electric field (compared to (2.60), the polarization vector is omitted) and $P(t)$ is the magnitude of the material's polarization. We are then interested in calculation of the macroscopic polarization of the matter. Macroscopic polarization is determined by the mean value of the operator $\hat{c}^+ + \hat{c}$, i.e. $P = N_{\mathrm{at}}\langle\langle \hat{c}^+ + \hat{c} \rangle\rangle = N_{\mathrm{at}}\mathrm{Tr}(\hat{c}^+ + \hat{c})\hat{\varrho}$, where N_{at} stands for the density of atoms and $\hat{\varrho}$ is a one–atom density matrix.

Let's assume in this section that light is polarized having for instance the σ^+ polarization (which is the eigenstate of the polarization vector in the sample). We therefore could omit the polarization vector in the wave equation and also we can assume interaction with only one of the two–level systems within the model of atoms. The calculations below therefore lead to the well known model of Optical Bloch Equations (OBE). Calculations which include both spins are in chapter 5.

Hamiltonian of the problem can be extracted from (2.40) assuming now that the energy of photons does not generally coincide with the energy of the excited electrons:

$$\hat{H} = \hat{H}_0 + \hat{V} = \begin{pmatrix} 0 & 0 \\ 0 & E_{\mathrm{X}} \end{pmatrix} + dE(t) \begin{pmatrix} 0 & 1 \\ 1 & 0 \end{pmatrix} . \tag{2.64}$$

Symbol E_{X} stands for the energy difference between the ground and the excited state of the system. Because of the structure of the Hamiltonian, it is convenient to use the interaction picture. We perform the transformation:

$$\hat{U}_0(t - t_0) = \begin{pmatrix} 1 & 0 \\ 0 & \mathrm{e}^{-\mathrm{i}\omega_{\mathrm{X}} t} \end{pmatrix} , \tag{2.65}$$

$$\hat{V}_{\mathrm{I}}(t - t_0) = \hat{U}_0^+(t - t_0)\hat{V}(t)\hat{U}_0(t - t_0) = dE(t) \begin{pmatrix} 0 & \mathrm{e}^{-\mathrm{i}\omega_{\mathrm{X}}(t-t_0)} \\ \mathrm{e}^{\mathrm{i}\omega_{\mathrm{X}}(t-t_0)} & 0 \end{pmatrix} , \tag{2.66}$$

where we defined $\omega_{\mathrm{X}} = E_{\mathrm{X}}/\hbar$. Using the definition (2.60), we see that the nondiagonal terms in the matrix $\hat{V}_{\mathrm{I}}$ contain two oscillating parts: one oscillates slowly and one rapidly. We expect the main contribution from the slowly oscillating part and therefore the other one is neglected. This approximation is called *Rotating Wave Approximation* (RWA). After setting $t_0 = 0$, we get the result:

$$\hat{V}_{\mathrm{I}} = \frac{d}{2} \begin{pmatrix} 0 & \mathcal{E}^*(t)\mathrm{e}^{-\mathrm{i}\delta\omega t} \\ \mathcal{E}(t)\mathrm{e}^{\mathrm{i}\delta\omega t} & 0 \end{pmatrix} , \tag{2.67}$$

where the definition of the detuning $\delta\omega = \omega_{\mathrm{X}} - \omega_0$ was used. Density matrix is obviously a square 2×2 matrix. At this stage, we can directly use the equation of motion for density matrix in the interaction picture (2.32) and we get:

$$\mathrm{i}\hbar\frac{\partial}{\partial t}\hat{\varrho}_{\mathrm{I}} = \frac{d}{2} \begin{pmatrix} \mathcal{E}^*(t)\mathrm{e}^{-\mathrm{i}\delta\omega t}\varrho_{21} - \mathcal{E}(t)\mathrm{e}^{\mathrm{i}\delta\omega t}\varrho_{12} & \mathcal{E}^*(t)\mathrm{e}^{-\mathrm{i}\delta\omega t}(\varrho_{22} - \varrho_{11}) \\ \mathcal{E}(t)\mathrm{e}^{\mathrm{i}\delta\omega t}(\varrho_{11} - \varrho_{22}) & \mathcal{E}(t)\mathrm{e}^{\mathrm{i}\delta\omega t}\varrho_{12} - \mathcal{E}^*(t)\mathrm{e}^{-\mathrm{i}\delta\omega t}\varrho_{21} \end{pmatrix} . \tag{2.68}$$

Now we use some identities, namely $\varrho_{12} = \varrho_{21}^*$ and $\varrho_{11} + \varrho_{22} = 1$. We define a microscopic polarization $\tilde{p} = \tilde{\varrho}_{21}$ and inversion $\tilde{n} = \frac{1}{2}(\tilde{\varrho}_{22} - \tilde{\varrho}_{11} + 1)$ where we used the tilde in order to denote variables in interaction picture. The quantities in the Schrödinger picture are: $p = \tilde{p}\mathrm{e}^{-\mathrm{i}\omega_X t}$ and $n = \tilde{n}$. Using the new quantities, the equations of motion can be written as follows:

$$\left[\frac{\partial}{\partial t} + \Gamma_1\right] n(t) = \frac{d}{\hbar}\mathrm{Im}\left[\mathcal{E}^*(t)\mathrm{e}^{-\mathrm{i}\delta\omega t}p(t)\right] , \tag{2.69}$$

$$\left[\frac{\partial}{\partial t} + \Gamma_2\right] p(t) = i\frac{d}{2\hbar}\mathcal{E}(t)\mathrm{e}^{\mathrm{i}\delta\omega t}[2n(t) - 1] . \tag{2.70}$$

The quantities Γ_1 and Γ_2 represent the population relaxation and dephasing rates, respectively, as discussed in the section 2.3. The equations above are known as *Optical Bloch Equations*. There exist many equivalent forms of the equations, see e.g. [13, 16, 19, 20, 21]. Assuming $\Gamma_1 = \Gamma_2 = \delta\omega = 0$ and $\mathcal{E}(t) = \mathcal{E}_0$, we find the solutions in a form of periodic oscillations with the Rabi frequency

$$\omega_{\mathrm{R}} = \frac{\mathcal{E}_0 d}{\hbar}\,. \tag{2.71}$$

The whole problem is now described by a system of equations (2.63), (2.69)–(2.70). The whole closed system of equations is called *Maxwell–Bloch Equations*. The structure of the equations is, however, inconvenient for analytic solutions because of the spatial derivatives (one then cannot solve the equations locally) and because of the nonlinearity of the OBE. The system of equations is usually simplified in two stages. First, we take the optical field as a source term and therefore we assume that it obeys the homogeneous wave equation (2.63) with right hand side equal to zero. The OBE are then solved and we calculate the system polarization which then plays a role of the source term for the induced field. The second approximation is, that the functions $E(t)$, $p(t)$ and $n(t)$ are expanded into series [21]:

$$E(t) = E^{(0)}(t) + E^{(1)}(t) + E^{(3)}(t) + \cdots\,, \tag{2.72}$$

$$p(t) = p^{(1)}(t) + p^{(3)}(t) + \cdots\,, \tag{2.73}$$

$$n(t) = n^{(2)}(t) + n^{(4)}(t) + \cdots \tag{2.74}$$

The term $E^{(0)}(t)$ is the source term of the optical field. Solution of equations is simplified since the function $p^{(3)}(t)$ can be found by direct integration. The wave equation is then linear and therefore solvable analytically. The appropriate equations are:

$$p^{(1)} = -\mathrm{i}\frac{d}{2\hbar}\mathrm{e}^{-\Gamma_2 t}\int_{-\infty}^{t}\mathrm{e}^{\Gamma_2 t'}\mathcal{E}^{(0)}(t')\mathrm{e}^{\mathrm{i}\delta\omega t'}\,\mathrm{d}t'\,, \tag{2.75}$$

$$n^{(2)} = \frac{d}{\hbar}\mathrm{e}^{-\Gamma_1 t}\int_{-\infty}^{t}\mathrm{e}^{\Gamma_1 t'}\mathrm{Im}\left[(\mathcal{E}^{(0)}(t'))^{*}\mathrm{e}^{-\mathrm{i}\delta\omega t'}p^{(1)}(t')\right]\,\mathrm{d}t'\,, \tag{2.76}$$

$$p^{(3)} = \mathrm{i}\frac{d}{2\hbar}\mathrm{e}^{-\Gamma_2 t}\int_{-\infty}^{t}\mathrm{e}^{\Gamma_2 t'}\mathcal{E}^{(0)}(t')\mathrm{e}^{\mathrm{i}\delta\omega t'}[2n^{(2)}(t') - 1]\,\mathrm{d}t'\,. \tag{2.77}$$

The perturbative approach can be used only under consideration of weak excitation field in order to allow the separation of the wave equation and the Bloch equations and to ensure that the series in expansion (2.72)–(2.74) converge. This requirement allows us to calculate the response up to any desired order, in the case of FWM to the third order.

In four–wave mixing experiments, one usually uses ultrashort pulses with duration of picoseconds. If we focus only on the perturbative solution of the Bloch equations and not on the solution of the whole set of equations, we can approximate the excitation pulses by delta functions. The pulses arrive on the sample in a certain order, let's assume for instance $t_1 < t_3 < t_2$ (this order is chosen in order to get the response in the correct FWM direction). The above integrals can be then solved analytically with substitution of the field $\mathcal{E}^{(0)}$ by the respective fields $\mathcal{E}_1$, $\mathcal{E}_3$ and $\mathcal{E}_2$ from the top to the bottom equation. The diffraction direction is then obviously $\boldsymbol{K}_1+\boldsymbol{K}_2-\boldsymbol{K}_3$ and $-\boldsymbol{K}_1+\boldsymbol{K}_2+\boldsymbol{K}_3$ and we learn that the temporal order determines the diffraction direction.

The dynamics of the third–order polarization and therefore the dynamics of the field radiated by the two–level system is, according to (2.77), monoexponential after arrival

of the last pulse. This is quite natural since the population grating created by the first two optical pulses represents a diffraction grating for the last pulse. The response of the system is then expected to be instantaneous and to relax monoexponentially according to dephasing time of the created coherence.

In order to show all main features of the third–order response of atomic systems, one should discuss also inhomogeneously broadened systems. More details can be found i.e. in [15, 16, 21]. In such systems, the variable $\delta\omega$ is not a constant for all particles but it varies due to variations of the energy of the excited state in the particular two–level system (these variations can be caused e.g. by size distribution within an ensemble of nanocrystals) or due to variations of energy of the excitation field (caused by Doppler effect in gases). The third–order optical response is then given by a sum over all particles what is effectively an integral over the distribution of $\delta\omega$. As a result, third–order fields radiated by particles add to the sum with various phases and the overall field diminishes very rapidly in time. This decrease may be much faster than the damping described by dephasing constants. Using a strong third pulse, phases of the two–level systems may be inverted and after some time delay, the contributions to the overall polarization may add constructively. A strong pulse is therefore observed in the third–order response and this pulse is called *photon echo*. The temporal delay between the third pulse and the peak of photon echo is equal to the temporal delay between the second and the last pulse. Calculations of such phenomenon are beyond the scope of this work so they are not present here. It is only to be noted that the perturbative equations (2.75–2.77) cannot be used and it is necessary to use a nonperturbative approach.

Clearly OBE may be used only in the weak excitation regime, i.e. $n^{(2)} \ll 1$. In addition, OBE cannot be used in the strong interaction regime with optical fields. The reason is, that the strong interaction cannot be evaluated perturbatively according to the separation into Maxwell and Bloch equations. One then needs the full system of Maxwell–Bloch equations.

The last note concerns atom–atom correlations. These correlations are overestimated in OBE since the description using single two–level systems a priori conserve them. Dephasing of these correlations then must be phenomenologically included to equations e.g. by modification of dephasing rate Γ_2.

Chapter 3

Semiconductors

3.1 Introduction

The main point of this thesis is the description of the third–order optical response of semiconductors. After an illustrative discussion of atomic systems in section 2.4, semiconductors are introduced. This chapter gives a brief overview of the main properties of semiconductors and their nanostructures with a special attention paid to the symmetry of the crystal lattice and optical excitations since they predominantly determine the polarization of the third–order nonlinear optical response.

The chapter begins in section 3.2 by an introduction of band structure, electrons and holes and their bound states–excitons. In section 3.3, symmetry of excitons and their spin are introduced. Coherent precession of the spin and its relaxation are discussed. Excitons are not independent particles because of their mutual Coulomb interactions and the consequences are discussed in section 3.4. Exciton–photon coupling is reviewed at the end of that section. The last section 3.5 then introduces semiconductor nanostructures and shows how the aforementioned phenomena are described in such systems.

3.2 Band structure and excitons

3.2.1 Electron bands

Semiconductors are solid materials in which the atoms are arranged in a periodic lattice. The distances between atoms are comparable to atomic radii and therefore electrons are shared by all atoms within the whole volume of a crystal. The lattice made of positive charges is then felt by electrons as an effective periodic potential V_0. Since the potential is a superposition of the potential of an attractive Coulomb interaction between an electron and nuclei and a repulsive interaction between the electron and other electrons, its concrete profile is generally unknown; however, it is possible to consider some of its basic properties in order to express the electron wavefunction, the constants which are involved in this wavefunction are then measured in an experiment.

We will need only an information about the spatial symmetry of the potential, i.e. the spatial symmetry of the crystal lattice since it determines the symmetry of the whole system. We take into account both spatial symmetries: translational and rotational. Strictly speaking, one should take into account the translational–rotational symmetry since electrons may propagate through the crystal lattice. There is not, however, any theory which describes the electron states on the basis of this symmetry and one thus has to approximate calculations by assuming the translational symmetry and subsequent perturbative inclusion of the rotational symmetry.

The translational symmetry of the lattice leads to a periodical electron wavefunction in the form of Bloch states $|\lambda\boldsymbol{k}\rangle$ [13]: $\langle\boldsymbol{r}|\,\lambda\boldsymbol{k}\rangle = \mathrm{e}^{\mathrm{i}\boldsymbol{k}\cdot\boldsymbol{r}}u_\lambda(\boldsymbol{k},\boldsymbol{r})/\sqrt{\Omega}$, where λ denotes electron quantum numbers except wave vector $\boldsymbol{k}$, Ω is a normalization volume and $u_\lambda(\boldsymbol{k},\boldsymbol{r})$ is *Bloch function*. Due to existence of crystal boundaries, one must define boundary conditions. One usually considers *periodical boundary conditions* in order to conserve translational symmetry. Crystal surface is accounted for as a perturbation which leads to formation of *surface states*. Surface becomes important in *nanostructures* in which it cannot be taken into account only perturbatively (see section 3.5). Inserting of the expression for Bloch state into Schrödinger equation, one gets the basic equation for Kane's k–p theory [13].

Fermi level lies in the *energy gap* (*band gap*) in semiconductors and therefore the system of electrons stay in the ground state even at high temperatures. The bands above the Fermi level are called *conduction bands* and the levels below the Fermi level are called *valence bands*. At temperatures up to few hundreds Kelvins and considering interactions with visible optical fields, one may take into account only the lowest lying conduction band and few topmost valence bands. Interaction with optical field (if allowed by polarization selection rules) then causes excitation of an electron from a valence band to the conduction band creating a conduction electron and a valence *hole* (this is a state in the valence band which is not populated by electrons).

Dispersions of electrons in bands may be calculated using numerous methods which differ in the rate of approximations and precision of results. Usage of these methods for analytical expression of electron energies within a small region of wave vectors is, however, inconvenient and therefore approximations are often used. Neglecting possible k–linear terms, one often uses the *effective mass approximation* — using the advanced theories, one calculates positions and energies of band extrema and effective masses in order to express the dispersion with the highest possible accuracy using proportionality $E(\boldsymbol{k}) \propto |\boldsymbol{k}|^2 m_{\lambda,\mathrm{eff}}^{-1}$, where $m_{\lambda,\mathrm{eff}}$ is the effective mass. The band extrema often arise at high–symmetry points of the reciprocal lattice. Energy near a band extreme is expressed as:

$$E_\lambda(\boldsymbol{k}) \approx E_{\lambda,\boldsymbol{k}_0} + \frac{\hbar^2|\boldsymbol{k}-\boldsymbol{k}_0|^2}{2m_{\lambda,\mathrm{eff}}}\,, \tag{3.1}$$

$$m_{\lambda,\mathrm{eff}} = \hbar^2\left[\left.\frac{\partial^2 E_\lambda(\boldsymbol{k})}{\partial\boldsymbol{k}^2}\right|_{\boldsymbol{k}=\boldsymbol{k}_0}\right]^{-1}\,. \tag{3.2}$$

As well as the translational symmetry causes wave vector to be a good quantum number, rotational symmetry causes conservation of angular momentum. It is important to emphasize that this statement is valid only in the case of zero wave vector since nonzero wave vector causes breaking of the rotational symmetry. Angular momentum of electrons has two contributions: from the electron spin (spin operator $\hat{\boldsymbol{\sigma}}$) and orbital momentum (operator $\hat{\boldsymbol{L}}$). The two types of contributions to the angular momentum interact via spin–orbit coupling expressed by the Hamiltonian in the leading terms:

$$\hat{H}_{\mathrm{SO}} = A_{SO}\hat{\boldsymbol{\sigma}}\cdot\hat{\boldsymbol{L}}\,, \tag{3.3}$$

where A_{SO} is a constant which describes the strength of coupling. Commutation relations yield $[\hat{H}_{\mathrm{SO}},\hat{\boldsymbol{L}}] = -[\hat{H}_{\mathrm{SO}},\hat{\boldsymbol{\sigma}}]$. The quantum numbers which express orbital momentum and spin (and appropriate operators of projection to any axis) are not therefore good quantum numbers with respect to the spin–orbit Hamiltonian. It can be, however, shown that the

quantum numbers J and m_J connected with the operator of the overall angular momentum defined as:

$$\hat{\boldsymbol{J}} = \hat{\boldsymbol{L}} + \hat{\boldsymbol{\sigma}}\,, \tag{3.4}$$

are good quantum numbers since the operators $\hat{\boldsymbol{J}}$ and $\hat{J}_z$ commute with the Hamiltonian $\hat{H}_{\mathrm{SO}}$. Note that these operators do not commute with the operator $-\hbar^2\hat{\boldsymbol{p}}^2/2m_0$ of the kinetic energy of an electron (m_0 is an electron mass) what simply means that angular momentum is a good quantum number only for $\boldsymbol{k} = 0$ (at the Γ point of the reciprocal lattice). States of electrons are then described by the band index and angular momenta J and m_J. Such states are not, however, eigenstates of Hamiltonian away from the Γ point since $[\hat{\boldsymbol{J}}, \hat{\boldsymbol{p}}^2] \neq 0$. Also the dispersion is unknown because of spin–orbit interaction which is not diagonalized for $\boldsymbol{k} \neq 0$.

In order to calculate the energy dispersion of electrons in bands in the vicinity of the Γ point, k–p theory is often applied [13]. This theory is, however, valid only if one considers a large number of bare states $|\lambda \boldsymbol{k}_0\rangle$ in the expression of the eigenstates:

$$|\psi_{j\boldsymbol{k}}\rangle = \mathrm{e}^{-(\boldsymbol{k}-\boldsymbol{k}_0)\cdot\boldsymbol{r}} \sum_{\lambda} C_{\lambda j}(\boldsymbol{k}-\boldsymbol{k}_0)\, |\lambda \boldsymbol{k}{=}\boldsymbol{k}_0\rangle\ . \tag{3.5}$$

The energies and effective masses of the eigenstates are calculated by numerical matrix diagonalization procedure. Analytical calculations which involve only few bare states are not accurate and therefore Luttinger's theory [22, 23] is often used when calculating effective masses. Note that k–linear terms are not involved in the Luttinger's theory.

In order to discriminate between various types of angular momenta of electrons, the angular momentum of electrons which comes from the lattice symmetry and the spin number will be simply denoted as *spin* while the angular momentum which comes from orbital motion in e.g. confining potential will be called *orbital momentum*.

3.2.2 Excitons

As noted above, excitation of an electron from the valence to the conduction band creates a pair particle–antiparticle represented by the electron and the hole. An electron and a hole have opposite electric charges and therefore they are attracted by Coulomb interaction. Depending on the electron–hole relative motion, bound and unbound states exist, the former quasiparticle is called *exciton*. Performing separation of the wavefunction $\psi(\boldsymbol{r}_{\mathrm{e}}, \boldsymbol{r}_{\mathrm{h}}) = \chi(\boldsymbol{r})\phi(\boldsymbol{\rho})$, where the subscripts 'e' and 'h' resolve an electron and a hole, respectively, $\boldsymbol{\rho} = \boldsymbol{r}_{\mathrm{e}} - \boldsymbol{r}_{\mathrm{h}}$ being a relative position, $\boldsymbol{r} = (m_{\mathrm{e}}\boldsymbol{r}_{\mathrm{e}} + m_{\mathrm{h}}\boldsymbol{r}_{\mathrm{h}})/(m_{\mathrm{e}} + m_{\mathrm{h}})$ being the center of mass position and defining the total mass $M = m_{\mathrm{e}} + m_{\mathrm{h}}$ and the reduced mass $m_{\mathrm{r}}^{-1} = m_{\mathrm{e}}^{-1} + m_{\mathrm{h}}^{-1}$, we can write Schrödinger equation in a two–band model:

$$-\left[\frac{\hbar^2\nabla^2_{\boldsymbol{r}}}{2M} + \frac{\hbar^2\nabla^2_{\boldsymbol{\rho}}}{2m_{\mathrm{r}}} + V(|\boldsymbol{\rho}|)\right] \chi_{\boldsymbol{k}}(\boldsymbol{r})\phi_\lambda(\boldsymbol{\rho}) = E_{\boldsymbol{k}nLL_z}\chi_{\boldsymbol{k}}(\boldsymbol{r})\phi_\lambda(\boldsymbol{\rho})\,, \tag{3.6}$$

where $\boldsymbol{k}$ and λ the quantum numbers arising from the equation, $\boldsymbol{k}$ being center of mass wave vector of the exciton. Function $\chi(\boldsymbol{r})$ is clearly harmonic wave $\chi_{\boldsymbol{k}}(\boldsymbol{r}) = \mathrm{e}^{-\mathrm{i}\boldsymbol{k}\cdot\boldsymbol{r}}$ and the resulting equation for $\phi_\lambda(\boldsymbol{\rho})$ is called *Wannier equation*. By introducing $V(|\boldsymbol{\rho}|) = e^2/\epsilon_0|\boldsymbol{\rho}|$, Wannier equation is equal to the Schrödinger equation for hydrogen atom. The variable ϵ_0 stands here for static dielectric constant.

Since the solution of the hydrogen atom problem is well known, the Wannier equation is not solved here and only the results are listed. The spatial dependence of the function

$\phi_\lambda(\boldsymbol{\rho})$ will not be used in the latter text so it is not given here explicitly. Quantum numbers which follow from the solution of Wannier equation (parameter λ) are: the principal quantum number n, orbital momentum L and its projection to the quantization axis L_z. The principal quantum number n has positive integer values, the integer L can be then $0, 1, \ldots, n-1$ and $L_z = -L, -L+1, \ldots, +L$. The ground state is nondegenerate since $n = 1$, $L = L_z = 0$. Energy of exciton is determined by the principal quantum number and center of mass motion:

$$E_n(\boldsymbol{k}) = -E_\mathrm{R}\frac{1}{n^2} + \frac{\hbar^2|\boldsymbol{k}|^2}{2M}\,, \tag{3.7}$$

where the quantity E_R is the exciton Rydberg energy defined as $E_\mathrm{R} = e^4 m_\mathrm{r}/2\epsilon_0^2\hbar^2$. The energy spectrum is discrete and the Rydberg energy represents the binding energy of the ground state. It is possible, according to hydrogen atom, to ionize excitons if the relative motion of the electron and hole has sufficiently high energy. Such pairs of electrons and holes then form a continuum of states. The energy spectrum of excitons is depicted in Fig. 3.1. The exciton Bohr radius is defined as $a_\mathrm{B} = \hbar^2\epsilon_0/e^2 m_\mathrm{r}$. The discussion of the exciton spin is in the next section.

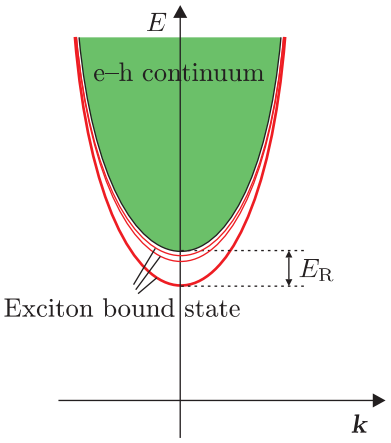

Figure 3.1: Dispersion of electron–hole pairs. The bottom thick solid line denotes the ground state of bound exciton, other solid lines then depict dispersions of excited exciton states. The filled area then stands for the continuum of unbound states.

In this thesis, excitons are treated as plane waves which are given by the motion of center of mass. No attention is paid to the relative motion of fermions which is assumed to be just an internal degree of freedom. Under these assumptions, excitons obey Bose statistics [8, 9, 10] and the fermionic nature can be described as a perturbation in the low density limit. We can then define an annihilation operator for an exciton with wave vector $\boldsymbol{k}$ in the ground state:

$$\hat{B}_{\boldsymbol{k}} = \iint \psi_{\boldsymbol{k}100}(\boldsymbol{r}_\mathrm{e}, \boldsymbol{r}_\mathrm{h})\hat{c}(\boldsymbol{r}_\mathrm{e})\hat{d}(\boldsymbol{r}_\mathrm{h})\,\mathrm{d}\boldsymbol{r}_\mathrm{e}\,\mathrm{d}\boldsymbol{r}_\mathrm{h}\,, \tag{3.8}$$

where $\hat{c}(\boldsymbol{r})$ annihilates an electron at the given position and $\hat{d}(\boldsymbol{r})$ annihilates a hole. Excitons may be coupled to the electromagnetic field as already noted. An exciton may be created by absorption of a photon and decays radiatively, i.e. when the exciton annihilates, a photon is radiated. The interaction Hamiltonian has the following form in the semiclassical picture in the dipole approximation:

$$\begin{aligned}\hat{H}_\mathrm{int} &= -\mathrm{i}d\sum_{\boldsymbol{k}}\int E(\boldsymbol{r},t)\left[\hat{B}_{\boldsymbol{k}}\mathrm{e}^{\mathrm{i}\boldsymbol{k}\cdot\boldsymbol{r}} - \hat{B}^+_{\boldsymbol{k}}\mathrm{e}^{-\mathrm{i}\boldsymbol{k}\cdot\boldsymbol{r}}\right]\mathrm{d}\boldsymbol{r} \approx \\ &\approx -\mathrm{i}d\sum_{\boldsymbol{k}}\int\left[E^{(+)}(\boldsymbol{r},t)\hat{B}_{\boldsymbol{k}}\mathrm{e}^{\mathrm{i}\boldsymbol{k}\cdot\boldsymbol{r}} - E^{(-)}(\boldsymbol{r},t)\hat{B}^+_{\boldsymbol{k}}\mathrm{e}^{-\mathrm{i}\boldsymbol{k}\cdot\boldsymbol{r}}\right]\mathrm{d}\boldsymbol{r}\,,\end{aligned} \tag{3.9}$$

where the last equality is valid in the rotating wave approximation. The symbol d is the dipole matrix element and the oscillating electric field was separated to positive and negative frequency parts according to (2.60). Note that there are dipole selection rules

which are discussed in the next section together with the exciton spin. In the full quantum description, the interaction Hamiltonian has the form:

$$\hat{H}_{\mathrm{int}} = \mathrm{i}\hbar g \sum_{\boldsymbol{k}} [\hat{a}_{\boldsymbol{k}} \hat{B}^{+}_{\boldsymbol{k}} - \hat{a}^{+}_{\boldsymbol{k}} \hat{B}_{\boldsymbol{k}}] \,. \tag{3.10}$$

3.2.3 The most frequent crystal structures

I use references to *crystal structures* in the following text and therefore I give a brief overview of the two most frequent structures. I introduce the zinc–blende and wurtzite structure.

The zinc–blende structure belongs to the cubic space group. The unit cell is a cube, see Fig. 3.2a. The associated point group is $\mathrm{T_d}$ [24] and the typical representants are most I–VII copper–halides (CuBr, CuCl), most III-V semiconductors like GaAs and some of II–VI, e.g. CdTe, ZnTe, ZnSe. Band structure of a crystal in the vicinity of the band gap is depicted in Fig. 3.2b. The lowest conduction band has Γ_6 symmetry and valence bands have Γ_7 and Γ_8 symmetries. The Γ_7 band is split–off (Γ_8 is the topmost valence band) as a consequence of spin–orbit coupling by a positive energy Δ_{SO}. However, in some crystals, e.g. in CuCl, the spin–orbit coupling has a negative sign and thus the Γ_7 band is the topmost. In crystals with positive spin–orbit coupling, the Γ_7 band is usually neglected since the energy splitting is much higher than other exchange–induced splittings. The Γ_8 band is then fourfold spin degenerate at the Γ point. The angular momentum of the holes is $\frac{3}{2}$ and the particular bands then refer to projections to the quantization axis. At nonzero wave vector, the degeneracy of the valence band is partially removed and two twofold spin degenerate bands are appropriate for light–hole (lh, $m_J = \pm\frac{1}{2}$) and heavy–hole (hh, $m_J = \pm\frac{3}{2}$) bands.

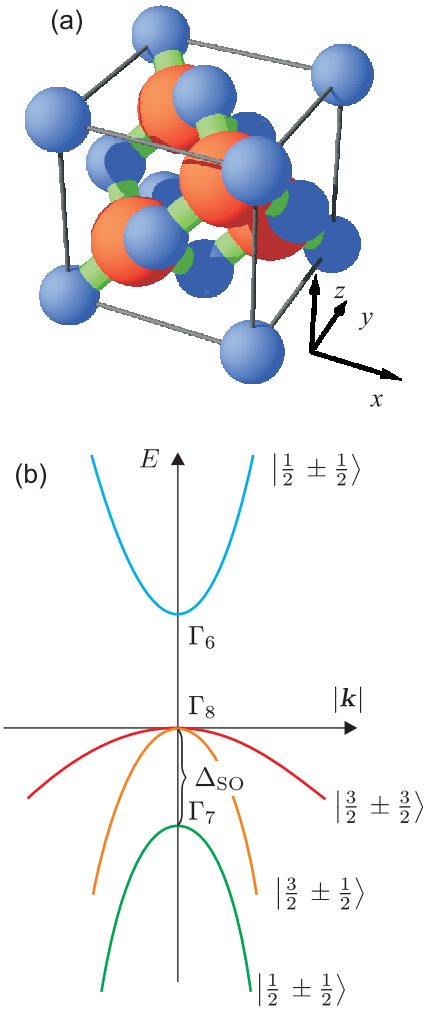

Figure 3.2: Unit cell (a) and band structure (b) of crystals with zinc–blende structure.

In the zinc–blende structure, operator of the angular momentum transforms like Γ_4 representation in space and it is antisymmetric under time reversal (K^-). Operator of momentum has the (Γ_5, K^-) symmetry properties and electromagnetic field couples to the states with the symmetry Γ_5. As will be shown later, there are three exciton states with Γ_5 symmetry in cubic crystals with linear polarizations X, Y and Z. Only the transverse states are coupled to electromagnetic field and thus there are eight excitons and only two of them are dipole–active. Heavy–hole and light–hole bands are mixed within these states and the ratio of excitation of the respective bands is 3 : 1.

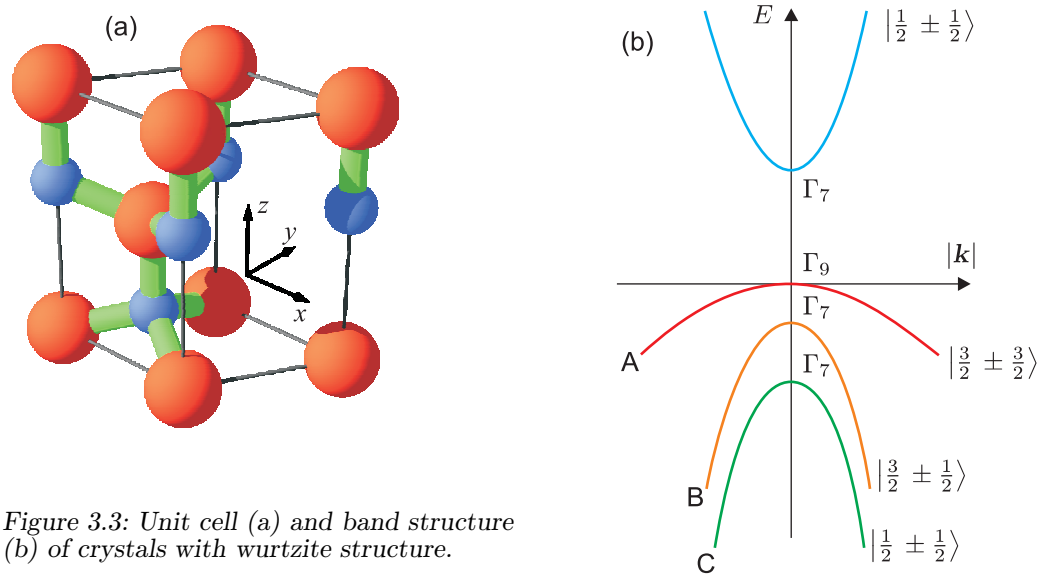

Figure 3.3: Unit cell (a) and band structure (b) of crystals with wurtzite structure.

The wurtzite crystal structure is hexagonal and the unit cell is depicted in Fig. 3.3a. The point group appropriate for wurtzite structure is C_{6v} and the typical crystals are II–VI alloys, e.g. ZnO, CdS, CdSe. The band structure is depicted in Fig. 3.3b — the lowest conduction band has a Γ_7 symmetry and valence bands have Γ_7, Γ_7 and Γ_9 symmetries, respectively. All valence bands are twofold spin degenerate and they are labeled with decreasing energy as the A, B and C band. The respective bands are the split–off band with $J = \frac{1}{2}$ and $m_J = \pm\frac{1}{2}$, the light–hole band $J = \frac{3}{2}$, $m_J = \pm\frac{1}{2}$ and the heavy–hole band $J = \frac{3}{2}$, $m_J = \pm\frac{3}{2}$. The splitting of hh and lh bands is nonzero at the Γ point, on the contrary to zinc–blende crystals. Usually, the topmost band has the Γ_9 symmetry (hh band). In most applications, only this band is considered and therefore, when compared to crystals with zinc–blende structure, the lh band is omitted.

The operator of angular momentum has the (Γ_2 and Γ_5, K^-) symmetry, the operator of momentum has the (Γ_1 and Γ_5, K^-) symmetry. Electromagnetic field is coupled to the Γ_1 state (polarization Z) and Γ_5 exciton states ($\sigma^\pm$ polarizations). There are two dipole–active and two dipole–inactive states in each band. As a consequence, optical fields are coupled to four exciton states when taking into account both A and B bands, on the contrary to crystals with zinc–blende structure in which only two states are dipole–active.

3.3 Exciton spin

3.3.1 Exciton spin

Spin of electrons and holes was neglected in the preceding discussion of excitons. The point was to show the consequence of the Coulomb attraction (which doesn't depend on particle spin) between electrons and holes — formation of bound states. In this section, I take into account spins of electrons and holes and also the exchange interaction will be considered. I restrict the following discussion to the Γ point of the reciprocal lattice. The reason is again that I want to exclude a complex discussion of the coupling of the exciton spin and orbital momentum caused by the exciton motion which results in mixing of states with different spins. This point is discussed later. Another restriction which is done throughout the rest of this thesis is, that excitons are assumed to be in their ground states, i.e. the

orbital momentum of the relative electron–hole motion is assumed to be $L = 0$ and the principal quantum number is $n = 1$.

An electron and a hole confined within the exciton wavefunction have some spins which are not, however, further good quantum numbers for the exciton. Although Coulomb interaction has the full rotational symmetry (and cannot break the symmetry), spins of fermions interact via exchange interaction which has a lower symmetry given by properties of the crystal lattice. According to the definition of the hole spin (3.4), one can define the exciton spin and its operator:

$$\hat{\boldsymbol{J}} = \hat{\boldsymbol{J}}^{\mathrm{c}} - \hat{\boldsymbol{J}}^{\mathrm{v}} + \hat{\boldsymbol{L}}^{\mathrm{e-h}} = \hat{\boldsymbol{J}}^{\mathrm{e}} + \hat{\boldsymbol{J}}^{\mathrm{h}} + \hat{\boldsymbol{L}}^{\mathrm{e-h}}\,, \tag{3.11}$$

where we put $\hat{\boldsymbol{L}}^{\mathrm{e-h}} = 0$ for the relative motion of the electron–hole pair since excitons were assumed to be in the ground ($1s$) states. The symbols $\hat{\boldsymbol{J}}^{\mathrm{c}} = \hat{\boldsymbol{J}}^{\mathrm{e}}$ denote the spin (total angular momentum) of an electron in a conduction band, $\hat{\boldsymbol{J}}^{\mathrm{v}}$ then stands for the spin of an electron in a valence band and one can define $\hat{\boldsymbol{J}}^{\mathrm{h}} = -\hat{\boldsymbol{J}}^{\mathrm{v}}$ as the spin of the hole. It can be shown that the operators $\hat{\boldsymbol{J}}$ and $\hat{J}_z$ of the exciton spin and its projection to the quantization axis commute with the exchange Hamiltonian $\hat{H}_{\mathrm{exch}} = A_{\mathrm{exch}}\hat{\boldsymbol{J}}^{\mathrm{e}} \cdot \hat{\boldsymbol{J}}^{\mathrm{h}}$ and then the exciton spin and its projection are good quantum numbers.

Because of the rotational symmetry of the potential for electrons and holes, it is convenient to derive symmetrized wavefunctions at the Γ point — these wavefunctions will become useful in the procedure of construction of Hamiltonians from invariant terms (which is described below). We consider a crystal with some symmetry of the lattice represented by a symmetry point group — here I choose $\mathrm{T_d}$ point group for cubic crystals with zinc–blende structure. The conduction band states are s–like, the orbital part of the electron angular momentum is represented by the Γ_1 representation of the $\mathrm{T_d}$ point group. Spin is represented by the Γ_6 representation so the conduction band has the symmetry according to the representation $\Gamma_1 \otimes \Gamma_6 = \Gamma_6$ (which is twofold degenerate). The valence band is p–like, therefore the orbital part of the angular momentum transforms like Γ_5 and thus the valence band wavefunctions transform like $\Gamma_5 \otimes \Gamma_6 = \Gamma_7 \oplus \Gamma_8$. The Γ_8 band is fourfold degenerate and the Γ_7 band is twofold degenerate. The basis functions of conduction electrons are represented by spinors and the basis functions for valence electrons may be found in Ref. [25]. The states with $J = \frac{3}{2}$ have the symmetry Γ_8 and the spit–off band electrons transform like Γ_7 ($J = \frac{1}{2}$).

Let's consider only excitons formed by holes from the light hole (lh) band or the heavy hole (hh) band. They will have then symmetry $\Gamma_6 \otimes \Gamma_8 = \Gamma_3 \oplus \Gamma_4 \oplus \Gamma_5$. Wavefunctions may be determined by calculation of the symmetrized products of electron and hole wavefunctions with help of tables of characters [24]. The results can be found in Refs. [25, 26]. The above definition of the spin (3.11) based on the operator of angular momentum is not always convenient and the word "exciton spin" will be used in the following text in sense of the symmetrized basis even though symmetrized states are not always eigenstates of Hamiltonian. Spin "x" then, for example, means in cubic lattices that the exciton is a superposition of states with angular momenta ± 1. Note that symmetrized wavefunctions are not generally eigenstates of the Hamiltonian even at the Γ point.

Concerning dipole interaction, it can be shown [27] that the symmetry must be conserved during the interaction. Since photons have spin ± 1, they transform like Γ_5 and thus couple only to the states with Γ_5 symmetry in the $\mathrm{T_d}$ point group. These states are three, polarized in the directions of principal axes. States which couple to photons are called *dipole–active* or *bright states* and those which do not couple are called *dipole–inactive* or *dark states*.

3.3.2 Exciton Hamiltonian

The exciton Hamiltonian can be written in the form:

$$\hat{H}_{\mathrm{exc}} = \hat{H}_{\mathrm{e}} \otimes \mathbb{1}^{\mathrm{h}} + \hat{H}_{\mathrm{h}} \otimes \mathbb{1}^{\mathrm{e}} + \hat{H}_{\mathrm{e-h}}\,, \tag{3.12}$$

where the first term on the right hand side stands for the electron Hamiltonian, the second term for the hole Hamiltonian and the last term represents the electron–hole interaction. The operators $\mathbb{1}^{\mathrm{e}}$ and $\mathbb{1}^{\mathrm{h}}$ are the identity operators on the subspace of electrons and holes, respectively. Symmetrized wavefunctions of electrons and holes are usually eigenstates of their Hamiltonians at the Γ point in bulk crystals and the Hamiltonians are then diagonal in the basis of symmetrized wavefunctions. The electron–hole interaction contains the Coulomb interaction: direct Coulomb interaction has Γ_1 symmetry and thus doesn't couple symmetrized states. The exchange interaction has, however, a lower symmetry and it may cause mixing of symmetrized states which would result in the fact that the symmetrized wavefunctions are no longer eigenstates of the whole exciton Hamiltonian. The consequence of the mixing of symmetrized states is, that populations of symmetrized states change in time due to their coupling and therefore the overall spin of a system excited by polarized light may be nonstationary.

The exciton Hamiltonian may be diagonalized by the same procedure as described above for holes. It is possible to perform precise calculations with the help of k–p theory. The result of this theory are energies and effective masses calculated on the basis of material constants. This method is robust and very precise. One may, however, want only to determine which states are coupled and the coupling strength may be determined from an experiment. The theory, which was developed in order to provide a tool for these calculations, is called *method of invariants* [25, 26, 27]. Using this method, one writes the Hamiltonian on the basis of symmetry considerations from the terms which are invariant under the point group symmetry operations. Every term is introduced in the Hamiltonian with some constant which may be then obtained from an experiment. If the basis of states is small, this method is powerful since it allows one to construct Hamiltonian taking into account any arbitrary symmetry breaking effects including external fields or wave vector.

The invariant terms of the Hamiltonian are constructed as follows. First, the symmetry point group of the particle under influence of all symmetry–breaking effects is determined from the transformation properties of the system. Then all operators which might contribute to the Hamiltonian are found and matrices in the basis of symmetrized wavefunctions are calculated. Every matrix is then characterized by its transformation properties within the point group and it is represented by an appropriate representation. The invariant terms are then constructed as products of the matrices appropriate for operators — these terms must transform like Hamiltonian, i.e. they must be invariant under all symmetry operations of the point group. This requirement implies transformation like Γ_1 with respect to operations of the point group and like K^+ with respect to time reversal.

The procedure of the construction of invariant terms for the $\mathrm{T_d}$ point group is described in details in Refs. [25, 26] with the resulting Hamiltonians. Since the method of invariants may be used for excitons as well as for electrons and holes, we can start our discussion by the invariant terms of electrons. Electron spin operator (vector of matrices $\vec{\boldsymbol{\sigma}}$) transforms like Γ_4 and K^-, the momentum operator (vector $\boldsymbol{Q}$) transforms as Γ_5 and K^+. The Hamiltonian then cannot contain terms linear in $\vec{\boldsymbol{\sigma}}$ and $\boldsymbol{Q}$ due to their symmetry. Product $\sum_j \sigma_j \sigma_j = \mathbb{1}$ is not involved in the Hamiltonian and no other products of the type $\sigma_j \sigma_\ell$ satisfy the symmetry requirements. Energy of conduction electrons at the Γ point therefore

do not depend on their spin. Wave vector dependence of energy has the lowest–order term $\boldsymbol{Q}^2$ since $\Gamma_5 \otimes \Gamma_5$ contains Γ_1 and it transforms like K^+. There are higher–order terms (always even due to time reversal symmetry) but they are usually neglected in the parabolic band approximation. The spin–orbit coupling Hamiltonian is constructed from matrices σ_j in the first order and scalars Q_ℓ in an odd order. The first term with the correct symmetry is $\sigma_x Q_x(Q_y^2 - Q_z^2) + \sigma_y Q_y(Q_z^2 - Q_x^2) + \sigma_z Q_z(Q_x^2 - Q_y^2)$. This term causes anisotropic conduction band splitting, the bands for the two spins have their minima at certain wave vector $\boldsymbol{Q}_0 \neq 0$ and $-\boldsymbol{Q}_0$, respectively. The terms of higher order in wave vector are usually neglected since they have a minimal influence on the electron energy. The Hamiltonian for an electron in the conduction band has the form:

$$\hat{H}_\mathrm{e} = E_1^\mathrm{e}\mathbb{1}^\mathrm{e} + \gamma_1^\mathrm{e}\mathbb{1}^\mathrm{e}\boldsymbol{Q}^2 + \gamma_2^\mathrm{e}\Big[\sigma_x Q_x\Big(Q_y^2 - Q_z^2\Big) + \sigma_y Q_y\Big(Q_z^2 - Q_x^2\Big) + \sigma_z Q_z\Big(Q_x^2 - Q_y^2\Big)\Big]\,. \quad (3.13)$$

The energy $E_1^\mathrm{e} = E_\mathrm{g}$ is the band gap energy (energy is measured from the top of the valence band) and $\gamma_1^\mathrm{e} = \frac{\hbar^2}{2m_\mathrm{e}}$ is the kinetic energy prefactor and contains information about the effective electron mass. Using the method of invariants, we get a better result than using the k–p approximation, the constants in the invariant expansion are, however, unknown and they must be calculated microscopically. This method is, indeed, helpful when one wants to verify validity of the microscopic calculations: based on the symmetry considerations, one may design an experiment in which particular constants are measured and they can be then compared to the calculated values.

Concerning valence band, the Hamiltonian for holes can be constructed in the similar way as the Hamiltonian for the conduction band. The result is, however, more complex since one should substitute the 2×2 matrix for electron spin operator σ^e by the 4×4 matrix for hole angular momentum operator $\vec{\boldsymbol{J}}^\mathrm{h}$ (symmetry Γ_4, K^-). Without going into details, the resulting Hamiltonian with terms up to Q^2 follows (the terms Q^3 are assumed to be negligible compared to other terms) [26, 28, 29]:

$$\begin{aligned}\hat{H}_\mathrm{h} = {}& \gamma_1^\mathrm{h}\mathbb{1}^\mathrm{h}Q^2 + c_Q^\mathrm{h}[Q_x\{\mathbf{J}_x, \mathbf{J}_y^2 - \mathbf{J}_z^2\} + c.p.] + \\ & + \gamma_2^\mathrm{h}[(3Q_z^2 - Q^2)(3\mathbf{J}_z^2 - \vec{\boldsymbol{J}}^2) + 3(Q_x^2 - Q_y^2)(\mathbf{J}_x^2 - \mathbf{J}_y^2)] + \\ & + 2\gamma_3^\mathrm{h}(Q_y Q_z\{\mathbf{J}_y, \mathbf{J}_z\} + c.p.)\,,\end{aligned} \quad (3.14)$$

where *c.p.* stands for cyclic permutation of indices. Besides the k–linear term, the Hamiltonian contains the same terms as the phenomenological Hamiltonian by Luttinger [23] who has formulated an effective mass theory.

The exciton Hamiltonian is of the form (3.12) where the first two terms on the right hand side may be defined by (3.13) and (3.14). Motion of electrons and holes has no sense in the exciton picture and one should use motion of the center of mass instead. All terms with $\boldsymbol{Q}$ and Q_j are subtracted from the Hamiltonian and they are substituted by terms proportional to wave vector of exciton in $\hat{H}_\mathrm{e-h}$. The resulting Hamiltonian is then:

$$\hat{H} = \Delta_0 \mathbb{1}^\mathrm{e} \otimes \mathbb{1}^\mathrm{h} + \hat{H}_\mathrm{e-h}\,. \quad (3.15)$$

The constant Δ_0 is defined as $\Delta_0 = E_1^\mathrm{e} = E_\mathrm{g}$. The electron–hole interaction terms (including exciton dispersion) are constructed again by the method of invariants, using matrix and vector representations $\vec{\boldsymbol{J}}$, $\vec{\boldsymbol{\sigma}}$ and $\boldsymbol{Q}$. Results may be found in Ref. [26], the main features are listed here. Concerning terms which do not depend on the exciton wave vector, one finds the exchange Hamiltonian nonperturbed by any symmetry breaking effects:

$$\hat{H}_\mathrm{st} = \Delta_0 \mathbb{1}^\mathrm{e} \otimes \mathbb{1}^\mathrm{h} + \Delta_1 \vec{\boldsymbol{\sigma}} \cdot \vec{\boldsymbol{J}} + \Delta_2(\sigma_x \mathbf{J}_x^3 + c.p.)\,. \quad (3.16)$$

One usually assumes that the terms of the lowest order in contributing operators give the main contribution to the particle energy. The anisotropic exchange term (the last term on right hand side) can usually be neglected and the main contribution to the energies of excitons is assumed to come from the isotropic exchange term proportional to Δ_1. This term splits the dipole–inactive states with symmetry $\Gamma_3 \oplus \Gamma_4$ from the dipole–active states with symmetry Γ_5. The bright states are further split by the nonanalytical part of the exchange interaction to transverse ($\Gamma_{5\mathrm{T}}$) and longitudinal states ($\Gamma_{5\mathrm{L}}$) [25, 26].

Concerning wave vector dependent terms, they determine exciton dispersion and spin–orbit coupling. The spin–orbit coupling causes mixing of states when the wave vector is nonzero: the interaction proportional to the first order of wave vector is assumed to be the most important, its Hamiltonian reads:

$$\hat{H}_{\mathrm{SO}} = C_Q[Q_x\{\mathbf{J}_x, \mathbf{J}_y^2 - \mathbf{J}_z^2\} + c.p.] \otimes \mathbb{1}^{\mathrm{e}} \,. \tag{3.17}$$

This term is due to the spin–orbit term for holes with the only exception that the wave vector of the exciton is considered instead of the wave vector of a hole. For some wave vector directions, the Hamiltonian including k–linear term may be diagonalized. The wave vector dependent mixing of states may be also viewed as spin precession in time determined by periodical spin–flips of the spin of symmetrized states. Discussion of this temporal evolution is given in the next subsection.

3.3.3 Spin precession and relaxation

In this subsection, I discuss in detail the difference between the spin precession and relaxation. This discussion is important in order to realize which property is measured in FWM experiments and whether it is possible to detect k–dependent exchange interaction in ultrafast nonlinear spectroscopy. We must therefore strictly resolve coherent and incoherent changes of spin.

As discussed above, coupling between symmetrized exciton states may cause changes of the overall spin in time. It should be stressed here that this spin evolution is *coherent* — although spin changes, the system remains in a pure state. There is a big difference between the coherent precession of the spin and *spin relaxation*. Spin relaxation means that the spin is not in a pure state but rather in a mixed state as a consequence of an interaction with some heat bath, e.g. phonons, impurities etc. Spin relaxation is usually connected with momentum scattering in bulk crystals. For example electron spin relaxation by the D'yakonov and Perel's mechanism [30, 31, 32] is following. Spin of an electron undergoes precession which is wave vector–dependent. As the electron (randomly) changes propagation direction due to scattering, memory of the precession is lost. (There exists an effect of motional narrowing [32] if the particles are often scattered, however the overall spin still relaxes.)

In a homogeneous system of spins, coherent precession causes periodical changes of mean spin or magnetization since phases of all spins are correlated. In inhomogeneous systems, on the contrary, frequency of spin precession depends on a concrete particle and therefore the mean spin approaches an equilibrium value, similarly to the enhanced decay of overall polarization in OBE due to system's inhomogeneity. An effective spin relaxation due to inhomogeneity of the system is hardly distinguishable from the real relaxation, however it could be possible using a technique similar to photon echo or using FWM experiments.

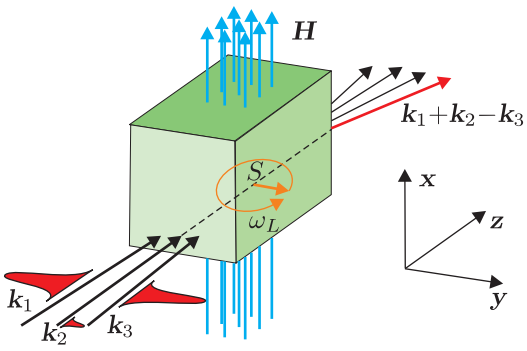

Figure 3.4: Schematic sketch of a FWM experiment in Voigt geometry. Spin of excited particles precess in the magnetic field and it is detected by a delayed third pulse.

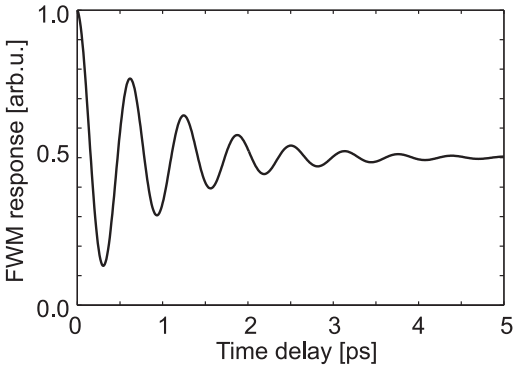

Figure 3.5: Sketch of output of FWM experiment according to the situation sketched in Fig. 3.4.

For an illustration, let's consider a FWM experiment in which the spin precesses as a consequence of applied magnetic field in Voigt configuration (see Fig. 3.4). Assume a bulk cubic crystal in a magnetic field which is oriented in the direction $\boldsymbol{x}$. Incoming pulses create a population of spin–oriented electrons in the sample (spins of holes usually relax on a very short time scale and are not therefore considered). Magnetic field causes coherent evolution (rotation) of the mean spin in the $\boldsymbol{yz}$ plane and therefore oscillation of the FWM signal as seen in Fig. 3.5. Due to spin relaxation, these oscillations are damped. From the curve schematically depicted in Fig. 3.5 one may easily determine the strength of coupling between the y and z–oriented states (effect of the magnetic field) and also the spin relaxation time, i.e. influence of incoherent effects. Difficulties arise when the relaxation time is shorter than the period of oscillations — in this case, one cannot determine the strength of coherent coupling. This is the case of coherent spin evolution which is caused by electron–hole exchange interaction. However, there are methods for indirect observation of exchange mixing, for example in high–k spectroscopy [26]. Spin precession might be also studied in four–wave mixing experiments as described in chapter 7.

3.4 Particle–particle interactions

Up to now, we considered a situation when only one electron–hole pair is excited in the whole volume of a crystal. In reality, there are usually more electron-hole pairs (excitons) within one crystal and then they interact via Coulomb interaction. This section then gives a review of exciton–exciton interactions with their consequences and, at the end, exciton–photon interaction is discussed.

3.4.1 Exciton–exciton interactions

Excitons are composed of one electron and one hole with half–integer spins and therefore the overall spin of all excitons is integer. According to chapter 2 and its section 2.2, excitons should obey Bose statistics. As shown in theoretical works [8, 9, 10], excitons may be regarded as bosons but only under assumption of their low density. The reason is their composite nature — the electron and hole wavefunctions are spread in k–space what decreases the effect of Pauli blocking. Exclusion does not, however, vanish completely and its influence is proportional to exciton density.

In addition to Pauli exclusion, there exist Coulomb exciton–exciton interactions even though excitons are electrically neutral. One must take into account the exciton composite character again and calculate the Coulomb exciton–exciton interaction as a consequence of mutual electron–electron, hole–hole and electron–hole interactions. Since the exciton–exciton interactions reveal as the core of the wave mixing process, a special attention should be paid to their correct description.

In this subsection, only the Coulomb interactions are discussed. Pauli blocking reveals in the FWM experiment only as a modification of dipole interaction between excitons and photons which is discussed later in this section 3.4 and chapter 6. We can start our mathematical description with Eqs. (3.6) and (3.8). Excitons are assumed to be bosons with appropriate creation and annihilation operators defined by Eq. (3.8). Excitons interact via pair interactions and therefore the general Hamiltonian reads:

$$\hat{H} = \sum_{\lambda,\mu} h_{\lambda\mu} \hat{B}^+_\lambda \hat{B}_\mu + \frac{1}{2} \sum_{\lambda,\mu,\nu,\iota} \hat{W}_{\lambda\mu\nu\iota} \hat{B}^+_\lambda \hat{B}^+_\mu \hat{B}_\nu \hat{B}_\iota \,, \tag{3.18}$$

where $h_{\lambda\mu}$ describes energies of one–particle states and their spin precession (coherent evolution) and $W_{\lambda\mu\nu\iota}$ stands for pair particle–particle interactions (scattering). The first (one–particle) term is equivalent to the one–particle Hamiltonian (3.6) if the spin is included. The discussion of exciton–exciton interaction is then focused on the second term in the previous Hamiltonian. It should be stressed here that the one–exciton states are not influenced by the second term in (3.18) since the equation of motion for one–particle coherences, taking into account only the scattering term, reads:

$$i\hbar \frac{\partial}{\partial t} [\hat{B}^+_\lambda - (\hat{B}^+_\lambda)^2 \hat{B}_\lambda] = \Big[\hat{B}^+_\lambda - (\hat{B}^+_\lambda)^2 \hat{B}_\lambda \,, \sum_{\lambda,\mu,\nu,\iota} \hat{W}_{\lambda\mu\nu\iota} \hat{B}^+_\lambda \hat{B}^+_\mu \hat{B}_\nu \hat{B}_\iota \Big] = 0 \,. \tag{3.19}$$

Exciton–exciton interaction, according to 3.18, is evaluated as an interaction of all pairs of particles except electron–hole interaction within the contributing excitons (this interaction is already accounted for in one–particle energies). The general Hamiltonian including direct Coulomb and exchange interactions has the matrix elements [33]:

$$\begin{aligned} \hat{H}_{S_1 S_2 \leftarrow S_3 S_4}(\boldsymbol{K}, \boldsymbol{K'}, \boldsymbol{q}) = {} & \mathcal{S}^{\mathrm{X}}_{\mathrm{dir}}(S_1, S_2, S_3, S_4) \hat{H}^{\mathrm{X}}_{\mathrm{dir}}(\boldsymbol{K}, \boldsymbol{K'}, \boldsymbol{q}) + \\ & + \mathcal{S}^{\mathrm{X}}_{\mathrm{exch}}(S_1, S_2, S_3, S_4) \hat{H}^{\mathrm{X}}_{\mathrm{exch}}(\boldsymbol{K}, \boldsymbol{K'}, \boldsymbol{q}) + \\ & + \mathcal{S}^{\mathrm{e}}_{\mathrm{exch}}(S_1, S_2, S_3, S_4) \hat{H}^{\mathrm{e}}_{\mathrm{exch}}(\boldsymbol{K}, \boldsymbol{K'}, \boldsymbol{q}) + \\ & + \mathcal{S}^{\mathrm{h}}_{\mathrm{exch}}(S_1, S_2, S_3, S_4) \hat{H}^{\mathrm{h}}_{\mathrm{exch}}(\boldsymbol{K}, \boldsymbol{K'}, \boldsymbol{q}) \,, \end{aligned} \tag{3.20}$$

where the Hamiltonian was separated to the sum of terms containing a *spin part* and a *momentum part*. Initial states have spins S_3, S_4 and the final states have spins S_1 and S_2. The spin part then fully determines the symmetry of the interaction with respect to the spin of incoming and outgoing excitons. The four lines in the above Hamiltonian stand for four scattering processes [10, 33]: direct boson–boson scattering (first line), exchange of bosons (second line) and exchanges of electrons and holes, respectively (third and fourth line). Momentum parts of the Hamiltonian may be evaluated by direct integration if the exciton wavefunction and potential are known [33], the spin parts are then given by formulas:

$$\mathcal{S}^{\mathrm{X}}_{\mathrm{dir}}(S_1,S_2,S_3,S_4) = \langle S_3|\, S_1\rangle \langle S_4|\, S_2\rangle \ , \tag{3.21}$$

$$\mathcal{S}^{\mathrm{X}}_{\mathrm{exch}}(S_1,S_2,S_3,S_4) = \langle S_3|\, S_2\rangle \langle S_4|\, S_1\rangle \ , \tag{3.22}$$

$$\mathcal{S}^{\mathrm{e}}_{\mathrm{exch}}(S_1,S_2,S_3,S_4) = \sum_{s_e,s'_e}\sum_{j_h,j'_h} \langle S_3|\, s_e j_h\rangle \left\langle S_4|\, s'_e j'_h\right\rangle \left\langle s'_e j_h\right|\, S_1\rangle \left\langle s_e j'_h\right|\, S_2\rangle \ , \tag{3.23}$$

$$\mathcal{S}^{\mathrm{h}}_{\mathrm{exch}}(S_1,S_2,S_3,S_4) = \mathcal{S}^{\mathrm{e}}_{\mathrm{exch}}(S_2,S_1,S_3,S_4)\,. \tag{3.24}$$

The summations on the third line are performed over electron and hole spins, respectively. Concerning direct scattering and exchange of bosons, it can be shown that:

$$\mathcal{S}^{\mathrm{X}}_{\mathrm{exch}}(S_1,S_2,S_3,S_4)\hat{H}^{\mathrm{X}}_{\mathrm{exch}}(\boldsymbol{Q},\boldsymbol{Q}',\boldsymbol{q}) = \mathcal{S}^{\mathrm{X}}_{\mathrm{dir}}(S_2,S_1,S_3,S_4)\hat{H}^{\mathrm{X}}_{\mathrm{dir}}(\boldsymbol{Q},\boldsymbol{Q}',\boldsymbol{Q}'-\boldsymbol{Q}-\boldsymbol{q})\,. \tag{3.25}$$

Both processes obviously have very similar symmetries with respect to the spins of incoming and outgoing excitons. Symmetries of boson– and fermion–related processes are, however, considerably different as follows from (3.21)–(3.24). This fact will be the crucial point in the latter discussion of wave mixing processes.

According to [10], we classify exciton–exciton interactions as *direct scattering* (boson–boson interactions) and *exchange scattering* (exchange of fermions). The scattering Hamiltonian may be then rewritten in the following form:

$$\begin{aligned}\hat{H}_{\mathrm{SD}} = {} & \frac{1}{4}\sum_{\boldsymbol{k},\boldsymbol{k}'}\sum_{\boldsymbol{q}}\sum_{S,S'} V_{\mathrm{d}}(\boldsymbol{q},\tfrac{1}{2}(\boldsymbol{k}-\boldsymbol{k}'))\hat{B}^{+}_{S,\boldsymbol{k}+\boldsymbol{q}}\hat{B}^{+}_{S',\boldsymbol{k}'-\boldsymbol{q}}\hat{B}_{S,\boldsymbol{k}}\hat{B}_{S',\boldsymbol{k}'} + H.c. + \\ & + \frac{1}{4}\sum_{\boldsymbol{k},\boldsymbol{k}'}\sum_{\boldsymbol{q}}\sum_{j_h,s_e}\sum_{j'_h,s'_e} V_{\mathrm{x}}(\boldsymbol{q},\tfrac{1}{2}(\boldsymbol{k}-\boldsymbol{k}'))\hat{B}^{+}_{j'_h s_e,\boldsymbol{k}+\boldsymbol{q}}\hat{B}^{+}_{j_h s'_e,\boldsymbol{k}'-\boldsymbol{q}}\hat{B}_{j_h s_e,\boldsymbol{k}}\hat{B}_{j'_h s'_e,\boldsymbol{k}'} + H.c.\,,\end{aligned} \tag{3.26}$$

where $H.c.$ means the Hermitian conjugated terms. Functions V_{d} and V_{x} then stand for effective potentials for the direct scattering and exchange scattering, respectively. As will be shown later, symmetry of the above Hamiltonian with respect to exciton spins determines polarization selection rules in FWM. Matrix elements of the spin part of Hamiltonian $\hat{H}_{\mathrm{SD}}$ (which is directly evaluated from the general Hamiltonian (3.20)) may be found in chapter 6, Tabs. 6.1–6.4 for exchange scattering (spin part of Hamiltonian of direct scattering is diagonal). Because of the use of brakets of the form $\langle S|\, s_e j_h\rangle$ in (3.23)–(3.24), matrix elements of the spin part of Hamiltonian $\hat{H}_{\mathrm{SD}}$ depend on the choice of an orthonormalized basis and therefore on the spin structure of dipole–active states.

One of the most striking and also important facts which arise in the tables is the big difference between Hamiltonians in the basis of dipole–active excitons with linear and circular spins, respectively. While it is diagonal in the basis of circular spins, there are off–diagonal terms in the linear basis. It implies that a two–exciton state which consists of two excitons with circular spins may scatter to another two–exciton state with two dipole–active excitons *preserving the circular polarizations* (the final state might be also dipole–inactive for zinc–blende structure of the lattice). Linear spins are not, on the contrary, necessarily preserved, i.e. a two–exciton state $|XX\rangle$ may be scattered to the state $|XX\rangle$ preserving spin but also to the state $|YY\rangle$.

3.4.2 Biexcitons

Bare electron or hole states (plane waves) are eigenstates of the one–particle Hamiltonian which doesn't describe particle–particle interactions. The system in the one–particle state may be then described by the use of such bare state. Excitations of the intrinsic semiconductor, however, involve always at least one electron and one hole. Two–particle states are perturbed by the mutual interaction and diagonalization of the electron–hole Hamiltonian leads to eigenstates with renormalized energies. One finds bound and unbound (scattering) electron–hole states due to the attractive nature of the Coulomb interaction between electrons and holes.

The same concept of finding of eigenstates of the two–exciton Hamiltonian (3.18) may be used. Excitons are eigenstates of the one–exciton Hamiltonian but "bare" two–exciton states of the form $\hat{B}^+_\lambda \hat{B}^+_\mu |0\rangle$ do not diagonalize the two–exciton Hamiltonian. Exciton–exciton interactions then may lead to formation of bound and/or unbound states, depending on whether the interactions are attractive or repulsive.

It can be shown [10, 34][1] that the exchange interaction between two excitons with the same circular spin is repulsive while it is attractive if the respective spins are contra–circular. Attractive interaction causes binding of two excitons to a complex called *bound biexciton*. Repulsive interaction, on the contrary, suppresses the possibility of the creation of a bound state, the states are then called *scattering states* or *unbound biexcitons*.

Dynamics of the system of two–exciton states may be generally described in two ways depending on the chosen basis. One can use the basis of "bare" two–exciton states $\hat{B}^+_\lambda \hat{B}^+_\mu |0\rangle$ and the nondiagonal Hamiltonian (3.18) or the basis of eigenstates — bound and unbound biexcitons. In most phenomenological theories, the quasi–diagonalized basis is used: one assumes that the repulsive exciton–exciton interaction may be considered as a perturbation, the attractive interaction is, however, treated analytically. The basis of the two–exciton states then consists of the bare two–exciton states with the spin configurations which do not allow formation of bound biexciton states, see e.g. Fig. 5.3 below in the WIBM model. This model is called Giant Oscillator Strength (GOS) model since the attractive exciton–exciton interaction is assumed to be enhanced with respect to the repulsive interaction implying impossibility of the use of perturbative approach and necessity of the use of the bound biexciton state in the basis of two–exciton states.

Dynamics of the GOS model is simple since the transitions from the one–exciton to the two–exciton state are simply described within the dipole approximation by dipole transitions. The bound biexciton state is also assumed to be coupled to one–exciton states by dipole interaction. Biexciton creation is therefore instantaneous after absorption of a photon if the system was in a one–exciton state. The GOS model is, however, an approximation which may be used in order to explain polarization selection rules for two–photon creation of a biexciton but not for description of the dynamics of this process since it was shown [35] that the biexciton formation is not instantaneous. In addition to this point, it is worthy to state that the idea of the instantaneous creation of biexcitons is not physically correct. Let's assume absorption of two photons with X polarizations. They are absorbed and the created state may be the biexciton state e.g. with the symmetry Γ_1 in a bulk cubic crystal [26, 36]. The pairs of excitons within the biexciton are then virtual states having spins XX, YY, etc. The spin–flip from the state XX to the state YY requires, however, some exciton–exciton interaction in order to provide an information about spin of one exciton to the second exciton. Immediate smearing of the mean polarization

[1] In a four–band model, where twofold degenerate valence and conduction bands are assumed.

of two–exciton states then means that this interaction has an infinite strength what is not physical. Assumption of a finite strength of exciton–exciton interaction then reveals a non–instantaneous formation of biexcitons what is an idea different from the GOS model. The spin–flip of the pair of exciton within the biexciton wavefunction was used in order to probe the biexciton formation dynamics in [35].

The last point which is discussed in the connection with biexcitons is their spin structure. This structure may be easily estimated in the four–band model on the basis of geometric or other considerations. Calculation of the spin structure of biexcitons in their ground state (i.e. state antisymmetrical with respect to exchange of two electrons or holes) can be based on symmetry consideration as well as the calculation of the exciton spin structure in a more complicated model which takes into account the full symmetry properties of the crystal lattice [26, 36, 37]. As a result, we find that the biexciton state with Γ_1 symmetry has the usual $\sigma^+\sigma^-$ two–photon selection rule (i.e. it can be created by absorption of two photons which have circular polarizations with opposite helicities). Due to consideration of four valence bands for a semiconductor with zinc–blende structure, there are five more biexciton states: two of them have the Γ_3 symmetry and three Γ_5 symmetry. The wavefunctions (spin structures) may be found in [26] for a semiconductor with the $\mathrm{T_d}$ symmetry point–group appropriate to the lattice. Concerning quantum wells, biexciton spin structures are listed in chapter 5.

3.4.3 Polaritons

Semiconductors are widely investigated using optical spectroscopy due to strong coupling between electrons and electromagnetic field (photons) which is discussed in this subsection. Strong exciton–photon coupling must be obviously taken into account in order to correctly describe the system dynamics and the spectra of the FWM signal. Although the polariton effect is well discussed in many textbooks, the main features important for understanding of the FWM signal dynamics are summarized in the following text.

Let's denote $\hat{a}_{S\boldsymbol{K}}$ to be an annihilation operator of a photon with polarization (spin) $S = \pm 1$ and wave vector $\boldsymbol{K}$. Exciton–photon coupling in the lowest order of perturbation theory may be described by the following Hamiltonian without use of the rotating wave approximation [38, 39]:

$$\begin{aligned}\hat{H} = &\sum_{S=\pm1}\sum_{\boldsymbol{K}} \hbar\omega_{\boldsymbol{K}} \hat{a}^+_{S,\boldsymbol{K}} \hat{a}_{S,\boldsymbol{K}} + \sum_{S}\sum_{\boldsymbol{k}} h_{S,\boldsymbol{k}} \hat{B}^+_{S,\boldsymbol{k}} \hat{B}_{S,\boldsymbol{k}} + \\ &+ \mathrm{i}\sum_{S}\sum_{\boldsymbol{K}} \left\{ \frac{\hbar\Omega_\mathrm{c}}{2} \left[\frac{\omega_\mathrm{X}}{\omega_{\boldsymbol{K}}}\right]^{1/2} \left(\hat{a}^+_{S,\boldsymbol{K}} \hat{B}_{S,\boldsymbol{K}} + \hat{a}_{S,-\boldsymbol{K}} \hat{B}_{S,-\boldsymbol{K}} - \hat{a}_{S,\boldsymbol{K}} \hat{B}^+_{S,\boldsymbol{K}} - \hat{a}^+_{S,-\boldsymbol{K}} \hat{B}^+_{S,-\boldsymbol{K}} \right) \right. \\ &\left. + \frac{\hbar\Omega_\mathrm{c}^2}{4\omega_{\boldsymbol{K}}} \left(\hat{a}^+_{S,\boldsymbol{K}} \hat{a}_{S,\boldsymbol{K}} + \hat{a}_{S,\boldsymbol{K}} \hat{a}_{S,-\boldsymbol{K}} \hat{a}_{S,\boldsymbol{K}} \hat{a}^+_{S,\boldsymbol{K}} + \hat{a}^+_{S,-\boldsymbol{K}} \hat{a}^+_{S,\boldsymbol{K}} \right) \right\}, \end{aligned} \tag{3.27}$$

where $\omega_{\boldsymbol{K}} = c|\boldsymbol{K}|/\varepsilon_\mathrm{b}$ is the photon energy, $h_{S,\boldsymbol{k}}$ is the exciton energy, ε_b stands for background dielectric constant and the exciton–photon coupling is determined by the strength:

$$\Omega_\mathrm{c} = 2\sqrt{2\pi} \frac{e}{\sqrt{\omega_\mathrm{X}}} \frac{p_\mathrm{cv}}{M} \phi(\boldsymbol{\rho}{=}0)\,. \tag{3.28}$$

I used the symbol e for electron charge, $\hbar\omega_\mathrm{X}$ for (transverse) exciton resonance energy, M for exciton mass and p_cv is the dipole matrix element $p_\mathrm{cv} = -\langle \psi_{\boldsymbol{K},\mathrm{c}} | \nabla | \psi_{\boldsymbol{K},\mathrm{v}} \rangle$, where

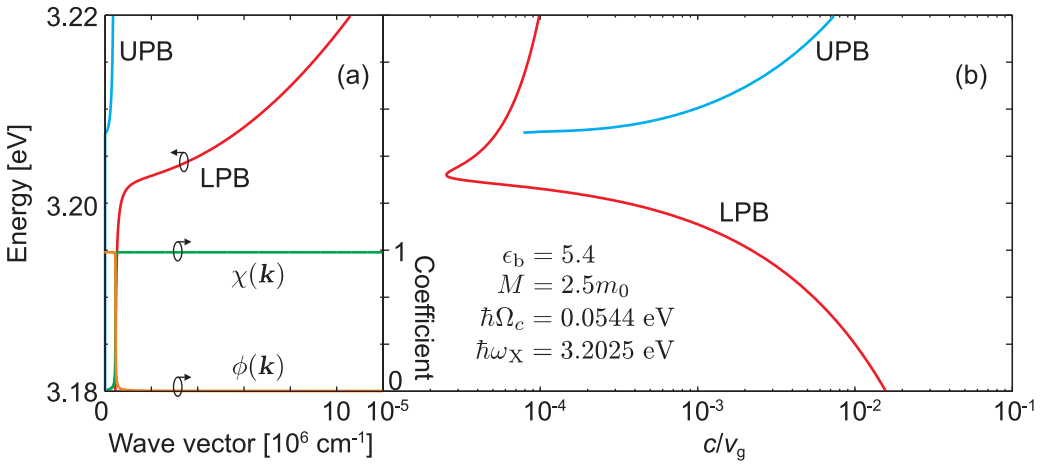

Figure 3.6: Dispersion of polaritons in CuCl and appropriate coefficients (a) according to (3.30) and dependence of group velocity on polariton energy (b).

$\psi_{\boldsymbol{K},\mathrm{c,v}}$ denote conduction electron and valence hole wavefunctions, respectively. In the resonant approximation when one takes $\omega_{\boldsymbol{K}} = |\boldsymbol{K}|c/\sqrt{\varepsilon_\mathrm{b}} \approx \omega_\mathrm{X}$, one gets the Hamiltonian (3.10) with $g = \Omega_\mathrm{c}/2$. It is possible to diagonalize the Hamiltonian using transformations described in Ref. [38]. One then gets a new set of operators which may be assigned to new quasiparticles — polaritons. In order to illustrate the diagonalization procedure, let's use the simplified Hamiltonian (3.10). We consider the Hamiltonian:

$$\hat{H} = \sum_{S=\pm1}\sum_{\boldsymbol{K}} \hbar\omega_{\boldsymbol{K}} \hat{a}^+_{S,\boldsymbol{K}} \hat{a}_{S,\boldsymbol{K}} + \sum_{S}\sum_{\boldsymbol{k}} h_{S,\boldsymbol{k}} \hat{B}^+_{S,\boldsymbol{k}} \hat{B}_{S,\boldsymbol{k}} - \\ -\mathrm{i}g \sum_{S=\pm1}\sum_{\boldsymbol{K}} \left(\hat{a}^+_{S,\boldsymbol{K}} \hat{B}_{S,\boldsymbol{K}} - H.c. \right). \tag{3.29}$$

This Hamiltonian can be diagonalized using operators for *polaritons* $\hat{P}_{LPB}$ and $\hat{P}_{UPB}$:

$$\begin{pmatrix} \hat{a}_{S,\boldsymbol{K}} \\ \hat{B}_{S,\boldsymbol{K}} \end{pmatrix} = \begin{pmatrix} \mathrm{i}\phi_S(\boldsymbol{K}) & \chi_S(\boldsymbol{K}) \\ \chi_S(\boldsymbol{K}) & \mathrm{i}\phi_S(\boldsymbol{K}) \end{pmatrix} \begin{pmatrix} \hat{P}_{LPB} \\ \hat{P}_{UPB} \end{pmatrix}, \tag{3.30}$$

where $\chi(\boldsymbol{K})$ and $\phi(\boldsymbol{K})$ are real functions which fulfill normalization condition $\chi^2_S(\boldsymbol{K}) + + \phi^2_S(\boldsymbol{K}) = 1$. After some algebra, one finds frequencies of polaritons:

$$\omega_{S,\boldsymbol{K}\pm} = \frac{\omega_{\boldsymbol{K}} + h_{S,\boldsymbol{K}}/\hbar}{2} \pm \sqrt{\tfrac{1}{4}(\omega_{\boldsymbol{K}} - h_{S,\boldsymbol{K}}/\hbar)^2 + (g/\hbar)^2}\,, \tag{3.31}$$

where the sign "+" in the subscript denotes the *upper polariton branch* (UPB) and the sign "−" denotes the *lower polariton branch* (LPB). The appropriate coefficients χ and ϕ are then:

$$\chi^2_S(\boldsymbol{K}) = \frac{\omega_{S,\boldsymbol{K}-} - \omega_{\boldsymbol{K}}}{\omega_{S,\boldsymbol{K}-} - \omega_{S,\boldsymbol{K}+}}\,, \tag{3.32}$$

$$\phi^2_S(\boldsymbol{K}) = \frac{\omega_{S,\boldsymbol{K}+} - \omega_{\boldsymbol{K}}}{\omega_{S,\boldsymbol{K}+} - \omega_{S,\boldsymbol{K}-}}\,. \tag{3.33}$$

The corresponding inverse transformation reads:

$$\begin{pmatrix} \hat{P}_{LPB} \\ \hat{P}_{UPB} \end{pmatrix} = \begin{pmatrix} -\mathrm{i}\phi_S(\boldsymbol{K}) & \chi_S(\boldsymbol{K}) \\ \chi_S(\boldsymbol{K}) & -\mathrm{i}\phi_S(\boldsymbol{K}) \end{pmatrix} \begin{pmatrix} \hat{a}_{S,\boldsymbol{K}} \\ \hat{B}_{S,\boldsymbol{K}} \end{pmatrix} . \tag{3.34}$$

The polariton dispersion according to (3.31) and coefficients (3.32)–(3.33) are plotted in Fig. 3.6 for illustration. In order to express wave vectors of the polaritons from the two branches as the functions of energy, it is necessary to use the general form of Hamiltonian (3.27) and the resulting dispersion relation reads:

$$K_\pm = \frac{\frac{M}{\hbar\omega_\mathrm{X}}(\omega^2-\omega_\mathrm{X}^2)+\frac{\omega^2}{c^2}\varepsilon_\mathrm{b}}{2} \pm \sqrt{\left(\frac{\frac{M}{\hbar\omega_\mathrm{X}}(\omega^2-\omega_\mathrm{X}^2)-\frac{\omega^2}{c^2}\varepsilon_\mathrm{b}}{2}\right)^2 + \frac{\omega^2}{c^2}\frac{M}{\hbar\omega_\mathrm{X}}\varepsilon_\mathrm{b}\Omega_\mathrm{c}^2} . \tag{3.35}$$

Symbol M stands for effective exciton mass and $\hbar\omega_\mathrm{X}$ is the energy of exciton in ground state. This equation may be further simplified using the following notation:

$$q_\mathrm{X}^2 = \frac{M}{\hbar\omega_\mathrm{X}}(\omega^2-\omega_\mathrm{X}^2) , \tag{3.36}$$

$$q_\mathrm{L}^2 = \frac{\omega^2}{c^2}\varepsilon_\mathrm{b} , \tag{3.37}$$

$$\widetilde{\Omega}_\mathrm{c}^2 = \frac{\omega^2}{c^2}\frac{M}{\hbar\omega_\mathrm{X}}\varepsilon_\mathrm{b}\Omega_\mathrm{c}^2 , \tag{3.38}$$

where ε_b stands for background dielectric constant and $q_\mathrm{L}^2(\omega)$ is the background photon dispersion. The simplified equation (3.35) then reads [40]:

$$q_\pm = \frac{q_\mathrm{X}^2+q_\mathrm{L}^2}{2} \pm \sqrt{\left(\frac{q_\mathrm{X}^2-q_\mathrm{L}^2}{2}\right)^2 + \widetilde{\Omega}_\mathrm{c}^2} . \tag{3.39}$$

In the following text, I will assume excitation below exciton resonance or in the resonance. Taking into account Fig. 3.6a, it is clear that mostly the lower polariton branch is excited while influence of the UPB may be neglected. Therefore UPB will not be taken into account and only the LPB is discussed.

As seen in Fig. 3.6a, photons couple to polaritons resonantly in the whole spectral range from 0 to $\hbar\omega_\mathrm{X}$ (exciton resonance). At low energies, the dispersion curve is similar to the dispersion of photons while it obeys parabolic exciton–like dispersion above the exciton resonance energy. The coefficients χ and ϕ then clearly show the exciton– and photon–likeness of polaritons: at low energies, the polariton is photon–like while it reveals as an exciton in the part with parabolic dispersion, cf. Fig. 3.6a. Variation of exciton– and photon–likeness over the energy spectrum leads to a strong dependence of group velocity on energy of the polariton as shown in Fig. 3.6b [26] and therefore it leads also to a strong dependence of dephasing rate on energy [41].

As seen from the Hamiltonians (3.27) and (3.29), wave vector is explicitly conserved in the dipole interaction in the strong coupling regime. This conservation is implied by an assumption of the symmetry with respect to all translations allowed by the lattice periodicity and therefore by an assumption of an infinite crystal. Presence of the crystal surface nevertheless breaks the translational symmetry and therefore wave vector needn't be conserved during penetration of photons to the crystal. Wave vector(s) of excited polariton(s) is, however, unambiguously determined by the wave vector of incoming photons

what leads to the light refraction. Problem of refraction is complicated when photons are significantly coupled to more than one polariton branch because one needs to state what is the ratio of populations of the polaritons from the particular branches. The problem was solved by introducing phenomenologically the so–called *additionally boundary conditions* (ABC) [42]. There is, on the other hand, an exact solution based only on the Maxwell boundary conditions (MBC) [40]. The theory is summarized and applied in chapter 6.

3.5 Semiconductor nanostructures

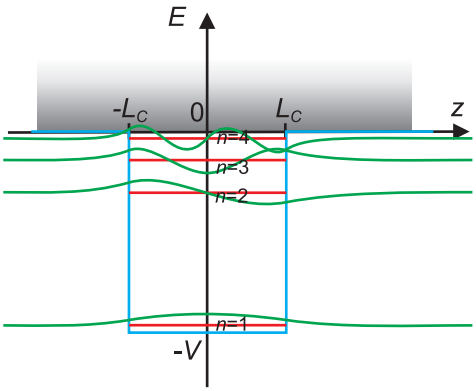

Figure 3.7: Considered profile of the QW potential in the z direction (blue line), wavefunctions of bound states (green lines) and energetical spectrum of the states (black lines and the shaded area).

Semiconductor nanostructures are finite semiconductor crystals with spatial dimensions of the order of nanometer, i.e. comparable to the distances between atoms. Finiteness of the crystal causes quantization of energies of the allowed states of electrons. However, real crystals with dimensions much larger than interatomic distances reveal quasi–continuous bands of allowed states, i.e. quantization may be effectively neglected. When going to nanoscale with crystal dimensions, spacing in energy between states becomes large enough to assume that the states have a discrete energy spectrum (states are no longer denoted by wave vector but one introduces symmetric and antisymmetric linear combinations of states with opposite wave vector).

Electron wavefunctions may be confined in real crystals in 0, 1, 2 or 3 dimensions producing 3–dimensional systems (*bulk crystals*), 2–dimensional systems (*quantum wells*), 1–dimensional systems (*quantum wires*) and 0–dimensional systems (*quantum dots* or *nanocrystals*), respectively.

One may take a two–dimensional structure for illustration (quantum well). Confining potential is a constant in the xy plane and its profile in the z direction is depicted in Fig. 3.7. In the parabolic band approximation and assuming $V \to \infty$, one–particle wavefunctions read:

$$\phi(z) = \frac{\mathcal{N}}{2\pi\Omega} \mathrm{e}^{i\boldsymbol{k}_{\parallel}\cdot\boldsymbol{r}} \begin{cases} \sin(k_z z) \\ \cos(k_z z) \end{cases} , \tag{3.40}$$

where $\boldsymbol{k}_{\parallel}$ stands for the in–plane wave vector and Ω is the area of the xy plane surface. Boundary and normalization conditions then determine [13] $\mathcal{N} = 2/L_c$ and quantization of energy and wave vector: $k_z = \frac{\pi}{2L_c}(2n-1)$ for even and without the last -1 term for odd states, $E = \frac{\pi^2}{8m}\frac{\hbar^2}{L_c^2}(2n-1)^2$ for even and again without the last -1 term in the parentheses for the odd states. Symbol n stands for the principal quantum number of the electron motion in the confining potential. This number is positive integer and quantizes the electron energies in the direction perpendicular to the quantum well. Concerning the overall electron wavefunction, it is determined by the following quantum numbers: x and y component of the wave vector (in–plane wave vector $\boldsymbol{k}_{\parallel}$), band index, spin and its projection, parity and principal quantum number of the motion in the confining potential.

Similarly to bulk crystals, we define angular momentum of electrons using (3.4) and angular momentum of excitons by (3.11) thanks to the full rotational symmetry of the confining potential around the axis z. Lowered symmetry causes mixing of bands and therefore eigenstates of electron or exciton Hamiltonian needn't be symmetrized even when the in–plane wave vector is zero. Symmetrized wavefunctions of electrons, holes and excitons and invariant Hamiltonians for QWs with various symmetries are derived in chapter 5.

Performing the same procedure, we may calculate wavefunctions of electrons in other low–dimensional structures, i.e. quantum wires and quantum dots. Due to different dimensionalities, quantum structures reveal different conservation laws and therefore spin relaxation processes and dipole interaction with optical field are specific for every structure. We discuss these features in the following paragraphs and we focus on quantum wells and dots only.

Quantum wells reveal in–plane translational symmetry which is determined only by the translational symmetry of the bulk crystal lattice in the given directions. As a consequence, in–plane momentum is conserved and wave vector is a good quantum number. Dipole interaction is then nonlocal and the OBE cannot be used for modeling of the nonlinear optical response of QWs as shown later. Concerning wave vector conservation in dipole interaction, only the in–plane momentum is conserved. Due to energy conservation, however, one finds that coherently re–emitted photons have the wave vector equal to the excitation photons. This fact is important in the four–wave mixing experiment and it will be used later.

As discussed above, quantum wells may be also invariant under certain point symmetry operations (reflections, rotations, inversion) what results in conservation of angular momentum, however presence of the confining potential breaks the symmetry of the original 3D lattice and mixing of states with different angular momenta and splitting of states with different symmetries may occur at the Γ point. The most important splitting is the light hole–heavy hole splitting, i.e. splitting of the valence bands (degenerate in zinc–blende bulk crystals) with angular momenta $j_z = \frac{1}{2}$ and $\frac{3}{2}$, respectively. This splitting is similar to splitting caused by stress in the direction of the axis z.

Spin relaxation processes are very similar to those in bulk crystals, they may be, however, suppressed by usage of certain orientations of the growth axis [43]. The main reason for the spin relaxation is the momentum scattering and inhomogeneous broadening (usually even more pronounced when compared to bulk) for the effective spin relaxation.

Discussion of quantum dots (QDs) is even more complicated [44]. Due to confinement in more than one dimension, the confining potential has nontrivial symmetry with respect to point group operations. One usually assumes a cube or a sphere as model potentials, more sophisticated shapes are often used in realistic models. In order to simplify the discussion here, we consider the potential with the spherical symmetry. Point group symmetry is determined only by the lattice symmetry in spherical QDs and therefore spin (its projection) is conserved. The confining potential clearly produces an additional orbital momentum of electrons $\boldsymbol{L}_{\mathrm{con}}$ and thus one defines the total angular momentum of an electron:

$$\hat{\boldsymbol{F}} = \hat{\boldsymbol{L}}_{\mathrm{con}} + \hat{\boldsymbol{J}}\,. \tag{3.41}$$

Discussion of spin structure is beyond this thesis, it may be found e.g. in Refs. [45, 46, 47, 48]. Quantum dots have no translational symmetry and therefore the electron states are localized in dots (there may exist some hopping, we omit this possibility here and we consider homogeneous materials with low concentration of nanocrystals). Dipole interaction is then local and optical response should be modeled using OBE adapted for semiconductor dots.

Due to missing wave vector, relaxation cannot be caused by momentum scattering. Nevertheless the electron–phonon interaction is stronger compared to bulk and QWs and therefore interaction with phonons is the most important spin relaxation mechanism.

Chapter 4

Description of four–wave mixing experiments

4.1 Introduction

The aim of this chapter is to introduce various models and approaches to theoretical description of four–wave mixing experiments on semiconductors and their nanostructures. The dimensionality of the considered system is of a big importance since the process of wave mixing is strongly influenced by the nature of the excited particles.

The most striking difference may be found between bulk materials and quantum dots. Energies of excitons form bands in a bulk crystal and the states are delocalized (i.e. characterized by a wave vector) due to translational symmetry. In quantum dots, on the contrary, states are localized due to the lack of translational symmetry and they reveal discrete energetical spectrum because of the confinement. An ensemble of noninteracting quantum dots then clearly form an atomic–like system (the main difference is, that excitations do not obey Fermi statistics).

It is clear from the above discussion that the two mentioned structures (3D and 0D) need a completely different approach when describing interaction with optical field. While wave vector conservation is required in bulk, localization is important in dots. This discrepancy may be illustrated on the following example: let's consider a system of localized (i) and delocalized (ii) noninteracting bosons and three incoming optical fields denoted by wave vectors $\boldsymbol{k}_1$, $\boldsymbol{k}_2$ and $\boldsymbol{k}_3$. These three fields interact with three independent sorts of particles in the system (ii), resolved by appropriate wave vectors. Since bosons do not influence one the other, there is no way how the waves could mix and therefore no FWM signal is expected. On the contrary, every localized boson interacts with all three fields in the system (i) providing a possibility of wave mixing. These facts may be expressed mathematically. Interaction of a delocalized boson (e.g. exciton) with quantized field is given by the Hamiltonian [13]:

$$\hat{H}_{\mathrm{int}}^{\mathrm{del}} = -\mathrm{i}\hbar \sum_{\boldsymbol{k}} g_{\boldsymbol{k}} \left[\hat{b}_{\boldsymbol{k}}^{+} \hat{a}_{\boldsymbol{k}} - \hat{b}_{\boldsymbol{k}} \hat{a}_{\boldsymbol{k}}^{+} \right], \tag{4.1}$$

where $\hat{b}^{+}$ is a creation operator of a particle and $\hat{a}^{+}$ is creation operator of the field. The variable $g_{\boldsymbol{k}}$ stands for the coupling coefficient. We can do a Fourier transform in order to rewrite the Hamiltonian in real space with assumption that $g_{\boldsymbol{k}} = g$:

$$\hat{a}_{\boldsymbol{k}} = \frac{1}{\sqrt{\Omega}} \int \mathrm{e}^{-\mathrm{i}\boldsymbol{k}\cdot\boldsymbol{r}} \hat{a}(\boldsymbol{r}) \, \mathrm{d}\boldsymbol{r} \,, \qquad \hat{b}_{\boldsymbol{k}} = \frac{1}{\sqrt{\Omega}} \int \mathrm{e}^{-\mathrm{i}\boldsymbol{k}\cdot\boldsymbol{r}} \hat{b}(\boldsymbol{r}) \, \mathrm{d}\boldsymbol{r} \,, \tag{4.2}$$

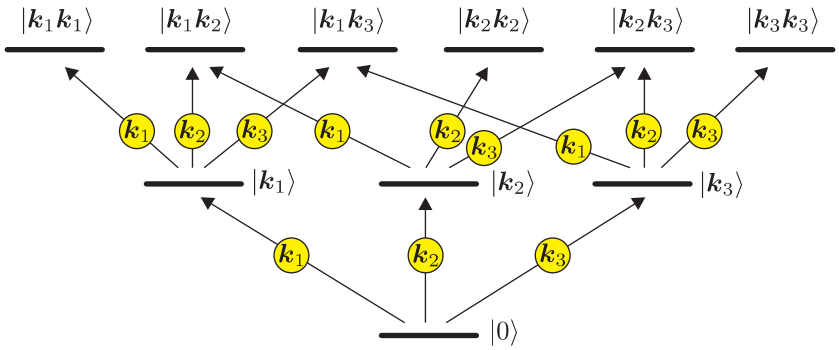

Figure 4.1: Level scheme appropriate for the system of bosons described by their wave vectors. Dipole interactions are depicted as arrows with the appropriate wave vectors. Interaction with fields with wave vectors $\boldsymbol{k}_1$, $\boldsymbol{k}_2$ and $\boldsymbol{k}_3$ only is considered.

$$\hat{H}_{\mathrm{int}}^{\mathrm{del}} = -\mathrm{i}\hbar\frac{g}{\Omega}\sum_{\boldsymbol{k}}\int \mathrm{d}\boldsymbol{r}\int \mathrm{d}\boldsymbol{r}'[\mathrm{e}^{\mathrm{i}\boldsymbol{k}\cdot(\boldsymbol{r}-\boldsymbol{r}')}\hat{b}^{+}(\boldsymbol{r})\hat{a}(\boldsymbol{r}') - H.c.] = \\ = -\mathrm{i}\hbar\frac{g}{\Omega}\int\left[\hat{b}^{+}(\boldsymbol{r})\hat{a}(\boldsymbol{r}) - \hat{b}(\boldsymbol{r})\hat{a}^{+}(\boldsymbol{r})\right]\mathrm{d}\boldsymbol{r}\,, \tag{4.3}$$

where Ω is a normalization volume. A localized boson, on the contrary, interacts with the light field independently of its wave vector:

$$\hat{H}_{\mathrm{int}}^{\mathrm{loc}} = -\mathrm{i}\hbar\frac{g}{\Omega}\left[\hat{b}^{+}(\boldsymbol{r}_0)\hat{a}(\boldsymbol{r}_0) - \hat{b}(\boldsymbol{r}_0)\hat{a}^{+}(\boldsymbol{r}_0)\right] = -\mathrm{i}\hbar\frac{g}{\Omega}\sum_{\boldsymbol{k}}\left[\mathrm{e}^{-\mathrm{i}\boldsymbol{k}\cdot\boldsymbol{r}_0}\hat{b}^{+}(\boldsymbol{r}_0)\hat{a}_{\boldsymbol{k}} - \mathrm{e}^{\mathrm{i}\boldsymbol{k}\cdot\boldsymbol{r}_0}\hat{b}(\boldsymbol{r}_0)\hat{a}_{\boldsymbol{k}}^{+}\right]. \tag{4.4}$$

The coordinate $\boldsymbol{r}_0$ is fixed for every single excitation. For a system of bosons, one should integrate over $\boldsymbol{r}_0$ in order to develop the Hamiltonian appropriate for the whole ensemble. This Hamiltonian then wouldn't mathematically differ from (4.3). The point is, that only operators of the type $(\hat{b}^{+}(\boldsymbol{r}_0))^m$ contribute to the polarization due to spatial isolation of particular bosons. In dense media, site–to–site hopping is allowed and therefore also operators $\hat{b}^{+}(\boldsymbol{r})\hat{b}^{+}(\boldsymbol{r}')\cdots$, $\boldsymbol{r}\neq\boldsymbol{r}'$ contribute to the macroscopic polarization. Spatial correlations then prevent creation of the third–order response if the wave vectors of incident beams are not equal.

In order to rigorously prove that the delocalized states do not produce wave mixing signal, one can develop a density matrix formalism for delocalized states. The basis of excitations is composed of states characterized by wave vector and we can, in accordance to a system of photons, define creation operators $\hat{b}_{\boldsymbol{k}}^{+}$ of particles. Because of wave vector conservation, we can reduce the basis for the density matrix description only to the states with wave vectors equal to wave vectors of the components of optical field. Considering third–order response, we can neglect the states consisting of three and more particles. The level scheme appropriate for the system is depicted in Fig. 4.1 with all dipole interactions involved within the selected basis of particles. The path of evolution of the density matrix towards the coherence in the FWM direction $\boldsymbol{k}_1+\boldsymbol{k}_2-\boldsymbol{k}_3$ is schematically shown in Fig. 4.2 where e.g. the coherence $\varrho_{\boldsymbol{k}_1\boldsymbol{k}_2,0}$ represents a two–photon coherence between the state with particles with wave vectors $\boldsymbol{k}_1$, $\boldsymbol{k}_2$ and the ground state. In the result, the coherence described by the density matrix element $\varrho_{\boldsymbol{k}_1\boldsymbol{k}_2,\boldsymbol{k}_3}$ is nonzero. Looking at the level scheme in Fig. 4.1, one concludes that there is no dipole interaction and therefore this coherence is not coupled to the optical field. Although the coherence is created, it expresses only some

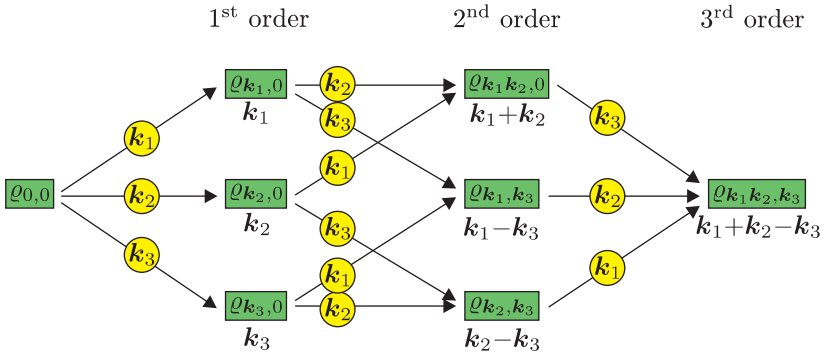

Figure 4.2: Evolution of the density matrix elements for the system of delocalized bosons from the ground state in the 0–th order to the coherence denoted by the wave vector $\boldsymbol{k}_1+\boldsymbol{k}_2-\boldsymbol{k}_3$ in the third order. The encircled symbols denote wave vectors of incoming light and symbols in boxes stand for nonzero density matrix elements induced by particular dipole interaction which induce creation of a coherence in the diffraction direction.

correlation between particles but does not necessarily mean that the field in the given direction is radiated. In the system of localized states, on the contrary, every one–photon coherence is coupled to the optical field.

The systems of localized and delocalized states must be obviously discussed separately and different models must be applied to their description. The following chapters are therefore separated to the part concerning low–dimensional structures (chapter 5) and bulk crystals (chapters 6–7). The aim of the rest of this chapter is to overview the existing models which were applied for description of FWM experiments on semiconductors. I discuss only the models used for description of 3D and 2D structures since 0D structures are well modeled using OBE — a detailed discussion may be found in chapter 5.

Discussed models can be in general divided to two groups: *microscopic theories* and *OBE–like models*. The former models are established on microscopical description of electron potential, electron–hole interactions and exciton–photon interactions. Equations of motion are derived on the basis of electron and hole Hamiltonian. The models developed from optical Bloch equations are, on the contrary, rather phenomenological. Their advantage is in their simple structure since calculations can be done perturbatively and one can obtain analytical solution of the equations of motion. The precision of OBE–like models is not, however, high because of their phenomenological nature. The two groups of theories are introduced and overviewed in the following text. microscopical theories in section 4.3.

4.2 Modified Optical Bloch Equations

Optical Bloch equations are simple in structure, therefore they were applied for description of FWM response of semiconductors. The basic idea is, that the FWM response of semiconductors is caused by Pauli blocking as well as in atomic systems and the OBE were then directly applied. This consideration is further supported by simplification of semiconductor Bloch equations [13] under assumption of weak excitation. An electron with spin $+\frac{1}{2}$ or $-\frac{1}{2}$ can be excited at any atomic site in the semiconductor, the spin of the excited electron depends on the polarization of the incoming field. Assuming excitation from the heavy–hole band, the σ^+ photon excites the electron with spin $-\frac{1}{2}$ and leaves

a hole with spin $+\frac{3}{2}$. No more electrons with spin $-\frac{1}{2}$ can be thus excited at the same atomic site providing the Pauli blocking effect. Using a system of levels similar to Fig. 2.1, one may model a system of two fermions with opposite spins at one site [1].

The mentioned system, however, cannot describe the observed effects connected with biexcitons, namely exciton–biexciton beating. One therefore performs a correction of the model by renormalization of the energy of the two–exciton state [1, 49, 50]. There is, however, another very important discrepancy between theory and experiment: the temporal evolution of the FWM response. It was shown both experimentally [51, 52] and theoretically [53, 54] (using microscopic theories) that the FWM signal from semiconductors is not instantaneous after optical excitation but its maximum is delayed with respect to the time of arrival of the last excitation pulse. Note that this effect is not caused by inhomogeneous broadening (it is not the photon echo) as proven experimentally [21]. The problem can be fixed (together with some polarization selection rules) by introduction of *excitation induced dephasing* (EID) [55, 56] for a polarization configuration of incoming pulses e.g. $\sigma^+\sigma^-\sigma^+$. The problem further remains if one assumes pulses with the same circular polarizations and time order of arrival $t_1, t_2 < t_3$ — in such case, the FWM response is predicted to immediately follow the last pulse while the peak is delayed in experiments. Consideration of local field effects (LFE) [21, 53, 57] then may correct this problem.

Besides temporal evolution, the usage of modified OBE (mOBE) is inaccurate in order to determine the polarization of the FWM response of semiconductors. Authors use various types of level schemes [58, 59, 60, 61, 62, 63, 64, 65] which may reasonably differ from the scheme in Fig. 2.1 considered above. It is not therefore easy to show that none of the schemes is able to predict polarization selection rules of FWM without any error. However I present calculations of polarization selection rules for few basic types of schemes in chapter 5. I include the schemes used in literature and also schemes appropriate for semiconductor quantum dots. The polarization selection rules are summarized in Tabs. 5.1 and 5.2. The correct polarization selection rules are figured for comparison and the conclusion is, that the OBE–like models are not sufficient for description of FWM on bulk semiconductors and quantum wells.

Although mOBE were successfully used for explanation of some basic features of FWM response of semiconductors, they have many limitations caused by their phenomenological nature and they cannot thus be used in a general situation. The last note concerning mOBE is, that the strong exciton–photon coupling is described perturbatively (in the first order) and one of the most important properties of semiconductors — polariton effect — is omitted. As a result, FWM response is expected to reveal discrete lines in spectra what is not in agreement with some experimental observations.

4.3 Microscopic theories

Besides the attempts to use optical Bloch equations for description of semiconductor third–order nonlinearities, the main theoretical approach was the microscopic description of a semiconductor using electron–hole Hamiltonian. Construction of such Hamiltonian is easy, there are only harmonic terms, particle–particle scattering terms and terms responsible for interaction with electromagnetic field. Derivation of equations of motion is straightforward, however they form an infinite system of coupled differential equations whose analytical solution is impossible. Various microscopic models then use some approximations in order to include all important informations to the dynamical equations on one side and to simplify the problem on the other.

The necessity of the development of microscopic theories comes from the fact that OBE–like models do not sufficiently reproduce the experimental data. The main features which are unexplained by OBE are the slow initial rise of the FWM signal, signal for temporal order of pulses $t_1, t_2 < t_3$ and polarization selection rules. As discussed in the previous section, there may be introduced several corrections of the OBE in order to describe the aforementioned phenomena, these corrections are, however, derived microscopically. In addition, corrected OBE still slightly differ from experiments mainly in their polarization selection rules. Microscopic theories are obviously of a big significance.

The basic classification of the microscopic theories can be done using two criteria: whether the four–particle correlations are included and whether the model describes electrons and holes or bound complexes — excitons. Based on the first criterion, we discriminate between semiconductor Bloch equations (SBE) where the four–particle correlations[1] are approximated by the products of two–particle correlations and more advanced theories where the four–particles correlations are taken into account. Factorization is then performed for six–particle correlation functions. The second criterion then allows us to discriminate between fully fermionic theories where both electrons and holes are considered and bosonized theories where excitons are the basic excitations in the system.

In the following subsections, theories are divided to three groups and they are briefly summarized. The groups are: semiconductor Bloch equations, four–particle correlation theories and bosonized theories.

4.3.1 Semiconductor Bloch equations

Semiconductor Bloch equations derived in Ref. [3, 13] were one the first microscopic theories applied to semiconductors in order to describe their nonlinear response to ultrafast optical excitation [66, 67, 68]. The structure of the equations is very similar to the optical Bloch equations. Differences are not, however, negligible and cause big differences in predictions of the two models. The aforementioned differences are three: in SBE, the eigenstates are not excitons but rather electrons and holes. In addition, these particles are not assumed to be independent but they interact via Coulomb interaction. The third difference is, that SBE are formulated in the reciprocal k–space while OBE are in real space. Formulation in k–space causes vanishing of the FWM response for noninteracting particles (see above) and it is thus clear that the FWM response is due to the particle–particle interactions. This point was proven also experimentally [54, 69].

Semiconductor Bloch equations are formulated for two bands, i.e. for the case when the valence and conduction bands are nondegenerate. Based on SBE, one can also derive equations for degenerate bands [6]. Denoting $\hat{c}^+_{\boldsymbol{k}}$ to be a fermionic operator for creation of an electron in the conduction band and $\hat{d}^+_{-\boldsymbol{k}}$ to be an operator for creation of a hole with wave vector $-\boldsymbol{k}$ in the valence band (i.e. annihilation of an electron with the wave vector $\boldsymbol{k}$ in the valence band), the total Hamiltonian reads [3, 13]:

$$\begin{aligned}\hat{H} = &\sum_{\boldsymbol{k}} \left[\varepsilon_{\mathrm{e}}(\boldsymbol{k})\hat{c}^+_{\boldsymbol{k}}\hat{c}_{\boldsymbol{k}} + \varepsilon_{\mathrm{h}}(\boldsymbol{k})\hat{d}^+_{\boldsymbol{k}}\hat{d}_{\boldsymbol{k}}\right] + \\ &+ \sum_{\boldsymbol{k},\boldsymbol{k}'}\sum_{\boldsymbol{q}\neq 0} V(\boldsymbol{q})\left[\hat{c}^+_{\boldsymbol{k}+\boldsymbol{q}}\hat{c}^+_{\boldsymbol{k}'-\boldsymbol{q}}\hat{c}_{\boldsymbol{k}'}\hat{c}_{\boldsymbol{k}} + \hat{d}^+_{\boldsymbol{k}+\boldsymbol{q}}\hat{d}^+_{\boldsymbol{k}'-\boldsymbol{q}}\hat{d}_{\boldsymbol{k}'}\hat{d}_{\boldsymbol{k}} - 2\hat{c}^+_{\boldsymbol{k}+\boldsymbol{q}}\hat{d}^+_{\boldsymbol{k}'-\boldsymbol{q}}\hat{d}_{\boldsymbol{k}'}\hat{c}_{\boldsymbol{k}}\right] - \\ &- \sum_{\boldsymbol{k}}\left[d_{\boldsymbol{k}}E(t)\hat{c}^+_{\boldsymbol{k}}\hat{d}^+_{-\boldsymbol{k}} + d^*_{\boldsymbol{k}}E^*(t)\hat{d}_{-\boldsymbol{k}}\hat{c}_{\boldsymbol{k}}\right], \end{aligned} \tag{4.5}$$

[1] Correlations between four fermions, see Refs. [3, 13]. The four–particle correlation terms have the form $\langle\hat{c}^+_{\boldsymbol{k}+\boldsymbol{q}}\hat{c}_{\boldsymbol{k}}\hat{d}^+_{-\boldsymbol{k}'}\hat{d}_{-\boldsymbol{k}'+\boldsymbol{q}}\rangle$, where $\hat{c}^+$ and $\hat{d}^+$ stand for creation operators of electrons and holes, respectively.

where $\varepsilon_{\mathrm{e}}(\boldsymbol{k})$ is the energy of an electron in the conduction band, $\varepsilon_{\mathrm{h}}(\boldsymbol{k})$ is the energy of a hole in the valence band (this energy is positive and equals $\varepsilon_{\mathrm{h}}(\boldsymbol{k}) = -\varepsilon_{\mathrm{v}}(\boldsymbol{k})$, where $\varepsilon_{\mathrm{v}}(\boldsymbol{k})$ is the energy of an electron in the valence band). Function $V(\boldsymbol{q})$ then determines the strength of the Coulomb interaction, $E(t)$ is the time–dependent amplitude of electric field and $d_{\boldsymbol{k}}$ is the dipole matrix element for a transition of an electron from the valence to the conduction band. The first line in (4.5) determines single–particle energies, the second line describes particle–particle Coulomb interactions and the third line stands for the dipole interaction with optical field. The single–particle energies are often approximated within the effective mass approximation by parabolic bands.

Similarly to OBE, one can define populations and polarizations as the mean values:

$$n_{\mathrm{e},\boldsymbol{k}} = \left\langle \hat{c}^{+}_{\boldsymbol{k}} \hat{c}_{\boldsymbol{k}} \right\rangle , \tag{4.6}$$

$$n_{\mathrm{h},\boldsymbol{k}} = \left\langle \hat{d}^{+}_{-\boldsymbol{k}} \hat{d}_{-\boldsymbol{k}} \right\rangle , \tag{4.7}$$

$$p^{*}_{\boldsymbol{k}} = \langle \hat{c}^{+}_{\boldsymbol{k}} \hat{d}^{+}_{-\boldsymbol{k}} \rangle . \tag{4.8}$$

The first two lines are simply the populations of the electron and hole states described by the wave vector $\boldsymbol{k}$, the third line is the interband polarization which couples to electromagnetic field. Using the following equation of motion, one can simply derive equations for the above defined variables:

$$i\hbar \frac{\partial}{\partial t} \langle \hat{A} \rangle = \langle [\hat{A}, \hat{H}] \rangle . \tag{4.9}$$

The full equations of motion are given in [3, 13]. Besides populations and polarization, they contain the so–called *four–particle correlations* on the right hand side, which are functions of the form $\langle \hat{c}^{+}_{\boldsymbol{k}+\boldsymbol{q}} \hat{d}^{+}_{\boldsymbol{k}'-\boldsymbol{q}} \hat{d}_{\boldsymbol{k}'} \hat{c}_{\boldsymbol{k}} \rangle$ with various combinations of creation and annihilation operators for electrons and holes. These four–particle correlations cannot be expressed by the functions (4.6)–(4.8). Equations of motion for the four–particle correlations involve six–particle correlation functions and it is clear that the system of dynamical equations is not closed. One then may perform truncation in order to get rid of the four–particle correlation functions. They are approximated using a projection technique described in [3]. As a result, the equations of motion have two contributions on the right hand side — a coherent and an incoherent one. Incoherent terms are caused by incoherent scattering events and are important in the high–excitation regime. In the low–density regime, they can be neglected and the nonlinear response of the system to the optical excitation may be described by the coherent part only. Using renormalized single–particle energies:

$$\varepsilon^{\mathrm{s}}_{\mathrm{h}}(\boldsymbol{k}) = \varepsilon_{\mathrm{h}}(\boldsymbol{k}) + \sum_{\boldsymbol{q} \neq 0} V(\boldsymbol{q}) , \tag{4.10}$$

the coherent semiconductor Bloch equations read:

$$\begin{aligned} \frac{\partial}{\partial t} p^{*}_{\boldsymbol{k}} = \mathrm{i} \Big[\varepsilon_{\mathrm{e}}(\boldsymbol{k}) + \varepsilon^{\mathrm{s}}_{\mathrm{h}}(\boldsymbol{k}) - \sum_{\boldsymbol{q} \neq 0} V(\boldsymbol{q}) (n_{\mathrm{e},\boldsymbol{k}+\boldsymbol{q}} + n_{\mathrm{h},\boldsymbol{k}+\boldsymbol{q}}) \Big] p^{*}_{\boldsymbol{k}} - \\ - \mathrm{i} \Big[d^{*}_{\boldsymbol{k}} E^{*}(t) + \sum_{\boldsymbol{q} \neq 0} V(\boldsymbol{q}) p^{*}_{\boldsymbol{k}+\boldsymbol{q}} \Big] (1 - n_{\mathrm{e},\boldsymbol{k}} - n_{\mathrm{h},\boldsymbol{k}}) , \end{aligned} \tag{4.11}$$

$$\frac{\partial}{\partial t} n_{\mathrm{e},\boldsymbol{k}} = -2\mathrm{Im} \left\{ \Big[d_{\boldsymbol{k}} E(t) + \sum_{\boldsymbol{q} \neq 0} V(\boldsymbol{q}) p_{\boldsymbol{k}+\boldsymbol{q}} \Big] p^{*}_{\boldsymbol{k}} \right\} , \tag{4.12}$$

$$\frac{\partial}{\partial t} n_{\mathrm{h},\boldsymbol{k}} = \frac{\partial}{\partial t} n_{\mathrm{e},\boldsymbol{k}} . \tag{4.13}$$

The above equations are not solvable analytically due to the Coulomb interaction which couples states with different wave vectors and thus several types of approximations are often used. Note that neglect of Coulomb interaction yields optical Bloch equations for an inhomogeneously broadened system of delocalized states as discussed in chapter 5 and no wave mixing is expected.

The first approximation is the assumption of weak excitation [3, 13]. One then neglects nonlinear terms in (4.11)–(4.13), note that the Coulomb coupling on the right hand side of (4.11) remains. This coupling is responsible for formation of excitons and after transformation to real space, one obtains equations which are of the same structure as OBE for an inhomogeneously broadened system.

The local field model is a more advanced approximation [21, 57]. The core assumption of this model is the assumption:

$$\sum_{\boldsymbol{q}\neq 0} V(\boldsymbol{q}) p_{\boldsymbol{k}+\boldsymbol{q}} \approx V p_{\boldsymbol{k}} \,. \tag{4.14}$$

The off–diagonal terms in Hamiltonian then yield:

$$d_{\boldsymbol{k}} E(t) + \sum_{\boldsymbol{q}\neq 0} V(\boldsymbol{q}) p_{\boldsymbol{k}+\boldsymbol{q}} = d_{\boldsymbol{k}} E(t) + V p_{\boldsymbol{k}} \,. \tag{4.15}$$

Dipole interaction is then renormalized by the local field generated by the polarization of other electron–hole pairs. The solution of equations of motion is then reasonably simplified.

The theory is further simplified in the stochastic theory [4, 53, 57] by dropping electron–hole pairs and introducing excitons as the bound states. The theory then contains bosons and saturation is described by a phenomenological saturation parameter ψ_{s}. The polarization at one site is given by the function $\psi(t)$ and its dynamical equation (of the form of nonlinear Schrödinger equation) reads [53]:

$$\frac{\partial}{\partial t}\psi(t) = -i(\Omega_{\mathrm{X}} - \mathrm{i}\Gamma)\psi(t) + \mathrm{i}dE(t)\left(1 - \frac{|\psi(t)|^2}{\psi_{\mathrm{s}}^2}\right) - \mathrm{i}V|\psi'(t)|^2\psi(t)\,, \tag{4.16}$$

where d is the dipole matrix element, $\hbar\Omega_{\mathrm{X}}$ is the exciton energy, $\Gamma = T_2^{-1}$ stands for exciton dephasing rate and $\psi'(t)$ is the exciton polarization at other sites. Parameter V describes site–to–site interactions. The first term in the equation describes nonperturbed evolution and dephasing of the polarization. The second term then stands for saturable dipole interaction and the last term for Coulomb interaction.

Although the approximations mentioned above simplify reasonably the structure of equations, they must be solved numerically.

Because of factorization of the four–particle correlation terms, the SBE (4.11)–(4.13) are not accurate in many cases. It is possible to develop polarization selection rules using SBE [6], these selection rules do not, however, take into account the symmetry of crystal lattice and also biexcitons are omitted. The more advanced theories which take into account four–particle correlations were therefore developed.

4.3.2 Four–particle correlation theories

Since the semiconductor Bloch equations, calculated within the Hartree–Fock approximation, do not describe many effects and overestimate the coherence of the system [70], more sophisticated theories were developed without factorization of four–particle correlation functions. These theories include usual equations of motion for electrons and holes and their core is in truncation of correlation functions. The procedure of truncation is often called *dynamical truncation*.

Comparison of the microscopically derived FWM using the model which involves dynamical truncation to SBE was firstly published by Axt and Victor [5, 71] and by Lindberg et al. in Ref. [70]. Bosonized theory which accounts for exciton–exciton correlations can be found in Ref. [8]. It follows that it is possible to truncate the six– and more–particle correlation functions when the interband polarization is created only by external optical fields and one is interested in the third–order optical response. Neglect of the four–particle correlations in SBE causes that some scattering and exchange mechanisms vanish in equations of motion. This neglect then may be crucial in the low–density regime when the density of carriers is far below the Mott density. The theory in Ref. [70] doesn't, however, describe biexcitons as the biexciton binding is neglected and therefore no features of the FWM connected with biexcitons may be described.

Theories which take into account four–particle correlations including biexcitons may be found in Refs. [54, 72, 73], the latter theory is applied to pump and probe experiments. The model presented by Schäfer et al. [54] introduces a nonlinear Schrödinger equation similar to (4.16) with the new source term which comes from four–particle correlations. Theory does not, however, include spin. A theory developed on the basis of excitons was published in Refs. [74, 75]. This theory takes into account exciton spin and thus it can be well applied to model FWM response of semiconductors but equations of motion are complex in structure and they require numerical evaluation. The theory clearly shows that the FWM signal comes from exciton–exciton correlations including both bound biexcitons and unbound two–exciton pairs.

4.3.3 Weakly interacting boson model

Microscopic theories described above were mostly developed for the two–band situation, i.e. without taking into account the spin of electrons and holes. It was found that in high–finesse microcavities, the normal mode splitting in nonlinear response is dependent on the polarization configuration [76] and therefore a spin–sensitive theory was necessary. In the weak excitation regime, the theory should describe four–particle correlations and therefore a simple extension of SBE for degenerate bands is not sufficient. The general theory by Östreich et al. [74, 75] is rigorous but too complex for special applications.

A theory which is capable of simple description of interacting excitons in semiconductor was developed in the framework of Weakly Interacting Boson Model (WIBM) [7, 76, 77, 78, 79]. The Hamiltonian of the model is bosonized and phenomenologically takes into account exciton–exciton Coulomb interactions and phase space filling (Pauli blocking) which comes from the composite character of excitons. All spins of excitons are not, however, taken into account, only the dipole–active states contribute. The Hamiltonian in k–space reads [77]:

$$\hat{H} = \hbar\omega_{\mathrm{e}} \sum_{\boldsymbol{k}} \left(\hat{b}^{+}_{\boldsymbol{k}+} \hat{b}_{\boldsymbol{k}+} + \hat{b}^{+}_{\boldsymbol{k}-} \hat{b}_{\boldsymbol{k}-} \right) +$$
$$+ \frac{\pi a_{\mathrm{B}}^2}{S} \sum_{\boldsymbol{k}_1,\boldsymbol{k}_2,\boldsymbol{k}_3} \Big[\hbar R \left(\hat{b}^{+}_{\boldsymbol{k}_1+} \hat{b}_{\boldsymbol{k}_2+} \hat{b}^{+}_{\boldsymbol{k}_3+} \hat{b}_{\boldsymbol{k}_1-\boldsymbol{k}_2+\boldsymbol{k}_3+} + \hat{b}^{+}_{\boldsymbol{k}_1-} \hat{b}_{\boldsymbol{k}_2-} \hat{b}^{+}_{\boldsymbol{k}_3+} \hat{b}_{\boldsymbol{k}_1-\boldsymbol{k}_2+\boldsymbol{k}_3-} \right) -$$
$$- \hbar W \hat{b}^{+}_{\boldsymbol{k}_1+} \hat{b}_{\boldsymbol{k}_2-} \hat{b}^{+}_{\boldsymbol{k}_3+} \hat{b}_{\boldsymbol{k}_1-\boldsymbol{k}_2+\boldsymbol{k}_3-} \Big] +$$
$$+ \sum_{\boldsymbol{k},\sigma=\pm} \left[\hbar\omega \hat{a}^{+}_{\boldsymbol{k}\sigma} \hat{a}_{\boldsymbol{k}\sigma} + \hbar g \left(\hat{a}^{+}_{\boldsymbol{k}\sigma} \hat{b}_{\boldsymbol{k}\sigma} + \hat{a}_{\boldsymbol{k}\sigma} \hat{b}^{+}_{\boldsymbol{k}\sigma} \right) \right] -$$
$$- \frac{\pi a_{\mathrm{B}}^2}{S} \sum_{\boldsymbol{k}_1,\boldsymbol{k}_2,\boldsymbol{k}_3} \sum_{\sigma=\pm} \hbar g \nu \left(\hat{b}_{\boldsymbol{k}_1\sigma} \hat{b}_{\boldsymbol{k}_2\sigma} \hat{a}^{+}_{\boldsymbol{k}_3\sigma} \hat{b}_{\boldsymbol{k}_1-\boldsymbol{k}_2+\boldsymbol{k}_3\sigma} + \hat{b}^{+}_{\boldsymbol{k}_1\sigma} \hat{a}_{\boldsymbol{k}_2\sigma} \hat{b}^{+}_{\boldsymbol{k}_3\sigma} \hat{b}_{\boldsymbol{k}_1-\boldsymbol{k}_2+\boldsymbol{k}_3\sigma} \right) . \quad (4.17)$$

The operators $\hat{b}^{+}_{\boldsymbol{k}\sigma}$ create an exciton with wave vector $\boldsymbol{k}$ and spin $\sigma = \pm$ and $\hat{a}^{+}_{\boldsymbol{k}\sigma}$ creates a photon. Variable $\hbar\omega_{\mathrm{e}}$ is then the exciton energy, $\hbar\omega$ is the photon energy, a_{B} is the exciton Bohr radius, g is the exciton–photon coupling coefficient, ν stands for nonlinear exciton–photon coupling coefficient and S stands for the normalization volume. The first line in (4.17) stands for exciton harmonic term and the second and the third line then for exciton–exciton interaction. The two–particle interactions are considered to be of two types: repulsive for excitons with the same spin and attractive for excitons with opposite spins. Spin sensitivity of the scattering process is caused by the composite character of excitons and therefore by the exchange interaction between excitons [10]. As a result, the energy of two–exciton pairs is renormalized (see Fig. 4.3). The last two lines in (4.17) stand for exciton–photon coupling — the fourth line is the usual term which describes photon energy and linear exciton–photon transitions. The last line is the nonlinear correction of the dipole interaction which describes also phase space filling.

Using Hamiltonian (4.17), it is possible to derive equations of motion. Instead of this standard procedure, the density matrix approach is used. It means that one defines density matrix elements:

$$\varrho^{m\alpha}_{n\beta} = \langle\langle |m\alpha\rangle\langle n\beta| \rangle\rangle , \quad (4.18)$$

where $|m\alpha\rangle$ denotes an m–exciton state with the spin projection α. Wave vector was neglected since the optical beams are all assumed to be perpendicular to the quantum well plane. The model is then similar to optical Bloch equations, and can be sketched in a level scheme in Fig. 4.3. In the equations of motion, dephasing rates are phenomenologically introduced and excitation induced dephasing is taken into account.

The equations of motion form a closed set of equations which can be solved by expansion into power series of the external optical field. On the contrary to OBE, the exciton–photon interaction is not taken into account perturbatively due to strong exciton–photon coupling in microcavities. The results of the model were used for explanation of various phenomena which arise in FWM experiments on semiconductor microcavities.

Compared to standard microscopic theories, the model is oversimplified since the wave vector is neglected and scattering terms are responsible only for renormalization of energy of two–particle states and EID which is introduced phenomenologically. A rigorous solution of equations of motion which may be derived from the Hamiltonian (4.17) may be generally complex and it would need numerical calculations.

The WIBM model, however, introduces several interesting simplifications which may be used in order to reduce the complexity of exact microscopic equations. Electron–hole pairs are approximated by excitons which are assumed to interact only weakly (in the

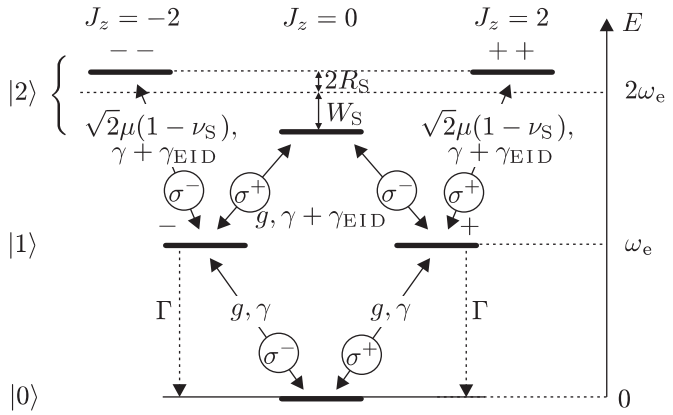

Figure 4.3: Six–level scheme for the Weakly Interacting Boson Model as introduced in Ref. [77]. Symbols in circles denote the polarizations of absorbed photons, symbols g, γ then stand for dipole matrix elements and dephasing rates for coherences. The rate γ_{EID} denotes additional dephasing due to excitation induced dephasing effect, ν_{S} is the parameter of band filling. Symbols Γ represent population relaxation rate.

weak excitation regime). Exciton–exciton interactions are then described by constants which depend on the spins of interacting excitons. The last important simplification is introduction of nonlinear correction to dipole interaction. Assumption of strong exciton–photon interaction then allows one to use the model under resonant excitation.

4.4 Conclusion

In this chapter, basic models for description of FWM experiments on semiconductors are overviewed. I have shown that structures with translational symmetry and structures with localized particles require different approaches — one uses OBE with success for the latter and various phenomenological or microscopic models for the former.

Application of OBE to bulk semiconductors is shown to provide considerable errors in predictions of dynamics and mainly polarization selection rules. For this reason, these models are not generally applicable, however they may be used under special conditions when a simplicity of the model is required. Microscopic theories are, on the contrary, accurate but integration of equations of motion cannot be performed analytically and numerical evaluation is time–consuming.

There are several points which make differences between atomic systems and bulk semiconductor and for these reasons, the systems require different descriptions. First, states are localized in atomic systems and delocalized in bulk crystals and therefore FWM response is generated in the former case even without particle–particle interactions while Coulomb interaction is responsible for wave mixing in the latter case. Also the role of Pauli blocking is quite different in the both cases.

Since the aim of this thesis is to describe influence of spin relaxation in semiconductors on FWM signal, a model with correct polarization selection rules should be used. One may use OBE for quantum dots but another model is needed for bulk semiconductors. Since there was not yet published any model with correct polarization selection rules of FWM on bulk semiconductors with a simple structure similar to OBE, a model based on description by delocalized states is developed in chapters 6 and 7.

Chapter 5

FWM on low–dimensional structures

5.1 Introduction

Theory in this section, which presents my original results, is focused on description of four–wave mixing on low–dimensional semiconductors, namely quantum dots and quantum wells. Quantum dots may be described in the same manner as atomic systems since they reveal discrete energetical levels of localized states. However, when compared to OBE developed in chapter 2, calculations must be extended by inclusion of spin and a correct statistics of excitations — model schemes are overviewed in section 5.2 where I develop polarization selection rules for FWM experiments and I outline the system's dynamics. Quantum wells, on the contrary, reveal in–plane translational symmetry and thus two components of wave vector are conserved. Energy conservation ensures in addition an effective conservation of full wave vector. The situation is therefore similar to bulk materials and one may therefore apply the 3D models also to quantum wells. Therefore I perform rather an extension of the model described in chapter 6 instead of development of an original model for 2D structures (see section 7.8). Excitons in quantum wells reveal, however, unique properties when compared to bulk, e.g. splitting of hh and lh bands, coupling of the states as a consequence of the exchange interaction at the Γ point or biexciton spin structure. For this reason, spin structure and effective Hamiltonians for particles are derived in section 5.3.

Phenomenological mOBE models used in literature (see section 4.2) involve the level schemes equivalent to those explored in section 5.2. Since any investigation of the complete polarization selection rules for mOBE models was not published yet, one should use the original results of section 5.2 to unambiguously state whether the mOBE models give the correct polarization selection rules or not. Discussion then results in the conclusion that mOBE models are not sufficient and this statement justifies development of a more accurate model for bulk semiconductors and quantum wells in chapter 6.

I consider no changes of spin during temporal evolution of states in nanocrystals in section 5.2. It is therefore possible to use only dipole–active states for description of nanocrystals. Extension by considering dipole–inactive states, spin precession and relaxation etc. is then straightforward.

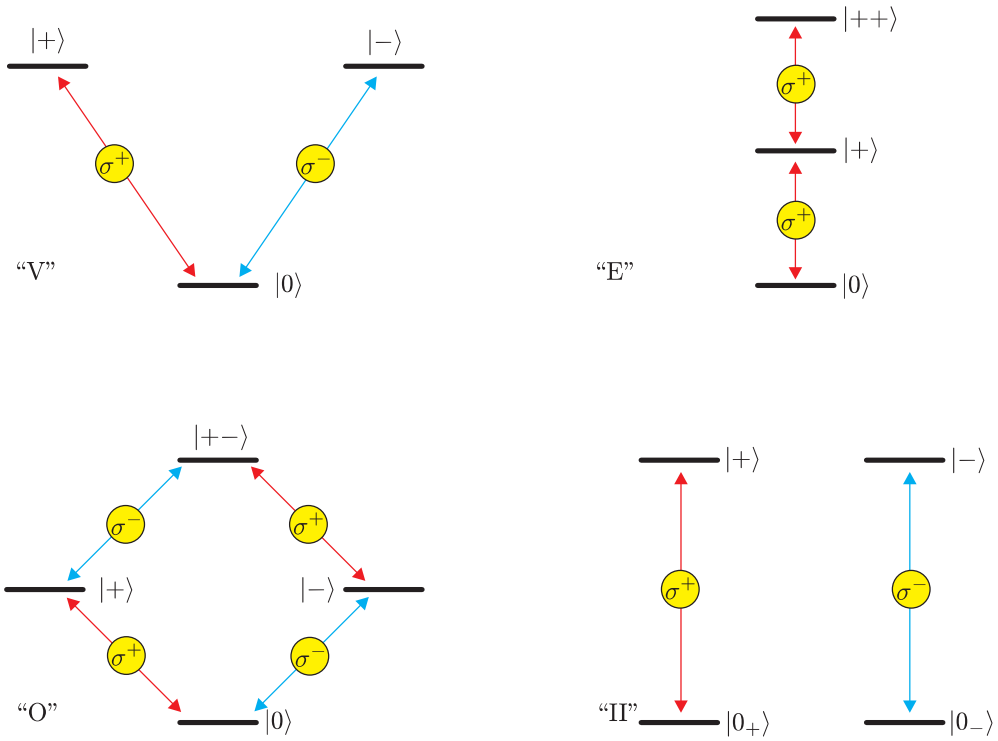

Figure 5.1: The level schemes appropriate for the four systems under investigation. The horizontal lines depict the possible states of the system and the arrows denote dipole couplings between the states. The encircled sign then represents the polarization for which the coupling is allowed.

5.2 Optical Bloch equations on quantum dots

In this section, I investigate four basic level schemes (see Fig. 5.1) which may be used in order to describe quantum dots under influence of the optical field. One uses the standard approach of OBE, however a more–level systems must be used instead of a two–level system due to spin. In addition, one must take the correct statistics of excitons into account.

States of nanocrystals obviously involve the ground state, one–exciton states, two–exciton states etc. Two and more–exciton states have, however, renormalized energies due to exciton–exciton interaction. We must therefore discriminate between the following situations:

- Energy renormalization is bigger than spectral width of the excitation pulse — usually in the strong confinement regime, one thus may neglect the influence of two–exciton states. In this case, one may use the "V" system presented in subsection 5.2.1.
- Excitations are considered to obey Fermi statistics — one uses the "O" system described in subsection 5.2.3.
- Energy renormalization is small — in weak confinement regime, two–exciton states must be taken into account and one uses the modified "O" system presented in subsection 5.2.3.

The "E" system is presented in subsection 5.2.2 in order to show the unique properties of excitations which obey Bose statistics. The "II" system then represents a system of nanocrystals in which one dipole transition is (randomly) blocked.

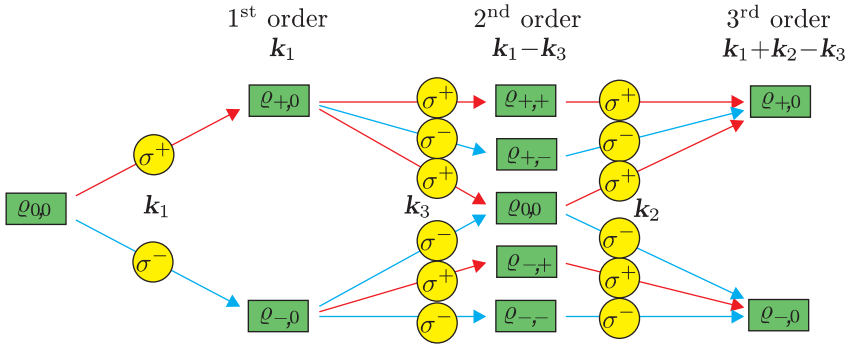

Figure 5.2: Scheme of the perturbative evolution of density matrix elements of a "V" system. At $t = 0$, the system is assumed to be in its ground state. The encircled symbols denote the spin of optical fields and the vectors in every column of circles stand for the field wave vector.

5.2.1 "V" system

The "V" system is used in order to model nanocrystals in the strong confinement regime in which two–exciton states aren't accessible by pumping by optical fields. The level scheme, according to Fig. 5.1, consists of the ground and two one–exciton states which are coupled to the electromagnetic field with two opposite polarizations. The Hamiltonian written in the basis of states $\{|0\rangle, |+\rangle, |-\rangle\}$ reads:

$$\hat{H} = \hat{H}_0 + \hat{V} = \begin{pmatrix} 0 & 0 & 0 \\ 0 & E_{\mathrm{X}} & 0 \\ 0 & 0 & E_{\mathrm{X}} \end{pmatrix} + E(t) \begin{pmatrix} 0 & d_+ & d_- \\ d_+ & 0 & 0 \\ d_- & 0 & 0 \end{pmatrix} . \tag{5.1}$$

The interaction term in interaction picture reads:

$$\hat{V}_{\mathrm{I}} = \frac{1}{2} \begin{pmatrix} 0 & d_+\mathcal{E}^*(t)\mathrm{e}^{-\mathrm{i}\delta\omega t} & d_-\mathcal{E}^*(t)\mathrm{e}^{-\mathrm{i}\delta\omega t} \\ d_+\mathcal{E}(t)\mathrm{e}^{\mathrm{i}\delta\omega t} & 0 & 0 \\ d_-\mathcal{E}(t)\mathrm{e}^{\mathrm{i}\delta\omega t} & 0 & 0 \end{pmatrix} . \tag{5.2}$$

The equations of motion follow directly from the Hamiltonian so they are not written here explicitly. However, for determination of the polarization state of the FWM response, one can draw a scheme of the evolution of the density matrix elements. Let's assume that the system is in the ground state before arrival of the pulses. Starting at $\varrho_{0,0} = 1$, various coherences are progressively excited. In Fig. 5.2, the paths for the FWM buildup are drawn when assuming $t_1 < t_3 < t_2$. There are many other nonzero coherences during the dynamics, only those which contribute to the FWM signal in the direction $\boldsymbol{k}_4 = \boldsymbol{k}_1 + \boldsymbol{k}_2 - \boldsymbol{k}_3$ are depicted. The FWM polarization is determined if one goes from the left to the right following the arrows with polarizations appropriate for the optical fields.

It can be shown that the predictions based on Fig. 5.2 are symmetric with respect to interchange of polarizations of the field "1" and "2", therefore the same FWM polarization is predicted if the temporal order $t_2 < t_3 < t_1$ is assumed. We can also interchange the temporal order of the fields "1" and "3" but there is one temporal order for which the FWM signal creation is forbidden. Due to Fermi statistics of the excitations, no FWM in the selected direction can be created if $t_1, t_2 < t_3$. Some signal is, however, diffracted to other two FWM directions.

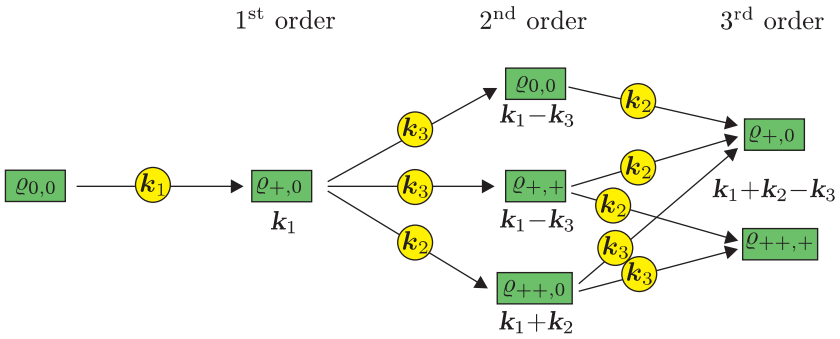

Figure 5.3: Scheme of the perturbative evolution of density matrix elements of an "E" system. At $t = 0$, the system is assumed to be in its ground state. The vectors in circles denote the wave vectors of optical fields which interact with the system. Vectors near the rectangles with density matrix elements denote the wave vector of the appropriate coherence.

One may perform linear transformation of the density matrix and Hamiltonian for determination of the polarization in the case when the excitation beams are linearly polarized. The structure will not change and for determination of the FWM polarization, one can draw the same scheme as shown in Fig. 5.2, where the signs "+" are substituted by X and the signs "−" by "Y".

From the above discussion, one may do the following conclusions about the "V" system:

- The FWM signal polarization (if any) does not depend on the temporal order of the incoming pulses.
- The FWM response is forbidden for $t_1, t_2 < t_3$.
- The FWM response is not forbidden for the polarizations of the pulses $\sigma^+\sigma^-\sigma^+$ and XYX.

An interesting property is, that the two opposite polarizations can influence on the other. This fact is due to the shared ground level. If a population grating with a definite spin is created, no additional particle could be created in the antinodes. This is a big difference when compared to the "O" system which is discussed below and where the spins are fully independent. As a consequence, we see the importance of inclusion of two–particle states with a correct symmetry to the level scheme.

5.2.2 "E" system

This system will be discussed only under influence of the optical field with one polarization in order to show the main differences from OBE. In this system, no Pauli blocking or energy renormalization of two–exciton states takes place. It will be shown that this system may be used for description of third–order optical response of bosons. In the interaction picture, the interaction term of Hamiltonian in the basis $\{|0\rangle, |+\rangle, |++\rangle\}$ is:

$$\hat{V}_{\mathrm{I}} = \frac{1}{2}\begin{pmatrix} 0 & d_+\mathcal{E}^*(t)\mathrm{e}^{-\mathrm{i}\delta\omega t} & 0 \\ d_+\mathcal{E}(t)\mathrm{e}^{\mathrm{i}\delta\omega t} & 0 & d_-\mathcal{E}^*(t)\mathrm{e}^{-\mathrm{i}\delta\omega t} \\ 0 & d_-\mathcal{E}(t)\mathrm{e}^{\mathrm{i}\delta\omega t} & 0 \end{pmatrix}. \tag{5.3}$$

Using this Hamiltonian, one can trace the path of relevant density matrix elements which are responsible for the FWM creation as depicted in Fig. 5.3. The scheme does not, nevertheless, depict the phase of the final state which may be important. The rule is, that

the change of the first index of density matrix element changes the phase of the final state by $\pi/2$ and the change of the second index due to dipole coupling causes the change of the phase by $-\pi/2$. It is then clear that for the temporal order of pulses $t_1, t_2 < t_3$, the two resulting one–photon coherences have the opposite phases (and the same magnitude) what causes no third–order signal. Under other temporal orderings of the pulses, the FWM signal is nonzero since the overall signal is given by a sum of three coherences which are of the same magnitude.

The link between bosons and the "E" system is following. Bosons form an infinite number of states involving one–particle, two–particle, etc. states. As can be shown, the states with three and more particles do not contribute to the third–order FWM response implying that the level scheme for description of FWM may be truncated at two–particle states producing exactly the "E" system. Noninteracting bosons might be expected to provide no wave mixing effect. However, as shown in chapter 4, localization of states provides a channel for wave mixing and therefore the system mixes the waves even though it is composed of bosons.

The "E" system can be extended in order to describe the spin. I discuss such system as an extension of the "O" system below.

5.2.3 "O" system

In this subsection, I discuss three systems: the "O" system and its two extensions. Discussion starts with description of a hypothetical system of two independent respective fermions which interact with two respective polarizations of the optical field. I derive polarization selection rules of such system in order to check whether the "O" level scheme used in mOBE theories gives correct polarization selection rules. The basic level scheme is then extended — first, Bose statistics of the particles is considered and then the consequences of exciton–exciton interactions are taken into account. The last model may be then applied to describe third–order optical response of semiconductor nanocrystals.

Two independent two–level systems which represent spin–resolved fermions differ considerably from the "V" system discussed above since the two–level systems do not share any state. The transform from two independent systems to the "O" scheme is natural when we define the basis using all possible states of the system which contains two fermions, see also Ref. [1] and section 2.2. The "O" system may be used to model the FWM response of semiconductor nanocrystals when the excitation beam is spectrally broad and covers both exciton and biexciton resonances.

I discuss separately three situations of polarizations of excitation beams in the following. These situations then represent all possible combinations of circular polarizations.

Assuming polarizations $\sigma^+\sigma^+\sigma^+$, we can conclude very briefly what happens. It is clear that this situation is equal to the well known two–level system. We thus expect the response with σ^+ polarization except the time order $t_1, t_2 < t_3$ when diffraction is forbidden (to the selected direction $\boldsymbol{k}_4$). Now let's assume the time order $t_1, t_3 < t_2$ and polarizations $\sigma^+\sigma^-\sigma^+$. In the second–order perturbation, nonzero density matrix elements are $\varrho^{(2)}_{0,0} = -\varrho^{(2)}_{+,+}$ as can be shown from equations of motion. The third–order response is then given by the coherences $\varrho^{(3)}_{-,0} = -\varrho^{(3)}_{+-,+}$. The macroscopic polarization is then zero and FWM is forbidden. For time order $t_1, t_2 < t_3$ and $t_3, t_2 < t_1$, the second–order coherences are the two–photon coherence $\varrho^{(2)}_{+-,0}$ and the spin coherence $\varrho^{(2)}_{+,-}$, respectively.

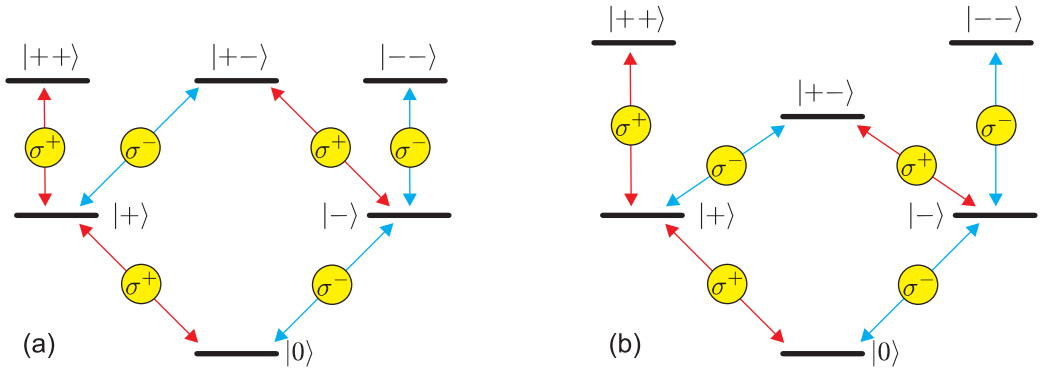

Figure 5.4: Level scheme for the modified "O" system considering noninteracting bosons (a) and interacting excitons (b).

The third–order polarization is the sum $\varrho^{(3)}_{+,0} + \varrho^{(3)}_{+-,+} = 0$ since:

$$\frac{\partial}{\partial t}\varrho^{(3)}_{+,0} = -\frac{\partial}{\partial t}\varrho^{(3)}_{+-,+} = \frac{d_+}{2}\mathcal{E}^*(t)\mathrm{e}^{-\mathrm{i}\delta\omega t}\varrho^{(2)}_{+-,0} - \frac{d_+}{2}\mathcal{E}(t)\mathrm{e}^{\mathrm{i}\delta\omega t}\varrho_{+,-}\,. \tag{5.4}$$

Response to polarization $\sigma^+\sigma^+\sigma^-$ is forbidden for any temporal order of pulses. Diffraction clearly occurs only when the pulses have the same circular polarizations. Assuming other than circular polarizations of the excitation beams, one can do a transform of the whole system to a new basis of spins. Special attention must be paid to the two–particle state, namely to the particle statistics. The transform for instance to linear polarizations considering fermions gives:

$$\begin{aligned}|+-\rangle = \frac{1}{\sqrt{2}}[|+\rangle|-\rangle - |-\rangle|+\rangle] = \frac{1}{2\sqrt{2}}[(|X\rangle + \mathrm{i}|Y\rangle)(|X\rangle - \mathrm{i}|Y\rangle) - \\ - (|X\rangle - \mathrm{i}|Y\rangle)(|X\rangle + \mathrm{i}|Y\rangle)] = -\frac{\mathrm{i}}{\sqrt{2}}[|X\rangle|Y\rangle - |Y\rangle|X\rangle] = -\mathrm{i}|XY\rangle\,.\end{aligned} \tag{5.5}$$

The shape of the level scheme for linear polarizations is not obviously changed, only the spins of the states are modified. The FWM response is allowed if the pulses have the same polarizations and forbidden if a projection to all directions does not give nonzero values of all polarizations. The FWM response is therefore forbidden for all combinations of polarizations XXY, XYX and YXX.

The dynamics of the response is the same compared to the two–level system and OBE. The reason is, that only two levels within the whole "O" scheme give contribution to the FWM signal.

Now I discuss a system of noninteracting bosons. As seen in the discussion of the "E" system, one may truncate the level scheme above the two–particle states and then one gets a scheme depicted in Fig. 5.4a. This level scheme is equal to the "O" scheme with the only difference that the two–exciton states in which excitons have equal spin are included. In addition, one must pay attention when transforming to another spin basis due to different transformation properties of two–particle states which obey Bose statistics. Using perturbative solution of the equations of motion, it can be shown that the polarization selection rules for the FWM response of this modified "O" system do not differ from those for the original "O" system, i.e. only if there is any polarization which

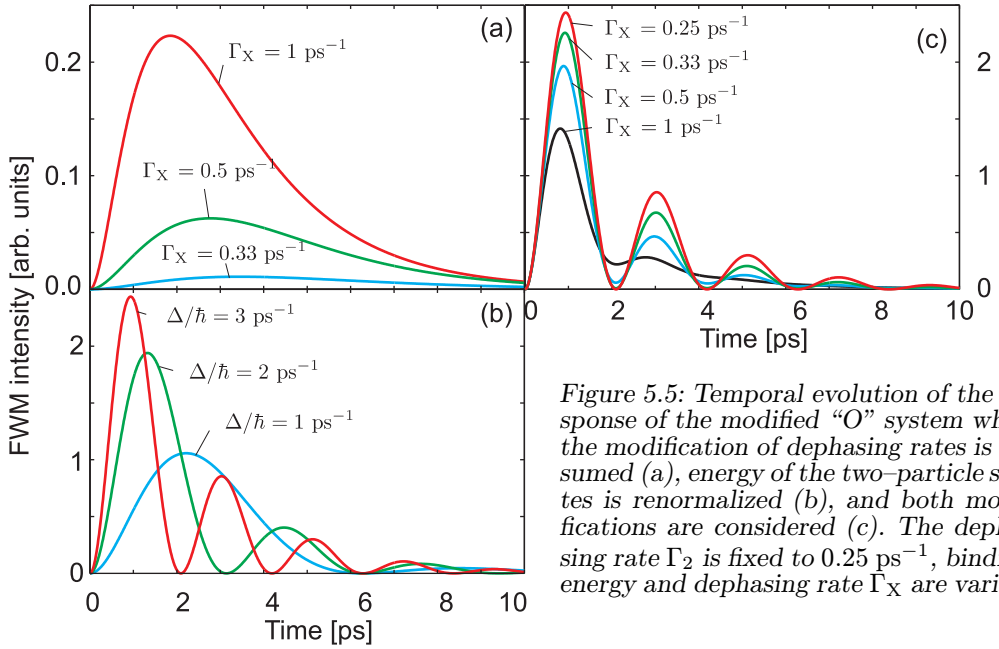

Figure 5.5: Temporal evolution of the response of the modified "O" system when the modification of dephasing rates is assumed (a), energy of the two–particle states is renormalized (b), and both modifications are considered (c). The dephasing rate Γ_2 is fixed to 0.25 ps^{-1}, binding energy and dephasing rate Γ_X are varied.

is common for all fields (i.e. projection to this polarization is nonzero for all fields), the FWM response is nonzero. Additionally, the response is zero when $t_1, t_2 < t_3$.

Considering interacting bosons in a realistic nanocrystal, energies and also strengths of dipole couplings of two–particle states are renormalized due to Coulomb and exchange interactions and also the dephasing time for the two–particle state may be modified, see Fig. 5.4b. Energy renormalization and change of dephasing rate influence the system dynamics and also the FWM polarization selection rules. Consider for instance time order of the delta–like pulses $t_1 < t_2 < t_3$ and polarizations $\sigma^+\sigma^-\sigma^+$. Let's denote Γ_2 dephasing rates for the coherences between the ground state and one–particle states, Γ_X for other one–photon coherences and Γ_{XX} for the two–photon coherences. Assuming weak excitation in resonance with one–particle excitation energy, dipole matrix elements for transitions from the ground state d and from the one–particle states d_2, and assuming energy renormalization of the two–particle energy by an amount $-\Delta$, we can calculate:

$$\varrho^{(0)}_{0,0}(t) = 1\,, \tag{5.6}$$

$$\varrho^{(1)}_{+,0}(t) = -\mathrm{i}\mathcal{E}(t_1)\frac{d}{\hbar}\mathrm{e}^{-\Gamma_2(t-t_1)}\,, \tag{5.7}$$

$$\varrho^{(2)}_{+-,0}(t) = -\mathcal{E}(t_1)\mathcal{E}(t_2)\frac{dd_2}{\hbar^2}\mathrm{e}^{\Gamma_X(t_2-t_1)}\mathrm{e}^{-\Gamma_{XX}(t-t_2)}\,, \tag{5.8}$$

$$\varrho^{(3)}_{+-,-}(t) = \mathrm{i}\mathcal{E}(t_1)\mathcal{E}(t_2)\mathcal{E}^*(t_3)\frac{d^2d_2}{\hbar^3}\mathrm{e}^{-\Gamma_2(t_2-t_1)}\mathrm{e}^{-\Gamma_{XX}(t_3-t_2)}\mathrm{e}^{-\Gamma_X(t-t_3)}\mathrm{e}^{\mathrm{i}\Delta(t_3-t_2)}\,, \tag{5.9}$$

$$\varrho^{(3)}_{+,0}(t) = -\mathrm{i}\mathcal{E}(t_1)\mathcal{E}(t_2)\mathcal{E}^*(t_3)\frac{dd_2^2}{\hbar^3}\mathrm{e}^{-\Gamma_2(t_2-t_1)}\mathrm{e}^{-\Gamma_{XX}(t_3-t_2)}\mathrm{e}^{-\Gamma_2(t-t_3)}\mathrm{e}^{\mathrm{i}\Delta(t_3-t_2)}\,. \tag{5.10}$$

The above density matrix elements are in the interaction picture and therefore it is necessary to transform them back to the Schrödinger picture by multiplication by a rapidly oscillating part. The radiated field is obviously proportional to the dipole matrix element and therefore we finally get for the FWM intensity:

$$I^{(3)}(t) = \left|d_2\varrho^{(3)}_{+-,+}\mathrm{e}^{-\mathrm{i}(\omega_0-\Delta)t} + d\varrho^{(3)}_{+,0}\mathrm{e}^{-\mathrm{i}\omega t}\right|^2 = \\ = d^2|\varrho^{(3)}_{+,0}(t_3)|^2\left|\mathrm{e}^{-\Gamma_X(t-t_3)}\mathrm{e}^{\mathrm{i}\Delta(t-t_3)} - \mathrm{e}^{-\Gamma_2(t-t_3)}\right|^2\,. \tag{5.11}$$

At $t = t_3$, the FWM intensity is obviously zero and it is nonzero for latter times if $\Gamma_2 \neq \Gamma_X$ or $\Delta \neq 0$. Change of dipole matrix elements has no influence on the dynamics. Difference of the dephasing rates causes slow initial rise of the signal and subsequent decrease, see Fig. 5.5a ($\Delta = 0$). The time when the FWM intensity peaks can be derived:

$$t_{\mathrm{peak}} = t_3 + \frac{\log \Gamma_X - \log \Gamma_2}{\Gamma_X - \Gamma_2} \approx \frac{1}{\Gamma_2}\,. \tag{5.12}$$

The last approximation is valid under assumption $\Gamma_X \approx \Gamma_2$. For $\Gamma_2 = \Gamma_X$ and $\Delta \neq 0$, the intensity of the FWM response is given by periodic oscillations which are modulated by exponential decrease as can be shown from (5.11), see Fig. 5.5b. The period of oscillations is given by the energy renormalization of the two–particle state. If both the energy and dephasing rates are modified due to the two–particle interactions, the dynamics of the FWM response is even more complex, cf. Fig. 5.5c. It is, however, important to note that the signal always starts to rise from $I(t = t_3) = 0$.

Temporal profile of the intensity of the FWM signal can be more complicated than the prediction (5.11) if other polarizations of the incoming pulses are chosen. It is natural to assume that the renormalization energy of the state $|+-\rangle$ is decreased by an amount Δ due to biexciton effect in semiconductors and the energy of the states $|++\rangle$ and $|--\rangle$ is increased by other amount Δ' due to mutual repulsion of the two particles. The FWM dynamics therefore in general involves more complex beating pattern.

It is important for polarization selection rules that, compared to the original "O" system, the response is allowed assuming e.g. $\sigma^+\sigma^-\sigma^+$ and XXY polarizations of incoming photons at any time order of pulses. The FWM response is, however, still forbidden for the combination $\sigma^+\sigma^+\sigma^-$ (in the $\boldsymbol{k}_1+\boldsymbol{k}_2-\boldsymbol{k}_3$ direction).

5.2.4 "II" system

The "II" system will be used in order to describe the response of nanocrystals in which one of the dipole transitions with a random spin is blocked e.g. by another trapped electron–hole pair, by an influence of imperfections etc. The nanocrystal will be modeled by two two–level systems (extension to two "E" systems is also possible) — the difference from the above "O" systems lies in the fact that only one of the two–level systems is allowed in each of the nanocrystals.

Evaluation of the dynamics of the system under investigation is very simple since we can calculate the response of the two two–level systems independently using the formalism developed above. Then we perform averaging over initial states of the system. It can be, however, shown that the whole calculation can be done using only one density matrix without need of subsequent averaging of the results. Let's define the basis $\{|0_+\rangle, |+\rangle, |0_-\rangle, |-\rangle\}$ and assume the density matrix 4×4 appropriate for the considered basis of states. There is no need to define two–particle states since the system cannot occupy them and the states involved in the basis are clearly the only possible states which can be occupied. The initial state of the density matrix is:

$$\hat{\varrho}(t{=}t_0) = \frac{1}{2}[|0_+\rangle\langle 0_+| + |0_-\rangle\langle 0_-|]\,. \tag{5.13}$$

The interaction Hamiltonian in interaction picture reads:

$$\hat{V}_{\mathrm{I}} = \frac{1}{2}\begin{pmatrix} 0 & d_+\mathcal{E}^*(t)\mathrm{e}^{-\mathrm{i}\delta\omega t} & 0 & 0 \\ d_+\mathcal{E}(t)\mathrm{e}^{\mathrm{i}\delta\omega t} & 0 & 0 & 0 \\ 0 & 0 & 0 & d_-\mathcal{E}^*(t)\mathrm{e}^{-\mathrm{i}\delta\omega t} \\ 0 & 0 & d_-\mathcal{E}(t)\mathrm{e}^{\mathrm{i}\delta\omega t} & 0 \end{pmatrix} . \tag{5.14}$$

It is useful to divide the density matrix to subblocks 2×2 since it can be shown from the above Hamiltonian that the off–diagonal subblocks remain zero during the system's evolution. The mean value of the creation operator $\hat{d}_+^+$ is:

$$\langle\langle \hat{d}_+^+ \rangle\rangle = \mathrm{Tr}\hat{\varrho}\hat{d}^+ = \langle\langle |+\rangle\langle 0_+| \rangle\rangle \,, \tag{5.15}$$

i.e. it is equal to the mean value within an isolated two–level system. The same thing can be shown for all creation and annihilation operators and thus the description by one density matrix is correct.

Assuming circularly polarized optical fields, it is clear that the third–order response arises only when the three polarizations are equal since one of the dipole transitions is forbidden in each system and there is no way how the polarizations could mix. One can show this fact also in the density matrix formalism: each circularly polarized pulse causes changes only in the appropriate diagonal subblock of the density matrix and therefore the subsystems do not influence one the other. According to the "O" system, different polarizations do not mix.

The difference from the "O" system comes if one assumes linearly polarized pulses. Every single system interacts only with an appropriate circularly polarized component of the polarization of the fields. One type of particles then interacts with the σ^+ component and the second type with the σ^- component providing an effective polarization mixing. For example for XXX excitation, the response is X–polarized, for XYX excitation, the response is Y–polarized. The "II" system therefore differs also from the modified "O" system where the response to the XXY excitation is forbidden while the "II" system gives the Y–polarized response.

The results obtained in this subsection are equal to the results of Ref. [2, 80] for the II system. However, there is a difference in the interpretation of the model system. The reason is, that the model system and equations of motion transform in a different way than the level scheme in the references.

5.2.5 Summary of polarization selection rules

In the above subsections, polarization selection rules for nanocrystals under different experimental conditions were developed. These polarization selection rules provide also a good test of the validity of the mOBE models when compared to experiments. A full list of polarization selection rules for all model systems described above is given in Tab. 5.1 for the temporal order of pulses $t_1, t_2 < t_3$. Table 5.2 then lists the polarization selection rules for all remaining time orders of pulses. All combinations of linear or circular polarizations are listed. The 'modified "O" system' is used in the meaning of the "O" system appropriate for bosons with energy renormalization and modification of dephasing rates described above (Fig. 5.4b). The last column of the tables gives the measured polarization selection rules in semiconductors according to Ref. [6].

Looking at the tables, we observe that only the modified "O" system reproduces the correct polarization selection rules except the combination $\sigma^+\sigma^- X$. Therefore none of the models discussed in this chapter describes correctly the FMW polarization in experiments on semiconductors. We may therefore conclude that it is not possible to describe the FWM response using the discussed OBE–like schemes without doing further corrections.

Input			Output polarization, $\boldsymbol{k}_4=\boldsymbol{k}_1+\boldsymbol{k}_2-\boldsymbol{k}_3$				
$\boldsymbol{k}_1$	$\boldsymbol{k}_2$	$\boldsymbol{k}_3$	"V"	"O"	modified "O"	"II"	Semiconductor
σ^+	σ^+	σ^+	0	0	σ^+	0	σ^+
σ^+	σ^+	σ^-	0	0	0	0	0
σ^+	σ^-	σ^+	σ^-	0	σ^-	0	σ^-
σ^-	σ^+	σ^+	σ^-	0	σ^-	0	σ^-
X	X	X	0	0	X	0	X
X	X	Y	0	0	Y	0	Y
X	Y	X	Y	0	Y	0	Y
Y	X	X	Y	0	Y	0	Y
σ^+	σ^-	X	X	0	X	0	*dbd.*

Table 5.1: Polarization selection rules for FWM response in various systems. The time order of arrivals of the excitation pulses is $t_1, t_2 < t_3$. In the last column, polarization selection rules for semiconductors are given (according to [6]), "dbd." means that the polarization is not well defined.

Input			Output polarization, $\boldsymbol{k}_4=\boldsymbol{k}_1+\boldsymbol{k}_2-\boldsymbol{k}_3$				
$\boldsymbol{k}_1$	$\boldsymbol{k}_2$	$\boldsymbol{k}_3$	"V"	"O"	modified "O"	"II"	Semiconductor
σ^+	σ^+	σ^+	σ^+	σ^+	σ^+	σ^+	σ^+
σ^+	σ^+	σ^-	0	0	0	0	0
σ^+	σ^-	σ^+	σ^-	0	σ^-	0	σ^-
σ^-	σ^+	σ^+	σ^-	0	σ^-	0	σ^-
X	X	X	X	X	X	X	X
X	X	Y	0	0	Y	Y	Y
X	Y	X	Y	0	Y	Y	Y
Y	X	X	Y	0	Y	Y	Y
σ^+	σ^-	X	X	0	X	0	*dbd.*

Table 5.2: Polarization selection rules for FWM response in various systems. The time order of arrivals of the excitation pulses is $t_1 > t_3$ or $t_2 > t_3$. In the last column, polarization selection rules for semiconductors are given (according to [6]), "dbd." means that the polarization is not defined.

5.3 Spin structure of excitons in quantum wells

In this section, I present my results of calculation of the spin structure of excitons and biexcitons in quantum wells. I derive also effective Hamiltonians for excitons and biexcitons at the Γ point of reciprocal lattice. Investigation of spin structure of excitons in quantum wells was published only for the case of the [001]–grown zinc–blende crystals [81], nevertheless biexciton spin structure is not investigated. Spin structure of excitons and biexcitons for other types of quantum wells (structure of the lattice, growth direction) cannot be found in literature.

Some calculations of biexciton wavefunctions may be found in literature [82], however the results are not sufficient since observations of mixed biexcitons [83, 84, 85]. Knowledge of the coupling terms in exciton Hamiltonian and knowledge of the spin structure of biexcitons may be very important when discussing wave mixing processes [86] as will be shown later. Materials with two most often used structures of the crystal lattices are considered — these with the zinc–blende and wurtzite structure (cf. section 3.2). Symmetry proper-

ties of quantum wells may be considerably influenced by the growth direction with respect to crystallographic axes: calculations for the zinc–blende structure are performed for the growth directions [001], [110] and [111]. Concerning wurtzite structure of crystals, I present results only for the growth direction [001] since other growth directions refer to the low–symmetry point group C_S. Spin is not then well defined and it is not generally conserved. The effective Hamiltonians lack any symmetry properties and contain many terms. In addition, QWs from the materials with wurtzite structure are not usually fabricated in other than [001] direction.

5.3.1 Zinc–blende in [001] direction

In this and the following two subsections, the materials which have the zinc–blende crystal structure (point group symmetry T_d) are considered. The twofold degenerate conduction band of bulk material has Γ_6 symmetry and the fourfold degenerate valence band has Γ_8 symmetry (see chapter 3, section 3.2). The split–off band with Γ_7 symmetry is neglected since usually the spin–orbit interaction is strong with respect to exchange interactions considered here and the valence bands do not mix. The growth axis (axis perpendicular to the plane of the QW) is in this section assumed to be parallel to the z crystallographic axis, i.e. the growth direction is [001]. The point group symmetry of such wells is D_{2d} [81, 24]. Using Ref. [24], we find that the symmetry of the heavy–hole (hh) band is Γ_6 and the symmetry of the light–hole (lh) band Γ_7. Symmetrized wavefunctions of holes are:

$$\begin{array}{lll} \Gamma_6: & \Phi_1 = |-1\rangle\,\beta = \left|\tfrac{3}{2}\ -\tfrac{3}{2}\right\rangle & \Big\} \text{hh} \\ & \Phi_2 = |1\rangle\,\alpha\ \ = \left|\tfrac{3}{2}\ +\tfrac{3}{2}\right\rangle & \Big\} \\ \Gamma_7: & \Phi_3 = \tfrac{1}{\sqrt{3}}[|-1\rangle\,\alpha + \sqrt{2}\,|0\rangle\,\beta] = \left|\tfrac{3}{2}\ -\tfrac{1}{2}\right\rangle & \Big\} \text{lh} \\ & \Phi_4 = \tfrac{1}{\sqrt{3}}[|1\rangle\,\beta + \sqrt{2}\,|0\rangle\,\alpha]\ \ = \left|\tfrac{3}{2}\ +\tfrac{1}{2}\right\rangle & \Big\} \end{array} \tag{5.16}$$

These wavefunctions are equal to those given in Ref. [25] for bulk material except for a different numbering of the states. The conduction band has Γ_6 symmetry and wavefunctions are denoted as α and β, respectively, depending on spin (projections $+\frac{1}{2}$ and $-\frac{1}{2}$, respectively). One then finds the symmetries of excitons to be $\Gamma_6 \otimes (\Gamma_6 \oplus \Gamma_7) = \Gamma_1 \oplus \Gamma_2 \oplus \Gamma_3 \oplus \Gamma_4 \oplus 2\Gamma_5$. The symmetrized exciton wavefunctions Ψ derived on the basis of multiplication tables [24] are listed below:

$$\begin{array}{lll} \Gamma_1: & \Psi_1 = \tfrac{1}{\sqrt{2}}[\Phi_2\alpha - \Phi_1\beta] \\ \Gamma_2: & \Psi_2^{(z)} = -\tfrac{\mathrm{i}}{\sqrt{2}}[\Phi_2\alpha + \Phi_1\beta] \\ \Gamma_3: & \Psi_3 = \tfrac{1}{\sqrt{2}}[\Phi_3\alpha - \Phi_4\beta] \\ \Gamma_4: & \Psi_4^{(z)} = -\tfrac{\mathrm{i}}{\sqrt{2}}[\Phi_3\alpha + \Phi_4\beta] \\ \Gamma_5: & \Psi_5^{(x)} = \tfrac{1}{\sqrt{2}}[\Phi_1\alpha + \Phi_2\beta] \\ & \Psi_6^{(y)} = \tfrac{\mathrm{i}}{\sqrt{2}}[\Phi_1\alpha - \Phi_2\beta] \\ & \Psi_7^{(x)} = \tfrac{1}{\sqrt{2}}[\Phi_4\alpha + \Phi_3\beta] \\ & \Psi_8^{(y)} = -\tfrac{\mathrm{i}}{\sqrt{2}}[\Phi_4\alpha - \Phi_3\beta] \end{array} \tag{5.17}$$

The symbols in parentheses in superscripts of Ψ denote the spin projection to the coordinate system of the quantum well. Since the QW lattice has the cubic symmetry, it is natural that the symmetrized states have linear polarizations according to bulk [25, 26]. The heavy–hole excitons have indices 1, 2, 5 and 6, the others are light–hole excitons.

Complexes of two excitons (biexcitons[1]) are allowed due to the symmetry of exciton–exciton exchange interaction as discussed above. This exchange interaction may cause

[1] Despite later statement of the use of the bipolariton model, the bound objects are called here biexcitons for clarity.

attraction of excitons if the wavefunction of the two–exciton complex is antisymmetric with respect to exchange of two electrons or holes (this may be shown using the exchange Hamiltonian (3.20)). Wavefunctions of biexcitons in the ground states are derived below according to [26], i.e. the biexciton envelope has the Γ_1^{++} symmetry and the wavefunction must be antisymmetric with respect to exchange of two electrons or holes. The symmetries of wavefunctions are given by the formula:

$$\Gamma_1^{++} \otimes [\Gamma_6 \otimes \Gamma_6]_- \otimes [(\Gamma_6 \oplus \Gamma_7) \otimes (\Gamma_6 \oplus \Gamma_7)]_- = 2\Gamma_1 \oplus \Gamma_3 \oplus \Gamma_4 \oplus \Gamma_5\,, \tag{5.18}$$

where $[A_1 \otimes A_2]_-$ denotes the antisymmetric part of the direct product of representations A_1 and A_2. Binding energies of biexcitons cannot be determined using only symmetry considerations but one may determine them from an experiment. By the same method as presented in Ref. [26], we construct two–hole wavefunctions with appropriate symmetry properties (antisymmetric with respect to exchange of the two holes and symmetric with respect to the crystallographic axes) and after multiplication by the electron part of the wavefunction which has the form $\alpha^{(1)}\beta^{(3)} - \beta^{(1)}\alpha^{(3)}$, we project the result on a basis of two–exciton states. The numbers in superscript distinguish here between two different electrons. The calculated biexciton wavefunctions are:

$$\begin{aligned}
\Gamma_1: \quad \Psi_1^{\mathrm{BX}} &= -\tfrac{1}{2\sqrt{2}}\,[\Psi_1^A\Psi_1^B + \Psi_2^A\Psi_2^B + \Psi_5^A\Psi_5^B + \Psi_6^A\Psi_6^B + P_{AB}] \\
\Psi_2^{\mathrm{BX}} &= -\tfrac{1}{2\sqrt{2}}\,[\Psi_3^A\Psi_3^B + \Psi_4^A\Psi_4^B + \Psi_7^A\Psi_7^B + \Psi_8^A\Psi_8^B + P_{AB}] \\
\Gamma_3: \quad \Psi_3^{\mathrm{BX}} &= \tfrac{1}{2\sqrt{2}}\,[\Psi_1^A\Psi_3^B + \Psi_2^A\Psi_4^B + \Psi_5^A\Psi_7^B - \Psi_6^A\Psi_8^B + P_{AB}] \\
\Gamma_4: \quad \Psi_4^{\mathrm{BX}} &= -\tfrac{\mathrm{i}}{2\sqrt{2}}\,[\Psi_1^A\Psi_4^B - \Psi_2^A\Psi_3^B - \Psi_5^A\Psi_8^B - \Psi_6^A\Psi_7^B + P_{AB}] \\
\Gamma_5: \quad \Psi_5^{\mathrm{BX}} &= \tfrac{1}{2\sqrt{2}}\,[\Psi_1^A\Psi_7^B + \Psi_2^A\Psi_8^B - \Psi_3^A\Psi_5^B + \Psi_4^A\Psi_6^B + P_{AB}] \\
\Psi_6^{\mathrm{BX}} &= -\tfrac{\mathrm{i}}{2\sqrt{2}}\,[\Psi_1^A\Psi_8^B - \Psi_2^A\Psi_7^B + \Psi_3^A\Psi_6^B + \Psi_4^A\Psi_5^B + P_{AB}]
\end{aligned} \tag{5.19}$$

The letters A and B distinguish between the two contributing excitons, P_{AB} means permutation of the excitons. In these wavefunctions, we identify pure lh or hh biexcitons with the usual symmetry Γ_1 which can be excited by $\sigma^+\sigma^-$–polarized fields (or, equivalently, by XX or YY–polarized fields). All other biexciton states are composed of holes from different bands (lh and hh) and we call these biexcitons *mixed*. Mixed biexcitons from A and B bands were observed in bulk hexagonal crystals [84, 85] and also in quantum wells [83]. Symmetries of mixed biexcitons are Γ_3 and Γ_4 with the wavefunction containing terms $xx - yy = \sigma^+\sigma^+ - \sigma^-\sigma^-$ for the former and $xy = \sigma^+\sigma^+ - \sigma^-\sigma^-$ for the latter. There are, in addition, states having Γ_5 symmetry which are not accessible by two–photon absorption if the optical beam is normal to the QW plane.

Spin structures of biexciton wavefunctions $xx+yy$ and $xx-yy$ mentioned above mean that the biexcitons may be created by absorption of two X or Y–polarized photons. One should, however, take care of the phase of the exciton and biexciton wavefunctions since they become important in FWM as shown below. Let's assume creation of a molecule by the XX pair and an induced decay by the Y photon. In both cases of wavefunctions $xx + yy$ and $xx - yy$, a Y–polarized exciton remains in the system, however the phase in the latter case is shifted by π with respect to the former case. This phenomenon may be important when attempting to observe mixed biexcitons experimentally: in time–resolved FWM experiments, the signals coming from biexcitons with different symmetries may partially cancel each other and the signal may be hardly observable. Beating between the levels and therefore signal amplitude obviously increases with increasing splitting between the contributing biexciton levels. One may solve the problem by turning the sample

around the normal axis. The directions x and y mentioned above are connected with the crystallographic axes. Usage of the polarizations RR ("R" means right linear polarization, $R = (X + Y)/\sqrt{2}$, "L" is then left linear polarization, $L = (X - Y)/\sqrt{2}$) gives $RR = \frac{1}{2}(XX + YY) + XY$ and therefore the former biexciton $xx + yy$ is excited while the latter one $xx - yy$ is not. Usage of the combination RL, on the other hand, suppresses excitation of the former and allows excitation of the latter. Appropriate selection of polarizations of the excitation beams then leads to selective excitation of the desired biexciton states.

Based on the symmetry considerations, one may construct an effective Hamiltonian appropriate for excitons and biexcitons as described in section 3.3. Here, we classify the particular terms in an effective Hamiltonian by the order of the involved exciton momentum. The zeroth order determines the spin precession between the symmetrized states at the Γ point. Diagonalization of the Hamiltonian at the Γ point then determines energies and spins of the states nonperturbed by the wave vector. Terms of the first order in wave vector are responsible for the spin precession whose strength is linear in the size of wave vector and if the terms are nonzero, they describe the strongest contributions to wave vector–dependent fermion–fermion exchange interaction. Terms of the second order in wave vector are responsible for dispersion and spin precession which may be, however, important if the first–order terms vanish. Third–order terms dominate if the nondiagonal terms of the first and second order are zero and, for example, they determine the D'yakonov–Perel's spin relaxation mechanism [30, 31].

The exciton Hamiltonian may be written in the form of Eq. (3.12), it is, however, better to perform a further separation:

$$\hat{H}_{\mathrm{X}} = \hat{H}_{\mathrm{e}} + \hat{H}_{\mathrm{h}} + \hat{H}_{\mathrm{e-h}} + \hat{H}_{Q}\,, \tag{5.20}$$

where the terms on the right hand side denote Hamiltonians of electrons, holes and electron–hole interaction, respectively, for zero wave vector. The last term represents the wave vector–dependent terms including electron, hole and electron–hole exchange terms. In this thesis, I present only the terms of the zeroth order in wave vector since Hamiltonians of the higher order terms in wave vector are complex in structure and they will not be used later in this thesis. Another reason is, that one usually excites the sample with wave vector perpendicular to the QW plane and therefore the in–plane wave vector is negligible.

The electron Hamiltonian is a constant, the hole Hamiltonian in the [001] zinc–blende quantum well introduces lh–hh splitting and we thus express it as follows:

$$\hat{H}_{\mathrm{h}} = \frac{\Delta_{\mathrm{lh}}}{2}\left(\hat{J}_z^2 - \frac{1}{4}\right)\,. \tag{5.21}$$

Energy of the lh excitons is shifted by the amount Δ_{lh} with respect to the lh excitons. Operator $\hat{\boldsymbol{J}} = (\hat{J}_x, \hat{J}_y, \hat{J}_z)$ is the matrix of the hole's angular momentum. We also define the electron spin matrix $\hat{\boldsymbol{\sigma}} = (\hat{\sigma}_x, \hat{\sigma}_y, \hat{\sigma}_z)$. The electron–hole exchange has the form [81]:

$$\begin{aligned}\hat{H}_{\mathrm{e-h}} = {} & \Delta_0 \mathbb{1}_{\mathrm{e}} \otimes \mathbb{1}_{\mathrm{h}} + \Delta_{11}(\hat{\sigma}_x\hat{J}_x + \hat{\sigma}_y\hat{J}_y) + \Delta_{12}\hat{\sigma}_z\hat{J}_z + \\ & + \Delta_{21}(\hat{\sigma}_x\hat{J}_x^3 + \hat{\sigma}_y\hat{J}_y^3) + \Delta_{22}\hat{\sigma}_z\hat{J}_z^3 + \\ & + \Delta_3[\hat{\sigma}_x\{\hat{J}_x, (\hat{J}_y^2 - \hat{J}_z^2)\} + \hat{\sigma}_y\{\hat{J}_y, (\hat{J}_x^2 - \hat{J}_z^2)\}]\,,\end{aligned} \tag{5.22}$$

where $\mathbb{1}_{\mathrm{e,h}}$ stand for identity matrices on a subspace of electrons and holes, respectively. The Hamiltonian is not diagonal in the basis of symmetrized wavefunctions (5.17) and therefore

there exist some couplings between the states even for zero wave vector (these couplings cause spin precession). The energies of the states which diagonalize the Hamiltonian are:

$$E_{5,7(6,8)} = \Delta_0 + \tfrac{1}{2}\Delta_{\rm lh} - \tfrac{1}{2}\Delta_{12} - \tfrac{13}{8}\Delta_{22} \pm \left[\left(-\tfrac{1}{2}\Delta_{\rm lh} + \Delta_{12} + \tfrac{7}{4}\Delta_{22}\right)^2 + 3\left(\Delta_{11} + \tfrac{7}{4}\Delta_{21} - \tfrac{1}{2}\Delta_3\right)^2\right]^{1/2},$$

$$E_{3,4} = \Delta_0 - \tfrac{1}{2}\Delta_{12} - \tfrac{1}{8}\Delta_{22} \mp \left(2\Delta_{11} + 5\Delta_{21} + \frac{3}{2}\Delta_3\right), \tag{5.23}$$

$$E_{1,2} = \Delta_0 + \Delta_{\rm lh} + \frac{3}{2}\Delta_{12} + \tfrac{27}{8}\Delta_{22} \mp \frac{3}{2}\left(\Delta_{21} - \Delta_3\right).$$

The above list of energies of the eigenstates does not tell anything about the spin structure of the states. Within the basis of the symmetrized states, the Hamiltonian (5.22) is block–diagonal. Four subblocks 1×1 refer to dipole–inactive states (Ψ_{1-4}) which are therefore the eigenstates of the Hamiltonian. The rest of the Hamiltonian are two subblocks 2×2 characterized by spin, i.e. dipole–active states with the same spin are coupled by the electron–hole exchange interaction. As a consequence, both (in–plane) linear and circular spins are good quantum numbers for excitons and they are conserved during coherent evolution of the system. Heavy–hole and light–hole subbands are not, on the contrary, good quantum numbers of excitons. Valence bands then become mixed in the exciton wavefunction.

When compared to bulk material, we may identify several differences in the Hamiltonian (5.22) [26]. First, the lh–hh splitting $\Delta_{\rm lh}$ is zero in bulk. This splitting of hole bands is caused by lowering of the crystal symmetry and is general for all quantum wells. Change of the sample thickness in the z direction causes direction anisotropy and therefore exchange terms proportional to in–plane and normal projections of the angular momenta differ in magnitudes, i.e. $\Delta_{11} \neq \Delta_{12}$ and $\Delta_{21} \neq \Delta_{22}$. The term proportional to Δ_3 has no correspondence in bulk and may be usually neglected since it is of the third order in the angular momentum of holes while the leading terms Δ_{11} and Δ_{12} are of the first order.

Biexciton Hamiltonian at the Γ point has 16 terms appropriate for the hole–hole exchange interaction (other interactions do not contribute). These terms are listed in Appendix A.1. Biexciton Hamiltonian couples only the terms with Γ_1 symmetry, all other terms are eigenstates of this Hamiltonian.

5.3.2 Zinc–blende in [011] direction

Concerning this growth direction, it is necessary to unambiguously define the coordinate system connected with the QW. Obviously $z = (y' + z')/\sqrt{2}$, where the primed coordinates are connected with crystallographic axes of the bulk material and the nonprimed coordinates are connected with the quantum well: the z direction is then perpendicular to the QW plane. Then we can define $x = x'$ and $y = (y' - z')/\sqrt{2}$.

It is clear from the above definition of the coordinate system that there may be a strong anisotropy in the plane of the quantum well since the directions x and y are not equivalent from the point of view of the crystallographic axes. Splitting of the states polarized in the respective directions x, y and z is then expected. As a consequence, circular polarization of photons is not generally conserved when propagating through the quantum well.

The point group symmetry of such QW is C_{2v}. The conduction band has Γ_5 symmetry as well as both hole subbands. The symmetrized hole wavefunctions are Φ_{1-4} given in (5.16), they only have the common symmetry Γ_5. The excitons have symmetries $2\Gamma_5 \otimes \Gamma_5 = 2(\Gamma_1 \oplus \Gamma_2 \oplus \Gamma_3 \oplus \Gamma_4)$ and one obtains with both hole subbands:

$$
\begin{aligned}
\Gamma_1: \quad & \Psi_1^{(z)} = -\tfrac{1}{\sqrt{2}}\left[\Phi_2\alpha - \Phi_1\beta\right] \\
& \Psi_2^{(z)} = -\tfrac{1}{\sqrt{2}}\left[\Phi_3\alpha - \Phi_4\beta\right] \\
\Gamma_2: \quad & \Psi_3^{(x)} = \tfrac{1}{\sqrt{2}}\left[\Phi_1\alpha + \Phi_2\beta\right] \\
& \Psi_4^{(x)} = \tfrac{1}{\sqrt{2}}\left[\Phi_4\alpha + \Phi_3\beta\right] \\
\Gamma_3: \quad & \Psi_5 = -\tfrac{\mathrm{i}}{\sqrt{2}}\left[\Phi_2\alpha + \Phi_1\beta\right] \\
& \Psi_6 = -\tfrac{\mathrm{i}}{\sqrt{2}}\left[\Phi_3\alpha + \Phi_4\beta\right] \\
\Gamma_4: \quad & \Psi_7^{(y)} = \tfrac{\mathrm{i}}{\sqrt{2}}\left[\Phi_1\alpha - \Phi_2\beta\right] \\
& \Psi_8^{(y)} = \tfrac{\mathrm{i}}{\sqrt{2}}\left[\Phi_4\alpha - \Phi_3\beta\right]
\end{aligned}
\tag{5.24}
$$

Exciton states with odd indexes are hh and those with even indexes are lh excitons. The wavefunctions are equal to the wavefunctions presented for the case of [001] orientation, they differ only in symmetry and index. Biexcitons have symmetries $3\Gamma_1 \oplus \Gamma_2 \oplus \Gamma_3 \oplus \Gamma_4$:

$$
\begin{aligned}
\Gamma_1: \quad & \Psi_1^{\mathrm{BX}} = \tfrac{1}{2\sqrt{2}}\left[\Psi_1^A\Psi_1^B + \Psi_3^A\Psi_3^B + \Psi_5^A\Psi_5^B + \Psi_7^A\Psi_7^B + P_{AB}\right] \\
& \Psi_2^{\mathrm{BX}} = \tfrac{1}{2\sqrt{2}}\left[\Psi_2^A\Psi_2^B + \Psi_4^A\Psi_4^B + \Psi_6^A\Psi_6^B + \Psi_8^A\Psi_8^B + P_{AB}\right] \\
& \Psi_3^{\mathrm{BX}} = \tfrac{1}{2\sqrt{2}}\left[\Psi_1^A\Psi_2^B + \Psi_3^A\Psi_4^B + \Psi_5^A\Psi_6^B + \Psi_7^A\Psi_8^B + P_{AB}\right] \\
\Gamma_2: \quad & \Psi_4^{\mathrm{BX}} = -\tfrac{1}{2\sqrt{2}}\left[\Psi_1^A\Psi_4^B - \Psi_2^A\Psi_3^B + \Psi_5^A\Psi_8^B - \Psi_6^A\Psi_7^B + P_{AB}\right] \\
\Gamma_3: \quad & \Psi_5^{\mathrm{BX}} = -\tfrac{1}{2\sqrt{2}}\left[\Psi_1^A\Psi_6^B - \Psi_2^A\Psi_5^B - \Psi_3^A\Psi_8^B + \Psi_4^A\Psi_7^B + P_{AB}\right] \\
\Gamma_4: \quad & \Psi_6^{\mathrm{BX}} = -\tfrac{1}{2\sqrt{2}}\left[\Psi_1^A\Psi_8^B - \Psi_2^A\Psi_7^B + \Psi_3^A\Psi_6^B - \Psi_4^A\Psi_5^B + P_{AB}\right]
\end{aligned}
\tag{5.25}
$$

Again, the first two biexcitons with Γ_1 symmetry are pure hh and lh, respectively. All the other biexcitons are mixed. The Γ_1 states have the usual structure $\sigma^+\sigma^- = XX + YY$, i.e. they may be excited by two photons with contra–circular polarizations or by two photons having parallel linear polarizations. The Γ_3 biexciton is accessible by two–photon absorption too, but by photons having polarizations $xy = \sigma^+\sigma^+ - \sigma^-\sigma^-$. Other biexciton states aren't accessible by two–photon absorption if the beams are perpendicular to the QW plane.

When compared to (5.21), the hole part of exciton Hamiltonian has one more term reflecting the in–plane anisotropy of the QW:

$$
\hat{H}_{\mathrm{h}} = c_0\mathbb{1}_{\mathrm{h}} + c_1\hat{J}_x^2 + c_2\hat{J}_z^2\,. \tag{5.26}
$$

This Hamiltonian is quite different from that in (5.21) — it splits the light– and heavy–hole subbands but additionally, it couples hole subbands via the term proportional to $\hat{J}_x^2$. This coupling causes also interaction between exciton subbands. The electron–hole exchange Hamiltonian can be expanded into the form:

$$
\begin{aligned}
\hat{H}_{\mathrm{e-h}} = {} & \Delta_0\mathbb{1}_{\mathrm{e}}\otimes\mathbb{1}_{\mathrm{h}} + \Delta_{11}\hat{\sigma}_x\hat{J}_x + \Delta_{12}\hat{\sigma}_x\{\hat{J}_x, \hat{J}_y^2\} + \Delta_{13}\hat{\sigma}_x\hat{J}_x^3 + \\
& + \Delta_{21}\hat{\sigma}_y\hat{J}_y + \Delta_{22}\hat{\sigma}_y\{\hat{J}_y, \hat{J}_x^2\} + \Delta_{23}\hat{\sigma}_y\hat{J}_y^3 + \\
& + \Delta_{31}\hat{\sigma}_z\hat{J}_z + \Delta_{32}\hat{\sigma}_z\{\hat{J}_z, \hat{J}_x^2\} + \Delta_{33}\hat{\sigma}_z\hat{J}_z^3\,.
\end{aligned}
\tag{5.27}
$$

This Hamiltonian is block–diagonal and couples pairs of the states with the same spin from the two principal exciton bands (light– and heavy–hole). Because of the simple structure of the Hamiltonian, its diagonalization is very simple but the result has many terms which are not given here explicitly.

The electron–hole exchange interaction at the Γ point conserves the spin (linear polarization) of the states. As expected in the initial discussion of the QW symmetry, linear spins are conserved since the symmetrized states are linearly polarized. Circular polarization is not, on the contrary, conserved due to the energy mismatch between states polarized in the x, y and z directions. A detailed calculation then shows that the Hamiltonian (5.27) causes coherent spin–flip between states with σ^+ and σ^- spins, each of them being from another hole band.

Besides the one–exciton contributions, the biexciton Hamiltonian contains only hole–hole exchange terms because electron–hole and electron–electron exchange terms are zero matrices. This Hamiltonian has 25 terms and I give them in Appendix A.2. The biexciton Hamiltonian couples all three states with symmetry Γ_1 while the states with symmetries Γ_{3-5} are the eigenstates of the Hamiltonian.

5.3.3 Zinc–blende in [111] direction

The point group symmetry of such quantum wells is C_{3v}. Electrons in the lowest conduction subband have wavefunctions with symmetry Γ_4 and the hole subbands have symmetries Γ_4, Γ_5 and Γ_5. On the contrary to (5.16), symmetrized wavefunctions of hole states have structure different from the bulk wavefunctions:

$$\begin{array}{lll} \Gamma_5: & \chi_1 = \frac{1}{\sqrt{2}}\left[\left|\frac{3}{2}\ -\frac{3}{2}\right\rangle - \mathrm{i}\left|\frac{3}{2}\ +\frac{3}{2}\right\rangle\right] & \Big\} \text{heavy holes,} \\ \Gamma_6: & \chi_2 = \frac{\mathrm{i}}{\sqrt{2}}\left[\left|\frac{3}{2}\ -\frac{3}{2}\right\rangle + \mathrm{i}\left|\frac{3}{2}\ +\frac{3}{2}\right\rangle\right] & \Big\} \\ \Gamma_4: & \chi_3 = \left|\frac{3}{2}\ -\frac{1}{2}\right\rangle & \Big\} \text{light holes.} \\ & \chi_4 = \left|\frac{3}{2}\ +\frac{1}{2}\right\rangle & \Big\} \end{array} \tag{5.28}$$

The exciton wavefunctions then have symmetries $\Gamma_4 \otimes (2\Gamma_4 \oplus \Gamma_5 \oplus \Gamma_6) = \Gamma_1 \oplus \Gamma_2 \oplus 3\Gamma_3$. The symmetrized exciton wavefunctions are:

$$\begin{array}{lll} \Gamma_1: & \Psi_1^{(z)} = & \frac{1}{\sqrt{2}}[\chi_3\alpha - \chi_4\beta] \\ \Gamma_2: & \Psi_2 = & -\frac{\mathrm{i}}{\sqrt{2}}[\chi_3\alpha + \chi_4\beta] \\ \Gamma_3: & \Psi_3^{(-)} = & \chi_3\beta \\ & \Psi_4^{(+)} = & \chi_4\alpha \\ & \Psi_5 = & \frac{1}{\sqrt{2}}[\mathrm{i}\chi_1 - \chi_2]\alpha \\ & \Psi_6 = & \frac{1}{\sqrt{2}}[\chi_1 - \mathrm{i}\chi_2]\beta \\ & \Psi_7^{(-)} = & \frac{1}{\sqrt{2}}[\chi_1 - \mathrm{i}\chi_2]\alpha \\ & \Psi_8^{(+)} = & \frac{1}{\sqrt{2}}[\mathrm{i}\chi_1 - \chi_2]\beta \end{array} \tag{5.29}$$

With χ_{1-4} defined by Eq. (5.28). Wavefunctions with indices $1-4$ refer to lh excitons and indices $5-8$ to hh excitons, respectively. The biexciton wavefunctions have symmetries $2\Gamma_1 \oplus 2\Gamma_3$:

$$\begin{array}{lll} \Gamma_1: & \Psi_1^{\mathrm{B}} = & \frac{1}{2}\left[\Psi_5^A\Psi_6^B - \Psi_7^A\Psi_8^B + P_{AB}\right] \\ & \Psi_2^{\mathrm{B}} = & -\frac{1}{2\sqrt{3}}\left[\Psi_1^A\Psi_1^B + \Psi_2^A\Psi_2^B + 2\Psi_3^A\Psi_4^B + P_{AB}\right] \\ \Gamma_3: & \Psi_3^{\mathrm{B}} = & -\frac{1}{2\sqrt{2}}\left[\Psi_1^A\Psi_5^B + \mathrm{i}\Psi_2^A\Psi_5^B + \sqrt{2}\Psi_4^A\Psi_8^B + P_{AB}\right] \\ & \Psi_4^{\mathrm{B}} = & \frac{1}{2\sqrt{2}}\left[-\Psi_1^A\Psi_6^B + \mathrm{i}\Psi_2^A\Psi_6^B + \sqrt{2}\Psi_3^A\Psi_7^B + P_{AB}\right] \\ & \Psi_5^{\mathrm{B}} = & \frac{1}{2\sqrt{2}}\left[\Psi_1^A\Psi_7^B + \mathrm{i}\Psi_2^A\Psi_7^B + \sqrt{2}\Psi_4^A\Psi_6^B + P_{AB}\right] \\ & \Psi_6^{\mathrm{B}} = & -\frac{1}{2\sqrt{2}}\left[\Psi_1^A\Psi_8^B - \mathrm{i}\Psi_2^A\Psi_8^B - \sqrt{2}\Psi_3^A\Psi_5^B + P_{AB}\right] \end{array} \tag{5.30}$$

The Γ_1 biexcitons are again pure lh and hh, respectively. The others are mixed having holes from both subbands. The Γ_1 biexcitons can be reached by usual two–photon transitions with photons having opposite circular polarizations or by two photons with parallel linear polarizations. The biexcitons with indices 3 and 4 can be excited by $\sigma^+\sigma^+$ and $\sigma^-\sigma^-$ photons, respectively. The last two biexcitons (5 and 6) do not couple to light field via two–photon transitions.

There is a big discrepancy between mixed biexcitons in quantum wells grown in directions [001] and [011] when compared to the growth direction [111]. Two-photon absorption is allowed in all quantum wells for circularly polarized light. The difference which may be seen in four–wave mixing experiments lies in the mixing of the spin pairs $\sigma^+\sigma^+$ and $\sigma^-\sigma^-$ in the biexciton wavefunction in the two former two cases while they are not mixed in the latter case. In [001] and [011] QWs, one then may induce annihilation of biexcitons using σ^-–polarized light when biexcitons were excited by absorption of two σ^+ photons. This is impossible in [111] wells showing that these wells presumably conserve circular polarizations due to their symmetry.

The exciton Hamiltonian has again only a constant contribution from an electron and the contribution from a hole can be expressed by Eq. (5.21). The electron–hole exchange term reads for this point group symmetry:

$$\begin{aligned}\hat{H}_{\mathrm{e-h}} = {} & \Delta_0 \mathbb{1}_{\mathrm{e}} \otimes \mathbb{1}_{\mathrm{h}} + \Delta_{11}(\hat{\sigma}_+\hat{J}_- + \hat{\sigma}_-\hat{J}_+) + \Delta_{12}\hat{\sigma}_z\hat{J}_z \\ & + \Delta_{21}(\hat{\sigma}_+\{\hat{J}_+,\hat{J}_-^2\} + \hat{\sigma}_-\{\hat{J}_-,\hat{J}_+^2\}) + \Delta_{22}\hat{\sigma}_z\hat{J}_z^3 + \\ & + \Delta_3(\hat{\sigma}_-\{\hat{J}_+,\{\hat{J}_+,\hat{J}_-\}\} + \hat{\sigma}_+\{\hat{J}_-,\{\hat{J}_+,\hat{J}_-\}\})\,.\end{aligned} \tag{5.31}$$

The new operators were introduced: $\hat{J}_+ = \hat{J}_x + \mathrm{i}\hat{J}_y$, $\hat{J}_- = \hat{J}_x - \mathrm{i}\hat{J}_y$, $\hat{\sigma}_+ = \hat{\sigma}_x + \mathrm{i}\hat{\sigma}_y$ and $\hat{\sigma}_- = \hat{\sigma}_x - \mathrm{i}\hat{\sigma}_y$. Although it is possible to analytically diagonalize such Hamiltonian, it has no sense since the results would have a too complex and inconvenient structure. Hamiltonian conserves the spin and couples the states from the lh and hh bands.

The biexciton Hamiltonian, on the contrary to the [001] and [011] oriented QWs, has nonzero contributions from the electron–electron and electron–hole exchange terms (in total 22 terms). This Hamiltonian is diagonal in the basis of symmetrized biexciton wavefunctions except for coupling of the states 1 and 2 (Γ_1 symmetry, pure lh and hh) and may be found in Appendix A.3.

5.3.4 Wurtzite in [001] direction

This quantum well has the same point group symmetry $\mathrm{C_{6v}}$ as bulk material. This point group is very similar to that $\mathrm{C_{3v}}$ of the zinc–blende QW grown in [111] direction. We then expect similar results in particular for the structure of the Hamiltonian. Electron wavefunctions have the symmetry Γ_7 and the hole wavefunctions Γ_7 (lh) and Γ_9 (hh), respectively. The exciton wavefunctions have symmetries $\Gamma_7\otimes(\Gamma_7\oplus\Gamma_9) = \Gamma_1\oplus\Gamma_2\oplus 2\Gamma_5\oplus\Gamma_6$:

$$\begin{aligned}
\Gamma_1: \quad & \Psi_1^{(z)} = \tfrac{1}{\sqrt{2}}\left[\Phi_3\alpha - \Phi_4\beta\right] \\
\Gamma_2: \quad & \Psi_2 \;\; = \tfrac{\mathrm{i}}{\sqrt{2}}\left[\Phi_3\alpha + \Phi_4\beta\right] \\
\Gamma_5: \quad & \Psi_3^{(-)} = \Phi_3\beta \\
& \Psi_4^{(+)} = \Phi_4\alpha \\
& \Psi_5^{(-)} = \Phi_1\alpha \\
& \Psi_6^{(+)} = \Phi_2\beta \\
\Gamma_6: \quad & \Psi_7 \;\; = \Phi_2\alpha \\
& \Psi_8 \;\; = \Phi_1\beta
\end{aligned} \tag{5.32}$$

Similarly to the C_{3v} group, wavefunctions with indices $1-4$ are appropriate for the lh excitons and wavefunctions with indices $5-8$ for the hh excitons, respectively. Only the excitons with Γ_5 symmetry are dipole–active and they are coupled to circularly–polarized light. The symmetrized biexciton wavefunctions have the symmetries $2\Gamma_1 \oplus \Gamma_5 \oplus \Gamma_6$:

$$\begin{aligned}
\Gamma_1: \quad \Psi_1^{\mathrm{B}} &= \tfrac{1}{2}\left[\Psi_5^A\Psi_6^B + \Psi_7^A\Psi_8^B + P_{AB}\right] \\
\Psi_2^{\mathrm{B}} &= -\tfrac{1}{2\sqrt{3}}\left[\Psi_1^A\Psi_1^B + \Psi_2^A\Psi_2^B + 2\Psi_3^A\Psi_4^B + P_{AB}\right] \\
\Gamma_5: \quad \Psi_3^{\mathrm{B}} &= \tfrac{1}{2\sqrt{2}}\left[\Psi_1^A\Psi_5^B - \mathrm{i}\Psi_2^A\Psi_5^B + \sqrt{2}\Psi_4^A\Psi_8^B + P_{AB}\right] \\
\Psi_4^{\mathrm{B}} &= -\tfrac{1}{2\sqrt{2}}\left[\Psi_1^A\Psi_6^B + \mathrm{i}\Psi_2^A\Psi_6^B - \sqrt{2}\Psi_3^A\Psi_7^B + P_{AB}\right] \\
\Gamma_6: \quad \Psi_5^{\mathrm{B}} &= -\tfrac{1}{2\sqrt{2}}\left[\Psi_1^A\Psi_8^B + \mathrm{i}\Psi_2^A\Psi_8^B - \sqrt{2}\Psi_3^A\Psi_5^B + P_{AB}\right] \\
\Psi_6^{\mathrm{B}} &= \tfrac{1}{2\sqrt{2}}\left[\Psi_1^A\Psi_7^B - \mathrm{i}\Psi_2^A\Psi_7^B + \sqrt{2}\Psi_4^A\Psi_6^B + P_{AB}\right]
\end{aligned} \tag{5.33}$$

The first two biexcitons are pure lh and hh with Γ_1 symmetry. The Γ_5 biexcitons are not directly accessible by two–photon absorption and the Γ_6 biexcitons have $\sigma^-\sigma^-$ and $\sigma^+\sigma^+$ orientations of dipoles, respectively (cf. the first two Γ_3 biexcitons in C_{3v}).

Similarly to C_{3v}, the electron Hamiltonian is a constant and the hole Hamiltonian is expressed by (5.21). The electron–hole exchange term reads:

$$\begin{aligned}
\hat{H}_{\mathrm{e-h}} = {} & \Delta_0 \mathbb{1}_{\mathrm{e}} \otimes \mathbb{1}_{\mathrm{h}} + \Delta_{11}(\hat{\sigma}_+\hat{J}_- + \hat{\sigma}_-\hat{J}_+) + \Delta_{12}\hat{\sigma}_z\hat{J}_z + \\
& + \Delta_{21}(\hat{\sigma}_+\{\hat{J}_+, \hat{J}_-^2\} + \hat{\sigma}_-\{\hat{J}_-, \hat{J}_+^2\}) + \Delta_{22}\hat{\sigma}_z\hat{J}_z^3 + \\
& + \mathrm{i}\Delta_3(\hat{\sigma}_+\{\hat{J}_z, \hat{J}_-\} - \hat{\sigma}_-\{\hat{J}_z, \hat{J}_+\})\,.
\end{aligned} \tag{5.34}$$

The imaginary unit preceding the constant Δ_3 follows directly from tables of coupling coefficients [24]. It arises due to usage of the unusual anticommutators $\{\hat{J}_z, \hat{J}_\pm\}$. One can easily verify that the last term in the above formula is Hermitian and has the K^+ symmetry with respect to the time reversal. This Hamiltonian couples excitons from the hh and lh bands with the same spin, i.e. it causes further splitting of the bands and conserves the spin.

The biexciton Hamiltonian has nonzero contributions for the C_{6v} point group from all fermion–fermion exchange terms. All its terms (22 terms in total) are then given in Appendix A.4. The biexciton Hamiltonian has two subblocks, one is appropriate for the Γ_1 biexcitons and the other for the Γ_5 and Γ_6 biexciton states.

When compared to the [111]–grown QW with zinc–blende structure, we find many similarities as expected. In both structures, circular spins of excitons are conserved even though there is mixing between the lh and hh bands. This spin conservation holds also for two–photon creation and annihilation of biexcitons. However, in the wurtzite [001] quantum wells, this circular spin may be partly destroyed due to spin precession of biexcitons. It is not, nevertheless, possible to flip the spin of the two–exciton state $\sigma^+\sigma^+$ to $\sigma^-\sigma^-$ on the contrary to zinc–blende [001] and [011] QWs.

Chapter 6

FWM on bulk materials: The model

6.1 Introduction

As stated above, there has not been published any model capable of fast derivation of polarization selection rules for FWM experiments on bulk semiconductors. Although the selection rules may be derived using microscopic theories, they require time–consuming numerical calculations. Therefore I present in this section a model which may considerably simplify calculations of polarization selection rules on bulk intrinsic semiconductors under assumption of weak excitation below exciton resonance. Using the model, one may also estimate dynamics of the FWM response and its polarization.

This model includes symmetry properties of the crystal lattice and therefore its predictions are expected to be correct with respect to polarization selection rules. Validity of the model is further verified in chapter 7. I start the discussion with basic considerations about the system under investigation, appropriate level of description etc. Based on these considerations, Hamiltonians appropriate for description of particular parts of the model are derived in the following sections 6.2–6.6. After the complete Hamiltonian of the problem is derived, a method of derivation of equations of motion is presented in section 6.7. The last section 6.8 briefly concludes the basic properties of the developed model and the discussion and solution of equations of motion is then presented in the next chapter 7.

Let us first investigate which processes take effect during formation of the FWM signal. Since the aim of the model is the description of the whole experiment including photons outside the crystal, we must take into account that the crystal is finite even though it is bulk. The situation is depicted in Fig. 6.1. The *external* photons (black arrows) propagate until they reach the crystal surface. This surface breaks the translational symmetry of the system air–crystal and therefore we must describe refraction of the electromagnetic field as a consequence of a difference of dielectric constants of air and crystal (its background dielectric constant which comes from other than considered resonances). The *internal* photons which penetrate below the crystal surface (orange arrows) are then coupled by dipole interaction to excitons (green arrows). Since the influence of surfaces is neglected in description of the exciton modes allowed by periodical boundary conditions, the dipole interaction conserves wave vector and it is described by the Hamiltonian (3.27). Dipole interaction is strong and therefore it cannot be described using perturbation theory. It is then more convenient to use polaritons instead of interacting exciton–photon system. Due to exciton–exciton interactions, it is clear that polariton–polariton scattering must be also

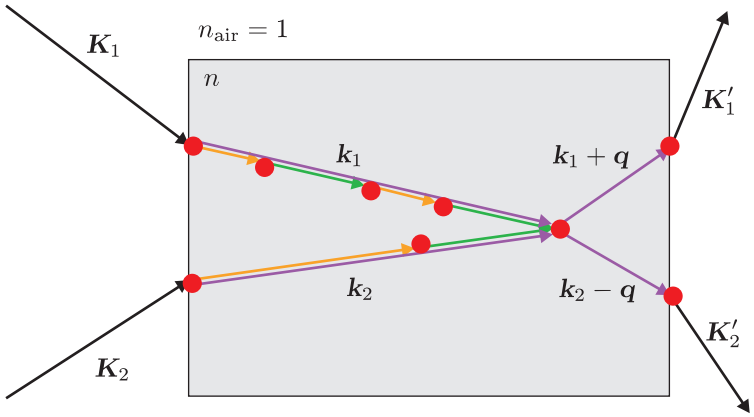

Figure 6.1: Sketch of particle–particle interactions in a two–beam experiment. Black lines depict photons outside the crystal, orange lines stand for photons inside the crystal with refractive index n. Green lines denote excitons and violet lines polaritons. Red circles show the places of interactions which must be considered in the model.

accounted for. Finally, one needs a description of penetration of electromagnetic field out of the crystal.

Besides the aforementioned phenomena, there are several effects which are not explicitly depicted in Fig. 6.1 and which must be also accounted for. These effects arise due to a special nature of polaritons: as discussed in section 3.4, exciton–exciton (polariton–polariton) scattering may cause strong correlations within the system of two–particle states resulting in formation of a bound state — biexciton (bipolariton). In addition to bound molecules, it is necessary to take into account special properties of polariton–polariton scattering as they may scatter due to exciton–exciton Coulomb interaction and also due to nonlinear dipole interaction [10]. This correction to the dipole interaction is caused by the composite character of excitons and Pauli exclusion principle and leads to a correction of the coupling of external photons to internal polaritons.

All features listed above are discussed in the following sections. After discussion of linear (section 6.2) and nonlinear coupling (section 6.3) of external photons to internal polaritons, polariton–polariton scattering is analyzed in section 6.4. Section 6.5 then introduces the concept of bipolaritons. Relaxation rates are discussed in section 6.6 and the last section 6.7 presents the method of derivation of equations of motion.

As stated in section 3.4, polaritons are eigenstates of a Hamiltonian accounting for electrons, holes and photons in semiconductor crystals. In our case, it is reasonable to consider them as the basic excitations of the crystal. We may then neglect the influence of the UPB as discussed above and only particles from the LPB are taken into account.

Hamiltonians of particle–particle interactions are known for exciton–exciton and exciton–photon interactions, we need, however, Hamiltonians for polaritons. We may do an approximation by the LPB polaritons with the help of (3.30) and we may use the substitutions:

$$\hat{a}_{S,\boldsymbol{k}} = \mathrm{i}\phi_S(\boldsymbol{k})\hat{P}_{\mathrm{LPB}}\,, \tag{6.1}$$

$$\hat{B}_{S,\boldsymbol{k}} = \chi_S(\boldsymbol{k})\hat{P}_{\mathrm{LPB}}\,. \tag{6.2}$$

Four–wave mixing is an experimental method in which generally three nondegenerate laser beams excite the sample and the response is detected in one of three FWM directions. These are $-\boldsymbol{K}_1+\boldsymbol{K}_2+\boldsymbol{K}_3$, $\boldsymbol{K}_1-\boldsymbol{K}_2+\boldsymbol{K}_3$ and $\boldsymbol{K}_1+\boldsymbol{K}_2-\boldsymbol{K}_3$. It is clear from the symmetry

consideration, that one may choose one of these three diffraction directions and develop a model which describes the appropriate FWM response. Responses in the other directions may be calculated using the same model, however the indices of directions must be changed according to the experimental situation. I choose the direction $\boldsymbol{K}_1+\boldsymbol{K}_2-\boldsymbol{K}_3$ as the diffraction direction (this is the same direction with respect to directions of incoming beams as in chapter 5).

The aforementioned diffraction directions are the diffraction directions in transmission, however the model may be applied also to the response measured in the reflection geometry. Diffraction directions are then defined as reflection of the diffraction directions by the plane of the crystal surface and the model presented below is suitable also for description of a signal diffracted to these directions.

At the beginning of development of a new model, I summarize the preconditions for it. I assume an optically thin (this property is justified below) bulk intrinsic semiconductor crystal with planparallel surfaces. Optical excitation below the exciton resonance is performed by optical pulses with nearly parallel wave vectors. The angle of incidence of all beams is then assumed to be zero. FWM signal may be described for the transmission geometry or reflection geometry (for the latter case, the requirement of an optically thin sample is not necessary). The crystal is not under influence of any external fields or mechanical stress, however the model may be further extended for these cases (see section 7.8). All spins of polaritons (excitons) and bipolaritons are taken into account. The temporal order of excitation pulses with wave vectors $\boldsymbol{K}_1$, $\boldsymbol{K}_2$ and $\boldsymbol{K}_3$, respectively, is arbitrary; these pulses couple to polaritons with wave vectors $\boldsymbol{k}_1$, $\boldsymbol{k}_2$ and $\boldsymbol{k}_3$, respectively, the FWM direction is $\boldsymbol{K}_1+\boldsymbol{K}_2-\boldsymbol{K}_3$ and the diffracted optical field couples to the polariton with wave vector $\boldsymbol{k}_4 = \boldsymbol{k}_1+\boldsymbol{k}_2-\boldsymbol{k}_3$.

6.2 Linear coupling of photons to crystal

As noted in section 3.4 of chapter 3, breaking of the crystal symmetry by the presence of the crystal surface causes refraction (and reflection) of photons which propagate towards the crystal surface. Refraction angles for all polariton branches are unambiguously determined by the angle of incidence of the incoming photons. Energy transfer to the particular branches cannot be, however, simply determined using some simple boundary conditions. Pekar [42] therefore phenomenologically introduced additional boundary conditions (ABC) additionally to Maxwell boundary conditions (MBC) [87] in order to solve the problem. Exact solution is possible using MBC [40] or performing microscopic calculations of exciton wavefunctions near the crystal surface [88, 89, 90].

In this thesis, polaritons are considered as polarization waves and therefore all phenomena connected with the inner structure of polaritons (their excitonic part) are omitted. This simplification leads to the loss of the effect of dead layer which is not, on the other hand, of any big significance in the presented model.

The coupling of *external* photons (from the point of view of the crystal) to *internal* polaritons in linear regime is calculated here. This calculation follows Ref. [40] and it is adapted for the use of Hamiltonian (3.27). Let's consider an incoming cw plane wave with frequency ω and wave vector perpendicular to the crystal surface[1]. I therefore drop the denotation of wave vectors by their direction and size since they are all parallel and I use notation $q = |\boldsymbol{q}|$. One starts with the one–dimensional wave equation valid for the

[1] Calculation may be performed for a general angle of incidence.

(complex) negative energy part of the intensity of electric field (for definition see (2.60)):

$$\frac{\partial^2}{\partial z^2}E(x,\omega)+\frac{\omega^2}{c^2}\int_{-\infty}^{+\infty}\epsilon(x-x',\omega)E(x',\omega)\,\mathrm{d}x'=\frac{\omega^2}{c^2}P(x,\omega)=s(x,\omega)\,, \tag{6.3}$$

where $E(x,\omega)$ is the electric field amplitude, ϵ is the medium dielectric constant and $P(x,\omega)$ is macroscopic polarization of external sources which are not involved in ϵ. Sources are considered in order to generate the incoming wave (this source is located in $x\to-\infty$) and the reflected wave (this source is in the transition region between the crystal and its surrounding). Using Fourier transform, one may solve the previous equation:

$$E(x,\omega)=\int_{-\infty}^{+\infty}\frac{\mathrm{d}q}{2\pi}\frac{s(q,\omega)\mathrm{e}^{\mathrm{i}qx}}{\frac{\omega^2}{c^2}\epsilon(q,\omega)-q^2}\,. \tag{6.4}$$

If the dielectric constant is known (analytically continued) in the whole complex plane, one may perform integration using the residuum theorem. We then find for the electric field inside the crystal:

$$E(x,\omega)=\sum_j s(q_j,\omega)R_j(\omega)\mathrm{e}^{\mathrm{i}q_jx}\,, \tag{6.5}$$

$$R_j=-\mathrm{i}\,\mathrm{Res}\frac{1}{q^2-\frac{\omega^2}{c^2}\epsilon(q,\omega)}\,, \tag{6.6}$$

where the symbol "Res" stands for residuum of the argument and wave vector q_j is assigned to the j–th residuum R_j. The source term $s(q,\omega)$ is assumed to be localized in space and therefore slowly varying in reciprocal space. Changes over the values of wave vectors assigned to residue are considered to be negligible and one may therefore use an approximation $s(q_j,\omega)\approx s_0(\omega)\ \forall q$. We may use the expansion:

$$\frac{1}{q^2-\frac{\omega^2}{c^2}\epsilon(q,\omega)}=\frac{\beta_+(q,\omega)}{q^2-q_+^2}+\frac{\beta_-(q,\omega)}{q^2-q_-^2}\,, \tag{6.7}$$

$$\beta_\pm(q,\omega)=\pm\frac{q_\mathrm{X}^2-q^2}{q_+^2-q_-^2}\,, \tag{6.8}$$

where we used the definitions (3.36)–(3.39). One then may evaluate the residuum terms:

$$R_\pm(\omega)=\frac{\beta_\pm(q_\pm,\omega)}{2q_\pm}\,. \tag{6.9}$$

The wave which penetrates to the crystal then has the magnitude of electric field expressed as [40]:

$$E(x,\omega)=s_0(\omega)\left[\frac{\beta_+(q_+(\omega),\omega)}{2q_+(\omega)}\mathrm{e}^{\mathrm{i}q_+(\omega)x}+\frac{\beta_-(q_-(\omega),\omega)}{2q_-(\omega)}\mathrm{e}^{\mathrm{i}q_-(\omega)x}\right]\,. \tag{6.10}$$

The ratio between fields generated by polaritons from the particular branches is clearly fixed by the above equation. Using MBE, one then may fix the reflection coefficient and the value of $s_0(\omega)$. Refractive indices for the respective polariton branches may be defined as:

$$n_\pm(\omega)=\frac{q_\pm(\omega)}{q_0(\omega)}\,, \tag{6.11}$$

where $q_0(\omega)$ is the wave vector of the incident field (outside the crystal). An effective refractive index may be then defined as:

$$\frac{1}{n_{\text{eff}}} = \frac{\beta_+}{n_+} + \frac{\beta_-}{n_-} \,. \tag{6.12}$$

Using the above definitions, transmission coefficient and the coefficient s_0 can be calculated:

$$t(\omega) = \frac{2n_{\text{eff}}(\omega)}{n_1 + n_{\text{eff}}(\omega)} \,, \tag{6.13}$$

$$s_0(\omega) = \frac{2n_{\text{eff}}(\omega)}{n_1 + n_{\text{eff}}(\omega)} \left[\frac{\beta_+(q_+(\omega),\omega)}{2q_+(\omega)} + \frac{\beta_-(q_-(\omega),\omega)}{2q_-(\omega)} \right]^{-1} E_0(\omega) \,. \tag{6.14}$$

Symbol $E_0(\omega)$ is the amplitude of the incident (external) electric field and n_1 denotes refractive index of the surrounding medium. It is important for our purposes what are the one–polariton coherences $\langle \hat{P}_{\text{LPB,UPB}}(\omega) \rangle$ in the system after optical excitation. They are determined by the coefficient $s_0(\omega)$ and by the coefficients ϕ and χ which reflect the photon–likeness of the polaritons. Taking into account the expression

$$E(q,t) = \langle \psi(t) | \hat{E}(q,t) | \psi(t) \rangle = \sqrt{\frac{2\pi\hbar\omega_q}{\Omega}} \left\langle \psi(t) \left| \hat{a}_q \mathrm{e}^{-\mathrm{i}\omega_q t} - \hat{a}_q^+ \mathrm{e}^{\mathrm{i}\omega_q t} \right| \psi(t) \right\rangle \,, \tag{6.15}$$

where $\hat{E}(q,t)$ denotes the operator of intensity of electric field in the mode described by the wave vector q and Ω stands for normalization volume, we may write:

$$\langle \hat{P}_{\text{LPB}}(\omega) \rangle = \mathrm{i}\phi(q_+) \frac{s_0}{\sqrt{\frac{2\pi\hbar\omega_q}{\Omega}}} \frac{\beta_+}{2q_+} \,, \tag{6.16}$$

$$\langle \hat{P}_{\text{UPB}}(\omega) \rangle = \chi(q_-) \frac{s_0}{\sqrt{\frac{2\pi\hbar\omega_q}{\Omega}}} \frac{\beta_-}{2q_-} \,. \tag{6.17}$$

At this stage, the problem of coupling of external electromagnetic field to internal polariton modes is fully solved. However, we assumed monochromatic (cw) plane incident waves while in real experiments, photons localized in space and time are used. Laser fields are localized in spatially narrow beams and they are pulsed in time, i.e. fields are spread in reciprocal space and energy. It is generally possible to take these two facts into account and to include all states with various energies and wave vectors to the model. In order to simplify the description, we can assume that the spread of beams in reciprocal space is not large (i.e. paraxial approximation). We may therefore consider that the central wave vector determines properties of all waves in the beam. Such approximation by a decisive wave is not, on the contrary, possible in the spectra of pulses. One of the reasons is, that the spectral width of 100 fs pulses is about 20 meV and properties of polaritons significantly differ over this spectral range (cf. Refs. [26, 41]). One then may choose one of the two approaches discussed below: either one calculates in the reciprocal space with respect to time (energy space), i.e. no dynamics is present during calculations, and the results are transformed to time space at the end or the spectrum of the pulse is divided to smaller parts, each of them represented by the central energy, and the same "representative" method as in the case of beams is used for each of the sub–pulses.

In order to illustrate how the optical pulse, nearly resonant with exciton, propagates in the crystal, I calculated the energy distribution along the propagation axis using the

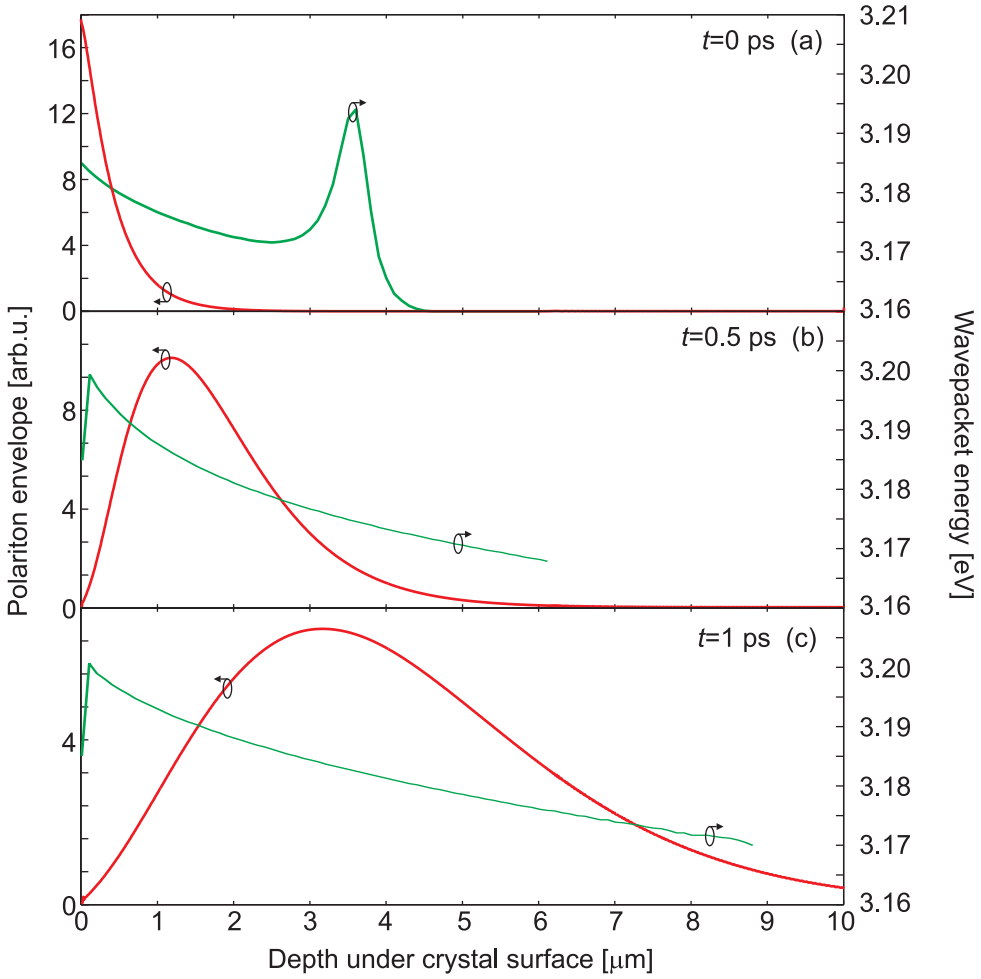

Figure 6.2: Polariton wavepacket (red) distortion and central frequency (green) as a function of the distance from surface after penetration of photons to a CuCl crystal. Figures depict various time delays after pulse incidence: 0 ps (a), 0.5 ps (b) and 1 ps (c). Spectral width of pulses is 20 meV and central energy 3.185 eV.

above formulas. The results are shown in Fig. 6.2 (biexciton resonance is not taken into account, even though it has a big influence on dispersion and also energy distribution). This calculation was performed for CuCl for parameters taken from Ref. [26]. Slightly after penetration of the optical pulse to the crystal, energy is concentrated below the crystal surface (Fig. 6.2a) and the pulse is not considerably distorted. After some time, the pulse distortion is more pronounced as seen in Fig. 6.2b. The reason is, that polaritons with low energy are mostly photon–like and therefore they propagate with high group velocity (see Fig. 3.6) while exciton–like polaritons have small group velocity and stay localized near the crystal surface. Distortion of the "polariton pulse" cannot be described in terms of wave equation in the slowly varying envelope approximation [14] since this approximation assumes negligible derivative of group velocity dispersion what is not clearly fulfilled slightly below exciton resonance. Exact calculation of the pulse propagation then requires description in the energy space.

Concerning calculation in the energy space, it is clear that one solves stationary problem, i.e. temporal evolution has no sense. One–photon coherences connected with polari-

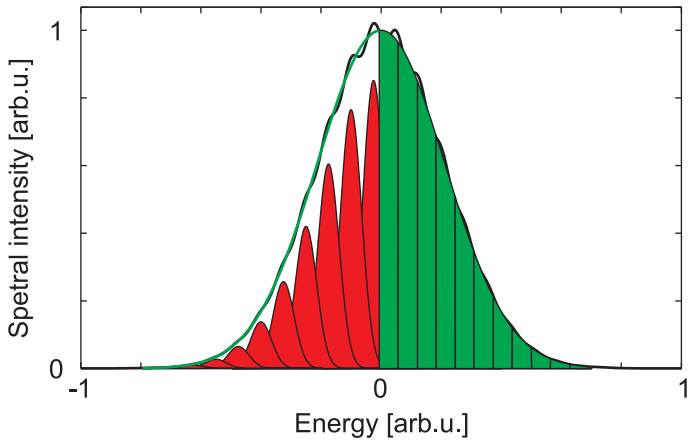

Figure 6.3: Decomposition of a Gaussian pulse (green envelope) to spectrally narrow parts. Red curves are Gaussians, their sum is the black envelope and green bars show decomposition to rectangular spectra.

ton branches are simply projections of one–photon coherences of the incoming optical fields as shown in the above formulas. Although calculation in the energy space is necessary for description of the photon–polariton coupling on the crystal surface, it is very inconvenient for description of other interactions. Nonlinear interactions are in general local in time and therefore the third–order response requires calculation of two convolutions over the energy spectrum. In addition, one is used to describe phenomenologically various dephasing processes by time constants and exponential decays in time. These phenomenological corrections may be included in calculations in energy space, however it is easier to perform calculations in time space.

The difficulties with complexity of the calculations may be overcome by separation of the broad spectrum of optical pulses to several narrow parts, each of them being represented by the central energy. Distortion of the spectrally narrow pulses is then considered to be determined only by the group velocity dispersion. Decomposition cannot be, however, done without an error since it is not possible to decompose the spectrum to narrow parts as sketched in Fig. 6.3 by green bars (the resulting temporal shape of the pulses wouldn't fulfill the condition of slow variation of the envelope). We may decompose the spectrum to Gaussian parts instead. The more parts are involved in the decomposition, the more precise the decomposition would be. One should, however, find a compromise since narrowing of spectra means that the pulses lengthen in time and relaxation dynamics looses sense. In addition, the more parts are involved in calculation, the more terms are involved in convolutions and the more complex the calculation is.

At this point, I do a crucial approximation in order to simplify the model. The approximation lies in an assumption of an optically thin sample when describing the FWM response in transmission or in an assumption of the measurement of the FWM signal in reflection geometry. These simplifications then allow us to consider only few parts of the polariton spectra as seen in Fig. 6.2. It is clear from the figure that only the exciton–like polaritons stay localized near the crystal surface at nonzero delays after excitation while the photon–like polaritons leave the crystal surface very quickly (propagation of the particles is determined by the group velocity, see Fig. 3.6). Considering thin samples, these photon–like polaritons leave the crystal and do not contribute to the FWM response.

When measuring in reflection geometry in thick samples, the decisive signal comes from the states localized near the surface as seen in Refs. [91, 92]. Since bipolaritons have also small group velocity, states resonant with bipolaritons should be also taken into account.

The discussed approximation allows us to neglect propagation effects in the sample: we consider that particles are excited in some optically thin layer which determines the FWM response and the propagation effects are simply described by dephasing and relaxation rates. Note that the approximation by an optically thin sample is not essential for the model and one may calculate propagation of the pulses through the crystal. The aim here is to determine polarization selection rules and therefore a thin crystal may be considered.

Now let's derive the dynamical equations for creation and annihilation of polaritons in a thin layer below the crystal surface. Dynamics of polaritons cannot be evaluated using projection described above due to dropping of the spatial coordinate. I use the formalism of dipole interaction instead, i.e. I consider the Hamiltonian for coupling of external photons to internal polaritons in the form:

$$\hat{H}_{\mathrm{DL}} = \mathrm{i} \sum_{S,\boldsymbol{K}} \mathcal{E}_{\boldsymbol{e},\boldsymbol{K}}(t) \mathrm{e}^{-\mathrm{i}\omega_{\boldsymbol{K}} t} \sum_{j} \mu_{jS,\boldsymbol{K}} \langle S | \boldsymbol{e} \rangle \hat{P}^{+}_{S,\boldsymbol{q}_j(\omega_{\boldsymbol{K}})} + H.c.\,, \tag{6.18}$$

where $\mu_{S,\boldsymbol{K}}$ is an effective coupling coefficient, $\mathcal{E}_{\boldsymbol{e},\boldsymbol{K}}(t)$ is a slowly varying envelope of electric field with wave vector $\boldsymbol{K}$ and polarization given by the vector $\boldsymbol{e}$. Symbol $\omega_{\boldsymbol{K}}$ is then frequency of the total intensity of electric field and $\boldsymbol{q}_j(\omega_{\boldsymbol{K}})$ is the wave vector of the j–th polariton band with energy $\hbar\omega_{\boldsymbol{K}}$. When deriving equations of motion, one introduces a dephasing rate Γ_2:

$$\Gamma_2 = \Gamma_2^* + \frac{1}{2}\Gamma_1 + \Gamma_{\mathrm{rad}}\,, \tag{6.19}$$

where the respective contributions to dephasing are: Γ_2^* is the pure dephasing, i.e. dephasing caused by incoherent interactions, Γ_1 is the relaxation rate (relaxation of population) and Γ_{rad} is the radiative decay rate. The last dephasing rate depends on group velocity v_{g} of polaritons — we may write $\Gamma_{\mathrm{rad}} \propto v_{\mathrm{g}}$. Using the two above equations, we may describe dynamics of photon–polariton coupling, however the coupling coefficients are unknown. Let's consider step–like excitation field $\mathcal{E}(t) = \mathcal{E}_0\Theta(t)$ where $\Theta(t)$ is the Heaviside step function. Mean polarization then follows:

$$\langle \hat{P}_{\boldsymbol{q}} \rangle = \frac{\mu}{\hbar}\frac{\mathcal{E}_0}{\Gamma_2}\mathrm{e}^{-\mathrm{i}\omega t}\left[1 - \mathrm{e}^{-\Gamma_2 t}\right]. \tag{6.20}$$

Taking into account the contribution for $t \to +\infty$ from the LPB (this term expresses the response to cw excitation under exciton resonance), we may derive from (6.10) and (6.16):

$$\mu = \mathrm{i}\hbar \frac{\phi(q_+)}{\sqrt{\frac{2\pi\hbar\omega_q}{\Omega}}} \frac{s_0}{\mathcal{E}_0} \frac{\beta_+\Gamma_2}{2q_+}\,. \tag{6.21}$$

6.3 Nonlinear coupling of photons to crystal

Linear coupling of photons to polaritons, which is discussed in the previous section 6.2, is valid for polaritons which obey Bose statistics. Excitons are not, however, exact bosons and therefore polaritons have also partial Fermi character. The Hamiltonian (6.18) then must be corrected. This correction is derived in this section.

As derived in Ref. [10], the Fermi character of excitons leads to a nonlinear correction of the exciton–photon interaction:[2]

$$\hat{H}_{\mathrm{DN}} = \mathrm{i}\sum_{\boldsymbol{k},\boldsymbol{k}'}\sum_{\boldsymbol{q}}\sum_{S,S'} G_{\mathrm{d}}(\boldsymbol{q}, \tfrac{1}{2}(\boldsymbol{k}-\boldsymbol{k}'))\hat{B}^{+}_{S,\boldsymbol{k}+\boldsymbol{q}}\hat{B}^{+}_{S',\boldsymbol{k}'-\boldsymbol{q}}\hat{B}_{S,\boldsymbol{k}}\hat{a}_{S',\boldsymbol{k}'} + H.c. + \\ + \mathrm{i}\sum_{\boldsymbol{k},\boldsymbol{k}'}\sum_{\boldsymbol{q}}\sum_{j_h,s_e}\sum_{j'_h,s'_e} G_{\mathrm{x}}(\boldsymbol{q}, \tfrac{1}{2}(\boldsymbol{k}-\boldsymbol{k}'))\hat{B}^{+}_{j'_h s_e,\boldsymbol{k}+\boldsymbol{q}}\hat{B}^{+}_{j_h s'_e,\boldsymbol{k}'-\boldsymbol{q}}\hat{B}_{j_h s_e,\boldsymbol{k}}\hat{a}_{j'_h s'_e,\boldsymbol{k}'} + H.c. \quad (6.22)$$

Using (6.2), we may derive the Hamiltonian using polariton operators:

$$\hat{H}_{\mathrm{DN}} = \mathrm{i}\sum_{\boldsymbol{k},\boldsymbol{k}'}\sum_{\boldsymbol{q}}\sum_{S,S'} G_{\mathrm{d}}(\boldsymbol{q}, \tfrac{1}{2}(\boldsymbol{k}-\boldsymbol{k}'))\chi_S(\boldsymbol{k}+\boldsymbol{q})\chi_S(\boldsymbol{k})\cdot \\ \cdot\hat{P}^{+}_{S,\boldsymbol{k}+\boldsymbol{q}}\hat{B}^{+}_{S',\boldsymbol{k}'-\boldsymbol{q}}\hat{P}_{S,\boldsymbol{k}}\hat{a}_{S',\boldsymbol{k}'} + H.c. + \\ + \frac{\mathrm{i}}{2}\sum_{\boldsymbol{k},\boldsymbol{k}'}\sum_{\boldsymbol{q}}\sum_{j_h,s_e}\sum_{j'_h,s'_e} G_{\mathrm{x}}(\boldsymbol{q}, \tfrac{1}{2}(\boldsymbol{k}-\boldsymbol{k}'))\chi_{j_h s_e}(\boldsymbol{k})\Big[\chi_{j'_h s_e}(\boldsymbol{k}+\boldsymbol{q})\hat{P}^{+}_{j'_h s_e,\boldsymbol{k}+\boldsymbol{q}}\hat{B}^{+}_{j_h s'_e,\boldsymbol{k}'-\boldsymbol{q}} + \\ + \chi_{j_h s'_e}(\boldsymbol{k}'-\boldsymbol{q})\hat{B}^{+}_{j'_h s_e,\boldsymbol{k}+\boldsymbol{q}}\hat{P}^{+}_{j_h s'_e,\boldsymbol{k}'-\boldsymbol{q}}\Big]\hat{B}_{j_h s_e,\boldsymbol{k}}\hat{a}_{j'_h s'_e,\boldsymbol{k}'} + H.c.\,, \quad (6.23)$$

where the operators $\hat{P}$ denote polariton operators from the LPB. This Hamiltonian has the same symmetry as the Hamiltonian for exciton–exciton scattering in (3.26) with respect to spins of polaritons. The processes described by this Hamiltonian are depicted in Fig. 6.4: the first line describes a *component–direct nonlinear coupling* where the spins of contributing particles are conserved. When a polariton is excited in the crystal, an incoming photon may not couple to the polariton mode given by the law of refraction. Instead, it couples to another mode and the polariton excited inside the crystal is simultaneously scattered. Total wave vector is conserved during this process. The second line in (6.22) then stands for *component exchange nonlinear coupling* what is the process similar to exchange of fermions in exciton–exciton scattering. Spins of the contributing particles may change and the dynamics of the interac-

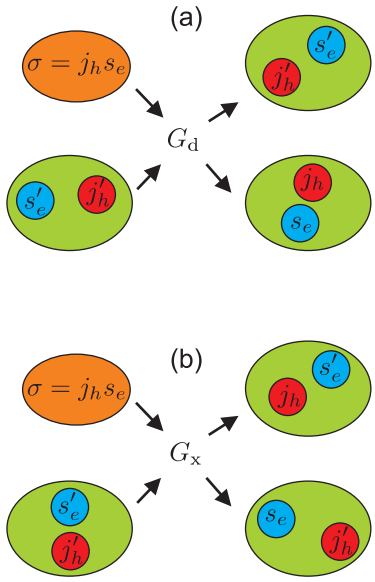

Figure 6.4: Schematic sketch of processes of component nonlinear coupling discussed in the text, according to [10].

[2] When compared to Ref. [10], there is an i prefactor which introduces the sums. This imaginary unit follows from the Hamiltonian of dipole interaction (3.29) (cf. Eq. (2.4) in [10]).

tion is equal to the dynamics of the component–direct nonlinear coupling. Component nonlinear coupling may cause basically two types of scattering processes:

- scattering on the surface due to variations of refractive index,
- scattering of the waves in the volume of the crystal.

Note that only the former process is discussed here since we are interested in the surface effects in this section. The volume phenomena are fully described by polariton–polariton scattering in section 6.4.

Component nonlinear couplings may be described using a nonlinear susceptibility which is related to polariton populations by $\epsilon_2(\boldsymbol{k}, \boldsymbol{k}_0, \boldsymbol{q}) \propto \langle \hat{P}^+_{\boldsymbol{k}_0} \hat{P}_{\boldsymbol{k}_0} \rangle$ where the wave vector $\boldsymbol{k}_0$ is the wave vector of the polariton, $\boldsymbol{k}$ is the wave vector of the photon and $\boldsymbol{q}$ is the exchanged momentum (spin numbers are omitted for clarity). Let's drop dependence of the nonlinear susceptibility on $\boldsymbol{k}$ and $\boldsymbol{k}_0$ since we may assume wave vectors are parallel to the propagation axis and they are therefore fixed. In order to calculate how external photons couple to internal polaritons according to (6.22), we may attempt to follow the method of Henneberger [40] which was shown in the previous section. We may rewrite wave equation (6.3) in reciprocal space:

$$-q^2 E(q,\omega) + \frac{\omega^2}{c^2} \int_{-\infty}^{+\infty} \epsilon_2(q-q',\omega) E(q') \,\mathrm{d}q' = s(q,\omega)\,. \tag{6.24}$$

Due to the convolution on the left hand side, one cannot extract $E(q,\omega)$ and therefore the derivation of (6.4) cannot be reproduced. One may instead use the wave equation in real space which contains only local interactions:

$$\nabla^2 E(\boldsymbol{r},\omega) + \frac{\omega^2}{c^2} \epsilon_2(\boldsymbol{r},\omega) E(\boldsymbol{r},\omega) = s(\boldsymbol{r},\omega)\,. \tag{6.25}$$

The nonlinear susceptibility in the above equation is proportional to (local) population of polaritons at the given spatial position and reflects creation of a nonlinear polarization as a consequence of partial Fermi character of polaritons. This phenomenon of local creation of polarization is well known from optical Bloch equations.

The wave equations (6.24)–(6.25) are only approximations since the nonlinear susceptibility does depend on the wave vectors $\boldsymbol{k}$ and $\boldsymbol{k}_0$. Eq. (6.24) would not thus be a simple convolution and Eq. (6.25) would not contain strictly local response to nonlinear terms. The spatial shape of the polariton wavefunction causes, on the contrary, a nonlocal response, i.e. mutual interaction of two excitons caused by their partial Fermi character takes place when the distance between excitons (distance of their centers of mass) is smaller than approximately four exciton Bohr radii [10]. The nonlocality of the response may be shown performing a transformation of the Hamiltonian (6.22) to real space using Fourier transform:

$$\begin{aligned}\hat{H}_{\mathrm{DN}} = {} & \mathrm{i} \sum_{S,S'} \int \mathrm{d}\boldsymbol{r} \int \mathrm{d}\boldsymbol{r}_1 \int \mathrm{d}\boldsymbol{r}_2 \, \mathcal{G}_{\mathrm{d}}(\boldsymbol{r}_1, \boldsymbol{r}_2, \boldsymbol{r}) \hat{B}^+_{S,\boldsymbol{r}_1+\boldsymbol{r}} \hat{B}^+_{S',\boldsymbol{r}_2-\boldsymbol{r}} \hat{B}_{S,\boldsymbol{r}_1} \hat{a}_{S',\boldsymbol{r}_2} + H.c. + \\ & + \mathrm{i} \sum_{j_h, s_e} \sum_{j'_h, s'_e} \int \mathrm{d}\boldsymbol{r} \int \mathrm{d}\boldsymbol{r}_1 \int \mathrm{d}\boldsymbol{r}_2 \, \mathcal{G}_{\mathrm{x}}(\boldsymbol{r}_1, \boldsymbol{r}_2, \boldsymbol{r}) \cdot \\ & \qquad \cdot \hat{B}^+_{j'_h s_e, \boldsymbol{r}_1+\boldsymbol{r}} \hat{B}^+_{j_h s''_e, \boldsymbol{r}_2-\boldsymbol{r}} \hat{B}_{j_h s_e, \boldsymbol{r}_1} \hat{a}_{j'_h s'_e, \boldsymbol{r}_2} + H.c.\,, \end{aligned} \tag{6.26}$$

$$\mathcal{G}_{\mathrm{d,x}}(\boldsymbol{r}_1, \boldsymbol{r}_2, \boldsymbol{r}) = \frac{1}{\Omega} \sum_{\boldsymbol{q},\boldsymbol{k}} G_{\mathrm{d,x}}(\boldsymbol{q}, \boldsymbol{k}) \mathrm{e}^{2i\boldsymbol{k}\cdot\boldsymbol{r}} \mathrm{e}^{\mathrm{i}\boldsymbol{q}\cdot(\boldsymbol{r}_1-\boldsymbol{r}_2+2\boldsymbol{r})}\,. \tag{6.27}$$

Clearly for $G_j(\boldsymbol{q},\boldsymbol{k}) \approx const$, j =d,x, one obtains:

$$\mathcal{G}_j(\boldsymbol{r},\boldsymbol{r}_1,\boldsymbol{r}_2) \approx \mathcal{G}_{j0}\,\delta(\boldsymbol{r})\delta(\boldsymbol{r}_1-\boldsymbol{r}_2)\,, \tag{6.28}$$

and the Hamiltonian (6.26) becomes local. Wannier excitons do not, however, reveal as excitations localized at one atomic site and therefore a nonlocal character of the interaction introduced by Hamiltonian (6.26) may be expected. From the point of view of light field, interaction described by the above Hamiltonian is local since the exciton Bohr radius is much smaller than the light wavelength. Approximation (6.28) is then of the same order as the dipole approximation. The Hamiltonian then reads:

$$\begin{aligned}\hat{H}_{\mathrm{DN}} = \mathrm{i}\mathcal{G}_{\mathrm{d0}} \sum_{S,S'} \int \mathrm{d}\boldsymbol{r}\; \hat{B}^{+}_{S,\boldsymbol{r}} \hat{B}^{+}_{S',\boldsymbol{r}} \hat{B}_{S,\boldsymbol{r}} \hat{a}_{S',\boldsymbol{r}} + H.c. + \\ + \mathrm{i}\mathcal{G}_{\mathrm{x0}} \sum_{j_h,s_e} \sum_{j'_h,s'_e} \int \mathrm{d}\boldsymbol{r}\; \hat{B}^{+}_{j'_h s_e,\boldsymbol{r}} \hat{B}^{+}_{j_h s'_e,\boldsymbol{r}} \hat{B}_{j_h s_e,\boldsymbol{r}} \hat{a}_{j'_h s'_e,\boldsymbol{r}} + H.c.\end{aligned} \tag{6.29}$$

As noted above, it is not possible to use the approach of Ref. [40] presented in section 6.2 in order to calculate the nonlinear coupling of photons to excitons. However, we may consider the scattering process as a perturbation and we evaluate the system's response in the first order of this perturbation. For the scattered wave, wave equation (6.3) is therefore assumed to be exact while the correction (6.23) must be considered for the incident wave and its transition to the reflected and transmitted wave through the crystal surface. Therefore equation (6.10) may be used for the intensity of electric field of the scattered waves. The coefficient $s_0(\omega)$ then should be calculated using the MBC. It is worthy to note that Eq. (6.10) is valid for any arbitrary propagation direction in an isotropic crystal, the angle of incidence is important in MBC.

Scattering of electromagnetic waves on the crystal boundary is caused by variations of the dielectric constant. Linear dielectric constant is constant over the whole crystal surface, however the nonlinear susceptibility varies with the density of locally excited polaritons as seen from the coupling Hamiltonian (6.29). Let's consider that the crystal is excited by two laser beams and therefore population grating of polaritons is created. The third beam then feels periodical modulation of the nonlinear refractive index what leads to scattering of the wave on the sample surface. In order to describe this process quantitatively, let's calculate the nonlinear susceptibility. Assuming an optical field with wave vector $\boldsymbol{k}$ and spin S and assuming the crystal in a one–polariton state $(\hat{P}^{+}_{S',\boldsymbol{k}_0}\cos\alpha + \sin\alpha)\,|0\rangle$, calculation of the susceptibility is straightforward and one gets in resonant approximation (3.29):

$$\epsilon_2(\boldsymbol{k},\Delta\boldsymbol{q}{=}0,\omega) = \frac{\epsilon_0}{2\pi\hbar^2} \int \frac{G^2(\boldsymbol{k}{-}\boldsymbol{q}')\cos^2\alpha}{\omega_{\mathrm{X}}^2 + \frac{\hbar\boldsymbol{q}'^2}{M}\omega_{\mathrm{X}} - \omega^2}\,\mathrm{d}\boldsymbol{q}' \approx \frac{\epsilon_0}{2\pi\hbar^2} \frac{\int G^2(\boldsymbol{k}{-}\boldsymbol{q}')\,\mathrm{d}\boldsymbol{q}'}{\omega_{\mathrm{X}}^2 + \frac{\hbar\boldsymbol{k}^2}{M}\omega_{\mathrm{X}} - \omega^2}\cos^2\alpha\,, \tag{6.30}$$

$$G^2(\boldsymbol{q}) = G^2_{\mathrm{d}}(\boldsymbol{q},0) + G^2_{\mathrm{x}}(\boldsymbol{q},0) + 2G_{\mathrm{d}}(\boldsymbol{q},0)G_{\mathrm{x}}(\boldsymbol{q},0)\delta_{SS'}\,. \tag{6.31}$$

Symbol ϵ_0 stands for vacuum dielectric constant. I assumed nearly parallel excitation beams and the last is valid if the variations of energy of excitons are smaller than the variations of G. One may perform a Fourier transform over $\boldsymbol{k}$ and the result may be written as:

$$\epsilon_2(\boldsymbol{r},\omega) = \epsilon_0 \sum_{S'} \frac{\langle \hat{B}^{+}_{S,\boldsymbol{r}} \hat{B}_{S,\boldsymbol{r}} \rangle}{2\pi\hbar^2} \frac{\int G^2(\boldsymbol{k}{-}\boldsymbol{q}')\,\mathrm{d}\boldsymbol{q}'}{\omega_{\mathrm{X}}^2 + \frac{\hbar\boldsymbol{k}^2}{M}\omega_{\mathrm{X}} - \omega^2}\,. \tag{6.32}$$

Let's consider that the population grating on the crystal surface causes a modulation of the refractive index:

$$n(x) = \sqrt{\epsilon + \epsilon_2(x)} \approx \sqrt{\epsilon}\left[1 + \frac{\epsilon_2(x)}{2\epsilon}\right] = n_0 + n_2 \cos \Lambda x \,, \tag{6.33}$$

where $n_0 = \sqrt{\epsilon}$ and $n_2 = \max \epsilon_2(x)/2\sqrt{\epsilon}$ and Λ denotes a period of an induced diffraction grating. Now let's consider an incident wave with amplitude E_i and a zero angle of incidence $\pi/2$. The reflected and transmitted waves may be expressed as sums:

$$E_\mathrm{r} = \sum_{j=0}^{\infty} r_j \cos^j \Lambda x \,, \tag{6.34}$$

$$E_\mathrm{t} = \sum_{j=0}^{\infty} t_j \cos^j \Lambda x \,. \tag{6.35}$$

The coefficients r_j and t_j are then evaluated using MBC. Calculation appropriate for the field polarized in the y direction (TE) is shown here, calculation for the TM polarization is then straightforward. Maxwell boundary conditions read:

$$E_\mathrm{i}(x) - E_\mathrm{r}(x) = E_\mathrm{t}(x) \,, \tag{6.36}$$

$$E_\mathrm{i}(x) n_1 = \sum_j [E_{\mathrm{r}j}(x) n_1 \cos \vartheta_{\mathrm{r}j} + E_{\mathrm{t}j} n(x) \cos \vartheta_{\mathrm{t}j}] \,, \tag{6.37}$$

where n_1 is refractive index of the medium around crystal. The fields were separated to the components which propagate in directions determined by the subscript j (diffraction order) and $\cos \vartheta_{\mathrm{r,t}j}$ are cosines of the propagation directions of the reflected and transmitted fields, respectively:

$$\tan \vartheta_{\mathrm{r}j} = \frac{\omega n_1 \Lambda j}{2\pi c} \tag{6.38}$$

and similarly for $\tan \vartheta_{\mathrm{t}j}$. Restricting to the first diffraction order, we may calculate the well known Fresnel formula for the variables E_i, r_0 and t_0:

$$r_0 = \frac{n_1 - n_0}{n_1 + n_0} E_\mathrm{i} \,, \tag{6.39}$$

$$t_0 = \frac{2n_1}{n_1 + n_0} E_\mathrm{i} \,. \tag{6.40}$$

MBC then yield amplitudes of the fields diffracted to the first order:

$$r_1 = t_1 \,, \tag{6.41}$$

$$t_1 = -\frac{2n_1 n_2}{n_1 + n_0} \left[n_1 \cos \vartheta_{\mathrm{r}1} + n_0 \cos \vartheta_{\mathrm{t}1}\right]^{-1} E_\mathrm{i} \,. \tag{6.42}$$

The coefficient $s_0(\omega)$ for the transmitted field diffracted to the first order may be then determined according to (6.14):

$$s_0(\omega) = -\frac{2n_1 n_2}{n_1 + n_0} \left[n_1 \cos \vartheta_{\mathrm{r}1} + n_0 \cos \vartheta_{\mathrm{t}1}\right]^{-1} \cdot \\ \cdot \left[\frac{\beta_+(q_+(\omega), \omega)}{2q_+(\omega)} + \frac{\beta_-(q_-(\omega), \omega)}{2q_-(\omega)}\right]^{-1} E_\mathrm{i}(\omega) \,. \tag{6.43}$$

The coefficient depends on the spin of the excited polariton and optical field through refractive index n_2. Although this spin dependence is not explicitly shown in (6.33), one may easily supplement formula (6.32) and rewrite (6.33) including spin numbers. I use an effective Hamiltonian for coupling of the incident wave to the diffracted polariton whose structure is similar to (6.18) in the model:

$$\hat{H}_{\mathrm{DN}} = \mathrm{i} \sum_{S,\boldsymbol{K},\boldsymbol{q}} \mathcal{E}_{\boldsymbol{e},\boldsymbol{K}}(t) \mathrm{e}^{-\mathrm{i}\omega_{\boldsymbol{K}} t} \kappa_{SS',\boldsymbol{K}} \langle S| \boldsymbol{e}\rangle \hat{P}^{+}_{S,\boldsymbol{k}(\boldsymbol{K})+\boldsymbol{q}} \hat{P}^{+}_{S',\boldsymbol{k}-\boldsymbol{q}} \hat{P}_{S',\boldsymbol{k}}\,, \tag{6.44}$$

$$\kappa_{SS',\boldsymbol{K}} = \hbar \frac{\phi(q_+)}{\sqrt{\frac{2\pi\hbar\omega_q}{\Omega}}} \frac{s_0(S,S')}{\mathcal{E}_0} \frac{\beta_+ \Gamma_2}{2q_+} \chi_{S'}(\boldsymbol{k}) \chi_{S'}(\boldsymbol{k}-\boldsymbol{q})\,, \tag{6.45}$$

where s_0 is given by (6.43) and $\boldsymbol{k}(\boldsymbol{K})$ expresses the refraction law. We may simply verify that this Hamiltonian gives the correct polariton polarization wave. Let's consider the crystal in a superposition of one–polariton states which form a population grating:

$$|\Psi\rangle = \frac{1}{\sqrt{2}} \left[\hat{P}^{+}_{\boldsymbol{k}_1} + \hat{P}^{+}_{\boldsymbol{k}_2}\right] |0\rangle\ . \tag{6.46}$$

Spin is omitted for clarity. Equation of motion for the diffracted polarization wave reads:

$$i\hbar\partial_t \langle \hat{P}_{\mathrm{diff}}\rangle = \langle [\hat{P}_{\mathrm{diff}}, \hat{H}_{\mathrm{DN}}]\rangle\,. \tag{6.47}$$

Assuming optical field in direction $\boldsymbol{K}_3$ and that the wave vector of the diffracted field is $\boldsymbol{k}_3+\boldsymbol{q}$, the equation of motion reads:

$$i\hbar\partial_t \langle \hat{P}_{\mathrm{diff}}\rangle = i\mathcal{E}_{\boldsymbol{K}_3}(t) \mathrm{e}^{i\omega_{\boldsymbol{K}_3} t} \kappa_{\boldsymbol{K}_3} \sum_{\boldsymbol{q}} \langle \hat{P}^{+}_{\boldsymbol{k}_1-\boldsymbol{q}} \hat{P}_{\boldsymbol{k}_1}\rangle\,. \tag{6.48}$$

The only nonzero contribution to the last mean value comes from correlation $\langle \hat{P}^{+}_{\boldsymbol{k}_2} \hat{P}_{\boldsymbol{k}_1}\rangle$ and thus $\boldsymbol{q} = \boldsymbol{k}_1 - \boldsymbol{k}_2$ and the diffraction direction is $\boldsymbol{k}_1 - \boldsymbol{k}_2 + \boldsymbol{k}_3$ what is the well known result.

6.4 Polariton–polariton interaction

Polaritons are composed of an exciton and a photon providing possibility of the Coulomb exciton–exciton and therefore polariton–polariton interaction. Let's denote polariton as $p = x + \gamma$, x representing a virtual exciton and γ representing a virtual photon. Polariton–polariton interaction may be then written as:

$$p \times p \;=\; (x+\gamma) \times (x+\gamma) \;=\; x\times x \;+\; 2x\times\gamma \;+\; \gamma\times\gamma\,. \tag{6.49}$$

The mutual particle–particle interactions clearly involve also photon–exciton and photon–photon interactions. Photons do not interact and therefore the polariton–polariton interaction consists only of exciton–exciton and photon–exciton scattering events. Exciton–exciton interaction is described by the standard Hamiltonian (3.26). The exciton–photon scattering term is zero for excitons which are exact bosons since the exciton–photon interaction is fully described by the linear term proportional to $\hat{B}^{+}\hat{a} + H.c.$. However, excitons are not exact bosons and one should take into account the component nonlinear coupling as discussed in the preceding section. Its Hamiltonian is written in Eq. (6.22). With the

help of (6.1)–(6.2), we may rewrite the Hamiltonians and we may connect them in one Hamiltonian:

$$\begin{aligned}\hat{H}_{SD} = \frac{1}{2}\sum_{\boldsymbol{k},\boldsymbol{k}'}\sum_{\boldsymbol{q}}\sum_{S,S'}\chi_S(\boldsymbol{k}+\boldsymbol{q})\chi_{S'}(\boldsymbol{k}'-\boldsymbol{q})\chi_S(\boldsymbol{k})\cdot \\ \cdot[-G_{\mathrm{d}}(\boldsymbol{q},\tfrac{1}{2}(\boldsymbol{k}-\boldsymbol{k}'))\phi_{S'}(\boldsymbol{k}')+V_d(\boldsymbol{q},\tfrac{1}{2}(\boldsymbol{k}-\boldsymbol{k}'))\chi_{S'}(\boldsymbol{k}')]\hat{P}^{+}_{S,\boldsymbol{k}+\boldsymbol{q}}\hat{P}^{+}_{S',\boldsymbol{k}'-\boldsymbol{q}}\hat{P}_{S,\boldsymbol{k}}\hat{P}_{S',\boldsymbol{k}'}+ \\ +\frac{1}{2}\sum_{\boldsymbol{k},\boldsymbol{k}'}\sum_{\boldsymbol{q}}\sum_{j_h,s_e}\sum_{j'_h,s'_e}\chi_{j'_h s_e}(\boldsymbol{k}+\boldsymbol{q})\chi_{j_h s'_e}(\boldsymbol{k}'-\boldsymbol{q})\chi_{j_h s_e}(\boldsymbol{k})[-G_{\mathrm{x}}(\boldsymbol{q},\tfrac{1}{2}(\boldsymbol{k}-\boldsymbol{k}'))\phi_{j'_h s'_e}(\boldsymbol{k}')+ \\ +V_x(\boldsymbol{q},\tfrac{1}{2}(\boldsymbol{k}-\boldsymbol{k}'))\chi_{j'_h s'_e}(\boldsymbol{k}')]\hat{P}^{+}_{j'_h s_e,\boldsymbol{k}+\boldsymbol{q}}\hat{P}^{+}_{j_h s'_e,\boldsymbol{k}'-\boldsymbol{q}}\hat{P}_{j_h s_e,\boldsymbol{k}}\hat{P}_{j'_h s'_e,\boldsymbol{k}'}\,. \qquad (6.50)\end{aligned}$$

Since we assume nearly parallel excitation beams, we may use the approximation $\boldsymbol{k}-\boldsymbol{k}'\approx 0$ and we may assume that the contribution to the FWM signal comes only from the scattering events with a small exchanged momentum $\boldsymbol{q}$. Therefore we may let $\boldsymbol{q}\approx 0$ and we may directly write the matrix elements of the Hamiltonian (with respect to the spin states of polaritons):

$$\mathbf{G}_{\mathrm{d}}(S_1,S_2,S_3,S_4) = G_{\mathrm{d}}(0,0)\,\langle S_1|\,S_3\rangle\,\langle S_2|\,S_4\rangle\,, \qquad (6.51)$$

$$\mathbf{G}_{\mathrm{x}}(S_1,S_2,S_3,S_4) = G_{\mathrm{x}}(0,0)\sum_{j_h,s_e}\sum_{j'_h,s'_e}\langle j_h,s_e|\,S_3\rangle\,\langle j'_h s'_e|\,S_4\rangle\,\langle S_1|\,j'_h,s_e\rangle\,\langle S_2|\,j_h,s'_e\rangle\,, \qquad (6.52)$$

$$\mathbf{V}_{\mathrm{d}}(S_1,S_2,S_3,S_4) = V_{\mathrm{d}}(0,0)\,\langle S_1|\,S_3\rangle\,\langle S_2|\,S_4\rangle\,, \qquad (6.53)$$

$$\mathbf{V}_{\mathrm{x}}(S_1,S_2,S_3,S_4) = V_{\mathrm{x}}(0,0)\sum_{j_h,s_e}\sum_{j'_h,s'_e}\langle j_h,s_e|\,S_3\rangle\,\langle j'_h s'_e|\,S_4\rangle\,\langle S_1|\,j'_h,s_e\rangle\,\langle S_2|\,j_h,s'_e\rangle\,. \qquad (6.54)$$

where S_1 and S_2 are spins of the final states, S_3 and S_4 are spins of the initial states. The matrices V_{d} and G_{d} are diagonal with respect to the basis composed of pairs (S_1S_2) and (S_3S_4), respectively. Spin is therefore conserved in all direct scattering processes. However, exchange processes are responsible for the change of the spins of the respective polaritons. Spin parts (right–hand side of (6.52) without $G_{\mathrm{x}}(0,0)$) of the matrices $\mathbf{G}_{\mathrm{x}}$ and $\mathbf{V}_{\mathrm{x}}$ (these spin parts are equivalent for both matrices) do not generally depend on the crystal symmetry, however the spin structure of dipole–active excitons depends on the crystal symmetry and therefore mutual scattering of optically excited polaritons is symmetry–dependent. For example in hexagonal crystals with wurtzite structure, dipole–active states with spin ± 1 have the simple structure $|+\rangle = \Phi_2\beta$ and $|-\rangle = \Phi_1\alpha$, respectively, with the Φ_j and α,β defined in chapter 5. Exchange scattering of the $|+\rangle$ and $|-\rangle$ polaritons then always leads to dipole–inactive states $\Phi_2\alpha$ and $\Phi_1\beta$ with spins ± 2. In cubic crystals, on the contrary, dipole–active states are superpositions of the states from the lh and hh band: $|+\rangle = \frac{1}{2}[\Phi_3\alpha + \sqrt{3}\Phi_1\beta]$ and $|-\rangle = \frac{1}{2}[\Phi_4\beta + \sqrt{3}\Phi_2\alpha]$. Exchange of electrons or holes then may lead to creation of the dipole–active pair $|+-\rangle$. Exchange scattering to dipole–active states is therefore allowed in crystals with zinc–blende structure what may result in a strong FWM response when compared with the response to $\sigma^+\sigma^+$ excitation.

The spin parts of exchange scattering for materials with zinc–blende and wurtzite structures are summarized in Tabs. 6.1–6.4. Only the parts of the matrices which contain dipole–active states are shown since this is the most important part. In Tabs. 6.1–6.2, the matrices for cubic crystals with zinc–blende structure are shown concerning linearly polarized polaritons (Tab. 6.1) and circularly polarized polaritons (Tab. 6.2). The Tabs. 6.3–6.4 depict the same properties considering a crystal with wurtzite structure. Note that the spin structure of dipole–active polaritons (excitons) in [001] QW with zinc–blende structure is

$\langle S_f\, S'_f \vert \mathbf{G}_\mathrm{x}/G_\mathrm{x}(0,0) \vert S\, S' \rangle$	$\vert X\rangle\,\vert X\rangle$	$\vert X\rangle\,\vert Y\rangle$	$\vert Y\rangle\,\vert X\rangle$	$\vert Y\rangle\,\vert Y\rangle$
$\langle X\vert\,\langle X\vert$	$\frac{1}{2}$	0	0	$-\frac{1}{8}$
$\langle X\vert\,\langle Y\vert$	0	$\frac{1}{2}$	$\frac{1}{8}$	0
$\langle Y\vert\,\langle X\vert$	0	$\frac{1}{8}$	$\frac{1}{2}$	0
$\langle Y\vert\,\langle Y\vert$	$-\frac{1}{8}$	0	0	$\frac{1}{2}$

Table 6.1: The spin part of the fermion exchange between two polaritons, from (6.52) for spins in the direction of the principal axes and crystal with zinc–blende structure. The rows stand for the initial states and the columns for the final states.

$\langle S_f\, S'_f \vert \mathbf{G}_\mathrm{x}/G_\mathrm{x}(0,0) \vert S\, S' \rangle$	$\vert+\rangle\,\vert+\rangle$	$\vert+\rangle\,\vert-\rangle$	$\vert-\rangle\,\vert+\rangle$	$\vert-\rangle\,\vert-\rangle$
$\langle+\vert\,\langle+\vert$	$\frac{5}{8}$	0	0	0
$\langle+\vert\,\langle-\vert$	0	$\frac{3}{8}$	0	0
$\langle-\vert\,\langle+\vert$	0	0	$\frac{3}{8}$	0
$\langle-\vert\,\langle-\vert$	0	0	0	$\frac{5}{8}$

Table 6.2: Same as Tab. 6.1 for circular spins of the polaritons.

equivalent to the spin structure of dipole–active polaritons in bulk crystals with wurtzite structure and therefore Tabs. 6.3–6.4 are valid also to most cubic quantum wells.

The most interesting and important property of the polariton–polariton scattering is the difference between the tables for linearly and circularly polarized particles. For circularly polarized particles, the spin of contributing polaritons is conserved or they may exchange spins one with the other. Linearly polarized particles, on the contrary, may change the spins to the states different from the initial states: the XX pair may scatter to the YY pair while scattering $++ \rightarrow --$ is always forbidden. As shown in chapter 5, level schemes for excitation of linearly or circularly polarized particles have the same structure, however considering particle–particle interaction, the analogy is broken. This fact will be mentioned later since it is crucial for polarization selection rules in FWM.

6.5 Bipolaritons

Biexcitons were already discussed within the giant oscillator strength model in section 3.4. I have mentioned with reference to Ref. [38, 93, 94] that the GOS model is a rough approximation because it doesn't describe the dynamics of the biexciton creation, however this dynamics may be important in the model of FWM response. One of the reasons of the fail of the GOS model is, that excitons and biexcitons are treated as independent particles, however biexciton is rather a linear combination of two–exciton states. The bipolariton model is further confirmed by experiments on bipolariton luminescence [95, 96, 97].

Exact description of the biexciton dynamics is impossible due to the structure of the exciton–exciton interaction. One therefore uses a model which is sufficiently accurate. I use the A.L. Ivanov's and H. Haug's bipolariton model [38] in this thesis. Bound molecules are called *bipolaritons* instead of biexcitons in order to reflect the fact that the strong dipole interaction is taken into account and polaritons are responsible for excitation–induced phenomena.

$\langle S_f\, S'_f \vert \mathbf{G}_{\mathrm{x}}/G_{\mathrm{x}}(0,0) \vert S\, S'\rangle$	$\vert X\rangle\,\vert X\rangle$	$\vert X\rangle\,\vert Y\rangle$	$\vert Y\rangle\,\vert X\rangle$	$\vert Y\rangle\,\vert Y\rangle$
$\langle X\vert\,\langle X\vert$	$\frac{1}{2}$	0	0	$-\frac{1}{2}$
$\langle X\vert\,\langle Y\vert$	0	$\frac{1}{2}$	$\frac{1}{2}$	0
$\langle Y\vert\,\langle X\vert$	0	$\frac{1}{2}$	$\frac{1}{2}$	0
$\langle Y\vert\,\langle Y\vert$	$-\frac{1}{2}$	0	0	$\frac{1}{2}$

Table 6.3: The spin part of the fermion exchange between two polaritons, from (6.52) for spins in the direction of the principal axes and crystal with wurtzite structure. The rows stand for the initial states and the columns for the final states.

$\langle S_f\, S'_f \vert \mathbf{G}_{\mathrm{x}}/G_{\mathrm{x}}(0,0) \vert S\, S'\rangle$	$\vert{+}{+}\rangle$	$\vert{+}{-}\rangle$	$\vert{-}{+}\rangle$	$\vert{-}{-}\rangle$
$\langle{+}{+}\vert$	1	0	0	0
$\langle{+}{-}\vert$	0	0	0	0
$\langle{-}{+}\vert$	0	0	0	0
$\langle{-}{-}\vert$	0	0	0	1

Table 6.4: Same as Tab. 6.3 for circular spins of the polaritons.

In the bipolariton model, excitons and bipolaritons are not considered as independent particles and one considers the bipolariton wavefunction in the form:

$$\hat{A}_{J,\boldsymbol{K}} = \frac{1}{\sqrt{\Omega}} \sum_{\boldsymbol{q}} \Psi_{\mathrm{m}}^{(J)}(\boldsymbol{q}) \hat{B}_{\boldsymbol{K}/2+\boldsymbol{q}} \hat{B}_{\boldsymbol{K}/2-\boldsymbol{q}}\,, \tag{6.55}$$

where Ω is the normalization volume and $\Psi_{\mathrm{m}}^{(J)}(\boldsymbol{q})$ is the bipolariton wavefunction in reciprocal space. The superscript J distinguishes between bipolariton internal states, $J = 0$ denotes the bipolariton ground state. In the following, I consider only the ground states of bipolaritons since they give the strongest contribution to the optical response, however excited states may be included in the model. The subscript J is then omitted in the operators of bipolariton in the ground state. I dropped the spin subscripts for clarity. One may express the two–exciton operators in the following way [93]:

$$\begin{aligned} \hat{B}_{\boldsymbol{K}/2+\boldsymbol{q}} \hat{B}_{\boldsymbol{K}/2-\boldsymbol{q}} &= \frac{1}{\sqrt{\Omega}} \sum_{J} \Psi_{\mathrm{m}}^{(J)*}(\boldsymbol{q}) \hat{A}_{J,\boldsymbol{K}} \approx \\ &\approx \frac{1}{\sqrt{\Omega}} \Psi_{\mathrm{m}}^{(0)*}(\boldsymbol{q}) \hat{A}_{\boldsymbol{K}}\,. \end{aligned} \tag{6.56}$$

This approximation is valid under assumption of resonant excitation with the bipolariton state $J = 0$. The bipolariton wavefunction $\Psi_{\mathrm{m}}^{(J)}(\boldsymbol{q})$ is calculated in order to diagonalize the Hamiltonian of polariton–polariton interaction and therefore the bipolariton state is the eigenstate of the polariton Hamiltonian including particle–particle interactions. Note that the bipolariton state defined by (6.55) is assumed to be the bound state. One should then add all unbound states (eigenstates of the polariton Hamiltonian) in order to have the full set of two–polariton wavefunctions. It is, indeed, impossible to find all these states analytically and therefore one may use the following approximation: let's assume that there exists a two–exciton state which is excited in an experiment and another two–exciton state which is probed. We approximate the basis of two–exciton states by the full set of bound

and unbound two–exciton states from which the aforementioned two–exciton states are subtracted and these *bare* two–exciton states are added to the basis. Let's denote the initial and the final two–exciton states by the wave vectors of the contributing particles using the notation $|\boldsymbol{k}'_1, \boldsymbol{k}'_2\rangle$ for the initial state and $|\boldsymbol{k}'_3, \boldsymbol{k}'_4\rangle$ for the final state ($\boldsymbol{k}'_1+\boldsymbol{k}'_2 = \boldsymbol{k}'_3+\boldsymbol{k}'_4$). The reduced bipolariton wavefunction then has the form:

$$\tilde{A}_{\boldsymbol{K}} = \hat{A}_{\boldsymbol{K}} - \frac{\delta(\boldsymbol{K}-\boldsymbol{k}'_1-\boldsymbol{k}'_2)}{\sqrt{\Omega}} \left[\Psi^{(0)}_{\boldsymbol{K}}\left(\tfrac{1}{2}(\boldsymbol{k}'_1-\boldsymbol{k}'_2)\right)\hat{B}_{\boldsymbol{k}'_1}\hat{B}_{\boldsymbol{k}'_2} + \Psi^{(0)}_{\boldsymbol{K}}\left(\tfrac{1}{2}(\boldsymbol{k}'_3-\boldsymbol{k}'_4)\right)\hat{B}_{\boldsymbol{k}'_3}\hat{B}_{\boldsymbol{k}'_4}\right]. \quad (6.57)$$

At this stage, we may use (6.56) in order to express the exciton–exciton interaction in the resonant approximation. The exciton–photon coupling is not included here, however the resonant approximation means that the two–polariton states are resonant with a bipolariton. Denoting the harmonic term of the Hamiltonian of two–particle states $\hat{H}_{\mathrm{E2}}$, we may write:

$$\begin{aligned}
&\hat{H}_{\mathrm{E2}} + \frac{1}{2\Omega}\sum_{\boldsymbol{k}\boldsymbol{k}'\boldsymbol{q}} W(\boldsymbol{q},\boldsymbol{k}-\boldsymbol{k}')\hat{B}^+_{\boldsymbol{k}+\boldsymbol{q}}\hat{B}^+_{\boldsymbol{k}'-\boldsymbol{q}}\hat{B}_{\boldsymbol{k}}\hat{B}_{\boldsymbol{k}'} \approx \\
&\quad\approx \sum_{\boldsymbol{K}} \varepsilon^m_{\boldsymbol{K}}\tilde{A}^+_{\boldsymbol{K}}\tilde{A}_{\boldsymbol{K}} + (E_{\boldsymbol{k}'_1}+E_{\boldsymbol{k}'_2})\hat{B}^+_{\boldsymbol{k}'_1}\hat{B}^+_{\boldsymbol{k}'_2}\hat{B}_{\boldsymbol{k}'_1}\hat{B}_{\boldsymbol{k}'_2} + \\
&\quad+(E_{\boldsymbol{k}'_3}+E_{\boldsymbol{k}'_4})\hat{B}^+_{\boldsymbol{k}'_3}\hat{B}^+_{\boldsymbol{k}'_4}\hat{B}_{\boldsymbol{k}'_3}\hat{B}_{\boldsymbol{k}'_4} + \\
&\quad+\frac{W(0,0)}{\Omega}\left[\hat{B}^+_{\boldsymbol{k}'_1}\hat{B}^+_{\boldsymbol{k}'_2}\hat{B}_{\boldsymbol{k}'_1}\hat{B}_{\boldsymbol{k}'_2} + \hat{B}^+_{\boldsymbol{k}'_3}\hat{B}^+_{\boldsymbol{k}'_4}\hat{B}_{\boldsymbol{k}'_3}\hat{B}_{\boldsymbol{k}'_4}\right] + \\
&\quad+\Big[\frac{M_2(\boldsymbol{k}'_1-\boldsymbol{k}'_2)}{\sqrt{\Omega}}\tilde{A}^+_{\boldsymbol{k}'_1+\boldsymbol{k}'_2}\hat{B}_{\boldsymbol{k}'_1}\hat{B}_{\boldsymbol{k}'_2} + \frac{M_2(\boldsymbol{k}'_3-\boldsymbol{k}'_4)}{\sqrt{\Omega}}\tilde{A}^+_{\boldsymbol{k}'_3+\boldsymbol{k}'_4}\hat{B}_{\boldsymbol{k}'_3}\hat{B}_{\boldsymbol{k}'_4} + H.c.\Big] + \\
&\quad+\frac{1}{2\Omega}\Big\{[W(\boldsymbol{k}'_1-\boldsymbol{k}'_3,\boldsymbol{k}'_3-\boldsymbol{k}'_4) + W(\boldsymbol{k}'_1-\boldsymbol{k}'_4,\boldsymbol{k}'_3-\boldsymbol{k}'_4)]\cdot \\
&\qquad\qquad\cdot\delta(\boldsymbol{k}'_1+\boldsymbol{k}'_2-\boldsymbol{k}'_3-\boldsymbol{k}'_4)\hat{B}^+_{\boldsymbol{k}'_1}\hat{B}^+_{\boldsymbol{k}'_2}\hat{B}_{\boldsymbol{k}'_3}\hat{B}_{\boldsymbol{k}'_4} + H.c.\Big\}, \qquad (6.58)
\end{aligned}$$

where $\varepsilon^m_{\boldsymbol{K}}$ denotes the energy of a bipolariton and $E_{\boldsymbol{k}}$ the energy of an exciton. The scattering strength $W(\boldsymbol{q},\boldsymbol{k})$ is defined as $W(\boldsymbol{q},\boldsymbol{k}) = V_x(\boldsymbol{q},\boldsymbol{k}) + V_d(\boldsymbol{q},\boldsymbol{k})$ and we do not approximate $\boldsymbol{q},\boldsymbol{k} \approx 0$ at this point since the exchanged momentum can be arbitrary in this Hamiltonian. M_2 is the coupling strength between a two–exciton state and the bipolariton given by [93]:

$$M_2(\boldsymbol{k}) = \sum_{\boldsymbol{q}} W(\boldsymbol{q})\Psi^{(0)}_{\mathrm{m}}(\boldsymbol{k}/2-\boldsymbol{q}). \quad (6.59)$$

The first term on right-hand side of (6.58) stands for the energy of bipolaritons and the second and the third term for the energies of the remaining two–exciton states. The first three terms then give the energy of the two–exciton states which are dominant in the optical response when the sample is excited resonantly with the bipolariton state. The fourth term describes the energy change of two–exciton states caused by the self–interaction — we do not consider this energy renormalization in the following since its influence on the FWM signal is negligible. The fifth term stands for the bipolariton creation and the last term describes direct scattering from the initial to the final state without interplay of the bipolariton. In the resonance with bipolariton, the last term may be neglected because the

bipolariton–mediated scattering is usually much stronger than the direct exciton–exciton scattering. The interaction Hamiltonian may be written in the polariton picture:

$$\hat{H}_{\mathrm{SB}} = \sum_{\Gamma_{\mathrm{m}}} \sum_{S,S'} \Big[\chi_S(\boldsymbol{k}_1') \chi_{S'}(\boldsymbol{k}_2') \mathbf{M}_2(\Gamma_{\mathrm{m}}, S, S') \tilde{A}^+_{\Gamma_{\mathrm{m}}, \boldsymbol{k}_1'+\boldsymbol{k}_2'} \hat{P}_{S,\boldsymbol{k}_1'} \hat{P}_{S,\boldsymbol{k}_2'} + \\ + \chi_S(\boldsymbol{k}_3') \chi_{S'}(\boldsymbol{k}_4') \mathbf{M}_2(\Gamma_{\mathrm{m}}, S, S') \tilde{A}^+_{\Gamma_{\mathrm{m}}, \boldsymbol{k}_3'+\boldsymbol{k}_4'} \hat{P}_{S,\boldsymbol{k}_3'} \hat{P}_{S,\boldsymbol{k}_4'} \Big] + H.c.\,, \tag{6.60}$$

where the spin was taken explicitly into account and I defined, assuming nearly parallel excitation beams:

$$\mathbf{M}_2(\Gamma_m, S_1, S_2) = \frac{M_2(0)}{\sqrt{\Omega}} \langle \Gamma_m | \, S_1, S_2 \rangle \ . \tag{6.61}$$

The subscript of the bipolariton operators distinguishes between bipolaritons in their ground states having various symmetries. The Hamiltonian (6.60) clearly shows the dynamics of the bipolariton creation [38]. First, bare two–polariton states are created e.g. by optical pumping. Coulomb interaction between the two polaritons causes their mutual scattering and creation of the bipolariton wavefunction as a consequence of the attractive nature of the polariton–polariton interaction. There exists an inverse process to the bipolariton creation: spontaneous annihilation. This process is responsible for bipolariton luminescence as verified experimentally [95, 96, 97]. The creation and annihilation of bipolariton may be seen as the following process:

$$\gamma(\boldsymbol{k}_1')+\gamma(\boldsymbol{k}_2') \rightarrow p(\boldsymbol{k}_1')+p(\boldsymbol{k}_2') \rightarrow m(\boldsymbol{k}_1'+\boldsymbol{k}_2'=\boldsymbol{k}_3'+\boldsymbol{k}_4') \rightarrow p(\boldsymbol{k}_3')+p(\boldsymbol{k}_4') \rightarrow \gamma(\boldsymbol{k}_3')+\gamma(\boldsymbol{k}_4')\,.$$

The letter m stands for the bipolariton. It is clear that the bipolariton wavefunction is not created immediately after optical pumping but its creation is a progressive process which continues until the population of the initial two–polariton states is completely relaxed. Bipolariton population therefore increases in time after optical pumping as shown experimentally [35]. This dynamics of bipolaritons has a big influence on the dynamics of the FWM response: since the biexciton creation is immediate in the GOS model, the biexciton response is instantaneous in OBE–like models [2]. Considering the bipolariton model, the response is not instantaneous since the bipolariton creation is not an instantaneous process.

6.6 Relaxation and dephasing rates

In the preceding sections of this chapter, all interactions, which must be taken into account when describing four–wave mixing experiments on semiconductors, were discussed and the appropriate Hamiltonians were derived. One may therefore easily derive equations of motion for the coherences which then lead to the FWM response. However, incoherent processes cause dephasing and relaxation of particles in realistic systems and these processes are not included in the Hamiltonian. Dephasing and relaxation terms then may be included phenomenologically. In this section, I discuss all dephasing and relaxation rates which will be subsequently added to the equations of motion in the next section.

Relaxation is an incoherent loss of population of a quantum–mechanical state accompanied by an increase of population of another state. The underlying mechanism is a spontaneous transition (from the point of view of the considered interactions) of a particle from one state to another. Dephasing is, on the contrary, a process which causes loss of a coherence of the type $\varrho_{j\ell}$ even if the populations ϱ_{jj} and $\varrho_{\ell\ell}$ are constant. Dephasing is driven by the loss of the aforementioned populations as shown in Eq. (2.59) and also by the loss of the correlations between the phases of the states $|j\rangle$ and $|\ell\rangle$ as shown in (2.50).

The rates will be demonstrated on an OBE–like scheme in order to illustratively show which types of rates contribute to the dynamics. Let's consider a scheme similar to the "O" scheme discussed in section 5.2 with an additional bipolariton level and two–polariton levels (see Fig. 6.5). The level scheme in Fig. 6.5 is similar to the scheme of the model which will be discussed in detail in the next section. Levels represent polariton and bipolariton states (wavepackets) denoted by spin and central wave vector (see section 6.2 for details). Since polaritons form a continuum in energy, all levels with energies from 0 to E^{X} should be essentially included in the scheme. As shown in section 6.2, the decisive part of the FWM signal may be described using states resonant with excitons and bipolaritons. Therefore I consider the ground state $|0\rangle$, the exciton–like one–polariton states $|\pm\rangle$, the exciton–like two–polariton state $|+-\rangle$[3], a two–polariton state resonant with bipolariton $|+-'\rangle$ and the bipolariton state $|m\rangle$.

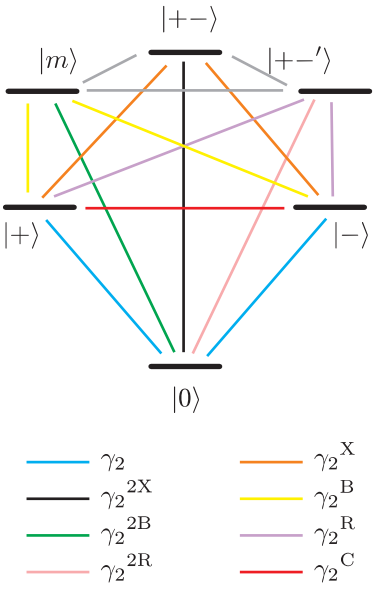

Figure 6.5: Sketch of all possible dephasing rates. Rates denoted by gray lines do not act in the model.

All relaxation and dephasing rates may be found in Fig, 6.5 by connecting all pairs of levels by lines and assigning a dephasing and a relaxation rate to every line. The lines which connect the levels $|j\rangle$ and $|\ell\rangle$ then shows dephasing of the coherences $\varrho_{j\ell}$ and $\varrho_{\ell j}$ and relaxation from the state $|j\rangle$ to the state $|\ell\rangle$ or vice versa. In the model, relaxation and dephasing rates are considered to not depend on the exciton spin, i.e. the rates connected with the '+' exciton are equal to the rates connected with the '−' exciton. We may therefore assign only one relaxation rate to both processes of relaxation from e.g. $|+\rangle$ to $|0\rangle$ and from $|-\rangle$ to $|0\rangle$. Further reduction of the number of considered rates is described in the following. Concerning relaxation processes, equations of motion involve many terms. Equation of motion for the population of the state $|+\rangle$ reads:

$$\partial_t \varrho_{+,+} = -\gamma_{1,1}\varrho_{+,+} - \gamma_{1,2}(\varrho_{+,+} - \varrho_{-,-}) + \gamma_{1,3}\varrho_{m,m} + \gamma_{1,4}\varrho_{+-,+-} + \gamma_{1,5}\varrho_{+-',+-'} \,. \tag{6.62}$$

The constants $\gamma_{1,1-5}$ are the phenomenological relaxation rates. The population of the ground state does not decay but, on the contrary, it increases in time since it is the state with the lowest energy and therefore it is the final state for relaxation from other (excited) states. Due to $\mathrm{Tr}\varrho = 1$, the equation of motion reads:

$$\partial_t \varrho_{0,0} = \gamma_{1,1}(\varrho_{+,+} + \varrho_{-,-}) + \dots \,, \tag{6.63}$$

where the terms which would follow the equation come from two–particle states.

In the following text, the rates with subscript '1' will be used for relaxation rates and rates with subscript '2' refer to dephasing rates. Decay of coherences are expressed simply by the equations of type:

$$\partial_t \varrho_{+-,+} = -\gamma_2^{\mathrm{X}} \varrho_{+-,+} \,. \tag{6.64}$$

The dephasing and relaxation rates determine unambiguously the dynamics of the loss of populations and coherences, however it is sometimes convenient to define associated

[3] There should be also states $|\pm\pm\rangle$ in the scheme due to Bose statistics of polaritons. However, these states are not important for the discussion of dephasing and relaxation rates and therefore they are omitted here.

constants to the rates — time constants. The definition of relaxation and dephasing times is $T = \gamma^{-1}$ with appropriate indices. Relaxation time is then the time after which the coherence or population decays to the 1/e of the initial value.

Looking at Fig. 6.5, we find that there may be in principle defined many dephasing and relaxation rates which describe the incoherent dynamics of the considered system. The aim of the following discussion is then to select only the rates which contribute to the dynamics of the third–order response. I show the relations between several rates and at the end, I give an estimate of the magnitudes of the rates.

Recalling the principle of the perturbative solution of OBE (2.72)–(2.74) and (2.75)–(2.77) which is common for all level schemes, clearly only the zero–order and second–order populations contribute to the third–order response. The only zero–order term is the initial population of the ground state which is stationary and therefore only dynamics of the second–order populations must be described. Eq. (6.62) then reduces to:

$$\partial_t \varrho^{(2)}_{+,+} = -\gamma_{1,1}\varrho^{(2)}_{+,+} + \gamma_{1,2}\varrho^{(2)}_{-,-} \,. \tag{6.65}$$

The two–particle populations are of the fourth and higher order and clearly do not contribute. The dynamics of the ground state is then described by (6.63) without the terms denoted by the dots. The aforementioned relaxation rates $\gamma_{1,1-2}$ will not be present in the equations of motion for the FWM response due to a special structure of the model. They contribute, on the other hand, in description of e.g. pump and probe experiments which is this model applicable to as noted above.

Concerning dephasing rates, we choose only the rates which may be assigned to coherences which contribute to the FWM response. Clearly coherences between two–particle states do not contribute to the third–order response since these coherences are at least of the fourth order in amplitude of optical field. All other coherences play a role in the dynamics of the FWM response as denoted in Fig. 6.5 by color lines. Considering the symmetry with respect to spin, we resolve eight types of coherences and therefore eight different dephasing times.

There are four zero–photon coherences in the model, i.e. coherences between the states with the same number of polaritons. Indeed, only the spin coherence $\varrho_{+,-}$ contributes to the third–order signal and therefore we do not take other coherences into account. Decay of the spin coherence is then described by the decay rate γ_2^{C}. There are four types of one–photon coherences to which we assign the following dephasing rates: γ_2 to $\varrho_{\pm,0}$, γ_2^{X} to $\varrho_{+-,\pm}$, γ_2^{B} to $\varrho_{m,\pm}$ and γ_2^{R} to $\varrho_{+-',\pm}$. There are three two–photon coherences, each of them associated with a dephasing rate: $\varrho_{+-,0}$ is associated with the rate $\gamma_2^{2\mathrm{X}}$, $\varrho_{+-',0}$ with $\gamma_2^{2\mathrm{R}}$ and $\varrho_{m,0}$ with $\gamma_2^{2\mathrm{B}}$.

One may estimate the values of the relaxation and dephasing times. Concerning relaxation times, they are usually of the order of 100 ps–10 ns. Dephasing times are, nevertheless, much shorter since coherences are sensitive to phases of the relevant states while populations do not reflect them as shown in section 2.3. The spin coherence of the type $\varrho_{+,-}$ is an exception — it is sensitive to the phases of the respective particle states, however these phases are highly correlated and therefore the dephasing time of the spin coherence γ_2^{C} is of the order comparable to the population relaxation time. We can do an upper estimate for the dephasing time using (2.50) and we get $T_2^{\mathrm{C}} \leq T_1^{\mathrm{X}}$. Using (2.50) and (2.59), the upper limit for dephasing time of one–photon coherences is $T_2 \leq 2T_1^{\mathrm{X}}$. For a better estimate, one writes:

$$\frac{1}{T_2} = \frac{1}{T_2^*} + \frac{1}{2T_1^{\mathrm{X}}} + \frac{1}{T_2^{\mathrm{inh}}}\,, \tag{6.66}$$

where T_2^* is the *pure dephasing* which comes from the processes which destroy the phase correlations between the states without population relaxation and T_2^{inh} is an effective dephasing caused by inhomogeneity of the system — the process is similar to the fast decay of the overall polarization in optical Bloch equations. Pure dephasing processes are usually much faster than population relaxation and therefore $T_1^{\mathrm{X}} \gg T_2 \approx 100$ fs–1 ps. Dephasing time of one–photon coherences connected with two–polariton states may differ considerably from the dephasing time T_2. This property may be illustrated in (6.66): due to scattering of two–polariton states, relaxation rate of their population is increased and therefore $T_2^{\mathrm{X}} < T_2$. There is no other dephasing process of the coherences $\varrho_{+-,\pm}$ and under assumption of weak polariton–polariton interaction, we may put $T_2^{\mathrm{X}} \approx T_2$. Bipolaritons are relatively stable particles and therefore we may consider also $T_2^{\mathrm{B}} \gtrsim T_2$. Population of the two–polariton state, which is not exciton–like ($|+-'\rangle$), relaxes rapidly due to radiative decay. Using (6.66), we find $T_2^{\mathrm{R}} < T_2$ and the difference may be in orders of magnitude. However, we cannot do a better estimate since the ratio of the dephasing times is sample–dependent. Decay of the two–photon coherences may be estimated by the inequality:

$$T_2^{\mathrm{2B}} \gg T_2^{\mathrm{X}} > 2T_2^{\mathrm{2X}} > 2T_2^{\mathrm{2R}}\,, \tag{6.67}$$

where the first inequality arises due to the stability of the bipolariton state. This dephasing time may be of the order of 10 ps. The decay time T_2^{2R} is again sample–dependent and may vary between tens of fs and units of picoseconds.

The aforementioned set of relaxation and dephasing rates may be arbitrarily modified and more rates may be introduced as an extension of the particular model presented in this chapter. One may e.g. consider that relaxation and dephasing rates depend on exciton spin.

6.7 Derivation of simplified equations of motion

I derived the effective Hamiltonian of the problem in the preceding sections. The total Hamiltonian then reads:

$$\hat{H}_{\mathrm{tot}} = \sum_{\boldsymbol{k}} \sum_{S,S'} h_{SS'\boldsymbol{k}} \hat{P}^+_{S,\boldsymbol{k}} \hat{P}_{S',\boldsymbol{k}} + \hat{H}_{\mathrm{DL}} + \hat{H}_{\mathrm{DN}} + \hat{H}_{\mathrm{SD}} + \hat{H}_{\mathrm{SB}}\,. \tag{6.68}$$

The particular parts of the Hamiltonian may be found in (6.18), (6.44), (6.50) and (6.60). The first term is the harmonic term which allows spin–flip processes with the assumption of wave vector conservation. The other terms describe the photon–polariton coupling and polariton–polariton interactions. Note that the term $\hat{H}_{\mathrm{SB}}$ acts only on two–polariton states resonant with the bipolariton state.

Derivation of equations of motion for the coherences of the type [4] $\langle \hat{O} \rangle = \langle \hat{P}^+_{\boldsymbol{k}} \cdots \hat{P}_{\boldsymbol{q}} \cdots \rangle$ is straightforward using the equation:

$$i\hbar \frac{\partial}{\partial t} \langle \hat{O} \rangle = \langle [\hat{O}, \hat{H}] \rangle\,. \tag{6.69}$$

[4] The averaging means here the quantum–mechanical mean value and ensemble averaging over the system. This averaging was denoted as $\langle\!\langle \cdots \rangle\!\rangle$, I will use the expression $\langle \cdots \rangle$ in the following since every averaging will be performed over the whole system.

The derived equations would then form an infinite system, however the goal of the theory is to derive simple equations which may be visualized by a few–level scheme similarly to OBE. In order to get a closed set of equations for a limited number of functions (coherences and populations), one must perform some simplifications. These simplification are described in the following subsections and they will be:

- Truncation of the scheme.
- Considering of Coulomb interaction as the first–order perturbation.
- Reduction of the number of states resolved by wave vector.

6.7.1 Truncation of the scheme

Equations of motion derived from the Hamiltonian (6.68) may be resolved by the number of polariton operators which are in the mean value on left hand side. According to microscopic theories, we may speak about one–polariton correlation functions of the form $\langle \hat{P}_{S,\boldsymbol{k}} \rangle$, two–polariton correlation functions $\langle \hat{P}_{S,\boldsymbol{K}} \hat{P}_{S',\boldsymbol{k}'} \rangle$, $\langle \hat{P}^+_{S,\boldsymbol{k}} \hat{P}_{S',\boldsymbol{k}'} \rangle$ and $\langle \hat{A}_{\Gamma,\boldsymbol{K}} \rangle$ etc. These correlation functions refer to two–particle[5] and four–particle correlation functions, respectively, in the microscopic theories (see chapter 4). It may be shown from equations of motion that correlation functions up to an infinite order in the number of particles contribute to the FWM signal due to coupling of m–particle correlation functions to $(m+2)$–particle correlation functions via Coulomb interaction. The aim of truncation is then elimination of the functions with high number of particles.

In microscopic theories, one uses the standard dynamical truncation scheme for the purpose of elimination of correlation functions with a high number of particles [5, 70, 71]. According to weakly interacting boson model [77], one may use, on the contrary, the density matrix formalism instead and this is the way how the scheme will be truncated in the presented theory. Instead of writing equations of motion for correlation functions of the type e.g. $\langle \hat{P}^+_{S_1,\boldsymbol{k}_1} \hat{P}^+_{S_2,\boldsymbol{k}_2} \rangle$, we use equations of motion for density matrix defined for m–particle states for m up to 2. Use of these equations of motion is clarified by the use of (2.37):

$$\varrho_{S_1\boldsymbol{k}_1,S_2\boldsymbol{k}_2} = \left\langle \hat{B}^+_{S_1,\boldsymbol{k}_1} \hat{B}^+_{S_2,\boldsymbol{k}_2} \right\rangle - \sum_S \sum_{\boldsymbol{k}} \left\langle \hat{B}^+_{S_1,\boldsymbol{k}_1} \hat{B}^+_{S_2,\boldsymbol{k}_2} \hat{B}^+_{S,\boldsymbol{k}} \hat{B}_{S,\boldsymbol{k}} \right\rangle . \tag{6.70}$$

Using the above definition, it may be shown that m–particle correlation functions are coupled in the density matrix formalism to m–particle correlation functions and therefore the set of equations, without considering dipole interaction, is closed for a fixed number of excited polaritons.

To conclude the above discussion, evolution of the system is described by the density matrix $\varrho(t)$, $\varrho(t{=}0) = |0\rangle\langle 0|$, i.e. only the population $\varrho_{0,0} = 1$ is nonzero at $t = 0$, other density matrix elements are zero. Electromagnetic field creates one–photon coherences of one–polariton states with respect to the ground state in the first order of perturbation theory. In the second order, one–polariton populations and two–photon coherences are created. At most three-photon coherences (i.e. correlations of the three–polariton states with respect to the ground state) may created after arrival of the last pulse, however these coherences are not coupled to electromagnetic field in the first order of the field amplitude, i.e. they do not contribute to the third–order response. We may therefore omit the influence of three– and higher–polariton states in equations of motion.

[5] In order to use the correct terminology and distinguish electrons and holes from polaritons, I use the term *particles* for fermions and polaritons for (bosonic) polaritons. Two–polariton correlation function is the four–particle correlation function.

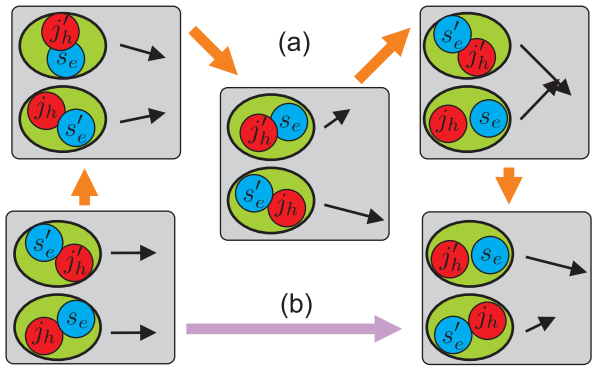

Figure 6.6: Multi–step (a) and one—step (b) scattering processes which lead from a defined initial state to another defined final state. Black lines denote wave vectors of excitons (green ellipses).

6.7.2 Coulomb interaction

Coulomb interaction causes difficulties in the model since it acts continually on two–polariton states and therefore the scattering from the pair $|S\boldsymbol{k}_1, S'\boldsymbol{k}_2\rangle$[6] involves the first–order scattering $|S\boldsymbol{k}_1, S'\boldsymbol{k}_2\rangle \rightarrow |\Sigma\boldsymbol{k}_3, \Sigma'\boldsymbol{k}_4\rangle$, a second–order process $|S\boldsymbol{k}_1, S'\boldsymbol{k}_2\rangle \rightarrow \rightarrow |\sigma\boldsymbol{k}, \sigma'\boldsymbol{k}'\rangle \rightarrow |\Sigma\boldsymbol{k}_3, \Sigma'\boldsymbol{k}_4\rangle$ and higher–order processes (see Fig. 6.6). However, we may consider that the polariton–polariton interaction is sufficiently weak (due to electric neutrality of polaritons) and we may therefore assume that higher–order processes do not considerably contribute to the scattering. The only case, when the Coulomb interaction must be taken into account up to higher orders, is the bipolariton effect.

I clarify this consideration by the following idea. Excitons are electrically neutral particles and therefore their mutual interaction is much weaker at high distances than monopole–monopole Coulomb interaction [10]. Considering scattering of exciton–like polaritons, they have high kinetic energy and they spatially separate immediately after exchange of some momentum and the first–order approximation is reasonable (we use the Hamiltonian $\hat{H}_{\mathrm{SD}}$ (6.50)). At bipolariton energy, polaritons spatially separate if the interaction is repulsive and they form a bound object if the interaction is attractive. Therefore we may use the first–order approximation for the former and we use the bipolariton model for the latter. The repulsive interaction is, however, neglected in the following due to fast decay of the coherence of the initial two–polariton state. Attractive interaction, on the contrary, effectively enhances the strength of the effective scattering process which becomes then important and we use the Hamiltonian $\hat{H}_{\mathrm{SB}}$ (6.60) for its description. It is important to emphasize that the perturbative description of the coupling of two–polariton states to the bipolariton state doesn't corrupt subsequent scattering events, it means that the influence of the initial and final state on the scattering dynamics is negligible. This statement is true due to high directionality of the incident fields and therefore due to localization of the initial and final states in reciprocal space.

6.7.3 Reduction of the number of states

Although the number of equations of motion was considerably reduced by assumption of the third–order response and by truncation of the considered coherences at two–particle states, the number of states involved in equations of motion is still infinite. Equations of motion couple states with all possible wave vectors and energies (note that polaritons form a continuum in energy).

[6] I use this short notation for the two–polariton state $\hat{P}^{+}_{S,\boldsymbol{k}_1}\hat{P}^{+}_{S',\boldsymbol{k}_2}|0\rangle$. It may be shortened to $|\boldsymbol{k}_1, \boldsymbol{k}_2\rangle$ when the spin is omitted.

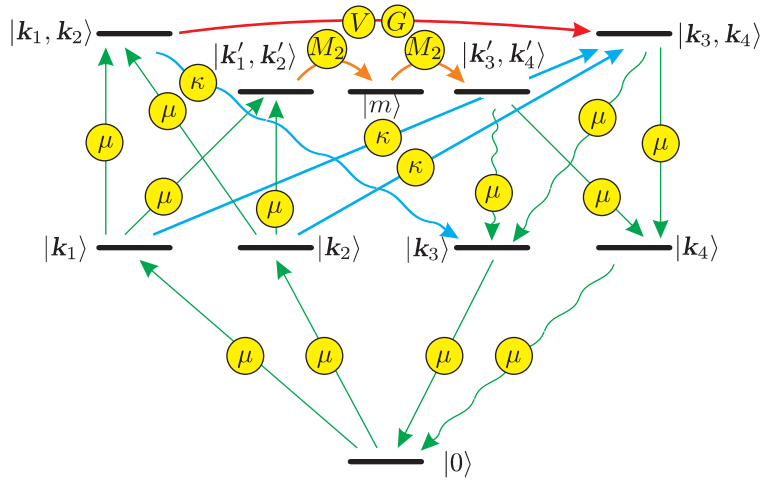

Figure 6.7: Level scheme which represents the model. Black lines represent considered states, green lines are linear dipole interactions. Other lines represent wave mixing processes: blue lines represent the diffraction channel, orange lines the bipolariton channel and red line the direct channel.

I discuss in section 6.2 how to overcome the problem of the polariton continuum: the spectrum of incoming pulses may be divided into parts and each of them may be then represented by a polariton state described by some central wave vector and energy. The more states are used, the more precise the model is, however the more complex calculations are. The aim of this thesis is to develop a model capable of description of the dynamics of polarization of the FWM signal. It is therefore not necessary to describe the dynamics of the states over the whole wide excitation spectrum and one may choose the most important contributions. As shown in section 6.2, the decisive contribution to the FWM signal comes from exciton–like polaritons and bipolaritons.

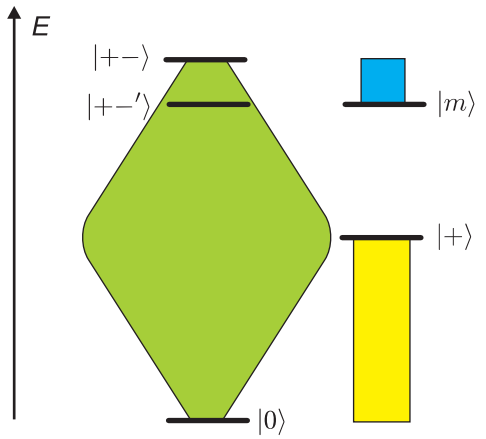

Figure 6.8: Sketch of available one–polariton (yellow), two–polariton (green) and bipolariton (blue) states. The width of the green field represents number of available states at the given energy. Black lines then stand for the states considered in the model.

Concerning one–polariton states, I take into account only the exciton–like one–polariton states with all possible spins. I choose also all exciton–like two–polariton states which are products of pairs of exciton–like one–polariton states. Then I consider bipolariton states with all possible spins. These bipolaritons are resonantly coupled to two–polariton states which are not exciton–like and therefore we must take these two–polariton states into account. There are, however, many two–polariton states which fulfill the resonant condition for coupling to a bipolariton. I approximate the full group of two–polariton states by one state with an effective dephasing rate and coupling coefficient. In order to simplify the calculation of effective coefficients, I take their values as if the polaritons in the two–polariton state had equal wave vectors. Besides the states coupled to bipolaritons, I take into account all states from the full 8×8 spin basis of two–polariton states.

The choice of the states described by the model is sketched in Fig. 6.8, wave vectors and spins are omitted for clarity. All possible states are depicted by yellow color (one–polariton states), green color (two–polariton states) and by blue color (bipolariton states). Width of the green column reflects the number of states with the energy depicted on the vertical axis. The chosen states are denoted by black horizontal lines. From bipolariton states, I select only the lowest lying state which resonantly couples to the optical field since other states cannot contribute to the FWM response due to wave vector conservation. The ensemble of two–polariton states resonant with bipolariton is approximated by one state with effective dephasing and coupling constants.

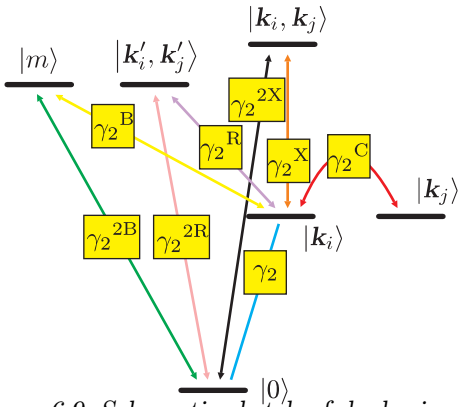

Figure 6.9: Schematic sketch of dephasing rates involved in the model and the coherences which they are related to.

Now the last stage of the reduction of the number of states may be undertaken. We are interested in the FWM response in the direction $\boldsymbol{k}_1+\boldsymbol{k}_2-\boldsymbol{k}_3$ created by excitation pulses with wave vectors $\boldsymbol{k}_1$, $\boldsymbol{k}_2$ and $\boldsymbol{k}_3$. Since the initial and final states are well defined, we may take into account in calculations only the states which are intermediate states of the system evolution between excitation and diffraction. Clearly the intermediate states are given by the wave vectors of the incoming fields and all states are sketched in the level scheme in Fig. 6.7. The states depicted in the Figure represent rather groups of states denoted by the wave vector: these groups contain polaritons with all possible combinations of spins. The notation $|\boldsymbol{q}, \boldsymbol{k}\rangle$ is then used in order to denote the exciton–like two–polariton state in which the particular polaritons have wave vectors $\boldsymbol{q}$ and $\boldsymbol{k}$, respectively, and all possible combinations of spins. The primed wave vectors $|\boldsymbol{q}', \boldsymbol{k}'\rangle$ have the meaning of the states which are coupled to the optical fields with wave vectors $\boldsymbol{k}$ and $\boldsymbol{q}$ and which are resonant with the bipolariton state. Reduction to only the states depicted in Fig. 6.7 is possible since we consider all interactions described by the Hamiltonian (6.68) in the first–order perturbation theory. Fig. 6.9 then illustrates dephasing rates involved in the model — the particular rates are assigned to coherences depicted as lines between appropriate states.

6.7.4 Equations of motion

The number of states was reduced in the preceding subsections to two– or less–particle states with wave vectors $\boldsymbol{k}_1$, $\boldsymbol{k}_2$, $\boldsymbol{k}_3$, $\boldsymbol{k}_4{=}\boldsymbol{k}_1{+}\boldsymbol{k}_2{-}\boldsymbol{k}_3$ and $\boldsymbol{k}_1{+}\boldsymbol{k}_2{=}\boldsymbol{k}_3{+}\boldsymbol{k}_4$ which are either exciton–like or resonant with bipolariton. In Fig. 6.7, we identify 10 groups of states containing 290 states denoted by wave vector and spin. It is then easy to define the density matrix and to write the Hamiltonian in the braket formalism:

$$
\begin{aligned}
\hat{H} = &\sum_{S\neq S'}\sum_{j=1}^{4} h_{SS'\boldsymbol{k}_j}\left|S'\boldsymbol{k}_j\middle\rangle\middle\langle S\boldsymbol{k}_j\right| + \sum_{\Gamma,\Gamma'} h_{\Gamma\Gamma'\boldsymbol{k}_1+\boldsymbol{k}_2}\left|\Gamma'\boldsymbol{k}_1{+}\boldsymbol{k}_2\middle\rangle\middle\langle\Gamma\boldsymbol{k}_1{+}\boldsymbol{k}_2\right| + \\
&+ \sum_{S_1,S_2}\sum_{S_3,S_4}\left[h_{S_1S_2,\boldsymbol{k}_1} + h_{S_3S_4,\boldsymbol{k}_2}\right]|S_2\boldsymbol{k}_1, S_4\boldsymbol{k}_2\rangle\langle S_1\boldsymbol{k}_1, S_3\boldsymbol{k}_2| + \\
&+ \sum_{S_1,S_2}\sum_{S_3,S_4}\left[h_{S_1S_2,\boldsymbol{k}_3} + h_{S_3S_4,\boldsymbol{k}_4}\right]|S_2\boldsymbol{k}_3, S_4\boldsymbol{k}_4\rangle\langle S_1\boldsymbol{k}_3, S_3\boldsymbol{k}_4| + \\
&+ \sum_{\boldsymbol{k}_1',\boldsymbol{k}_2'}\sum_{S_1,S_2}\sum_{S_3,S_4}\left[h_{S_1S_2,\boldsymbol{k}_1'} + h_{S_3S_4,\boldsymbol{k}_2'}\right]\left|S_2\boldsymbol{k}_1', S_4\boldsymbol{k}_2'\middle\rangle\middle\langle S_1\boldsymbol{k}_1', S_3\boldsymbol{k}_2'\right| + \\
&+ \sum_{\boldsymbol{k}_3',\boldsymbol{k}_4'}\sum_{S_1,S_2}\sum_{S_3,S_4}\left[h_{S_1S_2,\boldsymbol{k}_3'} + h_{S_3S_4,\boldsymbol{k}_4'}\right]\left|S_2\boldsymbol{k}_3', S_4\boldsymbol{k}_4'\middle\rangle\middle\langle S_1\boldsymbol{k}_3', S_3\boldsymbol{k}_4'\right| + \\
&+ \mathrm{i}\sum_{S}\mathcal{E}_{\boldsymbol{e}_1,\boldsymbol{K}_1}(t)\mathrm{e}^{-\mathrm{i}\omega_{\boldsymbol{K}_1}t}\mu_{S,\boldsymbol{K}_1}\langle S|\,\boldsymbol{e}_1\rangle\left[\,|S\boldsymbol{k}_1\rangle\langle 0| + \sum_{S'}\left|S\boldsymbol{k}_1, S'\boldsymbol{k}_2\middle\rangle\middle\langle S'\boldsymbol{k}_2\right|\right] + \\
&+ \mathrm{i}\sum_{S}\mathcal{E}_{\boldsymbol{e}_2,\boldsymbol{K}_2}(t)\mathrm{e}^{-\mathrm{i}\omega_{\boldsymbol{K}_2}t}\mu_{S,\boldsymbol{K}_2}\langle S|\,\boldsymbol{e}_2\rangle\left[\,|S\boldsymbol{k}_2\rangle\langle 0| + \sum_{S'}\left|S\boldsymbol{k}_2, S'\boldsymbol{k}_1\middle\rangle\middle\langle S'\boldsymbol{k}_1\right|\right] - \\
&- \mathrm{i}\sum_{S}\mathcal{E}^{*}_{\boldsymbol{e}_3,\boldsymbol{K}_3}(t)\mathrm{e}^{\mathrm{i}\omega_{\boldsymbol{K}_3}t}\mu_{S,\boldsymbol{K}_3}\langle\,\boldsymbol{e}_3|\,S\rangle\left[\,|0\rangle\langle S\boldsymbol{k}_3| + \sum_{S'}\left|S'\boldsymbol{k}_4\middle\rangle\middle\langle S\boldsymbol{k}_3, S'\boldsymbol{k}_4\right|\right] + \\
&+ \mathrm{i}\sum_{S}\mathcal{E}_{\boldsymbol{e}_1,\boldsymbol{K}_1}(t)\mathrm{e}^{-\mathrm{i}\omega_{\boldsymbol{K}_1}t}\kappa_{SS',\boldsymbol{K}_1}\langle S|\,\boldsymbol{e}_1\rangle\left[\,\left|S\boldsymbol{k}_3, S'\boldsymbol{k}_4\middle\rangle\middle\langle S'\boldsymbol{k}_2\right| + \left|S'\boldsymbol{k}_3, S\boldsymbol{k}_4\middle\rangle\middle\langle S'\boldsymbol{k}_2\right|\,\right] + \\
&+ \mathrm{i}\sum_{S}\mathcal{E}_{\boldsymbol{e}_2,\boldsymbol{K}_2}(t)\mathrm{e}^{-\mathrm{i}\omega_{\boldsymbol{K}_2}t}\kappa_{SS',\boldsymbol{K}_2}\langle S|\,\boldsymbol{e}_2\rangle\left[\,\left|S\boldsymbol{k}_3, S'\boldsymbol{k}_4\middle\rangle\middle\langle S'\boldsymbol{k}_1\right| + \left|S'\boldsymbol{k}_3, S\boldsymbol{k}_4\middle\rangle\middle\langle S'\boldsymbol{k}_1\right|\,\right] + \\
&+ \sum_{\boldsymbol{k}_1',\boldsymbol{k}_2'}\sum_{\Gamma}\sum_{S,S'}\delta^{\Gamma}_{S\boldsymbol{k}_1',S'\boldsymbol{k}_2'}\chi_S(\boldsymbol{k}_1')\chi_{S'}(\boldsymbol{k}_2')\mathbf{M}_2(\Gamma,S,S')\,|\Gamma\boldsymbol{k}_1{+}\boldsymbol{k}_2\rangle\langle S\boldsymbol{k}_1', S'\boldsymbol{k}_2'| + \\
&+ \sum_{\boldsymbol{k}_3',\boldsymbol{k}_4'}\sum_{\Gamma}\sum_{S,S'}\delta^{\Gamma}_{S\boldsymbol{k}_3',S'\boldsymbol{k}_4'}\chi_S(\boldsymbol{k}_3')\chi_{S'}(\boldsymbol{k}_4')\mathbf{M}^{*}_2(\Gamma,S,S')\left|S\boldsymbol{k}_3', S'\boldsymbol{k}_4'\middle\rangle\middle\langle\Gamma\boldsymbol{k}_1{+}\boldsymbol{k}_2\right| + \\
&+ \frac{1}{2}\sum_{S,S'}\chi_S(\boldsymbol{k}_2)[-G_{\mathrm{d}}(0,0)\phi_{S'}(\boldsymbol{k}_1) + V_{\mathrm{d}}(0,0)\chi_{S'}(\boldsymbol{k}_1)]\cdot \\
&\qquad\cdot\Big[\chi_S(\boldsymbol{k}_3)\chi_{S'}(\boldsymbol{k}_4)\left|S\boldsymbol{k}_3, S', \boldsymbol{k}_4\middle\rangle\middle\langle S'\boldsymbol{k}_1, S\boldsymbol{k}_2\right| + \\
&\qquad\qquad + \chi_S(\boldsymbol{k}_3)\chi_{S'}(\boldsymbol{k}_4)\left|S'\boldsymbol{k}_3, S, \boldsymbol{k}_4\middle\rangle\middle\langle S'\boldsymbol{k}_1, S\boldsymbol{k}_2\right|\Big] + \\
&+ \frac{1}{2}\sum_{j_h,s_e}\sum_{j_h',s_e'}\chi_{j_hs_e}(\boldsymbol{k}_2)[-G_{\mathrm{x}}(0,0)\phi_{j_h's_e'}(\boldsymbol{k}_1) + V_{\mathrm{x}}(0,0)\chi_{j_h's_e'}(\boldsymbol{k}_1)]\cdot \\
&\qquad\cdot\Big[\chi_{j_hs_e}(\boldsymbol{k}_3)\chi_{j_h's_e'}(\boldsymbol{k}_4)\left|j_hs_e\boldsymbol{k}_3, j_h's_e'\boldsymbol{k}_4\middle\rangle\middle\langle j_h's_e'\boldsymbol{k}_1, j_hs_e\boldsymbol{k}_2\right| + \\
&\qquad\qquad + \chi_{j_h's_e'}(\boldsymbol{k}_3)\chi_{j_hs_e}(\boldsymbol{k}_4)\left|j_h's_e'\boldsymbol{k}_3, j_hs_e\boldsymbol{k}_4\middle\rangle\middle\langle j_h's_e'\boldsymbol{k}_1, j_hs_e\boldsymbol{k}_2\right|\Big]\,. \qquad (6.71)
\end{aligned}
$$

One has generally more than one bipolariton state and thus more sets of states with primed wave vectors arise in the sums. They are then evaluated as follows. For every pair of polariton spins S, S' and a bipolariton spin Γ, there may exist a pair of effective wave vectors of polaritons $\boldsymbol{k}'_1, \boldsymbol{k}'_2$ such that the state $|S\boldsymbol{k}'_1, S'\boldsymbol{k}'_2\rangle$ is resonant with the bipolariton. Summation over pairs $\boldsymbol{k}'_1, \boldsymbol{k}'_2$ then goes over all two–polariton states which were found on the basis of the above statement. Function $\delta^{\Gamma}_{S\boldsymbol{k}'_1,S'\boldsymbol{k}'_2}$ is then one if the pair of wave vectors is assigned to the spins S, S' and Γ, otherwise it is zero.

Terms $h_{SS',\boldsymbol{k}}$ in (6.71) are the harmonic terms of polaritons. For $S = S'$, these terms determine energies of one–polariton states with spin S and wave vector $\boldsymbol{k}$. Nondiagonal terms for $S \neq S'$ then determine spin precession within the group of states with wave vector $\boldsymbol{k}$ — the element $h_{SS',\boldsymbol{k}}$ then defines coupling between the spins S and S'.

The first five lines in (6.71) are the harmonic terms of all states involved in the system reduced on the basis of thoughts discussed above. The next three terms stand for linear dipole coupling and the following two terms describe nonlinear dipole coupling, in particular the scattering on the crystal surface. The eleventh and twelfth term express formation and annihilation of bipolaritons and the last two terms stand for direct and exchange polariton–polariton scattering terms, respectively.

The level scheme appropriate for the reduced system of states with couplings denoted by arrows is depicted in Fig. 6.7. All coupling terms between the groups of states (denoted by wave vector) are shown and their strengths are depicted within the circles. According to the perturbational approach, arrows denote the directions in which the system evolves. The wavy lines denote radiation of photons in the FWM direction. Intensity of the FWM signal is then proportional to the appropriate coherences multiplied by assigned dipole momenta:

$$\begin{aligned} E^{(-)}_{\boldsymbol{k}_1+\boldsymbol{k}_2-\boldsymbol{k}_3}(t) \propto \sum_{S,\boldsymbol{e}} \boldsymbol{e}\,\langle \boldsymbol{e}|\, S\rangle \Bigg\{ & \mu_{S,\boldsymbol{K}_4}\Big[\varrho^{(3)}_{S\boldsymbol{k}_4,0}(t) + \sum_{S'} \varrho^{(3)}_{S'\boldsymbol{k}_3 S\boldsymbol{k}_4,S'\boldsymbol{k}_3}(t)\Big] + \\ & + \sum_{\boldsymbol{k}'_3,\boldsymbol{k}'_4} \mu_{S,\boldsymbol{K}_4} \sum_{S'} \varrho^{(3)}_{S'\boldsymbol{k}'_3 S\boldsymbol{k}_4,S'\boldsymbol{k}'_3}(t) + \\ & + \sum_{S'} \kappa_{SS',\boldsymbol{K}_4}\Big[\varrho^{(3)}_{S'\boldsymbol{k}_1 S\boldsymbol{k}_2,S'\boldsymbol{k}_3}(t) + \varrho^{(3)}_{S\boldsymbol{k}_1 S'\boldsymbol{k}_2,S'\boldsymbol{k}_3}(t)\Big]\Bigg\}. \end{aligned} \tag{6.72}$$

The first line describes radiation of photons resonant with exciton states, the second line stands for radiation of photons which come from the bipolariton annihilation. The last line then describes diffraction (nonlinear coupling) of photons on the output plane of the crystal. However, when considering an experiment in the reflection geometry, the last line should be substituted by the expression for the field reflected during coupling to the crystal according to (6.34) and (6.41)–(6.42).

6.8 Conclusions

In conclusion of this chapter, I stress the main point which we found to be essential for the model and also for a general description of FWM experiments. The existence of wave mixing in bulk semiconductor crystals is a consequence of the polariton–polariton interaction. Based on the nature of the interaction, we resolve three different channels denoted by the arrows which connect the two groups of states with wave vectors $\boldsymbol{k}_1$, $\boldsymbol{k}_2$ and $\boldsymbol{k}_3$, $\boldsymbol{k}_4$, respectively, in Fig. 6.7. Polariton–polariton interaction is, depending on the energy of their mutual motion, responsible for scattering of exciton–like polaritons and bipolariton–mediated scattering of polaritons resonant with the bipolariton. The former scattering channel is called the *direct channel* and the latter *bipolariton channel* in the following. The third wave mixing process occurs on the crystal boundary and it is due to partial Fermi character of polaritons — this effect is similar to the concept of transient grating and it will be denoted as *diffraction channel*. Each of the channels may be clearly resolved in (6.72) having its specific polarization selection rules.

Equations of motion directly follow from the Hamiltonian (6.71). I use the interaction picture and therefore the equation of motion (2.32). The density matrix in the interaction picture is denoted as $\tilde{\varrho}(t)$ and equations may be found in Appendix B.1.

In the following text, the validity of the used approach is checked and application of the model is shown.

Chapter 7

FWM on bulk materials: Results and discussion

7.1 Introduction

The previous chapter describes the method of derivation of equations of motion and the equations are established in its last section. The equations are derived on the basis of the scheme in Fig. 6.7 according to the arrows which connect particular levels — the arrows point from the source terms to the final states which are involved in equations (B.1)–(B.16). Equations therefore reveal the perturbative approach in which the system's evolution proceeds in one direction and interactions in the opposite direction with respect to the arrows are neglected.

In this section, I present a discussion of the model and some results from numerical calculations. The main point is a test whether the model is able to reproduce the phenomena experimentally observed on bulk semiconductors: polarization selection rules, temporal evolution of the signal, quantum beats and spectral profile of the FWM response. I show that the equations of motion are able to model all these features and therefore the presented model is believed to be sufficiently accurate.

Looking at Fig. 6.7 and Eqs. (B.1)–(B.16), one may construct a scenario of the FWM signal creation. This scenario may help in understanding the mechanism of wave mixing and FWM buildup and it is introduced in section 7.2. This discussion of wave mixing processes helps us to determine the FWM polarization selection rules in section 7.3 — dependence of the FWM polarization on the polarization of incoming pulses. In the next three sections, I discuss the dynamics of the model and its predictions from the point of view of time–resolved (TR–FWM, section 7.4), spectrally–resolved (SR–FWM, section 7.5) and time–integrated four–wave mixing (TI–FWM, section 7.6) experiments. I present simulations concerning various types of experiments and I give brief comments in the aforementioned sections. Concerning the obtained results, I compare the predictions of the model to experiments in section 7.7. This section is of a cardinal importance since I discuss whether the model is suitable for description of wave mixing on semiconductors.

The conclusion of the section 7.7 is, that the model is of a sufficient accuracy for our purposes and therefore I believe it may be used for description of bulk semiconductor crystals without action of external forces. One may, however, extend the model to lower–dimensional systems and systems under influence of external fields. The way, how the model may be extended, is presented in section 7.8. Section 7.9 then presents direct comparison of the results of the model to experimental data taken from literature. In the last section 7.10, I apply the model on a system in which the exciton states are coupled by a wave vector dependent interaction. I propose a method for direct measurement of these interactions which cause coherent spin–flip of particles and which were not yet measured using FWM.

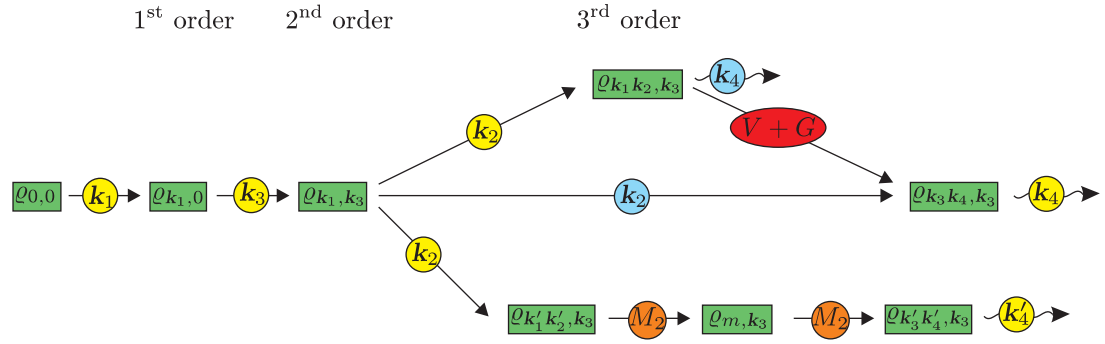

Figure 7.1: Sketch of the perturbative evolution of coherences in the model for $t_1 < t_3 < t_2$. Symbols in ellipses denote the types of coupling; the yellow circles stand for linear and blue circles for nonlinear dipole coupling.

7.2 Principle of wave mixing

7.2.1 Scenario of the wave mixing process

Excitons and polaritons are delocalized bosons and therefore, recalling the section 4.1, they give no wave mixing signal when they do not interact one with the other. Clearly particle–particle interactions are responsible for wave mixing [54, 69]. System of noninteracting bosons may be then drawn in a scheme according to Fig. 6.7 where the levels are connected only by green lines (dipole interactions). There is obviously no interconnection between the subsystem formed by states with wave vectors $\boldsymbol{k}_1$ and $\boldsymbol{k}_2$ and the subsystem of states with levels $\boldsymbol{k}_3$ and $\boldsymbol{k}_4$. The subsystems are interconnected by red, blue and orange lines which denote interactions which may cause wave mixing in the sample — these are the direct channel (red), the bipolariton channel (orange) and the diffraction channel (blue). The direct channel provides wave mixing through direct polariton–polariton scattering ("direct" means here one–step process without an intermediate state including direct and exchange Coulomb processes) — a two–polariton state may be scattered to another two–polariton state which then may belong to the second group of polaritons. The bipolariton channel mixes waves also by scattering, however multiple–step processes are allowed and the scattering is considered to be mediated by a bipolariton state. These two channels can be called *scattering channels* and the last, *diffraction channel*, provides wave mixing due to fractional Fermi character of polaritons.

The mechanism of wave mixing caused by direct or bipolariton–mediated scattering is identical, the two channels differ only by the dynamics (and polarization selection rules), however both provide an effective scattering from an initial state $|\boldsymbol{k}_1, \boldsymbol{k}_2\rangle$ or $|\boldsymbol{k}_1', \boldsymbol{k}_2'\rangle$ to a final state represented by other wave vectors. For the temporal order of excitation pulses $t_1, t_2 < t_3$ (these times denote times of arrival of pulses with wave vectors $\boldsymbol{K}_1$, $\boldsymbol{K}_2$ and $\boldsymbol{K}_3$, respectively), the scenario of wave mixing caused by scattering channels is as follows. The first two excitation pulses excite the crystal to the two–polariton state $|\boldsymbol{k}_1, \boldsymbol{k}_2\rangle$ or $|\boldsymbol{k}_1', \boldsymbol{k}_2'\rangle$. Since there are two polaritons in the crystal, they interact via Coulomb interaction and therefore they may exchange momentum and fermions (what leads to an effective spin exchange). The scattering process is continuous and leads to linear increase of populations in the states $|\boldsymbol{k}, \boldsymbol{q}\rangle$, $\boldsymbol{k} + \boldsymbol{q} = \boldsymbol{k}_1 + \boldsymbol{k}_2$ (the same property holds for the primed wave vectors). According to the wave vector conservation, also the state $|\boldsymbol{k}_3, \boldsymbol{k}_1 + \boldsymbol{k}_2 - \boldsymbol{k}_3\rangle$ becomes populated. After arrival of the last pulse with wave vector $\boldsymbol{K}_3$, light interacts with the

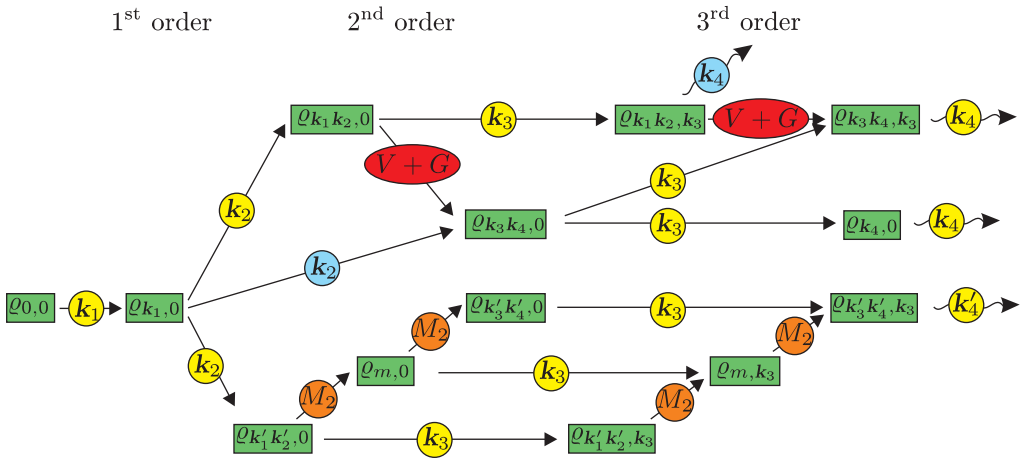

Figure 7.2: Sketch of the perturbative evolution of coherences in the model for $t_1 < t_2 < t_3$. Symbols in ellipses denote the types of coupling; the yellow circles stand for linear and blue circles for nonlinear dipole coupling.

polariton with wave vector $\boldsymbol{k}_3$ causing creation of a one–photon coherence in the direction $\boldsymbol{k}_1+\boldsymbol{k}_2-\boldsymbol{k}_3$ which is coupled to the output FWM field. Discussion of the temporal order e.g. $t_1 < t_3 < t_2$ is similar, however the field with wave vector $\boldsymbol{K}_3$ is "stored" in the coherence of the polariton $\boldsymbol{k}_3$ and when the two–polariton state $|\boldsymbol{k}_3, \boldsymbol{k}_4\rangle$ is created, this "stored" polariton acts like the outer electromagnetic field.

The mechanism of diffraction–induced wave mixing is quite different and it is rather similar to the processes in atomic systems. The FWM signal is created when the pulse with wave vector $\boldsymbol{K}_3$ doesn't arrive as the last one. Although the dynamics of the model allows creation of the diffraction–induced FWM signal for temporal order $t_1, t_2 < t_3$, it vanishes when $\gamma_2 = \gamma_2^{\mathrm{X}}$ since the last pulse creates one–photon coherences which have equal size but opposite phases and they cancel each other. This point is shown later when the equations of motion are solved perturbatively. Concerning the sequence of pulses when the pulse with wave vector $\boldsymbol{K}_2$ arrives as the last one, the first two pulses may create a diffraction grating (depending on their spins) which the last pulse diffracts on during coupling to polaritons on the crystal surface.

7.2.2 Perturbative solution of equations of motion: $t_1 < t_3 < t_2$

In this and the next subsections, equations of motion are solved perturbatively. Just for clarity, spin is not taken into account in the explicit solutions below, however it is considered in all later simulations. I use delta–like pulses which arrive in a definite time order. There are two principal temporal orderings of the pulses which may reveal quite different dynamics of the FWM signal: either the pulse with wave vector $\boldsymbol{K}_3$ arrives as the last one or not. All other time orders of arrivals of pulses induce very similar dynamics to one of the two cases which are mentioned in this and the next subsection. Here we investigate the case $t_1 < t_3 < t_2$ known from nanocrystals and atomic systems as the time order which produces FWM signal due to formation of a diffraction grating (in the interference pattern of the pulses with wave vectors $\boldsymbol{K}_1$ and $\boldsymbol{K}_3$, see Tab. 5.2). Evolution of coherences in the density matrix may be illustrated in a scheme known from chapter 5 — see Fig. 7.1. Let's denote:

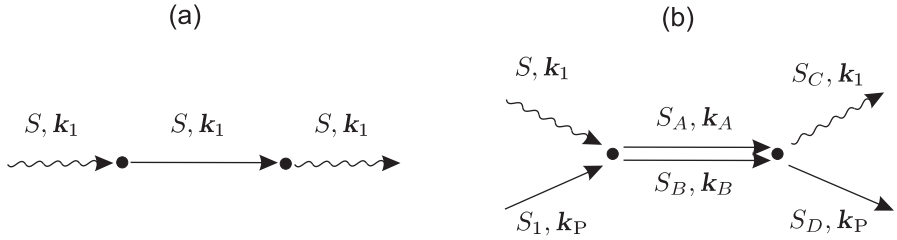

Figure 7.3: Feynman diagrams appropriate for the processes responsible for linear (a) and nonlinear (b) susceptibility. Arrows stand for polaritons and wavy lines for photons.

$$\mathcal{E}_{\boldsymbol{K}_j}(t) = \mathcal{E}_j \delta(t - t_j)\,, \qquad \omega_j = \omega_{\boldsymbol{K}_j}\,, \tag{7.1}$$

$$\omega_j^{\mathrm{X}} = h_{\boldsymbol{k}_j}/\hbar\,, \qquad \omega_{j'}^{\mathrm{X}} = h_{\boldsymbol{k}'_j}/\hbar\,, \tag{7.2}$$

$$\chi_j = \chi(\boldsymbol{k}_j)\,, \qquad \phi_j = \phi(\boldsymbol{k}_j)\,, \tag{7.3}$$

μ denote all linear dipole matrix elements and κ all nonlinear dipole matrix elements. Integrated equations of motion are then listed in Appendix B.2. Amplitude of the diffracted field yields, according to (6.72):

$$\begin{aligned} E^{(-)}_{\boldsymbol{k}_1+\boldsymbol{k}_2-\boldsymbol{k}_3} \propto \mu\tilde{\varrho}^{(3)}_{\boldsymbol{k}_3\boldsymbol{k}_4,\boldsymbol{k}_3}(t)\mathrm{e}^{-\mathrm{i}\omega_4^{\mathrm{X}}t}\mu\tilde{\varrho}^{(3)}_{\boldsymbol{k}_3\boldsymbol{k}'_4,\boldsymbol{k}_3}(t)\mathrm{e}^{-\mathrm{i}\omega_{4'}^{\mathrm{X}}t} + \\ + \kappa\tilde{\varrho}^{(3)}_{\boldsymbol{k}_1\boldsymbol{k}_2,\boldsymbol{k}_3}(t)\mathrm{e}^{-\mathrm{i}(\omega_1^{\mathrm{X}}+\omega_2^{\mathrm{X}}-\omega_3^{\mathrm{X}})t}\,. \end{aligned} \tag{7.4}$$

7.2.3 Perturbative solution of equations of motion: $t_1 < t_2 < t_3$

In this subsection, let's consider the temporal order of delta–like pulses $t_1 < t_2 < t_3$. The scheme of evolution of the system is depicted in Fig. 7.2. Equations of motion then give the temporal evolution of the system and may be found in Appendix B.3.

Coupling to the FWM field is the given by the formula:

$$\begin{aligned} E^{(-)}_{\boldsymbol{k}_1+\boldsymbol{k}_2-\boldsymbol{k}_3} \propto \mu\tilde{\varrho}^{(3)}_{\boldsymbol{k}_3\boldsymbol{k}_4,\boldsymbol{k}_3}(t)\mathrm{e}^{-\mathrm{i}\omega_4^{\mathrm{X}}t}\mu\tilde{\varrho}^{(3)}_{\boldsymbol{k}_3\boldsymbol{k}'_4,\boldsymbol{k}_3}(t)\mathrm{e}^{-\mathrm{i}\omega_{4'}^{\mathrm{X}}t} + \mu\tilde{\varrho}^{(3)}_{\boldsymbol{k}_4,0}(t)\mathrm{e}^{-\mathrm{i}\omega_4^{\mathrm{X}}t} \\ + \kappa\tilde{\varrho}^{(3)}_{\boldsymbol{k}_1\boldsymbol{k}_2,\boldsymbol{k}_3}(t)\mathrm{e}^{-\mathrm{i}(\omega_1^{\mathrm{X}}+\omega_2^{\mathrm{X}}-\omega_3^{\mathrm{X}})t}\,. \end{aligned} \tag{7.5}$$

7.3 FWM polarization selection rules

I investigate the dependence of the polarization of the FWM signal on polarizations of incoming fields in this section. The problem is very complex in general since the model, as described by equations of motion, may reveal very complex dynamics including various spin–flip mechanisms. It is possible to determine analytically polarization selection rules only in special cases when the Hamiltonian of spin precession may be diagonalized. In other cases, one needs numerical simulations, i.e. numerical solution of equations of motion using optical pulses with a realistic temporal profile.

In this section, I discuss the simplest cases of a bulk semiconductor without influence of external fields and without considering wave–vector dependent electron–hole exchange interaction. I consider zinc–blende and wurtzite crystal structures of the lattice. Concerning the wurtzite structure, only one of the exciton bands is taken into account (see section 3.2). There are therefore two dipole–active states in both cases and all other states are dipole–forbidden.

			zinc–blende		wurtzite	
$\boldsymbol{k}_1$	$\boldsymbol{k}_2$	$\boldsymbol{k}_3$	d	x	d	x
σ^+	σ^+	σ^+	σ^+	σ^+	σ^+	σ^+
σ^+	σ^+	σ^-	0	0	0	0
σ^+	σ^-	σ^+	0	0	0	0
σ^-	σ^+	σ^+	σ^-	σ^-	σ^-	0

			zinc–blende		wurtzite	
$\boldsymbol{k}_1$	$\boldsymbol{k}_2$	$\boldsymbol{k}_3$	d	x	d	x
X'	X'	X'	X'	X'	X'	X'
X'	X'	Y'	0	0	0	0
X'	Y'	X'	0	0	0	0
Y'	X'	X'	Y'	Y'	Y'	Y'

Table 7.1: Polarization selection rules of the diffraction channel for linear and circular polarizations in crystals with zinc–blende and wurtzite structure. The columns denoted as "d" stand for direct process and columns denoted "x" stand for exchange process. Symbols X' and Y' denote linear polarizations perpendicular one to the other, they have no fixed orientation with respect to crystallographic axes. The time order is $t_2 < t_3 < t_1$.

			zinc–blende		wurtzite	
$\boldsymbol{k}_1$	$\boldsymbol{k}_2$	$\boldsymbol{k}_3$	d	x	d	x
σ^+	σ^+	X'	σ^+	σ^+	σ^+	σ^+
σ^+	σ^-	X'	σ^+	σ^+	σ^+	0
σ^+	X'	σ^+	σ^+	σ^+	σ^+	σ^+
σ^+	X'	σ^-	σ^+	σ^+	σ^+	0
X'	σ^+	σ^+	X'	X'	X'	σ^+
X'	σ^+	σ^-	0	0	0	0

			zinc–blende		wurtzite	
$\boldsymbol{k}_1$	$\boldsymbol{k}_2$	$\boldsymbol{k}_3$	d	x	d	x
X'	X'	σ^+	X'	X'	X'	X'
X'	Y'	σ^+	X'	X'	X'	X'
X'	σ^+	X'	X'	X'	X'	X'
X'	σ^+	Y'	X'	X'	X'	X'
σ^+	X'	X'	σ^+	σ^+	σ^+	σ^+
σ^+	X'	Y'	0	0	0	0

Table 7.2: Polarization selection rules of the diffraction channel for linear and circular polarizations in crystals with zinc–blende and wurtzite structure. The columns denoted as "d" stand for direct process and columns denoted "x" stand for exchange process. Symbols X' and Y' denote linear polarizations perpendicular one to the other, they have no fixed orientation with respect to crystallographic axes. The time order is $t_2 < t_3 < t_1$.

As stated above, there are three channels responsible for wave mixing. It is therefore reasonable to separate the discussion of polarization selection rules for these three channels. Let's start discussion with the diffraction channel. The process responsible for the nonlinear susceptibility is depicted in the diagram in Fig. 7.3b. An incoming photon with spin S scatters with a polariton with spin S_1 to a two-polariton state with spins S_A and S_B. This two–polariton state then may scatter back to the direction of the incoming particles with spins S_C and S_D. If $S_C = S$, this process contributes to the nonlinear susceptibility and therefore the diffraction occurs for spins which involve the path:

$$S{+}S_1 \rightarrow S_A{+}S_B \rightarrow S{+}S_D\,. \tag{7.6}$$

For direct scattering processes (i.e. processes which conserve spins of particles), it is clear that $S_1 = S_D$. Exchange processes contribute to the nonlinear susceptibility when:

$$0 \neq \sum_{s_e,s'_e} \sum_{j_h,j'_h} \langle S|\, s_e j_h\rangle \left\langle S_D|\, s'_e j'_h\right\rangle \left\langle s'_e j_h\right|\, S\rangle \left\langle s_e j'_h\right|\, S_1\rangle\ . \tag{7.7}$$

The calculation of the right–hand side of the above inequality may be found in Tabs. 6.1–6.4. I performed calculations of dipole selection rules for optical beams with circular and linear polarizations for crystals with zinc–blende and wurtzite structure. Results are summarized in Tabs. 7.1–7.2.

The polarization selection rules for the diffraction path are developed and now I discuss the scattering paths. Consider that there are two degenerate dipole–inactive states and no spin–flip processes may occur. Clearly the field with any arbitrary polarization creates

polaritons with the same polarization — instead of drawing all spin states of polaritons in a scheme similar to Fig. 6.7, we may use the polarizations of excitation fields for polaritons with wave vectors $\boldsymbol{k}_1$, $\boldsymbol{k}_2$ and $\boldsymbol{k}_3$. For the polariton in the diffraction direction, it is necessary to use the states with orthogonal polarizations which couple to the electromagnetic field. The resulting scheme then consists of 13 levels and although dipole–active states may be excited by polariton–polariton scattering, they obviously do not contribute to the FWM signal and one may omit them.

It is clear that the spin mixing comes into play through the spin–dependence of the scattering processes. Imagine that two polaritons can scatter only if the spins are equal and the spins of incoming and outgoing polaritons are the same. In such a case, the FWM signal arises only when the projection of polarizations of all three incoming fields to one definite polarization is nonzero. Clearly the polarization selection rules come from the symmetries of the scattering matrices with respect to spins of incoming and outgoing particles. We may derive the appropriate equations for determination of the spin of the FWM signal:

$$\left|\psi^{\mathrm{D}}(\boldsymbol{k}_4)\right\rangle = \boldsymbol{P}_{\boldsymbol{k}_4} \sum_j \mathbf{W}(\alpha_j, \psi_3, \psi_1, \psi_2) \left|\alpha_j \boldsymbol{k}_4\right\rangle \,, \tag{7.8}$$

$$\left|\psi^{\mathrm{B}}(\boldsymbol{k}_4)\right\rangle = \boldsymbol{P}_{\boldsymbol{k}_4} \sum_j \mathbf{M}_2(\psi_1, \psi_2, \Gamma_s)\mathbf{M}_2^*(\alpha_j, \psi_3, \Gamma_s) \left|\alpha_j \boldsymbol{k}_4\right\rangle \,, \tag{7.9}$$

where $\boldsymbol{P}_{\boldsymbol{k}_4}$ is an operator of the spin projection on the polarization of optical field and summation goes over all spin states denoted as α_j. Functions $\psi_{1,2,3}$ denote spins of the respective incoming fields. The matrix $\mathbf{W}$ is defined as follows:

$$\mathbf{W} = (\mathbf{W}_{\mathrm{d}} + \mathbf{W}_{\mathrm{x}}) = 2\chi_1\chi_2(\mathbf{V}_{\mathrm{d}} + \mathbf{V}_{\mathrm{x}}) - (\phi_1\chi_2 + \chi_1\phi_2)(\mathbf{G}_{\mathrm{d}} + \mathbf{G}_{\mathrm{x}})\,. \tag{7.10}$$

Equation (7.8) describes polarization determined by the direct channel and equation (7.9) then gives the polarization of the bipolariton–mediated response (bipolariton channel). Polarization selection rules are summarized in Tab. 7.3 for both zinc–blende and wurtzite crystal structures. Concerning the zinc–blende structure, it is necessary to resolve various orientations of excitation beams with respect to the crystallographic axes because of bipolaritons with other than Γ_1 symmetries. I choose the directions [001], [110] and [111]. In the table, the responses of particular channels are resolved (including separation of responses of particular bipolaritons in zinc–blende structure) and I put together responses of the bipolaritons with equal symmetries. The last column then gives the polarization selection rules from the direct channel according to Ref. [6] for comparison. The term "*dbd.*" means "depends on dynamics". It arises if the exchange and direct interactions give different polarizations.

Comparison of the columns "Σ" (calculation based on the presented model) and the column "[6]" (microscopic calculation without considering the bipolariton channel) shows the accuracy of the model since the values agree in all rows for the zinc–blende structure. There are unexpected discrepancies between the responses of the direct channel when compared the two respective crystal symmetries. These discrepancies arise for polarizations $\sigma^+\sigma^-\sigma^+$, $\sigma^+\sigma^-X'$, $\sigma^+X'\sigma^+$, $\sigma^+X'\sigma^-$ and $X'X'\sigma^+$ as a consequence of the difference between Tabs. 6.2 and 6.4 — exchange interaction doesn't couple states $\sigma^+\sigma^- \to \sigma^+\sigma^-$ in the crystals with wurtzite structure. However, the overall signal agrees for both structures in Tab. 7.3.

			Zinc–blende													Wurtzite					[6]
Polarizations			Direct				[001]			[110]			[111]			[001]					
$\boldsymbol{k}_1$	$\boldsymbol{k}_2$	$\boldsymbol{k}_3$	d	x	df.	Σ	Γ_1	Γ_3	Γ_5	Γ_1	Γ_3	Γ_5	Γ_1	Γ_3	Γ_5	d	x	df.	Σ	Γ_1	
σ^+	σ^+	σ^+	σ^+	σ^+	σ^+	σ^+	0	σ^+	σ^+	0	E	E	0	σ^+	σ^+	σ^+	σ^+	σ^+	σ^+	0	σ^+
σ^+	σ^+	σ^-	0	0	0	0	0	σ^-	σ^-	0	E	E	0	0	0	0	0	0	0	0	0
σ^+	σ^-	σ^+	σ^-	σ^-	σ^-	σ^-	σ^-	σ^-	0	σ^-	E	X	σ^-	0	σ^-	σ^-	0	σ^-	σ^-	σ^-	σ^-
σ^+	σ^+	X'	σ^+	σ^+	σ^+	σ^+	0	L	L	0	L	L	0	σ^+	σ^+	σ^+	σ^+	σ^+	σ^+	0	σ^+
σ^+	σ^-	X'	*dbd.*$\sim X'$	*dbd.*$\sim X'$	*dbd.*	*dbd.*	X'	X'	0	X'	L	X	X'	0	X'	*dbd.*$\sim X'$	0	*dbd.*	*dbd.*	X'	*dbd.*
σ^+	X'	σ^+	*dbd.*	*dbd.*	*dbd.*	*dbd.*	σ^-	E	σ^+	σ^-	E	E	σ^-	σ^+	E	*dbd.*	σ^+	*dbd.*	*dbd.*	σ^-	*dbd.*
σ^+	X'	σ^-	σ^+	σ^+	σ^+	σ^+	σ^+	E	σ^-	σ^+	E	E	σ^+	0	σ^+	σ^+	0	σ^+	σ^+	σ^+	σ^+
X'	σ^+	X'	*dbd.*	*dbd.*	*dbd.*	*dbd.*	X'	E	L	X'	L	E	X'	σ^+	E	*dbd.*	*dbd.*	*dbd.*	*dbd.*	X'	*dbd.*
X'	σ^+	Y'	*dbd.*	*dbd.*	X'	*dbd.*	Y'	E	L	Y'	L	E	Y'	σ^+	E	*dbd.*	*dbd.*	X'	*dbd.*	*dbd.*	*dbd.*
X'	X'	σ^+	X'	*dbd.*	X'	*dbd.*	σ^-	E	σ^+	σ^-	E	E	σ^-	σ^+	E	X'	*dbd.*	X'	*dbd.*	σ^-	*dbd.*
X'	Y'	σ^+	*dbd.*	*dbd.*	*dbd.*	*dbd.*	0	σ^+	σ^+	0	E	E	0	σ^+	σ^+	*dbd.*	*dbd.*	*dbd.*	*dbd.*	*dbd.*	*dbd.*
X'	X'	X'	X'	X'	X'	X'	X'	L	L	X'	L	L	X'	X'	X'	X'	X'	X'	X'	X'	X'
X'	X'	Y'	Y'	Y'	Y'	Y'	Y'	L	L	Y'	L	L	Y'	Y'	Y'	Y'	Y'	Y'	Y'	Y'	Y'
X'	Y'	X'	Y'	Y'	Y'	Y'	0	L	L	0	L	L	0	Y'	Y'	Y'	Y'	Y'	Y'	0	Y'

Table 7.3: Polarization selection rules for the third–order FWM response of semiconductors with zinc–blende and wurtzite crystal structure. For every structure, responses from the respective channels are resolved. The direct channel is further divided to its direct "d" and exchange "x" part. The column "df." is the response of the diffraction channel according to Tabs. 7.1–7.2 and the column titled "Σ" is the sum of the respective contributions of the direct and the diffraction channel. Concerning the bipolariton channel, its contributions are divided according to the symmetries of the bipolariton states, they are labeled "Γ_j". The column "[6]" then gives the polarization selection rules taken from the literature [6]. Circular polarizations are denoted $\sigma^\pm$ and linear X' and Y' — these symbols denote arbitrary (but perpendicular) linear polarizations, i.e. the polarization plane is not connected with crystallographic axes. The symbols X and Y, respectively, then stand for linear polarizations connected with the crystallographic axes x and y, respectively. The symbol L denotes some linear polarization which is not generally X, X', etc. for any orientation of linear polarizations of the incoming fields. The symbol E then denotes an elliptical polarization, 0 stands for zero signal and dbd. for the polarization "dependent on dynamics".

7.4 Time–resolved experiments

In time–resolved experiments, the temporal profile of the FWM response is measured using the up–conversion technique [14] when the time delays between the incident pulses are varied. Discussion of the time–resolved experiments therefore involves a discussion of the temporal profile of the FWM response and a discussion of the dynamics of polarization of the FWM signal after optical excitation of the sample. This section is focused mainly on the general FWM signal dynamics, however the latter subject is also discussed at the end of the section. Solutions of equations of motion from Appendices B.2 and B.3 are used in this and following sections, i.e. their perturbative solution using delta–like pulses.

Concerning the general dynamics of the FWM response, simplified equations which describe the FWM response are derived in the beginning. The discussion is then divided into parts appropriate for particular wave mixing channels: the direct channel, the bipolariton channel and the diffraction channel. The overall response is discussed afterwards.

I simplify the mathematical expressions by assuming the time order of the incoming optical pulses $t_1 < t_3 < t_2$. The FWM dynamics is then determined by Eqs. (B.21) and (B.23). With the help of (7.10) and putting $\omega_j^{\mathrm{X}} = \omega^{\mathrm{X}}$, we obtain:

$$\tilde{\varrho}^{(3)}_{\boldsymbol{k}_3\boldsymbol{k}_4,\boldsymbol{k}_3}(t) = F_{\tilde{\varrho}132}(t_1,t_2,t_3,t)\left[-\mathrm{i}\frac{W}{2\hbar}\chi_3\chi_4(t-t_2)+\frac{\kappa}{\mu}\right]\mathrm{e}^{-\gamma_2^{\mathrm{X}}(t-t_2)}\,, \tag{7.11}$$

$$\begin{aligned}\tilde{\varrho}^{(3)}_{\boldsymbol{k}_3\boldsymbol{k}'_4,\boldsymbol{k}_3}(t) = &-F_{\tilde{\varrho}132}(t_1,t_2,t_3,t)\frac{|M_2|^2}{\hbar^2}\cdot\\ &\cdot\left\{\frac{\mathrm{e}^{-\gamma_2^{\mathrm{R}}(t-t_2)}(t-t_2)}{\gamma_2^{\mathrm{B}}-\gamma_2^{\mathrm{R}}}-\frac{\mathrm{e}^{-\gamma_2^{\mathrm{R}}(t-t_2)}-\mathrm{e}^{-\gamma_2^{\mathrm{B}}(t-t_2)}}{(\gamma_2^{\mathrm{B}}-\gamma_2^{\mathrm{R}})^2}\right\},\end{aligned} \tag{7.12}$$

$$\begin{aligned}F_{\tilde{\varrho}132}(t_1,t_2,t_3,t) = &\frac{\mu^3}{\hbar^3}\mathcal{E}_1\mathcal{E}_2\mathcal{E}_3^*\mathrm{e}^{\mathrm{i}\omega^{\mathrm{X}}(t_1+t_2-t_3)}\mathrm{e}^{-\mathrm{i}(\omega_1 t_1+\omega_2 t_2-\omega_3 t_3)}\cdot\\ &\cdot\,\mathrm{e}^{-\gamma_2(t_3-t_1)}\mathrm{e}^{-\gamma^{\mathrm{C}}(t_2-t_3)}\Theta(t_3-t_1)\Theta(t_2-t_3)\Theta(t-t_2)\,.\end{aligned} \tag{7.13}$$

For the temporal order of pulses $t_1 < t_2 < t_3$, we may rewrite the equations (B.32), (B.34) and (B.35) as follows:

$$\tilde{\varrho}^{(3)}_{\boldsymbol{k}_4,0}(t) = F_{\tilde{\varrho}123}(t_1,t_2,t_3,t)\left[\mathrm{i}\frac{W}{2\hbar}\chi_3\chi_4(t_3-t_2)-2\frac{\kappa}{\mu}\right]\mathrm{e}^{-\gamma_2^{2\mathrm{X}}(t_3-t_2)}\mathrm{e}^{-\gamma_2(t-t_3)}, \tag{7.14}$$

$$\begin{aligned}\tilde{\varrho}^{(3)}_{\boldsymbol{k}_3\boldsymbol{k}_4,\boldsymbol{k}_3}(t) = &F_{\tilde{\varrho}123}(t_1,t_2,t_3,t)\cdot\\ &\cdot\left[-\mathrm{i}\frac{W}{2\hbar}\chi_3\chi_4(t-t_2)+2\frac{\kappa}{\mu}\right]\mathrm{e}^{-\gamma_2^{2\mathrm{X}}(t_3-t_2)}\mathrm{e}^{-\gamma_2^{\mathrm{X}}(t-t_3)}\,,\end{aligned} \tag{7.15}$$

$$\begin{aligned}F_{\tilde{\varrho}123}(t_1,t_2,t_3,t) = &\frac{\mu^3}{\hbar^3}\mathcal{E}_1\mathcal{E}_2\mathcal{E}_3^*\mathrm{e}^{i\omega^{\mathrm{X}}(t_1+t_2-t_3)}\mathrm{e}^{-\mathrm{i}(\omega_1 t_1+\omega_2 t_2-\omega_3 t_3)}\cdot\\ &\cdot\,\mathrm{e}^{-\gamma_2(t_2-t_1)}\Theta(t_2-t_1)\Theta(t_3-t_2)\Theta(t-t_3)\,.\end{aligned} \tag{7.16}$$

The formula for the bipolariton channel is complicated and it is not given here, the contribution of the bipolariton channel was omitted in the formula for $\tilde{\varrho}^{(3)}_{\boldsymbol{k}_4,0}$. However, as both the direct and the bipolariton channel are scattering channels, their dynamics is similar and it is not necessary to write the formulas explicitly. It is sufficient to state that the response of the bipolariton channel is proportional to $F_{\tilde{\varrho}123}(t_1,t_2,t_3,t)$ and the expression which follows is real.

Let's discuss first the direct channel only. Its response is given by the term $\tilde{\varrho}^{(3)}_{\boldsymbol{k}_3\boldsymbol{k}_4,\boldsymbol{k}_3}(t)$ in Eq. (7.11) for $t_1 < t_3 < t_2$ without the contribution of $\frac{\kappa}{\mu}$. The temporal evolution

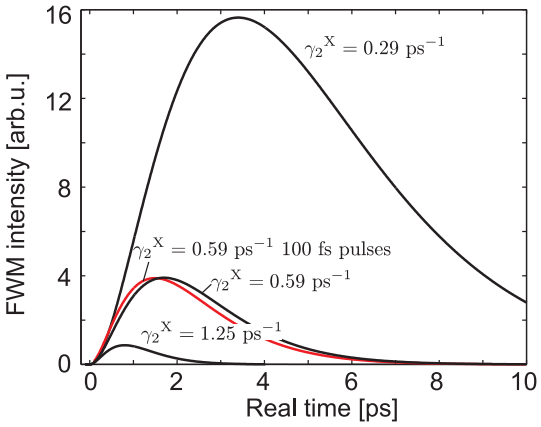

Figure 7.4: TR–FWM response of the direct channel according to equations of motion in Appendix B.2, $t_1 = t_2 < t_3 = t_2 + 0.5$ ps (black lines) and comparison to calculation with 100 fs pulses (red). Dephasing rate γ_2^X is varied.

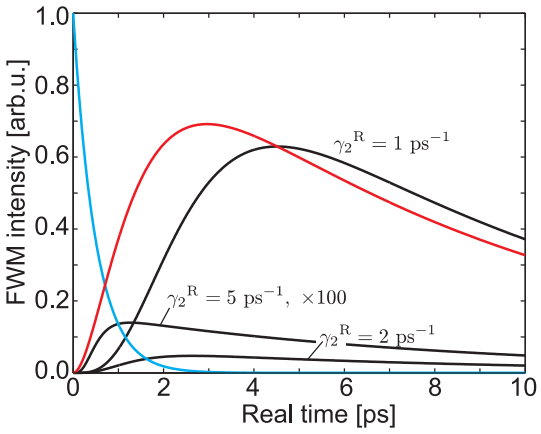

Figure 7.5: TR–FWM of the bipolariton channel according to Appendix B.1, $t_1 = t_3 < t_2$. Parameters: $\gamma_2^X = 0.0623$ ps^{-1} and γ_2^R is varied. Blue line is coherent population of the initial state, red line is the coherent population of the bipolariton and black lines show the response.

is clearly proportional to $(t - t_2)\exp[-\gamma_2^X(t - t_2)]$. For the second temporal ordering of pulses, $t_1 < t_2 < t_3$, the FWM response is proportional to the sum $\tilde{\varrho}^{(3)}_{\boldsymbol{k}_4,0}(t) + \tilde{\varrho}^{(3)}_{\boldsymbol{k}_3\boldsymbol{k}_4,\boldsymbol{k}_3}(t)$ from (7.14)–(7.15) without the contribution of $\frac{\kappa}{\mu}$ again (the diffraction channel). In this case, is seems that the dynamics of the response would have a complex structure when compared to the $t_1 < t_3 < t_2$ case, however the term (7.14) and a part of (7.15) subtract and the resulting polarization yields:

$$\langle \hat{P}^+_{\boldsymbol{k}_4}\rangle(t) = -\mathrm{i}\frac{W}{2\hbar}\chi_3\chi_4 F_{\tilde{\varrho}123}(t_1,t_2,t_3,t)\mathrm{e}^{-\gamma_2^{2X}(t_3-t_2)} \cdot \\ \cdot \left[(t-t_3)\mathrm{e}^{-\gamma_2^X(t-t_3)} + (t_3-t_2)(\mathrm{e}^{-\gamma_2^X(t-t_3)} - \mathrm{e}^{-\gamma_2(t-t_3)})\right]. \qquad (7.17)$$

Obviously the main part of the signal is proportional to $(t - t_3)\mathrm{e}^{-\gamma_2^X(t-t_3)}$, the other part is proportional to $(t_3 - t_2)[\mathrm{e}^{-\gamma_2^X(t-t_3)} - \mathrm{e}^{-\gamma_2(t-t_3)}]$ and it is small compared to the leading term since we consider $\gamma_2 \approx \gamma_2^X$. Intensity of the FWM signal from the direct channel then clearly evolves like $t'^2\exp\left[-2\gamma_2^X t'\right]$, where t' is the time delay after arrival of the last excitation pulse. For $t' = 0$, the FWM response is clearly zero and it slowly grows until it reaches a maximum value and then it decays. The FWM signal peaks at the time $t' = 1/\gamma_2^X$. Calculated temporal profiles of the intensity of the FWM signal from the direct channel are depicted in Fig. 7.4. Several values of dephasing rates are considered and numerical calculation with 100 fs pulses is included for comparison.

The response of the direct channel may be observed using bulk wurtzite semiconductors and polarizations of the incoming fields $\sigma^+\sigma^+\sigma^+$. Under these conditions, the bipolariton channel is dipole–forbidden and the contribution from the diffraction channel is generally negligible in bulk when compared to the response of the direct channel. The prediction of the temporal profile of the FWM response based on the presented model reproduces well the experimental observations [51, 52, 53, 54, 80]: the signal is zero at the time of arrival of the last excitation pulse and it starts instantaneously to rise. After some time delay which is not determined by delays between the respective pulses (on the contrary to

inhomogeneous atomic systems) the signal starts to decrease monotonously. The increase of the intensity of the FWM field is caused by continuous polariton–polariton scattering which is responsible for creation of the four–particle (four–fermion) correlations [21]. The subsequent decrease is then due to incoherent processes, namely incoherent dephasing.

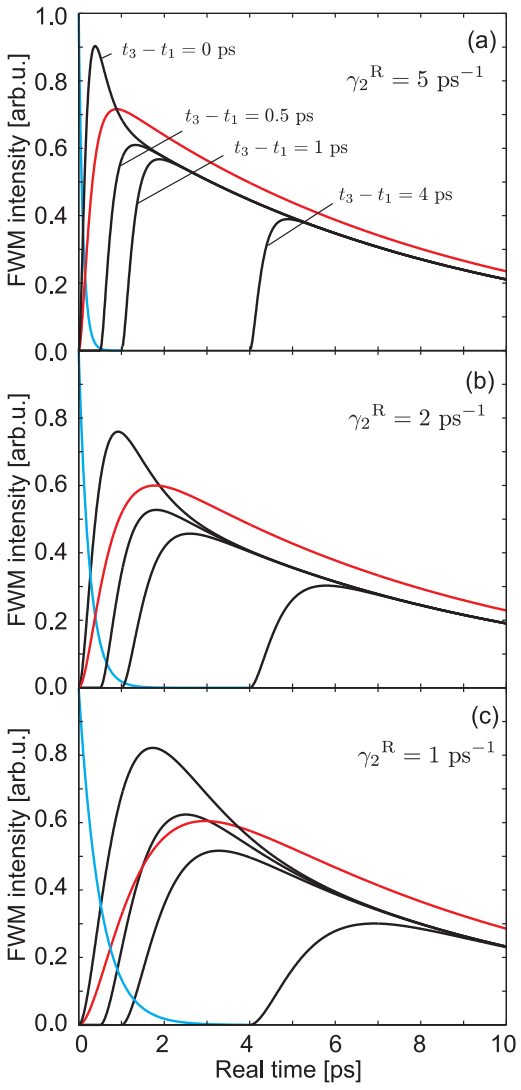

Figure 7.6: Calculated TR–FWM response of the bipolariton channel assuming $\gamma_2^{2B} = \gamma_2^{B} = 0.0623$ ps^{-1} *and* $\gamma_2^{2R} = \gamma_2^{R} = 5$ ps^{-1} *(a),* $\gamma_2^{2R} = \gamma_2^{R} = 2$ ps^{-1} *(b),* $\gamma_2^{2R} = \gamma_2^{R} = 1$ ps^{-1} *(c). Responses for time delays* $t_3 - t_1 = 0, 0.5, 1, 4$ ps *are plotted in all graphs (solid black lines). Squares of bipolariton coherence (red lines) and coherence of the initial two–polariton state (blue lines) are included for comparison.*

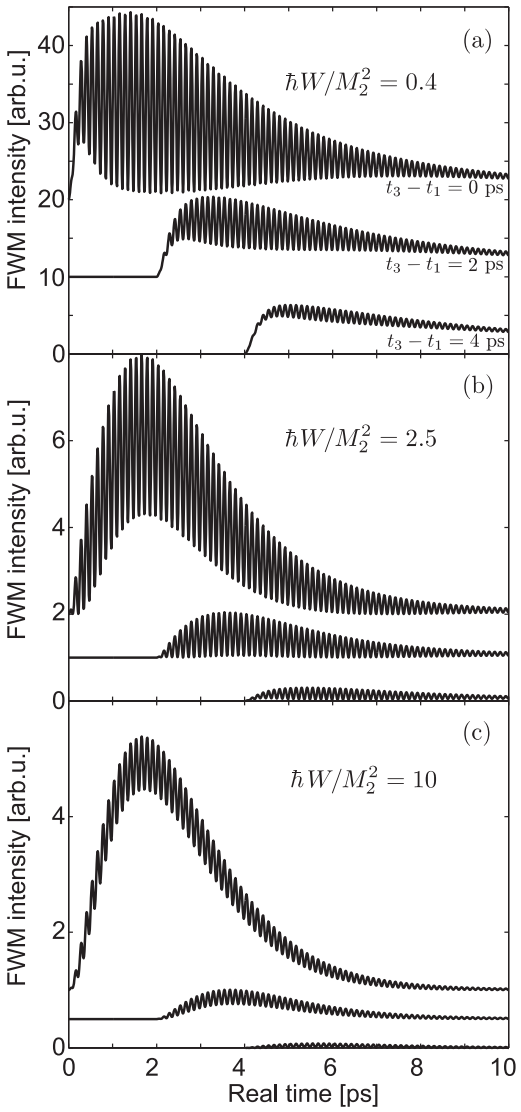

Figure 7.7: Simulated overall TR–FWM response assuming delta pulses, $\gamma_2^{2\mathrm{R}} = \gamma_2^{\mathrm{R}} = 5$ ps^{-1}, $\gamma_2^{2\mathrm{X}} = \gamma_2^{\mathrm{X}} = 0.59$ ps^{-1}, *and* $\gamma_2^{2\mathrm{B}} = \gamma_2^{\mathrm{B}} = 0.0625$ ps^{-1}, *time delays* $t_3 - t_1 = 0, 2, 4$ ps *and various ratios* $\hbar W/M_2^2 = 0.4$ *(a), 2.5 (b) and 10 (c).*

Temporal profile of the response of the bipolariton channel is more complicated than the response of the direct channel. It is caused by the fact that the dephasing time of the intermediate state for scattering (bipolariton state) is notably prolonged with respect to dephasing rates of the initial and the final photon–like two–polariton states. The dynamics of the bipolariton channel is plotted in Fig. 7.5 for the time order of excitation pulses $t_1 < t_3 < t_2$. In this case, the intensity of the FWM response starts to grow as $(t - t_3)^4$ as can be shown from (7.12). It peaks after a certain time and then it decays with the rate approximately γ_2^{B}. It is not possible to give an analytic expression for the time at which the FWM signal has its maximum value, however assuming $\gamma_2^{\mathrm{R}} \gg \gamma_2^{\mathrm{B}}$, we may estimate the peak time from the solution of equation:

$$t - t_2 = \frac{\gamma_2^{\mathrm{B}}}{(\gamma_2^{\mathrm{R}})^2}\, \mathrm{e}^{\gamma_2^{\mathrm{R}}(t-t_2)}\,. \tag{7.18}$$

Considering temporal order of the excitation pulses $t_1 < t_2 < t_3$, the dynamics of the FWM response is driven by one–step as well as two–step processes. Similarly to (7.14)–(7.15), the bipolariton–mediated response is zero since the appropriate coherences subtract. The signal then grows from zero and peaks after a nonzero delay, which is given by the dephasing rates γ_2^{R}, γ_2^{X}, $\gamma_2^{2\mathrm{B}}$ and by the delay $t_3 - t_2$ between the last two excitation pulses.

The temporal evolution of the signal for various sets of parameters and time delays are plotted in Fig. 7.6. The blue line in each figure shows the decay of a coherence connected with the initial two–polariton state $|\boldsymbol{k}_1'\boldsymbol{k}_2'\rangle$ which is driven by the dephasing rate $\gamma_2^{2\mathrm{R}}$. The coherence of the bipolariton state is depicted by the red line. This coherence decays at long times with the rate $\gamma_2^{2\mathrm{B}}$. Starting at time $t = t_2$, the bipolariton coherence is zero and it is increasing as long as the coherence of the initial state is nonzero as seen from the Fig. 7.6. The overall third–order coherence of the final states are zero at the time of arrival of the last pulse, as noted above. Consequently, it grows due to bipolariton–mediated scattering of the initial two–polariton state (two–step process) but also due to annihilation of bipolaritons built–up during the time delay between arrivals of the second and the third pulse (one–step process). Since the dephasing rate γ_2^{R} is big, one may expect that the one–step processes follow the temporal profile of the bipolariton coherence with fast onset near $t = t_3$. The two–step processes then contribute only at short delays $t_3 - t_2$ since the coherence of the initial state decays rapidly. This two–step process then causes a narrow peak of the FWM intensity at short times which vanishes for $t_3 - t_2 > 1/\gamma_2^{2\mathrm{R}}$ (cf. Fig. 7.6).

It is not possible to derive analytically a formula for determination of the time when the bipolariton–mediated FWM response peaks, however for $t_3 - t_2 > 1/\gamma_2^{2\mathrm{R}}$, one may calculate it:

$$t \approx t_3 + \frac{1}{\gamma_2^{\mathrm{R}}} \log \frac{\gamma_2^{\mathrm{R}}}{\gamma_2^{\mathrm{B}}}\,. \tag{7.19}$$

Using time–resolved experiments, one may determine the particular dephasing rates in the following way. Since the signal from the direct channel peaks at time $t' = 1/\gamma_2^{\mathrm{X}}$, the dephasing rate γ_2^{X} may be easily determined from the time delay between the arrival of the third pulse and the peak time of the FWM signal. Concerning the bipolariton channel, the dephasing rate γ_2^{B} may be extracted from the decay of the TR–FWM response at long times. Using (7.19) and (7.18), we may determine γ_2^{R} from the peak time and the other dephasing rates may be determined by fitting predictions of the model to experimental data where the delay $t_3 - t_2$ is varied.

Dynamics of the diffraction channel is quite different from the dynamics of the direct channel although both channels are degenerate in energy. Since diffraction on a transient grating is an instantaneous process, the onset of the TR–FWM response is also expected to be instantaneous as seen in (7.11). Decay of the signal is then expected with the rate γ_2^{X}. On the contrary to the time order $t_1 < t_3 < t_2$, the response of the diffraction channel is forbidden when $t_1, t_2 < t_3$ since no transient grating for diffraction to the direction $\boldsymbol{k}_1+\boldsymbol{k}_2-\boldsymbol{k}_3$ is created before arrival of the last pulse.

Taking into account the whole spectrum, i.e. contributions from all channels, it is clear that the TR–FWM response reveals beating as a consequence of the energy mismatch between the particular channels — beating frequency is $2\omega^{\mathrm{X}} - \omega^{\mathrm{BX}}$. The phase of beats is given by the time delay between the last two pulses. Looking at Eqs. (7.11)–(7.15), we observe a very interesting property which may cause a very peculiar polarization dynamics: the phases of the direct and the bipolariton channel are shifted by $\pi/2$ (and reflects the fact that a direct process may be understood as a virtual bipolariton–mediated process [98]). This feature affects also the phase of the beats of the FWM signal.

The amplitude of beating (as seen in Fig. 7.7) is determined by the ratio of the particular contributions of the respective channels (stronger beats in Fig. 7.7a show comparable effective coupling strengths for the two channels while in Fig. 7.7c, bipolariton response almost vanishes). The contrast of the beats is strongest when the responses of the direct plus diffraction and the bipolariton channels are equal. The contrast of beats evolves in time as the ratio of the two respective contributions vary due to dephasing. As seen from Fig. 7.7b, responses of the direct and bipolariton channel are not equal in magnitude (the bipolariton response is weaker) for $t_3 = t_1$ and therefore the relative amplitude of the beats is lower compared to the situation $t_3 = t_1 + 1$ ps. With increasing delay $t_3 - t_1$, the magnitudes equalize because of the faster decay of two–exciton states when compared to the bipolariton. The presented model can be then used in order to numerically decompose the contributions and to find the values of dephasing rates, the rate W/M_2^2 and the bipolariton binding energy.

The model predicts a very interesting property of the TR–FWM signal: when using polarizations XXX, the beats are shifted by an amount π with respect to excitation with polarizations XXY (see Fig. 7.8) as observed experimentally [99, 100]. The reason is, that the phases of the bipolariton–mediated response are equal under both excitation conditions. Phases of the direct channel, however, differ as can be shown in Tabs. 6.1 and 6.3. We find for the crystals which have e.g. wurtzite structure $\mathbf{G}_{\mathrm{x}}(X,X,X,X) = \frac{1}{2} = -\mathbf{G}_{\mathrm{x}}(X,X,Y,Y)$. Taking into account the fact that the polariton–polariton scattering is given predominantly by the exchange processes [10, 38], we find that the phases of the FWM response of the direct channel have opposite signs under the two different excitation conditions.

The above discussion was concerned in the FWM signal dynamics without resolving its polarization. However polarization may evolve in time as shown experimentally in [2, 101]. The origin of the polarization evolution lies in spin–flip processes and in the different dynamics of the respective channels. As seen from Tab. 7.3, the responses of all these channels do not always agree in polarization and therefore evolution of the total polarization follows the evolution of the channels.

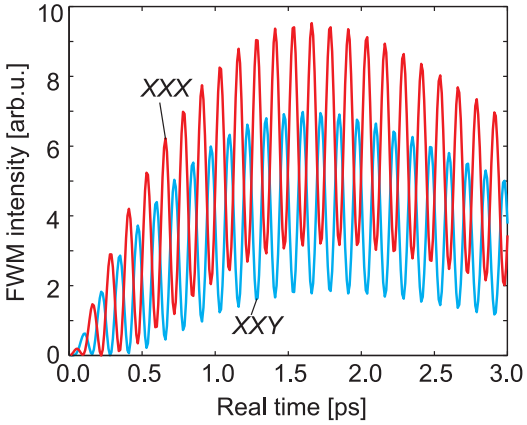

Figure 7.8: Detail of beats in simulated TR–FWM for the parameters given in Fig. 7.7 and $\hbar W/M_2^2 = 0.4$ assuming polarizations of the excitation beams XXX and XXY, respectively, $t_1 = t_2 = t_3$.

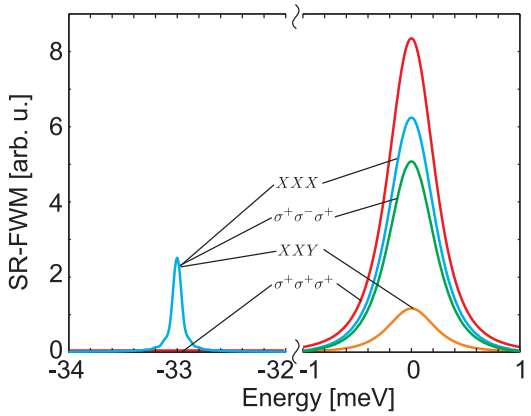

Figure 7.9: Calculated SR–FWM response of a semiconductor with the same parameters as in Fig. 7.8 for various polarizations of the excitation beams.

7.5 Spectrally–resolved experiments

Spectrally–resolved FWM (SR–FWM) is an experimental technique which brings an additional information to the TR–FWM measurements. In this type of experiment, spectra of the FWM response are measured (instead of its temporal profile in TR–FWM) and one varies the time delays between the incident pulses. Measured spectra show which energetical levels contribute to the signal and we can easily compare particular contributions from all scattering channels.

Performing SR–FWM experiments with different polarizations of the excitation beams, one can identify the relative strengths of various spin–dependent processes. I illustrate this fact in Fig. 7.9 where I depict the simulations of FWM spectra for polarizations XXX, XXY, $\sigma^+\sigma^+\sigma^+$ and $\sigma^+\sigma^-\sigma^+$ for CuCl which has zinc–blende crystal structure. (Experimental data for different polarization setups on GaAs QW may be found in Ref. [102].) The binding energy of bipolariton is 33 meV what is clearly the difference in the energies of the peaks. The energy is relative with respect to exciton resonance. At the bipolariton energy, the response is zero for the configuration $\sigma^+\sigma^+\sigma^+$ since bipolariton excitation is forbidden. The spectra of the bipolariton response for other spin setups are equal because of the spin structure of Γ_1 biexciton [26].

The spectra at the exciton resonance reveal the symmetry of matrices $\mathbf{W}_\mathrm{d}$ and $\mathbf{W}_\mathrm{x}$ appropriate for polariton–polariton scattering. There are two processes which contribute to scattering: direct boson scattering (subscript "d") and exchange of fermions (subscript "x"), the exchange is usually stronger [10]. As shown in Tabs. 6.1–6.4 for semiconductors with zinc–blende structure, the scattering is strongest for the process which scatters $\sigma^+\sigma^+ \to \sigma^+\sigma^+$ since the scattering matrix element is $W_\mathrm{x}(0,0)+W_\mathrm{d}(0,0)$ and therefore the response on the exciton resonance is strongest for the $\sigma^+\sigma^+\sigma^+$ configuration. For $\sigma^+\sigma^-\sigma^+$, the FWM signal comes both from direct and exchange scattering, however the exchange scattering is weaker than the scattering $XX \to XX$ and it is stronger than $XX \to YY$ and therefore the FWM signal has the intensity between the polarization setups XXX and XXY. Concerning linear polarizations, scattering $XX \to XX$ is stronger than $XX \to YY$ because direct scattering is forbidden in the latter case and the scattering matrix elements are $\frac{1}{2}W_\mathrm{x}(0,0)+W_\mathrm{d}(0,0)$ for the XXX excitation and $-\frac{1}{8}W_\mathrm{x}(0,0)$ for the XXY excitation.

The SR–FWM experiment can be used in order to compare the dynamics of the two channels by varying the time delays between pulses. In order to determine the relaxation rates γ_2^{2X}, γ_2^{2B} and γ_2^{2R}, the SR–FWM measurement is appropriate when varying the time delay $t_3 - t_1 > 0$ and $t_1 = t_2$. For long time delays, the decay of SR–FWM signal is given by γ_2^{2X} for the direct channel and by γ_2^{2B} for the bipolariton channel. For $(t_3 - t_1)\gamma_2^{2R} \leq 1$, the decay at the bipolariton energy is given by a combination of γ_2^{2R} and γ_2^{2B} but it should be possible to decompose the particular decay rates.

7.6 Time–integrated experiments

In time–integrated measurement (TI–FWM), the delays between pulses may be varied and the intensity of FWM response is integrated over time with no spectral resolution. Compared to TR–FWM and SR–FWM, this technique gives less informations but it is, however, a more simple experimental setup and thus TI–FWM is widely used in practice.

Using TI–FWM, one can accurately measure the dephasing rates of excitons γ_2 and the dephasing time for the spin coherence γ_2^C. Their measurement is as follows: to measure γ_2, we set $t_1 = t_2$, $t_3 - t_1 < 0$, i.e. the pulse 3 precedes other two pulses. The coherence created by the first pulse decays exactly with the rate γ_2. Since the TI–FWM signal is not sensitive to the phase of this coherence, the measured decay is driven by the rate γ_2. When setting $t_2 = t_3$ and $t_3 - t_1 < 0$, the decay rate of the created coherence is γ_2^C before arrival of the last pulse and thus one measures the spin coherence decay in such type of experiment.

7.7 Discussion of the features of the model

In order to check the applicability of the model developed in the previous chapter, I give in this section a summary of the features of FWM experiments and I compare them to predictions of the model discussed in the previous sections.

We may start with one of the most important phenomena of FWM on semiconductors — polarization selection rules. These selection rules, described theoretically in Ref. [6], are very unusual when compared to nanocrystals and atomic systems, see chapter 5. They indicate that the wave mixing has a different origin in semiconductors and systems of localized states. Comparison of polarization selection rules taken from [6] with predictions of the model is given in Tab. 7.1. We should compare the columns labeled "Σ" (predictions of the model) with the column "[6]" (microscopic theory and experiment). Other columns, which are appropriate to bipolariton channels, cannot be compared to experiments due to the lack of experimental data in publications. However, we may do some comparison to the experiment used in order to detect mixed biexcitons in quantum wells [83] — with the help of results of chapter 4, the polarization selection rules valid for quantum wells may be calculated and we may predict, under which polarizations of the excitation beams the mixed biexcitons may be seen in SR–FWM. These predictions then agree with the experimental results and we may therefore conclude that the model gives the correct predictions for polarization selection rules.

The second point to be discussed is the spectrum of the calculated FWM signal. One may use experimental data taken from [91, 92] for comparison. Typical spectra predicted by the model are plotted in Fig. 7.9. The main feature, namely that the maxima of the spectra arise at exciton and biexciton resonances, are well reproduced. However

the spectral widths of the peaks are determined mainly be dephasing rates in the model while they are determined by spectral widths of the excitation pulses in experiments. This discrepancy is a consequence of neglect of the continuum of states. The continuum is modeled by two "representative" resonances in order to considerably simplify the model and equations of motion. In conclusion, the main features of the SR–FWM signal are well reproduced by the model, however there are quantitative differences.

Concerning the temporal evolution of the FWM signal, there are two features to be discussed — exciton–biexciton beating and noninstantaneous response. Slow initial rise of the signal after optical excitation [51, 52, 53, 54, 80] is the most striking difference when compared to atomic systems. As discussed in section 7.4, this property is predicted by the model for both scattering channels, the FWM intensity starts at zero at the time of arrival of the third pulse and its peak is considerably delayed with respect to this excitation pulse. The time delay may be much larger than the pulse duration and does not arise as a consequence of inhomogeneity of the system (and the peak is not therefore a photon echo known from atomic systems). The response of the diffraction channel is, on the contrary, instantaneous but it doesn't give the main contribution to the FWM signal under weak excitation. As seen in simulations performed by Weiss et al. [53], the phase–space–filling signal (denoted here as the diffraction channel) has a faster dynamics and within the durations of pulses used in the experiment, the response may be viewed as instantaneous. Beating of the FWM response due to the biexciton binding energy is discussed in detail in section 7.4 and it is well predicted by the model presented in this thesis. The temporal evolution of the FWM response is, as shown above, also well reproduced by the model.

7.8 Extension of the model

The model, as presented in section 7.2, has many limitations and may be used only for bulk crystals which are not under influence of external fields and also some electron–hole exchange interactions are neglected. However the formulation presented in chapter 6 is more general and these perturbations may be fully taken into account.

The point is, that external fields, which do not change the wave vector of excitons and polaritons, may be generally understood as symmetry–breaking effects. Lowering of symmetry causes mixing of states and therefore an effective spin precession which may be seen as periodical changes of the spin of polaritons. One should, nevertheless, resolve between coherent and incoherent changes of spin: the former preserve the particle's coherence and therefore the particle contributes to the FWM signal while the latter processes destroy the particle's coherence and therefore the particle may no longer contribute to the diffracted signal (incoherent processes are described by phenomenological dephasing rates). The coherent changes of spin are fully described by generally wave vector dependent nondiagonal elements of the matrices $h_{SS',\boldsymbol{k}}$ which arise in the Hamiltonians (6.68) and (6.71) in the harmonic terms. The influence of magnetic and electric field, homogeneous static stress, crystal structure, etc., is therefore implicitly included in the model, one should, however, develop full equations of motion since the direct integration presented in chapter 7 doesn't take the nondiagonal terms in $h_{SS',\boldsymbol{k}}$ into account.

As noted above, the model may be also extended to quantum wells. The model is developed considering bulk crystals because of the requirement of wave vector conservation during polariton–polariton scattering processes and exciton–photon coupling. Quantum wells, on the contrary to bulk crystals, have only in–plane translational symmetry and therefore wave vector is well defined only in the plane of the quantum well (see section 3.5). As

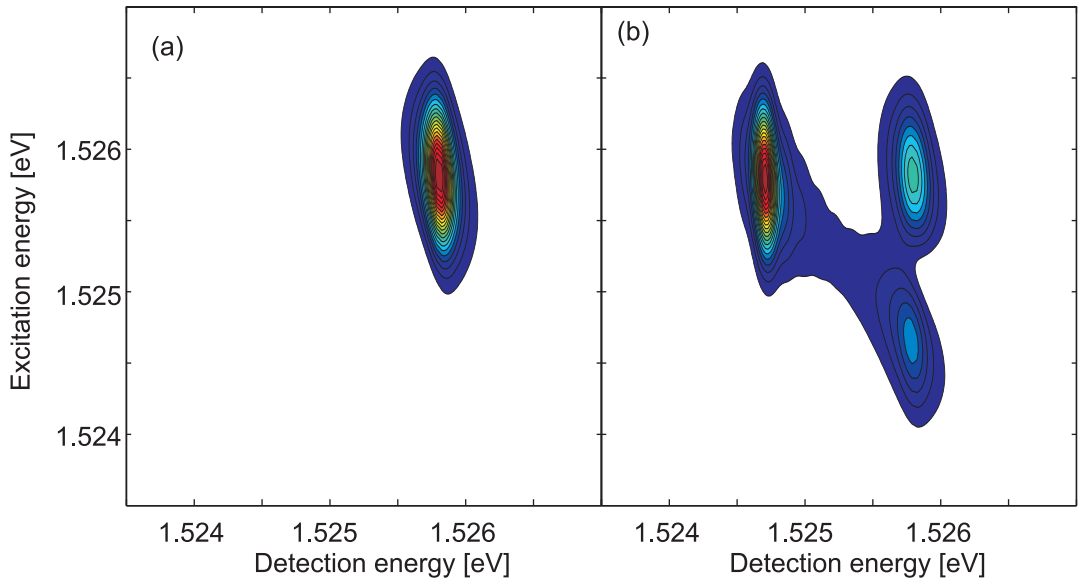

Figure 7.10: Simulation of the experimental data taken from Ref. [104], Fig. 1a (a) and Fig. 1b (b).

a consequence, excitons are coupled to photons with wave vectors in a cone and therefore wave vector is not necessarily conserved during photon absorption. As a consequence, the FWM response, which comes from the scattering channels, is not expected to be highly directional. Although only two components of the wave vectors are conserved, energy conservation ensures an effective conservation of all components and one may observe the response of the scattering channels in experiments with sufficient spatial resolution. Response from the diffraction channel remains directional since the diffraction grating is formed in the same way as on the surface of a bulk crystal.

When adapting the model to quantum wells, one should take into account several facts. The confining potential causes a change of an effective crystal structure and therefore the point group symmetry of the crystal. It is therefore necessary to calculate shapes of exciton and biexciton wavefunctions and to develop the one–particle Hamiltonian according to chapter 5. The correct crystal symmetry and growth axis must be taken into account in order to correctly describe the spin–flip processes and the spin structure of dipole–active excitons. The crystal structure also influences the symmetry of the bipolariton–mediated scattering. The second point concerning quantum wells is, that the effect of phase–space filling is more pronounced when compared to bulk. Its influence may be usually neglected in bulk crystals, however it may give the main contribution in quantum wells [103]. The third point to be discussed is the radiative lifetime and radiative dephasing of polaritons. Since the thickness of quantum wells is usually negligible, it is better to speak about excitons and their virtual excitation. Relaxation and dephasing of excitons is then linked to the uncertainty relations — the bigger is energy difference between a virtual (photon–like) level, the bigger are relaxation and dephasing rates.

The model is well applicable to quantum wells since wave vector (all three components) is effectively conserved as well as in bulk crystals. In structures with lower dimensionality like quantum wires and quantum dots, the model cannot work because wave vector is not conserved. One should therefore use another localized model, e.g. optical Bloch equations (see chapter 5).

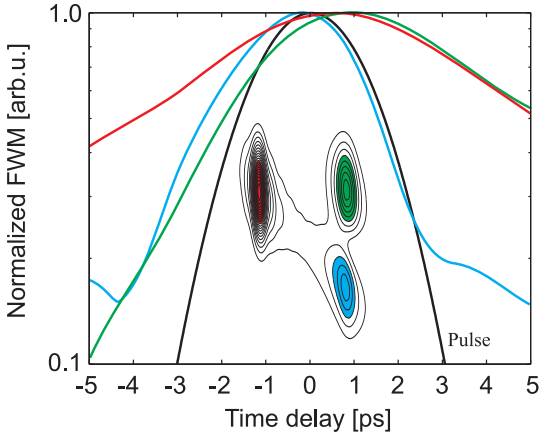

Figure 7.11: Simulation of the experimental data taken from Ref. [104], Fig. 2.

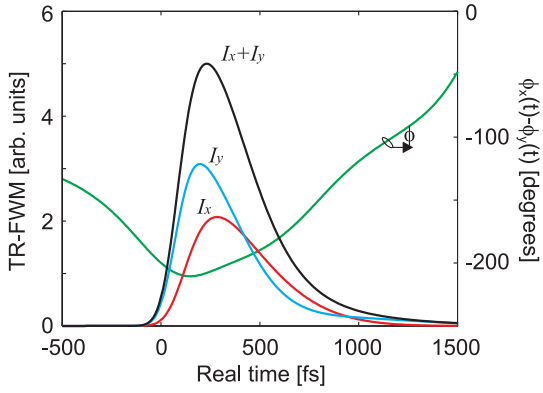

Figure 7.12: Simulated TR–FWM data taken from Fig. 4 in [101] using the presented model.

7.9 Simulations of experiments

In this section, I present calculations which were done in order to show whether the model is able to simulate experimental data. For this purpose, I have chosen experimental data published in literature and I performed numerical calculations. One type of simulations is a simulation of the validity of the model with respect to the so–called four–particle correlations, i.e. whether the model takes exciton–exciton correlations correctly into account. I took experimental data from Ref. [104], measured by a coherent excitation spectroscopy (CES) method, developed by the authors. This method is based on excitation of a quantum well by a spectrally broad pulse (direction $\boldsymbol{K}_1 = \boldsymbol{K}_2$) and subsequent scan of excited states by a spectrally narrow pulse in the direction $\boldsymbol{K}_3$. The response in the FWM direction $\boldsymbol{K}_1+\boldsymbol{K}_2-\boldsymbol{K}_3$ is then spectrally resolved and the sum of the detected energy and energy of the third ($\boldsymbol{K}_3$) field gives the energy of a dipole–active excited state.

I simulated experimental data from Fig. 1 in the cited paper, i.e. scan of SR–FWM with different energies of the third pulse. I considered the setup described in the paper and the values: $T_2 = 5$ ps, $T_2^{\mathrm{X}} = 4$ ps, $T_2^{\mathrm{B}} = 10$ ps, $T_2^{\mathrm{R}} = 0.8$ ps, $T_2^{2\mathrm{X}} = 2$ ps, $T_2^{2\mathrm{B}} = 5$ ps and $T_2^{2\mathrm{R}} = 0.4$ ps. The coupling strengths were chosen ad hoc $V_{\mathrm{X}} = 6 \cdot 10^{-9}$ eV, $G_{\mathrm{X}} = = 4 \cdot 10^{-6}$ eV, $M_2 = 1 \cdot 10^{-5}$ eV and $V_{\mathrm{d}} = V_{\mathrm{x}}/4$, $G_{\mathrm{d}} = G_{\mathrm{x}}/4$. The resulting graphs are plotted in Fig. 7.10a,b.

When changing the time delay $\tau = t_1 - t_3$ ($t_1 = t_2$) in calculations, the intensity of the response at various positions in graphs in Fig. 7.10 change. The maxima are not, however, localized at $\tau = 0$. As shown in the experiment in Ref. [104], they are displaced from the origin as seen in simulation in Fig. 7.11. Comparing to the experimental data, we find some differences, mainly that the simulated temporal displacements are much smaller than the experimental data. However, the model has many limitations and it is very simple and it is a success when it predicts some tendencies.

Comparing Figs. 7.10 and 7.11 with the experimental data published in [104], we find that the model is able to reproduce the experiment. Due to the lack of knowledge of the sample characteristic times, it is not possible to do a better comparison, nevertheless we may conclude that the four–particle correlations are described with good success. The spectral widths of the SR–FWM signals in the simulations do not agree with the experimental data since some relaxation times may be overestimated and also not all bipolariton states are taken into account in the calculations (bipolaritons with bigger wave vectors).

In order to show how powerful the model is in predictions of the dynamics of polarization, I simulated a TR-FWM experiments on GaAs multiple quantum wells described in Ref. [101] in Fig. 7.12. Buccafusca et al. measured the X– and Y–polarized components of the TR–FWM signal using two linearly polarized beams. The polarization planes were rotated by 60° one to the other. Also the time–resolved relative phase of the two detected polarizations was measured. The measurement then reveals the whole dynamics of the polarization of the FWM response. I simulated the experimental data using the presented model extended to quantum wells. Looking at Fig. 7.12, we may conclude that the basic characteristics are quite well reproduced by the model. There are still some inaccuracies which come probably from the fact that there are large uncertainties in the phenomenological constants. The peak positions as well as shapes of the curves are, however, in accordance to the experimental data. Also the temporal evolution of the relative phase agrees showing that the model is well applicable for a description of such experiments. Note that the $-180°$ phase shift at $t = 0$ is caused by the opposite sign of the scattering of two X–polarized polaritons: scattering to a pair of polaritons with X polarizations (X–polarized FWM response) has a positive sign while the scattering to the YY pair (Y–polarized FWM response) has a negative sign.

In conclusion, simulations presented in this section show the accuracy and limitations of the model presented in chapter 6.

7.10 Measurements of wave vector dependent interactions

7.10.1 Overview of the method

The model presented in chapter 6, as depicted in Fig. 6.7 gives an illustrative insight into the processes which are responsible for wave mixing in semiconductors. We clearly resolve three channels and based on their symmetry with respect to particle spin, polarization selection rules are determined algebraically in section 7.3. However these algebraic calculations are valid only under several conditions: we consider two dipole–active exciton states (eigenstates of the one–exciton Hamiltonian) which are degenerate in energy.

As discussed in section 3.3 and chapter 5, spin is not conserved in semiconductors when polaritons have a nonzero wave vector. The wave vector induced interaction then causes spin precession similar to precession in magnetic field. This precession cannot be, however, observed in standard pump and probe experiments or using another nonlinear time–resolved experimental technique in which the signal (induced change of the probe pulse intensity) is determined by populations of excitons. The reason is, that the FWM response comes only from particles with wave vectors $\boldsymbol{k}_1$, $\boldsymbol{k}_2$ and $\boldsymbol{k}_3$, respectively, while it comes from particles with a variety of wave vectors in pump and probe and other experiments. The overall response of an inhomogeneously broadened system of exciton spins is then similar to the enhanced decay of overall polarization known from optical Bloch equations — we may observe only a monotonous spin relaxation without any oscillations. There are experimental works in which a spontaneous spin–flip is measured using pump and probe method [105, 106, 107, 108, 109, 110, 111, 112] but from these experiments, it is obviously not possible to determine the (coherent) spin–flip rate as a function of wave vector.

It is, nevertheless, possible to use an indirect method for measurement of dispersion of polariton states. One may then numerically fit the dispersion curves which refer to dispersions of eigenenergies of polariton states. The appropriate methods are resonant Brillouin scattering, attenuated total reflection, hyper–Raman scattering etc. [26].

The idea of measurement of spin–flip processes using four–wave mixing was already illustrated in chapter 3. We excite a sample by the polarized light and we detect the spin of excited particles by a probe pulse. The problem is, however, that that spin precession takes place generally between all eight spin states of polaritons plus bipolariton effect must be accounted for. The proposed method for measurement of spin precession is following. We select a combination of polarizations of incoming beams from polarization selection rules of a system nonperturbed by wave vector dependent interaction under which the polarization of the response is stationary and well defined. Then we detect in a polarization perpendicular to the calculated direction. A nonzero signal is then expected to be a consequence of wave vector dependent interaction. For example, we may excite a crystal with zinc–blende structure by linearly polarized pulses with polarizations XXX. In the X polarization, the signal is dipole–allowed while it is forbidden in the Y polarization (see Tab. 7.3). A nonzero Y–polarized signal then indicates spin–flip processes (polarization setup of such measurement will be denoted as $XXX|Y$). The strength of k–linear interaction may be subsequently evaluated from the ratio of the intensity of the response with X and Y polarization, respectively.

Dynamics of the system of polaritons resolved in spin is too complex for analytical solution of equations of motion since coupling of spins occurs in every group of spin–resolved polaritons. It is more convenient to solve the equations numerically. I used the Hamiltonian (6.71) and the simplified level scheme for numerical calculations. I calculated the FWM response of bulk crystals with zinc–blende structure including k–linear interactions within the full basis of eight exciton and six biexciton states.

Calculations were performed for a CuBr crystal under several orientations with respect to the excitation beams. These orientations were [001], [110] and [111], respectively. Excitation was considered 10 meV below exciton resonance with pulses with duration 100 fs ($\sim$ 20 meV). Hamiltonian constructed by the method of invariants is taken from Refs. [26] and considering only k–linear terms, it reads:

$$\hat{H}_Q = \frac{1}{2} C_Q [Q_x \{\hat{J}_x, \hat{J}_y^2 - \hat{J}_z^2\} + c.p.] \otimes \mathbb{1}^{\mathrm{e}} + [(\Delta_{\mathrm{LT}} \cos\alpha \cos\beta \, |x\rangle\langle y| + c.p.) + H.c.] \,, \quad (7.20)$$

where Δ_{LT} stands for the LT splitting (nonanalytic exchange interaction), C_Q is the coupling strength, $\cos\alpha$, $\cos\beta$ and $\cos\gamma$ denote direction cosines of the wave vector and *c.p.* means cyclic permutation. Sample data are plotted in Fig. 7.13 — polarizations of incoming pulses are XXX and detection is in X (a,c) and Y polarization (b,d). The strength of k–dependent interaction C_Q is varied from 0 to $7.3 \cdot 10^{-6}$ eVμm [26]. Clearly the Y–polarized signal is caused by the spin precession due to k–linear interaction.

Calculations presented in Figs. 7.13a,c show that the signal in the dipole–forbidden polarization is by several orders of magnitude weaker than the signal in the dipole–allowed polarization. It might be therefore very hard to measure any sign of k–dependent interaction in TR–FWM experiments. However, looking at Figs. 7.13b,d, we find that the SR–FWM is better suitable for our purpose since the response in the dipole–forbidden polarization may be stronger than the response in the dipole–allowed polarization at some spectral positions.

Concerning the calculations, it is important to note that the spectral width of the bipolariton response is underestimated. In real experiments, also bipolaritons with higher wave vectors contribute to the FWM signal and thus spectra of the bipolariton response are usually significantly broader.

The reason, why the response on the spectral positions of the Γ_3 and Γ_5 bipolaritons as well as the response on the spectral position of excitons arise, needs further examination. Response in the dipole–forbidden polarization may be due to three processes:

- Spin–flip of polariton spin which results in the FWM response on the spectral position of exciton–like polariton states.
- Spin–flip of polariton spin which causes relaxation of dipole selection rules for excitation of bipolaritons.
- Spin–flip of bipolaritons.

We may study which of the mechanisms gives the strongest signal when looking at Fig. 7.14a. The plotted curves refer to calculations when the spin precession is taken into account for both polaritons and bipolaritons (black line), considering only spin–flip processes of bipolaritons (red) and considering only spin–flip processes of polariton spin (orange). The red and black curves differ only slightly and the orange curve is many orders of magnitude weaker indicating that the major process, which causes the FWM response under polarization setup $XXX|Y$ at the spectral position of bipolaritons, is the spin precession between bipolariton states.

It is known from Refs. [26, 113, 114] that the bipolariton spin precesses between all bipolariton states except for the Γ_1 bipolariton. Dipole selection rules imply following considering [001] propagation direction:

- The Γ_1 bipolariton is excited by two X–polarized pulses and the third X–polarized pulse annihilates it giving X–polarized FWM response.
- The state Γ_3^1 is excited and gives also the X–polarized response. It is coupled to the Γ_5 bipolaritons and considering the first–order processes, only the Γ_5^1 state contributes to the Y–polarized response.
- The state Γ_3^2 is excited, however it doesn't couple to the state Γ_5^1 which might give the Y–polarized response.
- States with Γ_5 symmetry are not coupled to the XX excitation field. Only the state Γ_5^1 contributes to Y–polarized response due to the spin structure XY and due to the coupling to the Γ_3^1 bipolariton (spin structure XX).

Clearly the FWM response with the dipole–forbidden polarization is due to coupling of bipolaritons as a consequence of wave vector dependent interaction. This statement may be proven by calculations when all bipolaritons are taken into account and only the state Γ_3^1 is omitted in calculations, see Fig. 7.14b.

The coupling energy between the two bipolariton states Γ_3^1 and Γ_5^1 is [26] $E_{\mathrm{k-lin}} = 2\sqrt{3}C_Q K_{\boldsymbol{k}_1+\boldsymbol{k}_2} \approx 2\sqrt{3}C_Q n_{\mathrm{b}} \varepsilon^{\Gamma_3^1}_{\boldsymbol{k}_1+\boldsymbol{k}_2}/\hbar c$, where n_{b} is background refractive index and $\varepsilon^{\Gamma_3^1}_{\boldsymbol{k}_1+\boldsymbol{k}_2}$ is the bipolariton energy. Energy of coupling, considering $C_Q = 7.3 \cdot 10^{-6}$ eVμm and $n_{\mathrm{b}} = 2.5$, is $E_{\mathrm{k-lin}} = 1.9$ meV what refers to 2.2 ps beating period. This coupling also causes shift of the resonance energies — their splitting was originally 1.5 meV and the interaction causes increase to 3.2 meV. Increase of the energy splitting between bipolariton states is clearly seen in calculation in Fig. 7.13d.

As seen in Fig. 7.14a, there is no response from the direct channel even though k–linear interaction couples pairs of exciton states. Two pairs of uncoupled dipole–active

states are created as a consequence of the symmetry breaking caused by the k–linear interaction [26], coupled excitons within each pair of states have symmetries Γ_4 and Γ_5. Using symmetry properties of the scattering matrices, it may be shown that no wave mixing is allowed. However when rotating the polarization of incoming fields, polarization selection rules change due to lack of invariance of elements which belong to the Γ_4 representation in the exchange scattering matrix with respect to rotations. Therefore when one selects other than X and Y polarizations of excitation pulses, he may observe a FWM signal in dipole–forbidden configuration as will be discussed later (cf. Fig. 7.15). The Y–polarized response in Fig. 7.14a is rather a numerical error and relaxation of dipole selection rules for bipolaritons does not induce any FWM signal in the particular case of [001] propagation axis. In other propagation directions, this effect may be important.

The FWM response is given by bipolaritons which have symmetries different from Γ_1 symmetry and therefore the orientation of the plane of polarization of incoming fields with respect to the crystallographic axes is very important. This property is illustrated in Fig. 7.15. Compared to the $XXX|Y$ configuration, the FWM response caused by k–linear interaction is by an order of magnitude weaker in the $RRR|L$ configuration. The respective R and L polarizations mean polarizations rotated by $+45°$ and $-45°$, respectively, with respect to the crystallographic axes x and y.

One may change time delays between excitation pulses in spectrally–resolved FWM experiments. Results of calculation of a two–beam experiment are plotted in Fig. 7.16a–b. The first graph shows the X response of a SR–FWM experiment when $t_1 = t_2$ and the time delay is $\tau = t_1 - t_3$, the second graph (b) then shows the Y–polarized response. It is interesting, that the graphs reveal quantum beats. These quantum beats then might be a sign of k–linear interaction. The period of beating in the Y–polarized response is 0.9 ps what is approximately one half of the aforementioned period 2.2 ps due to $\Gamma_3^1 \leftrightarrow \Gamma_5^1$ coupling. However, the bipolariton states are coupled to other states and therefore the beating period is slightly modified. Concerning the X–polarized response, the beating period is much shorter than theoretically estimated 1.1 ps showing a strong interplay of more than two bipolariton states.

7.10.2 Possible polarization setups

The previous subsection gives an overview of the phenomena connected with the k–linear interaction. In this subsection, I view the results of numerical calculations when polarizations of excitation beams and crystal orientations are changed. I selected polarizations from Tab. 7.3, for which the FWM response (without considering k–linear interaction) has a definite polarization. Then the influence of the k–linear interaction on the FWM response in the dipole–forbidden polarization is calculated. I do not give here the full list of the calculated results, only those which may be important for experiments are presented.

Calculations were done considering propagation directions [001], [110] and [111]. The direction [110] has low symmetry when compared to the other two cases and therefore spin is conserved only when polarizations of the excitation beams are X or Y. Numerical calculations confirmed that measurements in this direction would not give clear results and therefore propagation direction [110] is not further discussed.

In the following, I discuss a FWM signal which comes from bipolariton spin–flip and at the end of the subsection, influence of exciton–polariton spin–flip on FWM is shown.

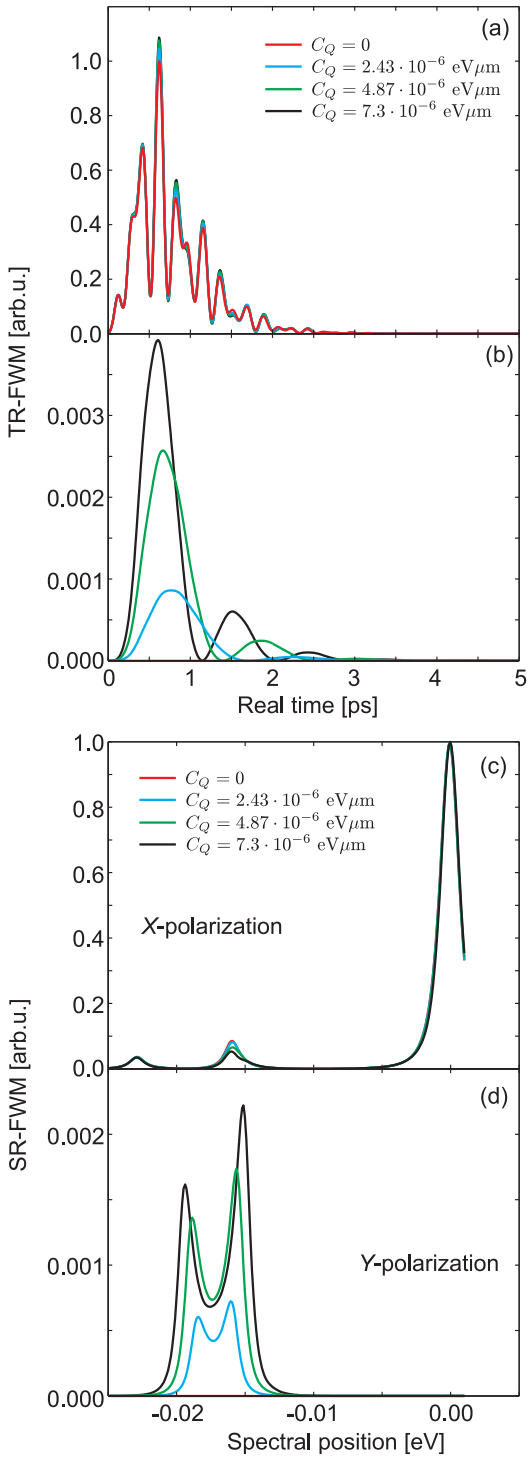

Figure 7.13: Simulated TR–FWM (a,b) and SR–FWM (c,d) response to XXX excitation and X (a,c) and Y (b,d) detection. Strength of k–linear interaction is varied.

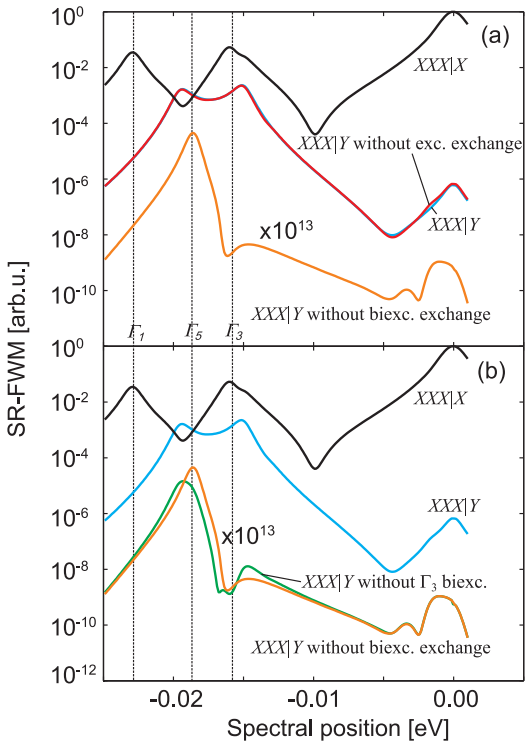

Figure 7.14: (a) Comparison of SR–FWM responses in $XXX|X$ and $XXX|Y$ setups including all interactions (black, blue) and neglecting k–linear interaction for polaritons (red) and bipolaritons (orange). (b) Same as (a) without the red line and showing response with all interactions when the Γ_3 bipolariton is missing (green).

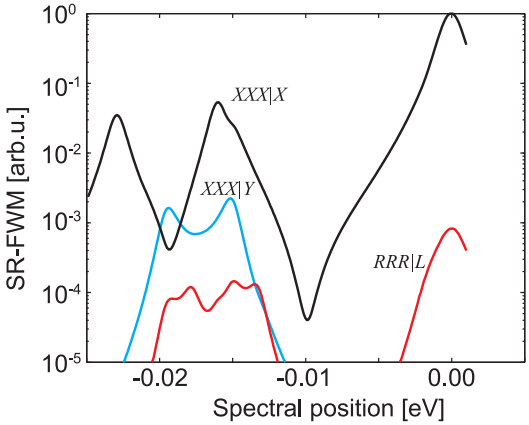

Figure 7.15: Comparison of $XXX|X$ (black), $XXX|Y$ (blue) and $RRR|L$ (red) responses in SR–FWM.

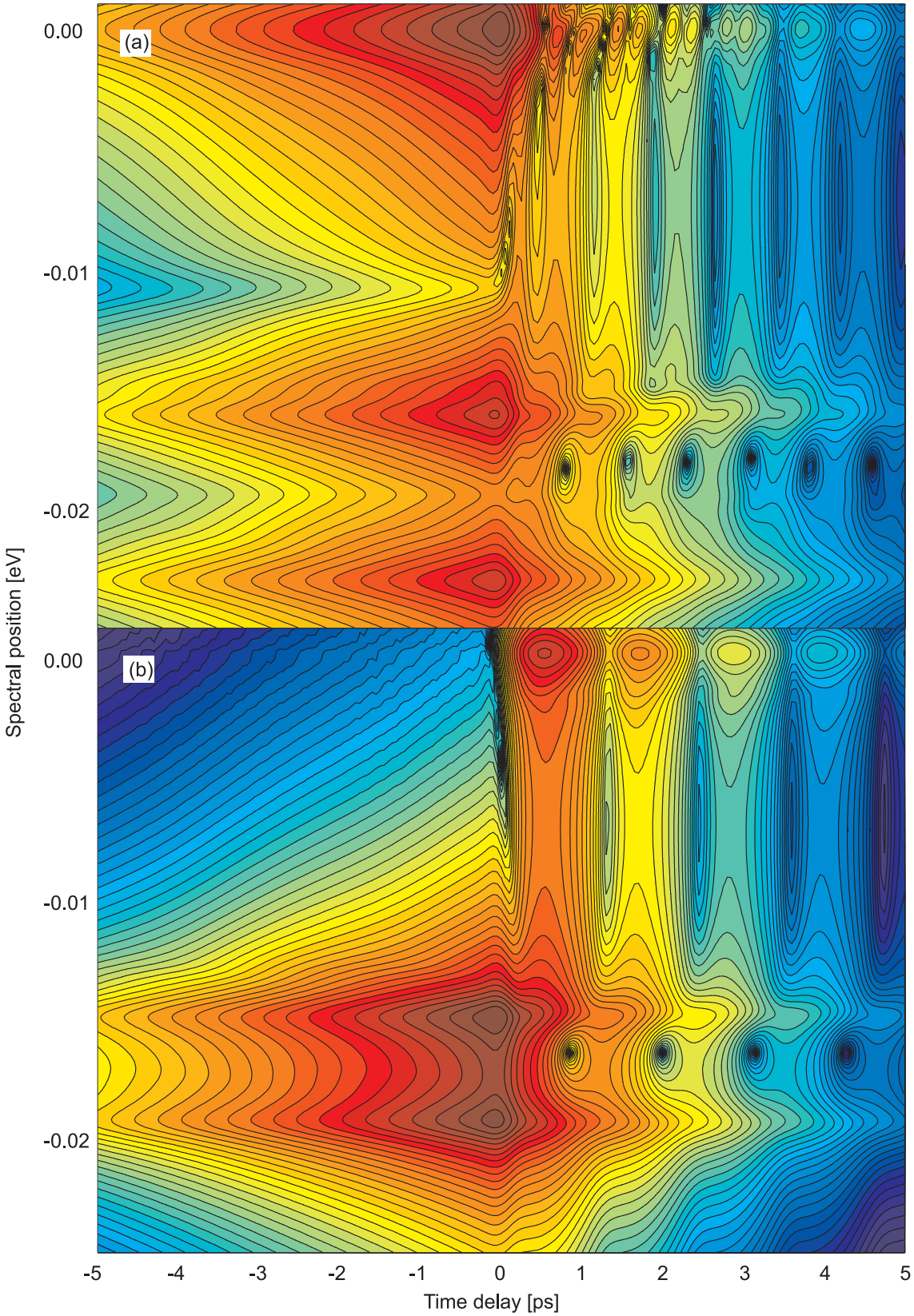

Figure 7.16: Simulated SR–FWM under $XXX|X$ and $XXX|Y$ when $t_1 = t_2$ and the delay $t_3 - t_2$ is varied. Plot is in log scale.

The $\boldsymbol{XXX|Y}$ configuration was already discussed in the previous subsection for the [001] propagation direction. Calculations for the [111] direction[1] reveal similar properties with two exceptions: the signal in the dipole–forbidden polarization is much weaker (by one order of magnitude) and the Γ_5 bipolariton is allowed in the dipole–active polarization. One may verify the hypothesis that the response is due to bipolariton spin–flip by measurement in the phase conjugation setup. Since the wave vector of bipolaritons is $\boldsymbol{k}_1 - \boldsymbol{k}_2 \approx 0$, the expected signal in the dipole–forbidden polarization is zero (see graph in Fig. 7.14b, green line).

The response in the setup $\boldsymbol{RRR|L}$[2] is very interesting when compared to $XXX|Y$ since the calculations show that it is not due to bipolariton spin–flip but due to relaxation of dipole selection rules for bipolaritons (see Fig. 7.17). However the signal is very weak (two orders of magnitude weaker than the dipole–allowed signal) and therefore only hardly measurable — the polariton spin–flip [28, 25, 26] is much less probable than the bipolariton spin–flip.

Polarization setup $\boldsymbol{XYX|X}$ is similar to the setup $XXX|Y$. Calculations show that the response is caused by the same effect — transitions between the states Γ_3^1 and Γ_5^1. Compared to the $XXX|Y$ situation, the transition goes in a reversed direction since the Γ_5^1 state is excited and the state Γ_3^1 is probed. This spin–flip process causes a better ratio between the signal in two respective polarizations — it is 1:23 in the $XXX|Y$ configuration and $1:10$ in the $XYX|X$ configuration. When using polarizations $\boldsymbol{RLR|R}$, the state Γ_3^1 is excited and Γ_5^1 is probed and the signal is weaker than in the $XYX|X$ configuration. Concerning the [111] direction, calculations show that the signal is due to relaxation of dipole selection rules, therefore it is very weak. The calculated spectra are plotted in Fig. 7.18.

The configuration $\boldsymbol{\sigma^+\sigma^-\sigma^+|\sigma^+}$ is very similar to the $XXX|Y$ and $XYX|X$ configurations since the signal is given by the spin–flip between bipolariton states Γ_3^1 and Γ_5^1, see Fig. 7.19. These two states arise in the response even though this polarization configuration is dipole–forbidden without k–linear interactions. The direction of propagation is very important since the signal vanishes in the [111] direction. In the $\boldsymbol{\sigma^+\sigma^+\sigma^-|\sigma^+}$ configuration, the dominant effect is again bipolariton spin–flip (see Fig. 7.20). The dipole–forbidden signal then vanishes in the [111] propagation direction because of its high symmetry.

When compared to the above polarization configurations, the responses in the configurations $\boldsymbol{\sigma^+X\sigma^-|\sigma^+}$ and $\boldsymbol{\sigma^+R\sigma^-|\sigma^+}$ are quite extraordinary. As seen in Fig. 7.21, the originally dipole–allowed response of the Γ_3 bipolariton is forbidden as a consequence of the k–linear interaction in the $\sigma^+X\sigma^-|\sigma^+$ configuration. On the contrary, it is allowed when the linear polarization is turned by 45°. Turning of the linear polarization in this configuration thus may be a good test for the validity of the presented calculations. In the [111] propagation direction, there is no response in this configuration of polarizations.

Now I discuss possible polarization setups under which the wave vector dependent interaction may be visualized at the exciton resonance in SR–FWM experiments. I considered pulses with duration 250 fs resonant with excitons in order to rule out influence of the bipolaritons (spectral width of the pulses is below 9 meV).

[1] For the [111] propagation direction, polarization is considered to be parallel with the projection of the crystallographic axis x on the crystal surface.

[2] To recall, R means a linear polarization rotated by 45° with respect to X, $R = (X + Y)/\sqrt{2}$ and L is a perpendicular linear polarization.

In the $\boldsymbol{XXX|Y}$ configuration, there is no response as already noted above while rotation of the polarization direction by 45° causes a nonzero signal in the configuration $\boldsymbol{RRR|L}$ in the [001] direction as seen in Fig. 7.23. Concerning the [111] propagation direction, spectra are not plotted in the graph but the response in the dipole–forbidden configuration arises for both $XXX|Y$ and $RRR|L$ configurations (not shown in the graph). We get very similar results also for the polarization setups $XYX|X$ and $RLR|R$.

Configurations $\boldsymbol{XXY|X}$ and $\boldsymbol{RRL|R}$ are similar to the aforementioned setups with linear polarizations, however there is a difference that the spectra are considerably assymetric and the maxima are shifted from the exciton resonance, see Fig. 7.24. I plotted by dashed lines also the responses for the configurations $XXY|X, Y$ in the [111] direction for comparison, the responses for configurations $RRL|R, L$ in the [111] direction are equal. Clearly the responses for [001] and [111] propagation directions are similar.

For circular polarizations, FWM response in the dipole–forbidden configuration is forbidden when considering [111] propagation axis except the $\sigma^+\sigma^+\sigma^+|\sigma^{+,-}$ configurations. The results for $\boldsymbol{\sigma^+\sigma^+\sigma^-|\sigma^{+,-}}$ and $\boldsymbol{\sigma^+\sigma^+\sigma^-|\sigma^{+,-}}$ for [001] propagation directions are plotted in Fig. 7.25. In the former configuration, the signal in the dipole–forbidden configuration is much weaker than the signal in the dipole–allowed configuration and it may be thus hard to detect it. In the latter situation, on the contrary, the difference is only one order of magnitude and this configuration is better suitable for an experiment.

7.10.3 Proposal of experimental setup

It seems from the calculated data that the polarization configuration $XYX|X$ might be the best one for experimental measurement of bipolariton spin–flip when the propagation direction is [001] and the exciton spin–flip might be seen when the propagation direction is [111].

Concerning bipolaritons, the proposed experimental setup is the following. The sample is excited by two spectrally narrow pulses ($\boldsymbol{K}_1$, $\boldsymbol{K}_2$) resonantly with the Γ_5 bipolaritons (energy 5.9103 eV, pulse duration 2 ps). The third spectrally narrow pulse then probes coherence of the Γ_3^1 bipolariton which is spectrally shifted and thus arise in the dipole–forbidden polarization at the spectral position of the Γ_5 bipolariton, see Fig. 7.22. In the $XYX|X$ setup, the (strong) signal is due to bipolariton spin–flip and it is almost comparable to the size of the dipole–allowed signal. On the contrary, in the $RLR|R$ configuration, the signal is very weak. Rotation of the polarizations with respect to the crystallographic axes clearly visualize the k–linear interaction of bipolaritons. In order to further support calculations, a similar experiment may be done in the phase conjugation geometry. In such case, no strong signal is expected since the bipolariton spin–flip is forbidden.

The exciton spin–flip which causes relaxation of the dipole selection rules for bipolaritons may be observed in the same configuration as described above, however a crystal cut and polished to have [111]–oriented surfaces is used. Under these conditions, bipolariton response is forbidden and one observes a signal in the $X'Y'X'|X'$ polarization configuration which does not change when rotating the polarizations around the propagation axis.

For a measurement of the exciton spin–flip on the exciton resonance, I propose the following measurement. Using the [001]–oriented sample, the system is excited by XXY pulses and the polarization X is selected for detection. No signal is expected and the relaxation of polarization selection rules due to wave vector dependent interaction may be seen when rotating all polarization by 45° — the response in the dipole–forbidden

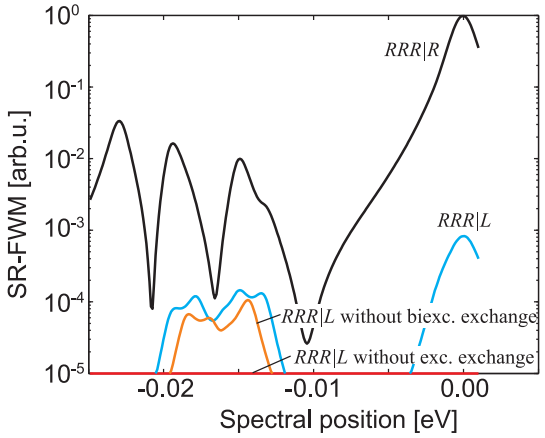

Figure 7.17: Simulation of SR–FWM response under $RRR|R$ and $RRR|L$ setups.

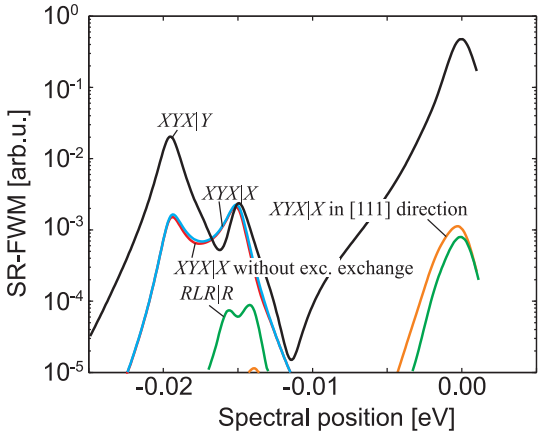

Figure 7.18: Simulation of SR–FWM response under $XYX|Y$, $XYX|X$ and $RLR|R$ setups.

polarization becomes nonzero, only by one order of magnitude weaker than the signal in the dipole–allowed polarization. In the resulting $RRL|R$ configuration, a nonzero signal should be seen, the rotation of the polarizations of the incoming beams and the detection with respect to crystallographic axes may be then used in order to verify that the signal in the dipole–forbidden configuration is not an experimental error. One may perform a similar measurement using the $\sigma^+\sigma^+\sigma^-|\sigma^{+,-}$ setup, however there is no possibility of verification that the nonzero signal is not just an artifact.

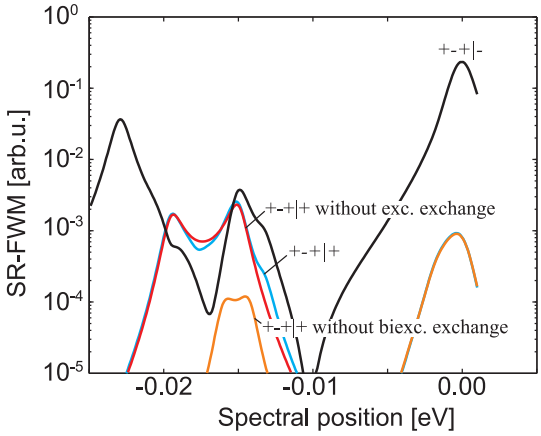

Figure 7.19: Simulation of SR–FWM response under $\sigma^+\sigma^-\sigma^+|\sigma^-$ and $\sigma^+\sigma^-\sigma^+|\sigma^+$ setups.

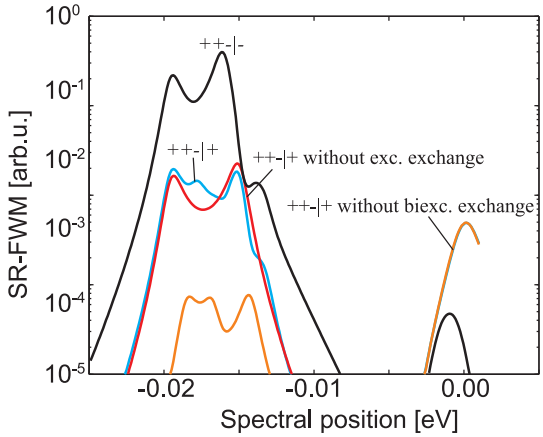

Figure 7.20: Simulation of SR–FWM response under $\sigma^+\sigma^+\sigma^-|\sigma^-$ and $\sigma^+\sigma^+\sigma^-|\sigma^+$ setups.

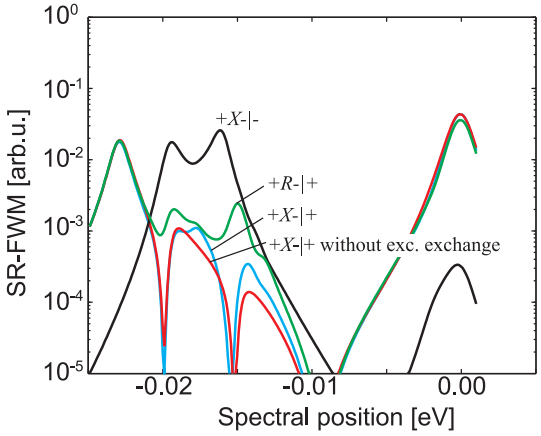

Figure 7.21: Simulation of SR–FWM response under $\sigma^+X\sigma^+|\sigma^-$, $\sigma^+X\sigma^+|\sigma^+$ and $\sigma^+R\sigma^+|\sigma^+$ setups.

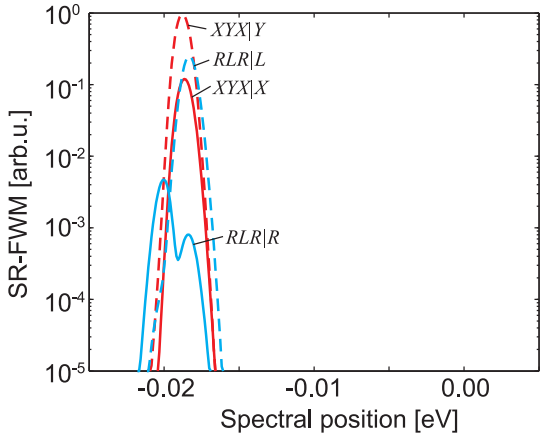

Figure 7.22: Simulated data for a proposed experiment for measurement of the wave vector dependent interaction with spectrally narrow pulses in setups $XYX|X,Y$ and $RLR|R,L$.

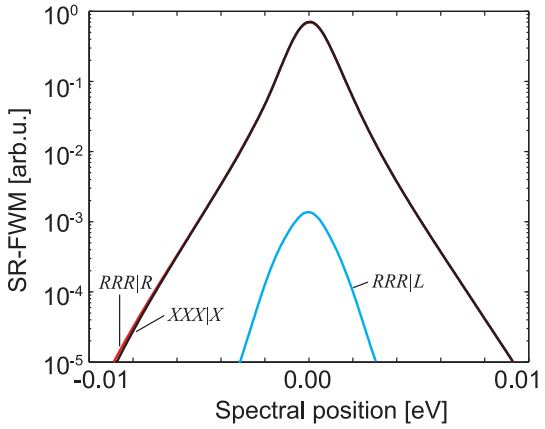

Figure 7.23: Simulation of SR–FWM response in [001] direction under $RRR|R, L$ and $XXX|X$ setups of excitation beams ($XXX|Y$ gives no response). Only the response of exciton–like polaritons is detected when using 250 fs pulses.

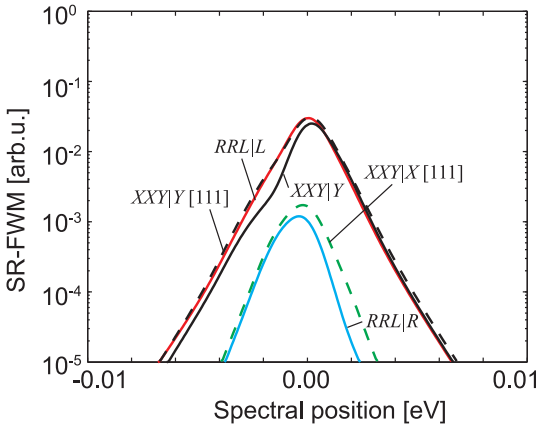

Figure 7.24: Simulation of SR–FWM response in [001] and [111] directions under $RRL|R, L$ and $XXY|X, Y$ setups of excitation beams ($XXX|Y$ gives no response in the [001] direction). Only the response of exciton–like polaritons is detected when using 250 fs pulses.

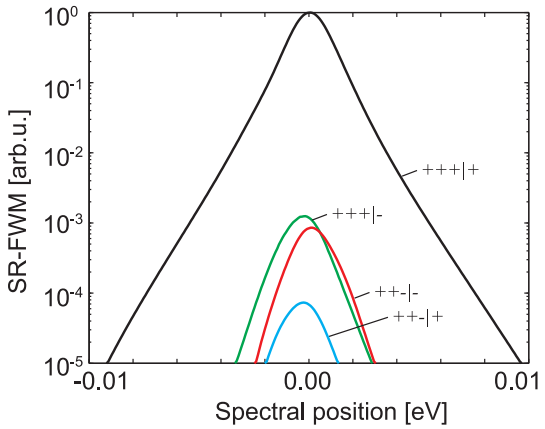

Figure 7.25: Simulation of SR–FWM response in [001] direction under $\sigma^+\sigma^+\sigma^+|\sigma^+, \sigma^-$ setups of excitation beams. Only the response of exciton–like polaritons is detected when using 250 fs pulses.

Chapter 8

Conclusions

In this thesis, I show the way how polarization selection rules of FWM experiments on semiconductors and their nanostructures may be determined. I show that polarization selection rules strongly depend on the system's dimensionality and therefore one must use different approaches for description of bulk semiconductors and quantum dots. This fact is illustrated in chapter 4 in which I show that delocalized (3D in bulk) noninteracting bosons cannot provide any wave mixing while localization (0D in quantum dots) opens a wave mixing channel even if the states do not interact one with the other. It is then clear that the principle of wave mixing differs in both systems and one may expect that polarization selection rules differ as well.

In quantum dots, wave mixing comes from the fact that every state interacts with optical fields in all directions. One may apply directly the concept of optical Bloch equations (OBE) to nanocrystals, however it must be extended in order to describe the spin and also the correct statistics of particles since excitons are bosons. I discuss various level schemes appropriate for description of FWM response of nanocrystals under different experimental conditions in chapter 5 and I derive polarization selection rules for these schemes.

Since the level schemes are equal to the level schemes used in literature for description of FWM response on bulk semiconductors and quantum wells, I investigate whether the theoretically derived and experimentally verified polarization selection rules are reproduced by any of the considered systems or not. The conclusion is, that none of the schemes is applicable to bulk semiconductors. This statement then justifies development of a new model for description of FWM on bulk semiconductors.

It is shown above that the wave mixing is caused by some particle–particle interaction in bulk semiconductors. I find two interactions which may provide wave mixing: Pauli blocking due to fractional Fermi character of excitons and exciton–exciton Coulomb interaction which causes polariton–polariton interaction. These two interactions then give rise to three different wave mixing channels well resolved in the developed model, which differ in polarization selection rules and their dynamics: the *direct channel* (Coulomb polariton–polariton scattering without any intermediate state), the *bipolariton channel* (bipolariton–mediated polariton–polariton scattering) and the *diffraction channel* (diffraction on a transient diffraction grating created at the sample's surface).

The wave mixing through the diffraction channel is very similar to the effect of Pauli blocking in atomic systems: excited polariton modes in the crystal create local minima and maxima of populations of electrons and holes. These variations form a grating and, as a consequence, the second–order susceptibility causes scattering of incident waves. This process is similar to the process of diffraction on a transient grating in atomic systems, however polarization selection rules reasonably differ in the atomic and the bulk systems.

The direct channel provides scattering of an initial two–polariton state in which polaritons have wave vectors $\boldsymbol{k}_1$ and $\boldsymbol{k}_2$ to a variety of states with wave vectors $\boldsymbol{k}_1+\boldsymbol{q}$ and $\boldsymbol{k}_2-\boldsymbol{q}$ due to wave vector conservation. But only the states in which one of the wave vectors equals $\boldsymbol{k}_3$ may interact with the field in the direction $\boldsymbol{k}_3$ (due to the aforementioned selection rule for wave vector for dipole interaction) and therefore this field causes population of strongly correlated states with wave vector $\boldsymbol{k}_1+\boldsymbol{k}_2-\boldsymbol{k}_3$. This population then radiates coherent FWM signal in the mentioned FWM direction. Polarization selection rules for the direct channel clearly reflect the symmetry of exciton–exciton interactions. The bipolariton channel acts in a similar way as the direct channel, but it has different dynamics and polarization selection rules due to the symmetry of the bipolariton states.

The sum of the particular responses of the three channels then gives the overall FWM response. Since the dynamics and polarization selection rules of the respective channels may differ considerably, the overall response reveals interesting phenomena. For example interference of the responses of the bipolariton and the direct channel cause beating of the signal because of the nonzero bipolariton binding energy. One may also observe some temporal evolution of the overall polarization if the polarizations of the responses of the respective channels differ for some setup of polarizations of the incident beams.

The model is formulated in the framework of polaritons which allows us to describe the FWM response over the whole spectral range of incident pulses. Considering an optically thin sample, it is possible to reduce the big number of states which influence the FWM creation to a few–level scheme with the structure similar to modified OBE known from literature. It is therefore possible to perform direct integration of equations and also to derive algebraic expressions for determination of polarization selection rules. Based on the algebraic calculations of selection rules, I verified that the model gives correct results when compared to data published in literature.

Since quantum wells reveal translational symmetry, I show how the model may be extended to describe two–dimensional structures. Then I show calculations in order to reproduce experimental data on GaAs quantum wells published in literature. I show in chapter 7 that the experimental data are well fitted using the presented model which may be therefore used for predictions of polarization dynamics and FWM spectra.

After a general discussion of the developed model, I present a discussion of a possibility of measurement of weak wave vector dependent interactions which cause spin–flips due to nonzero wave vector of excitons. The basic idea is following: without the symmetry breaking due to the interaction, the considered sample would reveal some polarization selection rules. Taking the interaction into account, these selection rules change slightly. This small change then may be observed as a relaxation of polarization selection rules for some dipole–forbidden configuration, i.e. the perturbation causes a nonzero signal of the FWM response in the polarization which is dipole–forbidden without taking the perturbation into account. Based on the calculated nonperturbed and perturbed spectra of the FWM response with the parameters of CuBr, I propose an experiment in which the strength of the interaction might be measured. I find several setups which I propose for a measurement of the exciton and biexciton spin precession using FWM spectroscopy.

The models for description of bulk semiconductors, quantum wells and quantum dots, proposed in this thesis, may be used in order to propose an experiment designed for detection of a general spin–flip process which takes place during evolution of the excited system as a consequence of an arbitrary symmetry–breaking effect. One may measure in this way for example influence of electric fields or homogeneous stress on exchange interactions. The model for description of bulk semiconductors then opens a possibility of development of new experimental techniques in ultrafast nonlinear laser spectroscopy.

Appendix A

Biexciton Hamiltonian in quantum wells

The terms of Hamiltonian appropriate for Biexciton Hamiltonian in quantum wells from a material with zinc–blende and wurtzite structure are listed below. Numbers in superscripts stand for the number of a particle: holes are numbered as $^{(2)}$ and $^{(4)}$ and electrons $^{(1)}$ and $^{(3)}$. Symbols P_{13} and P_{24} then permute superscripts in the preceding terms.

A.1 Zinc–blende in [001] direction

$$
\begin{aligned}
\text{h}-\text{h exchange}: \quad & \hat{J}_x^{(2)}\hat{J}_x^{(4)} + \hat{J}_y^{(2)}\hat{J}_y^{(4)} \\
& \hat{J}_z^{(2)}\hat{J}_z^{(4)} \\
& \hat{J}_x^{(2)}\{\hat{J}_x^{(4)}, \hat{J}_y^{(4)^2} - \hat{J}_z^{(4)^2}\} + \hat{J}_y^{(2)}\{\hat{J}_y^{(4)}, \hat{J}_x^{(4)^2} - \hat{J}_z^{(4)^2}\} + P_{24} \\
& \hat{J}_x^{(2)}\hat{J}_x^{(4)^3} + \hat{J}_y^{(2)}\hat{J}_y^{(4)^3} + P_{24} \\
& \{\hat{J}_x^{(2)}, \hat{J}_z^{(2)}\} \cdot \{\hat{J}_x^{(4)}, \hat{J}_z^{(4)}\} + \{\hat{J}_y^{(2)}, \hat{J}_z^{(2)}\} \cdot \{\hat{J}_y^{(4)}, \hat{J}_z^{(4)}\} \\
& \hat{J}_z^{(2)}\hat{J}_z^{(4)^3} + P_{24} \\
& \hat{J}_z^{(2)^2}\hat{J}_z^{(4)^2} \\
& (\hat{J}_x^{(2)^2} - \hat{J}_y^{(2)^2})(\hat{J}_x^{(4)^2} - \hat{J}_y^{(4)^2}) \\
& \{\hat{J}_x^{(2)}, \hat{J}_y^{(2)}\}\{\hat{J}_x^{(4)}, \hat{J}_y^{(4)}\} \\
& \hat{J}_z^{(2)^3}\hat{J}_z^{(4)^3} \\
& \hat{J}_z^{(2)}\{\hat{J}_x^{(2)}, \hat{J}_y^{(2)}\} \cdot \hat{J}_z^{(4)}\{\hat{J}_x^{(4)}, \hat{J}_y^{(4)}\} \\
& \hat{J}_z^{(2)^2}\{\hat{J}_x^{(2)}, \hat{J}_y^{(2)}\} \cdot \hat{J}_z^{(4)^2}\{\hat{J}_x^{(4)}, \hat{J}_y^{(4)}\} \\
& \hat{J}_z^{(2)^2}\{\hat{J}_x^{(2)}, \hat{J}_y^{(2)}\} \cdot \{\hat{J}_x^{(4)}, \hat{J}_y^{(4)}\} + P_{24} \\
& \{\hat{J}_x^{(2)}, \hat{J}_y^{(2)^2} - \hat{J}_z^{(2)^2}\} \cdot \{\hat{J}_x^{(4)^2}, \hat{J}_y^{(4)^2} - \hat{J}_z^{(4)^2}\} + \\
& \qquad + \{\hat{J}_y^{(2)}, \hat{J}_x^{(2)^2} - \hat{J}_z^{(2)^2}\} \cdot \{\hat{J}_y^{(4)}, \hat{J}_x^{(4)^2} - \hat{J}_z^{(4)^2}\} \\
& \hat{J}_x^{(2)^3}\hat{J}_x^{(4)^3} + \hat{J}_y^{(2)^3}\hat{J}_y^{(4)^3} \\
& \hat{J}_x^{(2)^3}\{\hat{J}_x^{(4)}, \hat{J}_y^{(4)^2} - \hat{J}_z^{(4)^2}\} + \hat{J}_y^{(2)^3}\{\hat{J}_y^{(4)}, \hat{J}_x^{(4)^2} - \hat{J}_z^{(4)^2}\} + P_{24}
\end{aligned}
\tag{A.1}
$$

A.2 Zinc–blende in [110] direction

$$
\begin{aligned}
\text{h}-\text{h exchange}: \; & \hat{J}_x^{(2)}\hat{J}_x^{(4)} \\
& \hat{J}_y^{(2)}\hat{J}_y^{(4)} \\
& \hat{J}_z^{(2)}\hat{J}_z^{(4)} \\
& \{\hat{J}_x^{(2)}\{\hat{J}_x^{(4)},\hat{J}_y^{(4)^2}\}\}+P_{24} \\
& \{\hat{J}_y^{(2)}\{\hat{J}_y^{(4)},\hat{J}_x^{(4)^2}\}\}+P_{24} \\
& \{\hat{J}_z^{(2)}\{\hat{J}_z^{(4)},\hat{J}_x^{(4)^2}\}\}+P_{24} \\
& \hat{J}_x^{(2)}\hat{J}_x^{(4)^3}+P_{24} \\
& \hat{J}_y^{(2)}\hat{J}_y^{(4)^3}+P_{24} \\
& \hat{J}_z^{(2)}\hat{J}_z^{(4)^3}+P_{24} \\
& \{\hat{J}_y^{(2)},\hat{J}_z^{(2)}\}\cdot\{\hat{J}_y^{(4)},\hat{J}_z^{(4)}\} \\
& \{\hat{J}_x^{(2)},\hat{J}_z^{(2)}\}\cdot\{\hat{J}_x^{(4)},\hat{J}_z^{(4)}\} \\
& \{\hat{J}_x^{(2)},\hat{J}_y^{(2)}\}\cdot\{\hat{J}_x^{(4)},\hat{J}_y^{(4)}\} \\
& \hat{J}_x^{(2)^3}\hat{J}_x^{(4)^3} \\
& \hat{J}_y^{(2)^3}\hat{J}_y^{(4)^3} \\
& \hat{J}_z^{(2)^3}\hat{J}_z^{(4)^3} \\
& \{\hat{J}_x^{(2)},\hat{J}_y^{(2)^2}\}\cdot\{\hat{J}_x^{(4)},\hat{J}_y^{(4)^2}\} \\
& \{\hat{J}_y^{(2)},\hat{J}_x^{(2)^2}\}\cdot\{\hat{J}_y^{(4)},\hat{J}_x^{(4)^2}\} \\
& \{\hat{J}_z^{(2)},\hat{J}_x^{(2)^2}\}\cdot\{\hat{J}_z^{(4)},\hat{J}_x^{(4)^2}\} \\
& \{\hat{J}_x^{(2)^3}\{\hat{J}_x^{(4)},\hat{J}_y^{(4)^2}\}\}+P_{24} \\
& \{\hat{J}_y^{(2)^3}\{\hat{J}_y^{(4)},\hat{J}_x^{(4)^2}\}\}+P_{24} \\
& \{\hat{J}_z^{(2)^3}\{\hat{J}_z^{(4)},\hat{J}_x^{(4)^2}\}\}+P_{24} \\
& \hat{J}_x^{(2)^2}\hat{J}_x^{(4)^2} \\
& \hat{J}_z^{(2)^2}\hat{J}_z^{(4)^2} \\
& \hat{J}_x^{(2)^2}\hat{J}_z^{(4)^2}+P_{24} \\
& \{\hat{J}_x^{(2)},\{\hat{J}_y^{(2)},\hat{J}_z^{(2)}\}\}\{\hat{J}_x^{(4)},\{\hat{J}_y^{(4)},\hat{J}_z^{(4)}\}\}
\end{aligned}
\tag{A.2}
$$

A.3 Zinc–blende in [111] direction

$$
\begin{array}{ll}
\text{e}-\text{e exchange}: & \hat{\sigma}_+^{(1)}\hat{\sigma}_-^{(3)} + P_{13} \\
& \hat{\sigma}_z^{(1)}\hat{\sigma}_z^{(3)} \\
\hline
\text{h}-\text{h exchange}: & \hat{J}_z^{(2)}\hat{J}_z^{(4)} \\
& \hat{J}_z^{(2)}\hat{J}_z^{(4)^3} + P_{24} \\
& \hat{J}_z^{(2)^3}\hat{J}_z^{(4)^3} + P_{24} \\
& \hat{J}_+^{(2)}\hat{J}_-^{(4)} + P_{24} \\
& \{\hat{J}_+^{(2)}, \{\hat{J}_+^{(4)}, \hat{J}_-^{(4)^2}\}\} + \{\hat{J}_-^{(2)}, \{\hat{J}_-^{(4)}, \hat{J}_+^{(4)^2}\}\} + P_{24} \\
& \{\hat{J}_+^{(2)}, \hat{J}_-^{(2)^2}\} \cdot \{\hat{J}_-^{(4)}, \hat{J}_+^{(4)^2}\} + P_{24} \\
& \hat{J}_+^{(2)^2}\hat{J}_-^{(4)^2} + P_{24} \\
& \{\hat{J}_z^{(2)}, \hat{J}_+^{(2)^2}\} \cdot \{\hat{J}_z^{(4)}, \hat{J}_-^{(4)^2}\} + P_{24} \\
& \mathrm{i}\{\hat{J}_+^{(2)^2}, \{\hat{J}_z^{(4)}, \hat{J}_-^{(4)^2}\}\} - \mathrm{i}\{\hat{J}_-^{(2)^2}, \{\hat{J}_z^{(4)}, \hat{J}_+^{(4)^2}\}\} + P_{24} \\
& (\hat{J}_-^{(2)^3} - \hat{J}_+^{(2)^3}) \cdot (\hat{J}_-^{(4)^3} - \hat{J}_+^{(4)^3}) \\
& \{\hat{J}_+^{(2)}, \hat{J}_-^{(2)}\} \cdot \{\hat{J}_+^{(4)}, \hat{J}_-^{(4)}\} \\
& (\hat{J}_+^{(2)^3} + \hat{J}_-^{(2)^3}) \cdot (\hat{J}_+^{(4)^3} + \hat{J}_-^{(4)^3}) \\
& \hat{J}_+^{(2)}\{\hat{J}_-^{(4)}, \{\hat{J}_+^{(4)}, \hat{J}_-^{(4)}\}\} + \hat{J}_-^{(2)}\{\hat{J}_+^{(4)}, \{\hat{J}_+^{(4)}, \hat{J}_-^{(4)}\}\} + P_{24} \\
& \{\hat{J}_+^{(2)}, \hat{J}_-^{(2)^2}\} \cdot \{\hat{J}_-^{(4)}, \{\hat{J}_+^{(4)}, \hat{J}_-^{(4)}\}\} + \{\hat{J}_-^{(2)}, \hat{J}_+^{(2)^2}\} \cdot \{\hat{J}_+^{(4)}, \{\hat{J}_+^{(4)}, \hat{J}_-^{(4)}\}\} + P_{24} \\
& \{\hat{J}_+^{(2)}, \{\hat{J}_+^{(2)}, \hat{J}_-^{(2)}\}\} \cdot \{\hat{J}_-^{(4)}, \{\hat{J}_+^{(4)}, \hat{J}_-^{(4)}\}\} + P_{24} \\
\hline
\text{e}-\text{hexchange}: & [\hat{\sigma}_z^{(1)}\hat{J}_z^{(2)} + P_{13}] + P_{24} \\
& [\hat{\sigma}_z^{(1)}\hat{J}_z^{(2)^3} + P_{13}] + P_{24} \\
& [\hat{\sigma}_-^{(1)}\hat{J}_+^{(2)} + \hat{\sigma}_+^{(1)}\hat{J}_-^{(2)} + P_{13}] + P_{24} \\
& [\hat{\sigma}_-^{(1)}\{\hat{J}_-^{(2)}, \hat{J}_+^{(2)^2}\} + \hat{\sigma}_+^{(1)}\{\hat{J}_+^{(2)}, \hat{J}_-^{(2)^2}\} + P_{13}] + P_{24} \\
& [\hat{\sigma}_+^{(1)}\{\hat{J}_-^{(2)}, \{\hat{J}_+^{(2)}, \hat{J}_-^{(2)}\}\} + \hat{\sigma}_-^{(1)}\{\hat{J}_+^{(2)}, \{\hat{J}_+^{(2)}, \hat{J}_-^{(2)}\}\} + P_{13}] + P_{24}
\end{array}
\tag{A.3}
$$

A.4 Wurtzite in [001] direction

$$
\begin{array}{ll}
\text{e}-\text{e exchange}: & \hat{\sigma}_+^{(1)}\hat{\sigma}_-^{(3)} + P_{13} \\
& \hat{\sigma}_z^{(1)}\hat{\sigma}_z^{(3)} \\
\hline
\text{h}-\text{h exchange}: & \hat{J}_z^{(2)}\hat{J}_z^{(4)} \\
& \hat{J}_z^{(2)^2}\hat{J}_z^{(4)^2} \\
& \hat{J}_z^{(2)^3}\hat{J}_z^{(4)^3} \\
& \hat{J}_z^{(2)}\hat{J}_z^{(4)^3} + P_{24} \\
& (\hat{J}_+^{(2)^3} + \hat{J}_-^{(2)^3}) \cdot (\hat{J}_+^{(4)^3} + \hat{J}_-^{(4)^3}) \\
& (\hat{J}_+^{(2)^3} - \hat{J}_-^{(2)^3}) \cdot (\hat{J}_+^{(4)^3} - \hat{J}_-^{(4)^3}) \\
& \hat{J}_+^{(2)}\hat{J}_-^{(4)} + P_{24} \\
& \{\hat{J}_+^{(2)}, \{\hat{J}_+^{(4)}, \hat{J}_-^{(4)^2}\}\} + \{\hat{J}_-^{(2)}, \{\hat{J}_-^{(4)}, \hat{J}_+^{(4)^2}\}\} + P_{24} \\
& \mathrm{i}(\{\hat{J}_+^{(2)}, \{\hat{J}_z^{(4)}, \hat{J}_-^{(4)}\}\} - \{\hat{J}_-^{(2)}, \{\hat{J}_z^{(4)}, \hat{J}_+^{(4)}\}\}) + P_{24} \\
& \{\hat{J}_+^{(2)}, \hat{J}_-^{(2)^2}\} \cdot \{\hat{J}_-^{(4)}, \hat{J}_+^{(4)^2}\} + P_{24} \\
& \mathrm{i}(\{\{\hat{J}_+^{(2)}, \hat{J}_-^{(2)^2}\}, \{\hat{J}_z^{(4)}, \hat{J}_+^{(4)}\}\} - \{\{\hat{J}_-^{(2)}, \hat{J}_+^{(2)^2}\}, \{\hat{J}_z^{(4)}, \hat{J}_-^{(4)}\}\}) + P_{24} \\
& \{\hat{J}_z^{(2)}, \hat{J}_-^{(2)}\} \cdot \{\hat{J}_z^{(4)}, \hat{J}_+^{(4)}\} + P_{24} \\
& \hat{J}_+^{(2)^2}\hat{J}_-^{(4)^2} + P_{24} \\
& \{\hat{J}_z^{(2)}, \hat{J}_+^{(2)^2}\} \cdot \{\hat{J}_z^{(4)}, \hat{J}_-^{(4)^2}\} + P_{24} \\
& \mathrm{i}(\{\hat{J}_+^{(2)^2}, \{\hat{J}_z^{(4)}, \hat{J}_-^{(4)^2}\}\} - \{\hat{J}_-^{(2)^2}, \{\hat{J}_z^{(4)}, \hat{J}_+^{(4)^2}\}\}) + P_{24} \\
\hline
\text{e}-\text{h exchange}: & [\hat{\sigma}_z^{(1)}\hat{J}_z^{(2)} + P_{13}] + P_{24} \\
& [\hat{\sigma}_z^{(1)}\hat{J}_z^{(2)^3} + P_{13}] + P_{24} \\
& [\hat{\sigma}_+^{(1)}\hat{J}_-^{(2)} + \hat{\sigma}_-^{(1)}\hat{J}_+^{(2)} + P_{13}] + P_{24} \\
& [\hat{\sigma}_+^{(1)}\{\hat{J}_+^{(2)}, \hat{J}_-^{(2)^2}\} + \hat{\sigma}_-^{(1)}\{\hat{J}_-^{(2)}, \hat{J}_+^{(2)^2}\} + P_{13}] + P_{24} \\
& \mathrm{i}[\hat{\sigma}_+^{(1)}\{\hat{J}_z^{(2)}, \hat{J}_-^{(2)}\} - \hat{\sigma}_-^{(1)}\{\hat{J}_z^{(2)}, \hat{J}_+^{(2)}\} + P_{13}] + P_{24}
\end{array}
\tag{A.4}
$$

Appendix B

Equations of motion of the model

B.1 General equations of motion

Equations of motion which arise directly from Hamiltonian (6.71) read:

$$[\mathrm{i}\hbar\partial_t+\gamma_2]\tilde{\varrho}^{(1)}_{S\boldsymbol{k}_1,0}(t) = \mathrm{i}\mathcal{E}_{\boldsymbol{e},\boldsymbol{K}_1}(t)\mathrm{e}^{-\mathrm{i}(\omega_{\boldsymbol{K}_1}-h_{SS\boldsymbol{k}_1}/\hbar)t}\mu_{S,\boldsymbol{K}_1}\langle S|\,\boldsymbol{e}\rangle + \\ + \sum_{S'\neq S} h_{S'S,\boldsymbol{k}_1}\mathrm{e}^{-\mathrm{i}(h_{S'S'\boldsymbol{k}_1}-h_{SS,\boldsymbol{k}_1})t/\hbar}\tilde{\varrho}^{(1)}_{0,S'\boldsymbol{k}_1}(t)\,, \tag{B.1}$$

$$[\mathrm{i}\hbar\partial_t+\gamma_2]\tilde{\varrho}^{(1)}_{S\boldsymbol{k}_2,0}(t) = \mathrm{i}\mathcal{E}_{\boldsymbol{e},\boldsymbol{K}_2}(t)\mathrm{e}^{-\mathrm{i}(\omega_{\boldsymbol{K}_2}-h_{SS\boldsymbol{k}_2}/\hbar)t}\mu_{S,\boldsymbol{K}_2}\langle S|\,\boldsymbol{e}\rangle + \\ + \sum_{S'\neq S} h_{S'S,\boldsymbol{k}_2}\mathrm{e}^{-\mathrm{i}(h_{S'S'\boldsymbol{k}_2}-h_{SS,\boldsymbol{k}_2})t/\hbar}\tilde{\varrho}^{(1)}_{0,S'\boldsymbol{k}_2}(t)\,, \tag{B.2}$$

$$[\mathrm{i}\hbar\partial_t+\gamma_2]\tilde{\varrho}^{(1)}_{0,S\boldsymbol{k}_3}(t) = \mathrm{i}\mathcal{E}^*_{\boldsymbol{e},\boldsymbol{K}_3}(t)\mathrm{e}^{+\mathrm{i}(\omega_{\boldsymbol{K}_3}-h_{SS\boldsymbol{k}_3}/\hbar)t}\mu_{S,\boldsymbol{K}_3}\langle \boldsymbol{e}|\,S\rangle - \\ - \sum_{S'\neq S} h^*_{S'S,\boldsymbol{k}_3}\mathrm{e}^{+\mathrm{i}(h_{S'S'\boldsymbol{k}_3}-h_{SS,\boldsymbol{k}_3})t/\hbar}\tilde{\varrho}^{(1)}_{S'\boldsymbol{k}_3,0}(t)\,, \tag{B.3}$$

$$[\mathrm{i}\hbar\partial_t+\gamma_2^{\mathrm{C}}]\tilde{\varrho}^{(2)}_{S\boldsymbol{k}_1,S'\boldsymbol{k}_3}(t) = \mathrm{i}\mathcal{E}_{\boldsymbol{e},\boldsymbol{K}_1}(t)\mathrm{e}^{-\mathrm{i}(\omega_{\boldsymbol{K}_1}-h_{SS\boldsymbol{k}_1}/\hbar)t}\mu_{S,\boldsymbol{K}_1}\langle S|\,\boldsymbol{e}\rangle\,\varrho^{(1)}_{S'\boldsymbol{k}_3,0}(t) + \\ +\mathrm{i}\mathcal{E}^*_{\boldsymbol{e},\boldsymbol{K}_3}(t)\mathrm{e}^{+\mathrm{i}(\omega_{\boldsymbol{K}_3}-h_{SS\boldsymbol{k}_3}/\hbar)t}\mu_{S,\boldsymbol{K}_3}\langle \boldsymbol{e}|\,S\rangle\,\tilde{\varrho}^{(1)}_{0,S\boldsymbol{k}_1}(t) + \\ + \sum_{\Sigma\neq S} h_{\Sigma S,\boldsymbol{k}_1}\mathrm{e}^{-\mathrm{i}(h_{\Sigma\Sigma,\boldsymbol{k}_1}-h_{SS,\boldsymbol{k}_1})t/\hbar}\tilde{\varrho}^{(2)}_{S'\boldsymbol{k}_3,\Sigma\boldsymbol{k}_1}(t) - \\ - \sum_{\Sigma'\neq S'} h^*_{\Sigma'S',\boldsymbol{k}_3}\mathrm{e}^{+\mathrm{i}(h_{\Sigma'\Sigma',\boldsymbol{k}_3}-h_{S'S',\boldsymbol{k}_3})t/\hbar}\tilde{\varrho}^{(2)}_{\Sigma'\boldsymbol{k}_3,S\boldsymbol{k}_1}(t)\,, \tag{B.4}$$

$$[\mathrm{i}\hbar\partial_t+\gamma_2^{\mathrm{C}}]\tilde{\varrho}^{(2)}_{S\boldsymbol{k}_2,S'\boldsymbol{k}_3}(t) = \mathrm{i}\mathcal{E}_{\boldsymbol{e},\boldsymbol{K}_2}(t)\mathrm{e}^{-\mathrm{i}(\omega_{\boldsymbol{K}_2}-h_{SS\boldsymbol{k}_2}/\hbar)t}\mu_{S,\boldsymbol{K}_2}\langle S|\,\boldsymbol{e}\rangle\,\varrho^{(1)}_{S'\boldsymbol{k}_3,0}(t) + \\ +\mathrm{i}\mathcal{E}^*_{\boldsymbol{e},\boldsymbol{K}_3}(t)\mathrm{e}^{+\mathrm{i}(\omega_{\boldsymbol{K}_3}-h_{SS\boldsymbol{k}_3}/\hbar)t}\mu_{S,\boldsymbol{K}_3}\langle \boldsymbol{e}|\,S\rangle\,\tilde{\varrho}^{(1)}_{0,S\boldsymbol{k}_2}(t) + \\ + \sum_{\Sigma\neq S} h_{\Sigma S,\boldsymbol{k}_2}\mathrm{e}^{-\mathrm{i}(h_{\Sigma\Sigma,\boldsymbol{k}_2}-h_{SS,\boldsymbol{k}_2})t/\hbar}\tilde{\varrho}^{(2)}_{S'\boldsymbol{k}_3,\Sigma\boldsymbol{k}_2}(t) - \\ - \sum_{\Sigma'\neq S'} h^*_{\Sigma'S',\boldsymbol{k}_3}\mathrm{e}^{+\mathrm{i}(h_{\Sigma'\Sigma',\boldsymbol{k}_3}-h_{S'S',\boldsymbol{k}_3})t/\hbar}\tilde{\varrho}^{(2)}_{\Sigma'\boldsymbol{k}_3,S\boldsymbol{k}_2}(t)\,, \tag{B.5}$$

$$[\mathrm{i}\hbar\partial_t+\gamma_2^{2\mathrm{X}}]\tilde{\varrho}^{(2)}_{0,S\boldsymbol{k}_1S'\boldsymbol{k}_2}(t) = \mathrm{i}\mathcal{E}_{\boldsymbol{e},\boldsymbol{K}_1}(t)\mathrm{e}^{-\mathrm{i}(\omega_{\boldsymbol{K}_1}-h_{SS\boldsymbol{k}_1}/\hbar)t}\mu_{S,\boldsymbol{K}_1}\langle S|\,\boldsymbol{e}\rangle\,\tilde{\varrho}^{(1)}_{0,S'\boldsymbol{k}_2}(t) + \\ +\mathrm{i}\mathcal{E}_{\boldsymbol{e},\boldsymbol{K}_2}(t)\mathrm{e}^{-\mathrm{i}(\omega_{\boldsymbol{K}_2}-h_{SS\boldsymbol{k}_2}/\hbar)t}\mu_{S,\boldsymbol{K}_2}\langle S|\,\boldsymbol{e}\rangle\,\tilde{\varrho}^{(1)}_{0,S\boldsymbol{k}_1}(t) +$$

$$+\sum_{\Sigma\neq S} h_{\Sigma S,\boldsymbol{k}_1}\mathrm{e}^{-\mathrm{i}(h_{\Sigma\Sigma,\boldsymbol{k}_1}-h_{SS,\boldsymbol{k}_1})t/\hbar}\tilde{\varrho}^{(2)}_{0,\Sigma\boldsymbol{k}_1S'\boldsymbol{k}_2}(t)+$$
$$+\sum_{\Sigma'\neq S'} h_{\Sigma'S',\boldsymbol{k}_2}\mathrm{e}^{-\mathrm{i}(h_{\Sigma'\Sigma',\boldsymbol{k}_2}-h_{S'S',\boldsymbol{k}_2})t/\hbar}\tilde{\varrho}^{(2)}_{0,S\boldsymbol{k}_1\Sigma'\boldsymbol{k}_2}\,, \tag{B.6}$$

$$\begin{aligned}[\mathrm{i}\hbar\partial_t+\gamma_2^{\mathrm{X}}]\tilde{\varrho}^{(3)}_{S\boldsymbol{k}_1S'\boldsymbol{k}_2,S''\boldsymbol{k}_3}(t) &= \mathrm{i}\mathcal{E}_{\boldsymbol{e},\boldsymbol{K}_1}(t)\mathrm{e}^{-\mathrm{i}(\omega_{\boldsymbol{K}_1}-h_{SS\boldsymbol{k}_1}/\hbar)t}\mu_{S,\boldsymbol{K}_1}\langle S|\,\boldsymbol{e}\rangle\,\tilde{\varrho}^{(2)}_{S''\boldsymbol{k}_3,S'\boldsymbol{k}_2}(t)+\\
&+\mathrm{i}\mathcal{E}_{\boldsymbol{e},\boldsymbol{K}_2}(t)\mathrm{e}^{-\mathrm{i}(\omega_{\boldsymbol{K}_2}-h_{SS\boldsymbol{k}_2}/\hbar)t}\mu_{S,\boldsymbol{K}_2}\langle S|\,\boldsymbol{e}\rangle\,\tilde{\varrho}^{(2)}_{S''\boldsymbol{k}_3,S\boldsymbol{k}_1}(t)+\\
&+\mathrm{i}\mathcal{E}^*_{\boldsymbol{e},\boldsymbol{K}_3}(t)\mathrm{e}^{+\mathrm{i}(\omega_{\boldsymbol{K}_3}-h_{SS\boldsymbol{k}_3}/\hbar)t}\mu_{S,\boldsymbol{K}_3}\langle \boldsymbol{e}|\,S\rangle\,\tilde{\varrho}^{(2)}_{0,S\boldsymbol{k}_1S'\boldsymbol{k}_2}(t)+\\
&+\sum_{\Sigma\neq S} h_{\Sigma S,\boldsymbol{k}_1}\mathrm{e}^{-\mathrm{i}(h_{\Sigma\Sigma,\boldsymbol{k}_1}-h_{SS,\boldsymbol{k}_1})t/\hbar}\tilde{\varrho}^{(3)}_{S''\boldsymbol{k}_3,\Sigma\boldsymbol{k}_1S'\boldsymbol{k}_2}(t)+\\
&+\sum_{\Sigma'\neq S'} h_{\Sigma'S',\boldsymbol{k}_2}\mathrm{e}^{-\mathrm{i}(h_{\Sigma'\Sigma',\boldsymbol{k}_2}-h_{S'S',\boldsymbol{k}_2})t/\hbar}\tilde{\varrho}^{(3)}_{S''\boldsymbol{k}_3,S\boldsymbol{k}_1\Sigma'\boldsymbol{k}_2}-\\
&-\sum_{\Sigma''\neq S''} h^*_{\Sigma''S'',\boldsymbol{k}_3}\mathrm{e}^{+\mathrm{i}(h_{\Sigma''\Sigma'',\boldsymbol{k}_3}-h_{S''S'',\boldsymbol{k}_3})t/\hbar}\tilde{\varrho}^{(3)}_{\Sigma''\boldsymbol{k}_3,S\boldsymbol{k}_1S'\boldsymbol{k}_2}(t)\,,\end{aligned} \tag{B.7}$$

$$\begin{aligned}[\mathrm{i}\hbar\partial_t+\gamma_2^{\mathrm{2R}}]\tilde{\varrho}^{(2)}_{S\boldsymbol{k}_1'S'\boldsymbol{k}_2',0}(t) &= \mathrm{i}\mathcal{E}_{\boldsymbol{e},\boldsymbol{K}_1}(t)\mathrm{e}^{-\mathrm{i}(\omega_{\boldsymbol{K}_1}-h_{SS\boldsymbol{k}_1}/\hbar)t}\mu_{S,\boldsymbol{K}_1}\langle S|\,\boldsymbol{e}\rangle\,\tilde{\varrho}^{(1)}_{0,S'\boldsymbol{k}_2}(t)+\\
&+\mathrm{i}\mathcal{E}_{\boldsymbol{e},\boldsymbol{K}_2}(t)\mathrm{e}^{-\mathrm{i}(\omega_{\boldsymbol{K}_2}-h_{SS\boldsymbol{k}_2}/\hbar)t}\mu_{S,\boldsymbol{K}_2}\langle S|\,\boldsymbol{e}\rangle\,\tilde{\varrho}^{(1)}_{0,S\boldsymbol{k}_1}(t)+\\
&+\sum_{\Sigma\neq S} h_{\Sigma S,\boldsymbol{k}_1}\mathrm{e}^{-\mathrm{i}(h_{\Sigma\Sigma,\boldsymbol{k}_1}-h_{SS,\boldsymbol{k}_1})t/\hbar}\tilde{\varrho}^{(2)}_{0,\Sigma\boldsymbol{k}_1'S'\boldsymbol{k}_2'}(t)+\\
&+\sum_{\Sigma'\neq S'} h_{\Sigma'S',\boldsymbol{k}_2}\mathrm{e}^{-\mathrm{i}(h_{\Sigma'\Sigma',\boldsymbol{k}_2}-h_{S'S',\boldsymbol{k}_2})t/\hbar}\tilde{\varrho}^{(2)}_{0,\Sigma'\boldsymbol{k}_2}\,,\end{aligned} \tag{B.8}$$

$$\begin{aligned}[\mathrm{i}\hbar\partial_t+\gamma_2^{\mathrm{R}}]\tilde{\varrho}^{(3)}_{S\boldsymbol{k}_1'S'\boldsymbol{k}_2',S''\boldsymbol{k}_3}(t) &= \mathrm{i}\mathcal{E}_{\boldsymbol{e},\boldsymbol{K}_1}(t)\mathrm{e}^{-\mathrm{i}(\omega_{\boldsymbol{K}_1}-h_{SS\boldsymbol{k}_1}/\hbar)t}\mu_{S,\boldsymbol{K}_1}\langle S|\,\boldsymbol{e}\rangle\,\tilde{\varrho}^{(2)}_{S''\boldsymbol{k}_3,S'\boldsymbol{k}_2}(t)+\\
&+\mathrm{i}\mathcal{E}_{\boldsymbol{e},\boldsymbol{K}_2}(t)\mathrm{e}^{-\mathrm{i}(\omega_{\boldsymbol{K}_2}-h_{SS\boldsymbol{k}_2}/\hbar)t}\mu_{S,\boldsymbol{K}_2}\langle S|\,\boldsymbol{e}\rangle\,\tilde{\varrho}^{(2)}_{S''\boldsymbol{k}_3,S\boldsymbol{k}_1}(t)+\\
&+\mathrm{i}\mathcal{E}^*_{\boldsymbol{e},\boldsymbol{K}_3}(t)\mathrm{e}^{+\mathrm{i}(\omega_{\boldsymbol{K}_3}-h_{SS\boldsymbol{k}_3}/\hbar)t}\mu_{S,\boldsymbol{K}_3}\langle \boldsymbol{e}|\,S\rangle\,\tilde{\varrho}^{(2)}_{0,S\boldsymbol{k}_1'S'\boldsymbol{k}_2'}(t)+\\
&+\sum_{\Sigma\neq S} h_{\Sigma S,\boldsymbol{k}_1}\mathrm{e}^{-\mathrm{i}(h_{\Sigma\Sigma,\boldsymbol{k}_1}-h_{SS,\boldsymbol{k}_1})t/\hbar}\tilde{\varrho}^{(3)}_{S''\boldsymbol{k}_3,\Sigma\boldsymbol{k}_1'S'\boldsymbol{k}_2'}(t)+\\
&+\sum_{\Sigma'\neq S'} h_{\Sigma'S',\boldsymbol{k}_2}\mathrm{e}^{-\mathrm{i}(h_{\Sigma'\Sigma',\boldsymbol{k}_2}-h_{S'S',\boldsymbol{k}_2})t/\hbar}\tilde{\varrho}^{(3)}_{S''\boldsymbol{k}_3,S\boldsymbol{k}_1'\Sigma'\boldsymbol{k}_2'}-\\
&-\sum_{\Sigma''\neq S''} h^*_{\Sigma''S'',\boldsymbol{k}_3}\mathrm{e}^{+\mathrm{i}(h_{\Sigma''\Sigma'',\boldsymbol{k}_3}-h_{S''S'',\boldsymbol{k}_3})t/\hbar}\tilde{\varrho}^{(3)}_{\Sigma''\boldsymbol{k}_3,S\boldsymbol{k}_1'S'\boldsymbol{k}_2'}(t)\,,\end{aligned} \tag{B.9}$$

$$\begin{aligned}[\mathrm{i}\hbar\partial_t+\gamma_2^{\mathrm{2B}}]\tilde{\varrho}^{(2)}_{\Gamma\boldsymbol{k}_1+\boldsymbol{k}_2,0}(t) &= \sum_{\boldsymbol{k}_1',\boldsymbol{k}_2'}\sum_{S,S'}\delta^{\Gamma}_{S\boldsymbol{k}_1',S'\boldsymbol{k}_2'}\chi_S(\boldsymbol{k}_1')\chi_{S'}(\boldsymbol{k}_2')\mathbf{M}_2(\Gamma,S,S')\tilde{\varrho}^{(2)}_{0,S\boldsymbol{k}_1'S'\boldsymbol{k}_2'}(t)+\\
&+\sum_{\Gamma'\neq\Gamma} h_{\Gamma'\Gamma,\boldsymbol{k}_1+\boldsymbol{k}_2}\mathrm{e}^{-\mathrm{i}(h_{\Gamma'\Gamma',\boldsymbol{k}_1+\boldsymbol{k}_2}-h_{\Gamma\Gamma,\boldsymbol{k}_1+\boldsymbol{k}_2})t/\hbar}\tilde{\varrho}^{(3)}_{S''\boldsymbol{k}_3,\Gamma'\boldsymbol{k}_1+\boldsymbol{k}_2}(t)\end{aligned} \tag{B.10}$$

$$\begin{aligned}[\mathrm{i}\hbar\partial_t+\gamma_2^{\mathrm{B}}]\tilde{\varrho}^{(3)}_{\Gamma\boldsymbol{k}_1+\boldsymbol{k}_2,S''\boldsymbol{k}_3}(t) &= \sum_{\boldsymbol{k}_1',\boldsymbol{k}_2'}\sum_{S,S'}\delta^{\Gamma}_{S\boldsymbol{k}_1',S'\boldsymbol{k}_2'}\chi_S(\boldsymbol{k}_1)\chi_{S'}(\boldsymbol{k}_2')\mathbf{M}_2(\Gamma,S,S')\tilde{\varrho}^{(3)}_{S''\boldsymbol{k}_3,S\boldsymbol{k}_1'S'\boldsymbol{k}_2'}(t)+\\
&+\mathrm{i}\mathcal{E}^*_{\boldsymbol{e},\boldsymbol{K}_3}(t)\mathrm{e}^{+\mathrm{i}(\omega_{\boldsymbol{K}_3}-h_{SS\boldsymbol{k}_3}/\hbar)t}\mu_{S,\boldsymbol{K}_3}\langle \boldsymbol{e}|\,S\rangle\,\tilde{\varrho}^{(2)}_{0,\Gamma\boldsymbol{k}_1+\boldsymbol{k}_2}(t)+\\
&+\sum_{\Gamma'\neq\Gamma} h_{\Gamma'\Gamma,\boldsymbol{k}_1+\boldsymbol{k}_2}\mathrm{e}^{-\mathrm{i}(h_{\Gamma'\Gamma',\boldsymbol{k}_1+\boldsymbol{k}_2}-h_{\Gamma\Gamma,\boldsymbol{k}_1+\boldsymbol{k}_2})t/\hbar}\tilde{\varrho}^{(3)}_{S''\boldsymbol{k}_3,\Gamma'\boldsymbol{k}_1+\boldsymbol{k}_2}(t)-\end{aligned}$$

$$- \sum_{\Sigma''\neq S''} h^{*}_{\Sigma''S'',\boldsymbol{k}_3} \mathrm{e}^{+\mathrm{i}(h_{\Sigma''\Sigma'',\boldsymbol{k}_3}-h_{S''S'',\boldsymbol{k}_3})t/\hbar} \tilde{\varrho}^{(3)}_{\Sigma''\boldsymbol{k}_3,\Gamma\boldsymbol{k}_1+\boldsymbol{k}_2}(t)\,, \quad \text{(B.11)}$$

$$\begin{aligned}
[\mathrm{i}\hbar\partial_t+\gamma^{2\mathrm{X}}_2]\tilde{\varrho}^{(2)}_{S=j_hs_e\boldsymbol{k}_3S'=j'_hs'_e\boldsymbol{k}_4,0}(t) &= \frac{1}{2}\chi_{S'}(\boldsymbol{k}_2)[-G_{\mathrm{d}}(0,0)\phi_S(\boldsymbol{k}_1)+V_{\mathrm{d}}(0,0)\chi_S(\boldsymbol{k}_1)]\cdot\\
&\cdot\chi_S(\boldsymbol{k}_3)\chi_{S'}(\boldsymbol{k}_4)\tilde{\varrho}^{(2)}_{0,S\boldsymbol{k}_1S'\boldsymbol{k}_2}(t)\cdot\\
&\cdot\mathrm{e}^{-\mathrm{i}\left(h_{SS,\boldsymbol{k}_1}+h_{S'S',\boldsymbol{k}_2}-h_{SS,\boldsymbol{k}_3}-h_{S'S',\boldsymbol{k}_4}\right)t}+P_{\boldsymbol{k}_1\boldsymbol{k}_2}+\\
&+\frac{1}{2}\chi_{j'_hs_e}(\boldsymbol{k}_2)[-G_{\mathrm{x}}(0,0)\phi_{j_hs'_e}(\boldsymbol{k}_1)+V_{\mathrm{x}}(0,0)\chi_{j_hs'_e}(\boldsymbol{k}_1)]\cdot\\
&\cdot\chi_S(\boldsymbol{k}_3)\chi_{S'}(\boldsymbol{k}_4)\tilde{\varrho}^{(2)}_{0,j_hs'_e\boldsymbol{k}_1j'_hs_e\boldsymbol{k}_2}(t)\cdot\\
&\cdot\mathrm{e}^{-\mathrm{i}\left(h_{j_hs'_ej_hs'_e,\boldsymbol{k}_1}+h_{j'_hs_ej'_hs_e,\boldsymbol{k}_2}-h_{SS,\boldsymbol{k}_3}-h_{S'S',\boldsymbol{k}_4}\right)t}+P_{\boldsymbol{k}_1\boldsymbol{k}_2}+\\
&+\mathrm{i}\mathcal{E}_{\boldsymbol{e},\boldsymbol{K}_1}(t)\mathrm{e}^{-\mathrm{i}(\omega_{\boldsymbol{K}_1}-h_{SS,\boldsymbol{k}_1}/\hbar)t}\kappa_{SS',\boldsymbol{K}_1}\langle S|\,\boldsymbol{e}\rangle\,\tilde{\varrho}^{(1)}_{0,S'\boldsymbol{k}_2}(t)+\\
&+\mathrm{i}\mathcal{E}_{\boldsymbol{e},\boldsymbol{K}_2}(t)\mathrm{e}^{-\mathrm{i}(\omega_{\boldsymbol{K}_2}-h_{SS,\boldsymbol{k}_2}/\hbar)t}\kappa_{S'S,\boldsymbol{K}_1}\left\langle S'\right|\boldsymbol{e}\rangle\,\tilde{\varrho}^{(1)}_{0,S\boldsymbol{k}_1}(t)+\\
&+\sum_{\Sigma\neq S}h_{\Sigma S,\boldsymbol{k}_3}\mathrm{e}^{-\mathrm{i}(h_{\Sigma\Sigma,\boldsymbol{k}_3}-h_{SS,\boldsymbol{k}_3})t/\hbar}\tilde{\varrho}^{(2)}_{0,\Sigma\boldsymbol{k}_3S'\boldsymbol{k}_4}(t)+\\
&+\sum_{\Sigma'\neq S'}h_{\Sigma'S',\boldsymbol{k}_4}\mathrm{e}^{-\mathrm{i}(h_{\Sigma'\Sigma',\boldsymbol{k}_4}-h_{S'S',\boldsymbol{k}_4})t/\hbar}\tilde{\varrho}^{(2)}_{0,S\boldsymbol{k}_3\Sigma'\boldsymbol{k}_4}\,, \qquad \text{(B.12)}
\end{aligned}$$

$$\begin{aligned}
[\mathrm{i}\hbar\partial_t+\gamma^{\mathrm{X}}_2]\tilde{\varrho}^{(3)}_{S=j_hs_e\boldsymbol{k}_3S'=j'_hs'_e\boldsymbol{k}_4,S''\boldsymbol{k}_3}(t) &= \frac{1}{2}\chi_{S'}(\boldsymbol{k}_2)[-G_{\mathrm{d}}(0,0)\phi_S(\boldsymbol{k}_1)+V_{\mathrm{d}}(0,0)\chi_S(\boldsymbol{k}_1)]\cdot\\
&\cdot\chi_S(\boldsymbol{k}_3)\chi_{S'}(\boldsymbol{k}_4)\tilde{\varrho}^{(3)}_{S''\boldsymbol{k}_3,S\boldsymbol{k}_1S'\boldsymbol{k}_2}(t)\cdot\\
&\cdot\mathrm{e}^{-\mathrm{i}\left(h_{SS,\boldsymbol{k}_1}+h_{S'S',\boldsymbol{k}_2}-h_{SS,\boldsymbol{k}_3}-h_{S'S',\boldsymbol{k}_4}\right)t}+P_{\boldsymbol{k}_1\boldsymbol{k}_2}+\\
&+\frac{1}{2}\chi_{j'_hs_e}(\boldsymbol{k}_2)[-G_{\mathrm{x}}(0,0)\phi_{j_hs'_e}(\boldsymbol{k}_1)+V_{\mathrm{x}}(0,0)\chi_{j_hs'_e}(\boldsymbol{k}_1)]\cdot\\
&\cdot\chi_S(\boldsymbol{k}_3)\chi_{S'}(\boldsymbol{k}_4)\tilde{\varrho}^{(3)}_{S''\boldsymbol{k}_3,j_hs'_e\boldsymbol{k}_1j'_hs_e\boldsymbol{k}_2}(t)\cdot\\
&\cdot\mathrm{e}^{-\mathrm{i}\left(h_{j_hs'_ej_hs'_e,\boldsymbol{k}_1}+h_{j'_hs_ej'_hs_e,\boldsymbol{k}_2}-h_{SS,\boldsymbol{k}_3}-h_{S'S',\boldsymbol{k}_4}\right)t}+P_{\boldsymbol{k}_1\boldsymbol{k}_2}+\\
&+\mathrm{i}\mathcal{E}_{\boldsymbol{e},\boldsymbol{K}_1}(t)\mathrm{e}^{-\mathrm{i}(\omega_{\boldsymbol{K}_1}-h_{SS,\boldsymbol{k}_1}/\hbar)t}\kappa_{SS',\boldsymbol{K}_1}\langle S|\,\boldsymbol{e}\rangle\,\tilde{\varrho}^{(3)}_{S''\boldsymbol{k}_3,S'\boldsymbol{k}_2}(t)+\\
&+\mathrm{i}\mathcal{E}_{\boldsymbol{e},\boldsymbol{K}_2}(t)\mathrm{e}^{-\mathrm{i}(\omega_{\boldsymbol{K}_2}-h_{SS,\boldsymbol{k}_2}/\hbar)t}\kappa_{S'S,\boldsymbol{K}_1}\left\langle S'\right|\boldsymbol{e}\rangle\,\tilde{\varrho}^{(3)}_{S''\boldsymbol{k}_3,S\boldsymbol{k}_1}(t)+\\
&+\mathrm{i}\mathcal{E}^{*}_{\boldsymbol{e},\boldsymbol{K}_3}(t)\mathrm{e}^{+\mathrm{i}(\omega_{\boldsymbol{K}_3}-h_{SS\boldsymbol{k}_3}/\hbar)t}\mu_{S,\boldsymbol{K}_3}\langle\boldsymbol{e}|\,S\rangle\,\tilde{\varrho}^{(2)}_{0,S\boldsymbol{k}_3S'\boldsymbol{k}_4}(t)+\\
&+\sum_{\Sigma\neq S}h_{\Sigma S,\boldsymbol{k}_3}\mathrm{e}^{-\mathrm{i}(h_{\Sigma\Sigma,\boldsymbol{k}_3}-h_{SS,\boldsymbol{k}_3})t/\hbar}\tilde{\varrho}^{(3)}_{S''\boldsymbol{k}_3,\Sigma\boldsymbol{k}_3S'\boldsymbol{k}_4}(t)+\\
&+\sum_{\Sigma'\neq S'}h_{\Sigma'S',\boldsymbol{k}_4}\mathrm{e}^{-\mathrm{i}(h_{\Sigma'\Sigma',\boldsymbol{k}_4}-h_{S'S',\boldsymbol{k}_4})t/\hbar}\tilde{\varrho}^{(3)}_{S''\boldsymbol{k}_3,S\boldsymbol{k}_3\Sigma'\boldsymbol{k}_4}-\\
&-\sum_{\Sigma''\neq S''}h^{*}_{\Sigma''S'',\boldsymbol{k}_3}\mathrm{e}^{+\mathrm{i}(h_{\Sigma''\Sigma'',\boldsymbol{k}_3}-h_{S''S'',\boldsymbol{k}_3})t/\hbar}\tilde{\varrho}^{(3)}_{\Sigma''\boldsymbol{k}_3,S\boldsymbol{k}_3S'\boldsymbol{k}_4}(t)\,, \qquad \text{(B.13)}
\end{aligned}$$

$$\begin{aligned}
[\mathrm{i}\hbar\partial_t+\gamma^{2\mathrm{R}}_2]\tilde{\varrho}^{(2)}_{\boldsymbol{k}'_3S'\boldsymbol{k}'_4,0}(t) &= \sum_{\Gamma}\delta^{\Gamma}_{S\boldsymbol{k}'_3,S'\boldsymbol{k}'_4}\chi_S(\boldsymbol{k}'_3)\chi_{S'}(\boldsymbol{k}'_4)\mathbf{M}^{*}_2(\Gamma,S,S')\tilde{\varrho}^{(2)}_{0,\Gamma}(t)+\\
&+\sum_{\Sigma\neq S}h_{\Sigma S,\boldsymbol{k}'_3}\mathrm{e}^{-\mathrm{i}(h_{\Sigma\Sigma,\boldsymbol{k}'_3}-h_{SS,\boldsymbol{k}'_3})t/\hbar}\tilde{\varrho}^{(2)}_{0,\Sigma\boldsymbol{k}'_3S'\boldsymbol{k}'_4}(t)+
\end{aligned}$$

$$+\sum_{\Sigma'\neq S'} h_{\Sigma' S',\boldsymbol{k}'_4}\mathrm{e}^{-\mathrm{i}(h_{\Sigma'\Sigma',\boldsymbol{k}'_4}-h_{S'S',\boldsymbol{k}'_4})t/\hbar}\tilde{\varrho}^{(2)}_{0,S\boldsymbol{k}'_3\Sigma'\boldsymbol{k}'_4}\,, \tag{B.14}$$

$$\begin{aligned}
[\mathrm{i}\hbar\partial_t+\gamma_2^{\mathrm{R}}]\tilde{\varrho}^{(3)}_{S\boldsymbol{k}'_3S'\boldsymbol{k}'_4,S''\boldsymbol{k}_3}(t) &= \sum_{\Gamma}\delta^{\Gamma}_{S\boldsymbol{k}'_3,S'\boldsymbol{k}'_4}\chi_S(\boldsymbol{k}'_3)\chi_{S'}(\boldsymbol{k}'_4)\mathbf{M}^*_2(\Gamma,S,S')\tilde{\varrho}^{(3)}_{S''\boldsymbol{k}_3,\Gamma}(t)+\\
&+\mathrm{i}\mathcal{E}^*_{\boldsymbol{e},\boldsymbol{K}_3}(t)\mathrm{e}^{+\mathrm{i}(\omega_{\boldsymbol{K}_3}-h_{SS\boldsymbol{k}_3}/\hbar)t}\mu_{S,\boldsymbol{K}_3}\langle\boldsymbol{e}|\,S\rangle\,\tilde{\varrho}^{(2)}_{0,S\boldsymbol{k}'_3S'\boldsymbol{k}'_4}(t)+\\
&+\sum_{\Sigma\neq S} h_{\Sigma S,\boldsymbol{k}'_3}\mathrm{e}^{-\mathrm{i}(h_{\Sigma\Sigma,\boldsymbol{k}'_3}-h_{SS,\boldsymbol{k}'_3})t/\hbar}\tilde{\varrho}^{(3)}_{S''\boldsymbol{k}_3,\Sigma\boldsymbol{k}'_3S'\boldsymbol{k}'_4}(t)+\\
&+\sum_{\Sigma'\neq S'} h_{\Sigma' S',\boldsymbol{k}'_4}\mathrm{e}^{-\mathrm{i}(h_{\Sigma'\Sigma',\boldsymbol{k}'_4}-h_{S'S',\boldsymbol{k}'_4})t/\hbar}\tilde{\varrho}^{(3)}_{S''\boldsymbol{k}_3,S\boldsymbol{k}'_3\Sigma'\boldsymbol{k}'_4}-\\
&-\sum_{\Sigma''\neq S''} h^*_{\Sigma'' S'',\boldsymbol{k}_3}\mathrm{e}^{+\mathrm{i}(h_{\Sigma''\Sigma'',\boldsymbol{k}_3}-h_{S''S'',\boldsymbol{k}_3})t/\hbar}\tilde{\varrho}^{(3)}_{\Sigma''\boldsymbol{k}_3,S\boldsymbol{k}'_3S'\boldsymbol{k}'_4}(t)\,,
\end{aligned} \tag{B.15}$$

$$\begin{aligned}
[\mathrm{i}\hbar\partial_t+\gamma_2]\tilde{\varrho}^{(3)}_{S'\boldsymbol{k}_4,0} &= -\mathrm{i}\mathcal{E}^*_{\boldsymbol{e},\boldsymbol{K}_3}(t)\mathrm{e}^{+\mathrm{i}(\omega_{\boldsymbol{K}_3}-h_{SS\boldsymbol{k}_3}/\hbar)t}\mu_{S,\boldsymbol{K}_3}\langle\boldsymbol{e}|\,S\rangle\,\tilde{\varrho}^{(2)}_{0,S\boldsymbol{k}_3S'\boldsymbol{k}_4}(t)-\\
&-\mathrm{i}\sum_{\boldsymbol{k}'_3,\boldsymbol{k}'_4}\mathcal{E}^*_{\boldsymbol{e},\boldsymbol{K}_3}(t)\mathrm{e}^{+\mathrm{i}(\omega_{\boldsymbol{K}_3}-h_{SS\boldsymbol{k}_3}/\hbar)t}\mu_{S,\boldsymbol{K}_3}\langle\boldsymbol{e}|\,S\rangle\,\tilde{\varrho}^{(2)}_{0,S\boldsymbol{k}'_3S'\boldsymbol{k}'_4}(t)-\\
&-\mathrm{i}\mathcal{E}^*_{\boldsymbol{e},\boldsymbol{K}_3}(t)\mathrm{e}^{+\mathrm{i}(\omega_{\boldsymbol{K}_3}-h_{SS\boldsymbol{k}_3}/\hbar)t}\kappa_{SS',\boldsymbol{K}_3}\langle\boldsymbol{e}|\,S\rangle\,\tilde{\varrho}^{(2)}_{0,S\boldsymbol{k}_1S'\boldsymbol{k}_2}(t)+\\
&+\sum_{\Sigma'\neq S'} h_{\Sigma' S',\boldsymbol{k}_4}\mathrm{e}^{-\mathrm{i}(h_{\Sigma'\Sigma',\boldsymbol{k}_4}-h_{S'S',\boldsymbol{k}_4})t/\hbar}\tilde{\varrho}^{(3)}_{0,\Sigma'\boldsymbol{k}'_4}\,.
\end{aligned} \tag{B.16}$$

The operator $P_{\boldsymbol{k}_1\boldsymbol{k}_2}$ means the preceding terms with permuted wave vectors $\boldsymbol{k}_1$ and $\boldsymbol{k}_2$.

B.2 Solution of equations of motion for $t_1 < t_3 < t_2$

$$\tilde{\varrho}^{(1)}_{\boldsymbol{k}_1,0}(t) = \frac{\mu}{\hbar}\mathcal{E}_1 \mathrm{e}^{-\mathrm{i}(\omega_1-\omega_1^{\mathrm{X}})t_1}\mathrm{e}^{-\gamma_2(t-t_1)}\Theta(t-t_1)\,, \tag{B.17}$$

$$\tilde{\varrho}^{(2)}_{\boldsymbol{k}_1,\boldsymbol{k}_3}(t) = \frac{\mu^2}{\hbar^2}\mathcal{E}_1\mathcal{E}_3^* \mathrm{e}^{-\mathrm{i}(\omega_1-\omega_1^{\mathrm{X}})t_1}\mathrm{e}^{\mathrm{i}(\omega_3-\omega_3^{\mathrm{X}})t_3}\,\cdot$$
$$\cdot\mathrm{e}^{-\gamma_2(t_3-t_1)}\mathrm{e}^{-\gamma_2^{\mathrm{C}}(t-t_3)}\Theta(t_3-t_1)\Theta(t-t_3)\,, \tag{B.18}$$

$$\tilde{\varrho}^{(3)}_{\boldsymbol{k}_1\boldsymbol{k}_2,\boldsymbol{k}_3}(t) = \frac{\mu^3}{\hbar^3}\mathcal{E}_1\mathcal{E}_2\mathcal{E}_3^* \mathrm{e}^{-\mathrm{i}(\omega_1-\omega_1^{\mathrm{X}})t_1}\mathrm{e}^{-\mathrm{i}(\omega_2-\omega_2^{\mathrm{X}})t_2}\mathrm{e}^{\mathrm{i}(\omega_3-\omega_3^{\mathrm{X}})t_3}\mathrm{e}^{-\gamma_2(t_3-t_1)}\,\cdot$$
$$\cdot\mathrm{e}^{-\gamma_2^{\mathrm{C}}(t_2-t_3)}\mathrm{e}^{-\gamma_2^{\mathrm{X}}(t-t_2)}\Theta(t_3-t_1)\Theta(t_2-t_3)\Theta(t-t_2)\,, \tag{B.19}$$

$$\tilde{\varrho}^{(3)}_{\boldsymbol{k}_1'\boldsymbol{k}_2',\boldsymbol{k}_3}(t) = \frac{\mu^3}{\hbar^3}\mathcal{E}_1\mathcal{E}_2\mathcal{E}_3^* \mathrm{e}^{-\mathrm{i}(\omega_1-\omega_1^{\mathrm{X}})t_3}\mathrm{e}^{-\mathrm{i}(\omega_2-\omega_{2'}^{\mathrm{X}})t_2}\mathrm{e}^{\mathrm{i}(\omega_3-\omega_3^{\mathrm{X}})t_3}\mathrm{e}^{-\gamma_2(t_3-t_1)}\,\cdot$$
$$\cdot\mathrm{e}^{-\gamma_2^{\mathrm{C}}(t_2-t_3)}\mathrm{e}^{-\gamma_2^{\mathrm{R}}(t-t_2)}\Theta(t_3-t_1)\Theta(t_2-t_3)\Theta(t-t_2)\,, \tag{B.20}$$

$$\tilde{\varrho}^{(3)}_{\boldsymbol{k}_3\boldsymbol{k}_4,\boldsymbol{k}_3}(t) = \frac{\mu^2}{\hbar^2}\mathcal{E}_1\mathcal{E}_2\mathcal{E}_3^* \mathrm{e}^{-\mathrm{i}(\omega_1-\omega_1^{\mathrm{X}})t_1}\mathrm{e}^{\mathrm{i}(\omega_3-\omega_3^{\mathrm{X}})t_3}\mathrm{e}^{-\gamma_2(t_3-t_1)}\mathrm{e}^{-\gamma_2^{\mathrm{C}}(t_2-t_3)}\mathrm{e}^{-\gamma_2^{\mathrm{X}}(t-t_2)}\,\cdot$$
$$\cdot\left\{\frac{\mu}{2\hbar}\chi_3\chi_4[2\chi_1\chi_2(V_{\mathrm{d}}+V_{\mathrm{x}})-(\phi_1\chi_2+\chi_1\phi_2)(G_{\mathrm{d}}+G_{\mathrm{x}})]\cdot\right.$$
$$\left.\cdot\frac{\mathrm{e}^{-\mathrm{i}(\omega_1^{\mathrm{X}}+\omega_2^{\mathrm{X}}-\omega_3^{\mathrm{X}}-\omega_4^{\mathrm{X}})(t-t_2)}-1}{\hbar(\omega_1^{\mathrm{X}}+\omega_2^{\mathrm{X}}-\omega_3^{\mathrm{X}}-\omega_4^{\mathrm{X}})}+\frac{\kappa}{\hbar}\right\}\mathrm{e}^{-\mathrm{i}(\omega_1^{\mathrm{X}}+\omega_2-\omega_3^{\mathrm{X}}-\omega_4^{\mathrm{X}})t_2}\,\cdot$$
$$\cdot\Theta(t_3-t_1)\Theta(t_2-t_3)\Theta(t-t_2)\,, \tag{B.21}$$

$$\tilde{\varrho}^{(3)}_{m,\boldsymbol{k}_3}(t) = -\mathrm{i}\frac{\mu^3 M_2}{\hbar^4}\mathcal{E}_1\mathcal{E}_2\mathcal{E}_3^* \mathrm{e}^{-\mathrm{i}(\omega_1-\omega_1^{\mathrm{X}})t_3}\mathrm{e}^{-\mathrm{i}(\omega_2-\omega_{2'}^{\mathrm{X}})t_2}\mathrm{e}^{\mathrm{i}(\omega_3-\omega_3^{\mathrm{X}})t_3}\mathrm{e}^{-\gamma_2(t_3-t_1)}\,\cdot$$
$$\cdot\frac{\mathrm{e}^{-\gamma_2^{\mathrm{R}}(t-t_2)}-\mathrm{e}^{-\gamma_2^{\mathrm{B}}(t-t_2)}}{\gamma_2^{\mathrm{B}}-\gamma_2^{\mathrm{R}}}\mathrm{e}^{-\gamma_2^{\mathrm{C}}(t_2-t_3)}\,\cdot$$
$$\cdot\Theta(t_3-t_1)\Theta(t_2-t_3)\Theta(t-t_2)\,, \tag{B.22}$$

$$\tilde{\varrho}^{(3)}_{\boldsymbol{k}_3'\boldsymbol{k}_4',\boldsymbol{k}_3}(t) = -\frac{\mu^3|M_2|^2}{\hbar^5}\mathcal{E}_1\mathcal{E}_2\mathcal{E}_3^* \mathrm{e}^{-\mathrm{i}(\omega_1-\omega_1^{\mathrm{X}})t_3}\mathrm{e}^{-\mathrm{i}(\omega_2-\omega_{2'}^{\mathrm{X}})t_2}\mathrm{e}^{\mathrm{i}(\omega_3-\omega_3^{\mathrm{X}})t_3}\mathrm{e}^{-\gamma_2(t_3-t_1)}\mathrm{e}^{-\gamma_2^{\mathrm{C}}(t_2-t_3)}\,\cdot$$
$$\cdot\left\{\frac{\mathrm{e}^{-\gamma_2^{\mathrm{R}}(t-t_2)}(t-t_2)}{\gamma_2^{\mathrm{B}}-\gamma_2^{\mathrm{R}}}-\frac{\mathrm{e}^{-\gamma_2^{\mathrm{R}}(t-t_2)}-\mathrm{e}^{-\gamma_2^{\mathrm{B}}(t-t_2)}}{(\gamma_2^{\mathrm{B}}-\gamma_2^{\mathrm{R}})^2}\right\}\cdot$$
$$\cdot\Theta(t_3-t_1)\Theta(t_2-t_3)\Theta(t-t_2)\,, \tag{B.23}$$

where $\Theta(t)$ denotes the Heaviside step function.

B.3 Solution of equations of motion for $t_1 < t_2 < t_3$

$$\tilde{\varrho}^{(1)}_{\boldsymbol{k}_1,0}(t) = \frac{\mu}{\hbar}\mathcal{E}_1 \mathrm{e}^{-\mathrm{i}(\omega_1-\omega_1^{\mathrm{X}})t_1}\mathrm{e}^{-\gamma_2(t-t_1)}\Theta(t-t_1)\,, \tag{B.24}$$

$$\tilde{\varrho}^{(2)}_{\boldsymbol{k}_1\boldsymbol{k}_2,0}(t) = \frac{\mu^2}{\hbar^2}\mathcal{E}_1\mathcal{E}_2 \mathrm{e}^{-\mathrm{i}(\omega_1-\omega_1^{\mathrm{X}})t_1}\mathrm{e}^{-\mathrm{i}(\omega_2-\omega_2^{\mathrm{X}})t_2}\cdot$$
$$\cdot\mathrm{e}^{-\gamma_2(t_2-t_1)}\mathrm{e}^{-\gamma_2^{2\mathrm{X}}(t-t_2)}\Theta(t_2-t_1)\Theta(t-t_2)\,, \tag{B.25}$$

$$\tilde{\varrho}^{(2)}_{\boldsymbol{k}'_1\boldsymbol{k}'_2,0}(t) = \frac{\mu^2}{\hbar^2}\mathcal{E}_1\mathcal{E}_2 \mathrm{e}^{-\mathrm{i}(\omega_1-\omega_1^{\mathrm{X}})t_1}\mathrm{e}^{-\mathrm{i}(\omega_2-\omega_{2'}^{\mathrm{X}})t_2}\cdot$$
$$\cdot\mathrm{e}^{-\gamma_2(t_2-t_1)}\mathrm{e}^{-\gamma_2^{2\mathrm{R}}(t-t_2)}\Theta(t_2-t_1)\Theta(t-t_2)\,, \tag{B.26}$$

$$\tilde{\varrho}^{(2)}_{\boldsymbol{k}_3\boldsymbol{k}_4,0}(t) = \frac{\mu}{\hbar}\mathcal{E}_1\mathcal{E}_2 \mathrm{e}^{-\mathrm{i}(\omega_1-\omega_1^{\mathrm{X}})t_1}\mathrm{e}^{-\gamma_2(t_2-t_1)}\mathrm{e}^{-\gamma_2^{2\mathrm{X}}(t-t_2)}\cdot$$
$$\cdot\left\{\frac{\mu}{2\hbar}\chi_3\chi_4[2\chi_1\chi_2(V_{\mathrm{d}}+V_{\mathrm{x}})-(\phi_1\chi_2+\chi_1\phi_2)(G_{\mathrm{d}}+G_{\mathrm{x}})]\cdot\right.$$
$$\left.\cdot\frac{\mathrm{e}^{-\mathrm{i}(\omega_1^{\mathrm{X}}+\omega_2^{\mathrm{X}}-\omega_3^{\mathrm{X}}-\omega_4^{\mathrm{X}})(t-t_2)}-1}{\hbar(\omega_1^{\mathrm{X}}+\omega_2^{\mathrm{X}}-\omega_3^{\mathrm{X}}-\omega_4^{\mathrm{X}})}+\frac{\kappa}{\hbar}\right\}\mathrm{e}^{-\mathrm{i}(\omega_1^{\mathrm{X}}+\omega_2-\omega_3^{\mathrm{X}}-\omega_4^{\mathrm{X}})t_2}\cdot$$
$$\cdot\Theta(t_2-t_1)\Theta(t-t_2)\,, \tag{B.27}$$

$$\tilde{\varrho}^{(2)}_{m,0}(t) = -\mathrm{i}\frac{\mu^2 M_2}{\hbar^3}\mathcal{E}_1\mathcal{E}_2 \mathrm{e}^{-\mathrm{i}(\omega_1-\omega_1^{\mathrm{X}})t_3}\mathrm{e}^{\mathrm{i}(\omega_2-\omega_{2'}^{\mathrm{X}})t_2}\mathrm{e}^{-\gamma_2(t_2-t_1)}\cdot$$
$$\cdot\frac{\mathrm{e}^{-\gamma_2^{2\mathrm{R}}t_2}}{\gamma_2^{2\mathrm{B}}-\gamma_2^{2\mathrm{R}}}[\mathrm{e}^{-\gamma_2^{2\mathrm{R}}(t-t_2)}-\mathrm{e}^{-\gamma_2^{2\mathrm{B}}(t-t_2)}]\cdot\Theta(t_2-t_1)\Theta(t-t_2)\,, \tag{B.28}$$

$$\tilde{\varrho}^{(2)}_{\boldsymbol{k}'_3\boldsymbol{k}'_4,0}(t) = -\frac{\mu^2|M_2|^2}{\hbar^4}\mathrm{e}^{-\mathrm{i}(\omega_1-\omega_1^{\mathrm{X}})t_3}\mathrm{e}^{\mathrm{i}(\omega_2-\omega_{2'}^{\mathrm{X}})t_2}\mathrm{e}^{-\gamma_2(t_2-t_1)}\cdot$$
$$\cdot\left\{\frac{\mathrm{e}^{-\gamma_2^{\mathrm{R}}(t-t_2)}(t-t_2)}{\gamma_2^{\mathrm{B}}-\gamma_2^{\mathrm{R}}}-\frac{\mathrm{e}^{-\gamma_2^{\mathrm{R}}(t-t_2)}-\mathrm{e}^{-\gamma_2^{\mathrm{B}}(t-t_2)}}{(\gamma_2^{\mathrm{B}}-\gamma_2^{\mathrm{R}})^2}\right\}\cdot$$
$$\cdot\Theta(t_2-t_1)\Theta(t-t_2)\,, \tag{B.29}$$

$$\tilde{\varrho}^{(3)}_{\boldsymbol{k}_1\boldsymbol{k}_2,\boldsymbol{k}_3}(t) = \frac{\mu^3}{\hbar^3}\mathcal{E}_1\mathcal{E}_2\mathcal{E}_3^* \mathrm{e}^{-\mathrm{i}(\omega_1-\omega_1^{\mathrm{X}})t_1}\mathrm{e}^{-\mathrm{i}(\omega_2-\omega_2^{\mathrm{X}})t_2}\mathrm{e}^{-\mathrm{i}(\omega_3-\omega_3^{\mathrm{X}})t_2}\mathrm{e}^{-\gamma_2(t_2-t_1)}\cdot$$
$$\cdot\mathrm{e}^{-\gamma_2^{2\mathrm{X}}(t_3-t_2)}\mathrm{e}^{-\gamma_2^{\mathrm{X}}(t-t_3)}\Theta(t_2-t_1)\Theta(t_3-t_2)\Theta(t-t_3)\,, \tag{B.30}$$

$$\tilde{\varrho}^{(3)}_{\boldsymbol{k}'_1\boldsymbol{k}'_2,\boldsymbol{k}_3}(t) = \frac{\mu^3}{\hbar^3}\mathcal{E}_1\mathcal{E}_2\mathcal{E}_3^* \mathrm{e}^{-\mathrm{i}(\omega_1-\omega_1^{\mathrm{X}})t_1}\mathrm{e}^{-\mathrm{i}(\omega_2-\omega_{2'}^{\mathrm{X}})t_2}\mathrm{e}^{-\mathrm{i}(\omega_3-\omega_3^{\mathrm{X}})t_3}\mathrm{e}^{-\gamma_2(t_2-t_1)}\cdot$$
$$\cdot\mathrm{e}^{-\gamma_2^{2\mathrm{R}}(t_3-t_2)}\mathrm{e}^{-\gamma_2^{\mathrm{R}}(t-t_3)}\Theta(t_2-t_1)\Theta(t_3-t_2)\Theta(t-t_3)\,, \tag{B.31}$$

$$\tilde{\varrho}^{(3)}_{\boldsymbol{k}_4,0}(t) = -\mathcal{E}_3^*\left[\frac{\mu}{\hbar}\tilde{\varrho}^{(2)}_{0,\boldsymbol{k}_3\boldsymbol{k}_4}(t_3)\mathrm{e}^{\mathrm{i}(\omega_3-\omega_3^{\mathrm{X}})t_3}+\frac{\mu}{\hbar}\tilde{\varrho}^{(2)}_{0,\boldsymbol{k}'_3\boldsymbol{k}'_4}(t_3)\mathrm{e}^{\mathrm{i}(\omega_3-\omega_{3'}^{\mathrm{X}})t_3}+\right.$$
$$\left.+\frac{\kappa}{\hbar}\tilde{\varrho}^{(2)}_{0,\boldsymbol{k}_1\boldsymbol{k}_2}(t_3)\mathrm{e}^{-\mathrm{i}(\omega_1^{\mathrm{X}}+\omega_2^{\mathrm{X}}-\omega_3-\omega_4^{\mathrm{X}})t_3}\right]\mathrm{e}^{-\gamma_2(t-t_3)}\Theta(t-t_3)\,, \tag{B.32}$$

$$\tilde{\varrho}^{(3)}_{m,\boldsymbol{k}_3}(t) = \frac{\mu}{\hbar}\mathcal{E}_3^*\mathrm{e}^{\mathrm{i}(\omega_3-\omega_3^{\mathrm{X}})t_3}\mathrm{e}^{-\gamma_2^{\mathrm{B}}(t-t_3)}\tilde{\varrho}^{(2)}_{0,m}(t_3)-\mathrm{i}\frac{\mu^3 M_2}{\hbar^4}\mathcal{E}_1\mathcal{E}_2\mathcal{E}_3^*\cdot$$
$$\cdot\mathrm{e}^{-\mathrm{i}(\omega_1-\omega_1^{\mathrm{X}})t_3}\mathrm{e}^{\mathrm{i}(\omega_2-\omega_{2'}^{\mathrm{X}})t_2}\mathrm{e}^{\mathrm{i}(\omega_3-\omega_3^{\mathrm{X}})t_3}\mathrm{e}^{-\gamma_2(t_2-t_1)}\mathrm{e}^{-\gamma_2^{2\mathrm{R}}(t_3-t_2)}\cdot$$
$$\cdot\frac{\mathrm{e}^{-\gamma_2^{\mathrm{R}}(t-t_3)}-\mathrm{e}^{-\gamma_2^{\mathrm{B}}(t-t_3)}}{\gamma_2^{\mathrm{B}}-\gamma_2^{\mathrm{R}}}\Theta(t_2-t_1)\Theta(t_3-t_2)\Theta(t-t_3)\,, \tag{B.33}$$

$$\tilde{\varrho}^{(3)}_{\boldsymbol{k}_3\boldsymbol{k}_4,\boldsymbol{k}_3}(t) = \frac{\mu}{\hbar}\mathcal{E}_3^*\mathrm{e}^{\mathrm{i}(\omega_3-\omega_3^{\mathrm{X}})t_3}\left[\mathrm{e}^{-\gamma_2^{\mathrm{X}}(t-t_3)}\tilde{\varrho}^{(2)}_{0,\boldsymbol{k}_3\boldsymbol{k}_4}(t_3)+\right.$$
$$\left.+\frac{\mu}{\hbar}\mathcal{E}_1\mathcal{E}_2\mathrm{e}^{-\mathrm{i}(\omega_1-\omega_1^{\mathrm{X}})t_1}\mathrm{e}^{-\gamma_2(t_2-t_1)}\mathrm{e}^{-\gamma_2^{2\mathrm{X}}(t_3-t_2)}\mathrm{e}^{-\gamma_2^{\mathrm{X}}(t-t_3)}\right.\,.$$

$$\cdot\Bigg\{\frac{\mu}{2\hbar}\chi_3\chi_4[2\chi_1\chi_2(V_\mathrm{d}+V_\mathrm{x})]-(\phi_1\chi_2+\chi_1\phi_2)(G_\mathrm{d}+G_\mathrm{x})\cdot$$
$$\cdot\frac{\mathrm{e}^{-\mathrm{i}(\omega_1^\mathrm{X}+\omega_2^\mathrm{X}-\omega_3^\mathrm{X}-\omega_4^\mathrm{X})(t-t_2)}-1}{\hbar(\omega_1^\mathrm{X}+\omega_2^\mathrm{X}-\omega_3^\mathrm{X}-\omega_4^\mathrm{X})}+\frac{\kappa}{\hbar}\Bigg\}\mathrm{e}^{-\mathrm{i}(\omega_1^\mathrm{X}+\omega_2-\omega_3^\mathrm{X}-\omega_4^\mathrm{X})t_2}\cdot$$
$$\cdot\Theta(t_2-t_1)\Theta(t_3-t_2)\Bigg]\Theta(t-t_3)\,, \tag{B.34}$$

$$\tilde{\varrho}^{(3)}_{\boldsymbol{k}_3'\boldsymbol{k}_4',\boldsymbol{k}_3}(t)=\frac{\mu}{\hbar}\mathcal{E}_3^*\mathrm{e}^{\mathrm{i}(\omega_3-\omega_3^\mathrm{X})t_3}\Bigg[\mathrm{e}^{-\gamma_2^\mathrm{R}(t-t_3)}\tilde{\varrho}^{(2)}_{0,\boldsymbol{k}_3'\boldsymbol{k}_4'}(t_3)-$$
$$-\mathrm{i}\frac{M_2}{\hbar}\frac{\mathrm{e}^{-\gamma_2^\mathrm{B}t_3}}{\gamma_2^\mathrm{B}-\gamma_2^\mathrm{R}}[\mathrm{e}^{-\gamma_2^\mathrm{R}(t-t_3)}-\mathrm{e}^{-\gamma_2^\mathrm{B}(t-t_3)}]\tilde{\varrho}^{(2)}_{0,m}(t_3)-$$
$$-\frac{|M_2|^2}{\hbar^2}\Bigg\{\frac{\mathrm{e}^{-\gamma_2^\mathrm{R}(t-t_3)}(t-t_3)}{\gamma_2^\mathrm{B}-\gamma_2^\mathrm{R}}-\frac{\mathrm{e}^{-\gamma_2^\mathrm{R}(t-t_3)}-\mathrm{e}^{-\gamma_2^\mathrm{B}(t-t_3)}}{(\gamma_2^\mathrm{B}-\gamma_2^\mathrm{R})^2}\Bigg\}\cdot$$
$$\cdot\tilde{\varrho}^{(2)}_{0,\boldsymbol{k}_1'\boldsymbol{k}_2'}(t_3)\Bigg]\Theta(t-t_3)\,. \tag{B.35}$$

Bibliography

[1] K. Bott et al., Phys. Rev. B **48**, 17418 (1993).

[2] E. Miller, M. Ebrahimzadeh, and D. M. Finlayson, editors, *Semiconductor Quantum Optoelectronics*, chapter Time–resolved polarimetry, The Scottish Universities Summer School in Physics, 1999, (by A. Smirl).

[3] M. Lindberg and S. W. Koch, Phys. Rev. B **38**, 3342 (1988).

[4] S. Schmitt-Rink, S. Mukamel, K. Leo, J. Shah, and D. S. Chemla, Phys. Rev. A **44**, 2124 (1991).

[5] K. Victor, V. M. Axt, and A. Stahl, Phys. Rev. B **51**, 14164 (1995).

[6] M. Lindberg, R. Binder, Y. Z. Hu, and S. W. Koch, Phys. Rev. B **49**, 16942 (1994).

[7] M. Kuwata-Gonokami, T. Aoki, C. Ramkumar, R. Shimano, and Y. P. Svirko, J. Lumm. **87–89**, 162 (2000).

[8] V. Chernyak and S. Mukamel, J. Opt. Soc. Am. B **13**, 1302 (1996).

[9] J. Inoue, T. Brandes, and A. Shimizu, Phys. Rev. B **61**, 2863 (2000).

[10] S. Okumura and T. Ogawa, Phys. Rev. B **65**, 035105 (2001).

[11] A. S. Davydov, *Quantum Mechanics*, Pergamon Press, Oxford, 1965.

[12] P. A. M. Dirac, *The Principles of Quantum Mechanics*, Clarendon Press, Oxford, 1958.

[13] H. Haug and S. W. Koch, *Quantum Theory of the Optical and Electronic Properties of Semiconductors*, World Scientific, London, 1990.

[14] J.-C. Diels, *Ultrashort Laser Pulse Phenomena: Fundamentals, Techniques, and Applications on a Femtosecond Time Scale*, Academic Press, San Diego, 1996.

[15] N. Bloemberger, editor, *Nonlinear spectroscopy: Proceedings of the International School of Physics "Enrico Fermi"*, North–Holland Pub. Co., Amsterdam, 1977.

[16] M. Sargent, M. O. Scully, and W. E. Lamb, *Laser Physics*, Addison–Wesley, London, 1974.

[17] H. J. Eichler, P. Günter, and D. W. Pohl, *Laser–Induced Dynamic Gratings*, Springer–Verlag, Berlin, 1986.

[18] J. M. Shacklette and S. T. Cundiff, Phys. Rev. B **66**, 045309 (2002).

[19] C. Cohen-Tannoudji, J. Dupont-Roc, and G. Grynberg, *Photons and Atoms: Introduction to Quantum Electrodynamics*, Wiley, New York, 1989.

[20] M. D. Levenson, *Introduction to Nonlinear Laser Spectroscopy*, Academic Press, San Diego, 1982.

[21] J. Shah, *Ultrafast Spectroscopy of Semiconductors and Semiconductor Nanostructures*, Springer–Verlag, Berlin, 1996.

[22] J. M. Luttinger and W. Kohn, Phys. Rev. **97**, 869 (1955).

[23] J. M. Luttinger, Phys. Rev. **102**, 1030 (1956).

[24] G. F. Koster, *Properties of the Thirty–Two Point Groups*, Massachusetts Institute of Technology, Cambridge, 1963.

[25] K. Cho, Phys. Rev. B **14**, 4463 (1976).

[26] B. Hönerlage, R. Lévy, J. B. Grun, C. Klingshirn, and K. Bohnert, Phys. Rep. **124**, 161 (1985).

[27] G. L. Bir and G. E. Pikus, *Symmetry and Strain–Induced Effects in Semiconductors*, Wiley, New York, 1974.

[28] S. Suga, K. Cho, and M. bettini, Phys. Rev. B **13**, 943 (1976).

[29] B. Hönerlage, U. Rössler, V. D. Phach, A. Bivas, and J. B. Grun, Phys. Rev. B **22**, 797 (1980).

[30] M. I. D'yakonov and V. I. Perel', Zh. Eksp. Teor. Fiz. **60**, 1954 (1971), [Soviet Phys. - JETP 38 1053 (1971)].

[31] F. Meier and B. P. Zakharchenya, editors, *Optical Orientation*, chapter 3, pages 73–131, Elsevier, Amsterdam, 1984, (by G. E. Pikus and A. N. Titkov).

[32] D. D. Awschalom, D. Loss, and N. Samarth, editors, *Semiconductor Spintronics and Quantum Computation*, chapter Spin Dynamics in Semiconductors, Springer–Verlag, Berlin, 2002, (by M. E. Flatté, J. M. Byers and W. H. Lau).

[33] C. Ciuti, V. Savona, C. Piermarocchi, A. Quattropani, and P. Schwendimann, Phys. Rev. B **58**, 7926 (1998).

[34] M. I. Sheboul and W. Ekardt, Phys. Stat. Sol. (b) **73**, 165 (1997).

[35] R. Spiegel et al., Phys. Rev. B **55**, 9866 (1997).

[36] C. Comte, Opt. Commun. **14**, 79 (1975).

[37] E. Hanamura, J. Phys. Soc. Jpn. **39**, 1506 (1975).

[38] A. L. Ivanov, H. Haug, and L. V. Keldysh, Phys. Rep. **296**, 237 (1998).

[39] J. J. Hopfield, Phys. Rev. **112**, 1555 (1958).

[40] K. Henneberger, Phys. Rev. Lett. **80**, 2889 (1998).

[41] E. Vanagas et al., J. Phys: Condens. Matter **14**, 3627 (2002).

[42] S. I. Pekar, Zh. Eksp. Teor. Fiz. **33**, 1022 (1957), [Soviet Phys. JETP **6**, 785 (1958)].

[43] Y. Ohno, R. Terauchi, T. Adachi, F. Matsukura, and H. Ohno, Physica E **6**, 817 (2000).

[44] U. Woggon, *Optical Properties of Semiconductor Quantum Dots*, volume 136 of *Springer Tracts in Modern Physics*, Springer, Berlin, 1996.

[45] A. L. Efros et al., Phys. Rev. B **54**, 4843 (1996).

[46] A. I. Tartakovskii et al., Phys. Rev. Lett. **93**, 057401 (2004).

[47] S. V. Nair and Y. Masumoto, Phys. Stat. Sol. (b) **224**, 739 (2001).

[48] I. Kang and F. W. Wise, J. Opt. Soc. Am. B **14**, 1632 (1997).

[49] E. J. Mayer et al., Phys. Rev. B **50**, 14730 (1994).

[50] G. Finkelstein, S. Bar-Ad, O. Carmel, and I. Bar-Joseph, Phys. Rev. B **47**, 12964 (1993).

[51] D. S. Kim et al., Phys. Rev. Lett. **69**, 2725 (1992).

[52] D. S. Kim, J. Shah, T. C. Damen, L. N. Pfeiffer, and W. Schäfer, Phys. Rev. B **50**, 5775 (1994).

[53] S. Weiss, M.-A. Mycek, J.-Y. Bigot, S. Schmitt-Rink, and D. S. Chemla, Phys. Rev. Lett. **69**, 2685 (1992).

[54] W. Schäfer et al., Phys. Rev. B **53**, 16429 (1996).

[55] H. Wang et al., Phys. Rev. Lett. **71**, 1261 (1993).

[56] H. Wang et al., Phys. Rev. A **49**, R1551 (1994).

[57] M. Wegener, D. S. Chemla, S. Schmitt-Rink, and W. Schäfer, Phys. Rev. A **42**, 5675 (1990).

[58] K. Victor et al., Z. Phys. B **99**, 197 (1996).

[59] G. O. Smith et al., Sol. State Commun. **94**, 373 (1995).

[60] E. J. Mayer et al., Phys. Rev. B **51**, 10909 (1995).

[61] H. Schneider and K. Ploog, Phys. Rev. B **49**, 17050 (1994).

[62] T. F. Albrecht et al., Phys. Rev. B **54**, 4436 (1996).

[63] T. Häupl, H. Nickolaus, F. Henneberger, and A. Schülzgen, Phys. Stat. Sol. (b) **194**, 219 (1996).

[64] D. Bennhardt, P. Thomas, R. Eccleston, E. J. Mayer, and J. Kuhl, Phys. Rev. B **47**, 13485 (1993).

[65] K. Bott et al., J. Opt. Soc. Am. B **13**, 1026 (1996).

[66] M. Lindberg, R. Binder, and S. W. Koch, Phys. Rev. A **45**, 1865 (1992).

[67] S. Schmitt-Rink et al., Phys. Rev. B **46**, 10460 (1992).

[68] Y. Z. Hu et al., Phys. Rev. B **49**, 14382 (1994).

[69] A. L. Smirl, M. J. Stevens, X. Chen, and O. Buccafusca, Phys. Rev. B **60**, 8267 (1999).

[70] M. Lindberg, Y. Z. Hu, R. Binder, and S. W. Koch, Phys. Rev. B **50**, 18060 (1994).

[71] V. M. Axt and A. Stahl, Z. Phys. B **93**, 195 (1997).

[72] U. Rössler, Phys. Stat. Sol. (b) **234**, 385 (2002).

[73] G. Bartels et al., Phys. Rev. B **55**, 16404 (1997).

[74] T. Östreich, K. Schönhammer, and L. J. Sham, Phys. Rev. Lett. **74**, 4698 (1995).

[75] T. Östreich, K. Schönhammer, and L. J. Sham, Phys. Rev. B **58**, 12920 (1998).

[76] M. Kuwata-Gonokami et al., Phys. Rev. Lett. **79**, 1341 (1997).

[77] Y. P. Svirko, M. Shirane, H. Suzuura, and M. Kuwata-Gonokami, J. Phys. Soc. Jpn. **68**, 674 (1999).

[78] T. Aoki, M. Kuwata-Gonokami, and A. A. Yamaguchi, Phys. Rev. Lett. **82**, 3108 (1999).

[79] H. Suzuura, Y. P. Svirko, and M. Kuwata-Gonokami, Sol. State Commun. **108**, 289 (1998).

[80] A. L. Smirl, W. J. Walecki, X. Chen, and O. Buccafusca, Phys. Stat. Sol. (b) **204**, 16 (1997).

[81] U. Rössler, S. Jorda, and D. Brodio, Sol. State Commun. **73**, 209 (1990).

[82] S. B.-T. de Leon and B. Laikhtman, Eurohys. Lett. **59**, 728 (2002).

[83] H. P. Wagner, W. Langbein, and J. M. Hvam, Phys. Rev. B **59**, 4584 (1999).

[84] S. Adachi et al., Phys. Rev. B **67**, 205212 (2003).

[85] S. Adachi et al., Phys. Stat. Sol. (b) **240**, 348 (2003).

[86] S. Adachi et al., Phys. Rev. B **55**, 1654 (1997).

[87] M. Born and E. Wolf, *Principles of Optics: Electromagnetic Theory of Propagation, Interference and Diffraction of Light*, Pergamon Press, London, 1959.

[88] V. M. Axt and A. Stahl, Sol. State Commun. **77**, 189 (1991).

[89] K. Victor, V. M. Axt, and A. Stahl, Z. Phys. B **92**, 35 (1993).

[90] E. A. Muljarov and R. Zimmermann, Phys. Rev. B **66**, 235319 (2002).

[91] D. Weber et al., Phys. Rev. B **55**, 12848 (1997).

[92] C. Mann, W. Langbein, U. Woggon, and A. L. Ivanov, Phys. Rev. B **64**, 235206 (2001).

[93] A. L. Ivanov and H. Haug, Phys. Rev. B **48**, 1490 (1993).

[94] A. L. Ivanov, M. Hasuo, N. Nagasawa, and H. Haug, Phys. Rev. B **52**, 11017 (1995).

[95] E. Tokunaga, A. L. Ivanov, S. V. Nair, and Y. Masumoto, Phys. Rev. B **59**, R7837 (1999).

[96] E. Tokunaga, A. L. Ivanov, S. V. Nair, and Y. Masumoto, Phys. Stat. Sol. (b) **221**, 359 (2000).

[97] E. Tokunaga, K. Kurihara, M. Baba, Y. Masumoto, and M. Matsuoka, Phys. Rev. B **64**, 045209 (2001).

[98] Y. H. Ahn et al., Phys. Rev. Lett. **89**, 237403 (2002).

[99] S. Adachi, Y. Takagi, and S. Takeyama, J. Cryst. Growth **214**, 819 (2000).

[100] S. Ishihara, H. Ohyama, Y. Kadoya, and M. Yamanishi, Physica E **7**, 572 (2000).

[101] O. Buccafusca, X. Chen, W. J. Walecki, and A. L. Smirl, J. Opt. Soc. Am. B **15**, 1218 (1998).

[102] V. M. Axt et al., Phys. Stat. Sol. (b) **221**, 205 (2000).

[103] A. Thilagam, Phys. Rev. B **59**, 3027 (1999).

[104] E. Finger et al., Phys. Stat. Sol. (b) **234**, 424 (2002).

[105] S. Bar-Ad and I. Bar-Joseph, Phys. Rev. Lett. **68**, 349 (1992).

[106] M. Z. Maialle, E. A. de Andrada e Silva, and L. J. Sham, Phys. Rev. B **47**, 15776 (1993).

[107] A. Vinattieri, J. Shah, T. C. Damen, and D. S. Kim, Phys. Rev. B **50**, 10868 (1994).

[108] O. Ikeuchi, S. Adachi, H. Sasakura, and S. Muto, J. Appl. Phys. **93**, 9634 (2003).

[109] A. Tackeuchi, T. Kuroda, S. Muto, and O. Wada, Physica B **272**, 318 (1999).

[110] A. Miller et al., J. Appl. Phys. **86**, 3734 (1999).

[111] A. R. Cameron, P. Riblet, and A. Miller, Phys. Rev. Lett. **76**, 4793 (1996).

[112] H. Kalt et al., Phys. Stat. Sol. (b) **221**, 477 (2000).

[113] R. Levy, B. Hönerlage, and J. B. Grun, Phys. Rev. Lett. **44**, 1355 (1980).

[114] B. Hönerlage, R. Levy, and J. B. Grun, Phys. Rev. B **24**, 3211 (1981).

Summary

Model Calculation of Four–Wave Mixing Polarization and Dynamics in Bulk and Confined Semiconductors

Semiconductor nanostructures and electron spin are two fields which the research on semiconductors is recently focused on. Scientists believe that the interconnection of the two aforementioned fields will provide direct applications mainly in electronics (spintronics) or computer science (quantum computers).

One of the tasks of recent research is to establish methods which may be used in order to investigate properties of new materials. From the point of view of theory, it is then necessary to describe experimental methods, to develop a model which may be used to simulate the experiments and to interpret the measured data in details.

Changes of the spin states of electrons and nuclei in semiconductors are usually very fast, of the order of hundreds of femtoseconds. To monitor these changes, one needs ultrafast experimental methods which are well suitable for such high temporal resolution. With the development of ultrafast laser sources, optical spectroscopy with high temporal resolution was established and used for probing of dynamics of photoexcited carriers in semiconductors.

Four-wave mixing is one of the nonlinear techniques of ultrafast optical spectroscopy. This method involves excitation of a sample by three coherent optical fields with well defined directions of propagation. When restricted to third-order processes, these fields are mixed in the sample and they produce diffracted fields propagating in three new directions: if the incoming fields have wave vectors $\boldsymbol{K}_1$, $\boldsymbol{K}_2$ and $\boldsymbol{K}_3$, the new fields have the wave vectors $-\boldsymbol{K}_1+\boldsymbol{K}_2+\boldsymbol{K}_3$, $\boldsymbol{K}_1-\boldsymbol{K}_2+\boldsymbol{K}_3$ and $\boldsymbol{K}_1+\boldsymbol{K}_2-\boldsymbol{K}_3$. In atomic systems, the process of wave mixing may be understood in terms of the creation of a diffraction grating as a consequence of bleaching of absorption in the pattern produced by the interference of two optical fields and subsequent diffraction of the third field. In semiconductors, however, this model fails and therefore another model is needed.

In my thesis, I present a theoretical work in the field of ultrafast optical spectroscopy of semiconductors and their nanostructures. I present a model which was developed in order to describe and interpret four-wave mixing experiments on intrinsic semiconductors. This model was designed with a special attention paid to the polarizations of incoming and outgoing optical fields and therefore it takes care of the spins of electrons and holes (and excitons) during the whole temporal evolution of the system.

Although there exist many theories capable of description of four-wave interactions in semiconductors, the presented model is based on an original approach to the problem. The models, which may be found in the literature, can be divided generally into two groups: microscopic theories and phenomenological Optical Bloch Equations-like models. The former theories are based on microscopic Hamiltonian of electrons in semiconductors taking into account their spin, band index etc. Predictions of these models are in a good agreement with experiments and were very successful. The disadvantage of microscopic models is, however, that the dynamical equations have a quite complex structure and one must therefore solve them numerically. The Optical Bloch Equations (OBE), on the other hand, provide simple dynamical equations which may be solved analytically using delta-like excitation pulses. Their nature is, however, phenomenological. Optically inactive states are not taken into account and particle-particle interactions are not considered to be sensitive to spin. The aim of the model presented in the thesis is to connect advantages of the two sorts of known models: to develop a model simple in structure whose dynamical

equations may be solved analytically (by direct integration) and to describe correctly the evolution of the spin of carriers in the semiconductor.

The model is believed to be very useful for experimentalists. In standard experiments, one may measure the decay of coherence or the dynamics of an incoherent spin relaxation. The applicability of the four-wave mixing experiments may be, however, much wider and one may use it for measurements of the coherent evolution of the spin orientation of electrons and excitons (spin precession). Results of the thesis then may be used in order to design such an experiment and to understand and interpret the experimental data.

The thesis is introduced by a summary of the fundamentals of many-body physics and semiconductor physics. I discuss afterwards the recent models used for description of the four-wave mixing experiments including OBE which are applied to atomic systems for comparison. For various types of level schemes in the OBE section, I derive polarization selection rules in order to demonstrate that OBEs may fail when applied to semiconductors. The text then continues with a detailed description of the procedure of development of the new model starting with a microscopic Hamiltonian and discussing all approximations used when simplifying the complex microscopic foundations. The last part of the thesis then presents results and their discussion.

The model was developed to be universal for any arbitrary symmetry of the semiconductor crystal lattice. Basic excitations of the semiconductor crystal are considered to be described by the full basis (with respect to spin) of bosonized excitons with wavefunctions symmetrized with respect to the crystal symmetry. Due to the bosonization procedure, the model is valid only under assumption of weak excitation (low density limit). Effective exciton Hamiltonians may then be derived using the method of invariants in order to identify directions of spin precession.

The model takes into account the strong exciton-photon interaction which is responsible for the polariton effect. The four-wave mixing signal is then considered to be produced by resonant processes over the whole range of energies up to the exciton resonance since the electron-hole continuum is not considered.

The core of the model lies in the wave mixing process induced by the polariton-polariton scattering. I take into account all terms in the scattering Hamiltonian, direct and exchange, and therefore the symmetry of the scattering processes is correct with respect to the spins of polaritons. Scattering events, which are not resonant with biexcitons, are described perturbatively in the first order since they are assumed to be sufficiently weak. Processes resonant with biexcitons are, on the contrary, described up to an infinite order in scattering events using the bipolariton model. Usage of this model then provides better predictions of the dynamics of creation and annihilation of the molecule of two excitons and again the correct symmetry of the effective scattering processes with respect to the spin of incoming and outgoing polaritons. The model then involves the sum of both contributions from the direct (off-resonant) and the bipolariton (resonant part with biexcitons) channels. Besides these two scattering channels, the response which comes from Pauli blocking is accounted for.

After development of the model applicable to bulk crystals, I discuss its possible modifications in order to adapt it also for quantum wells and quantum dots. The model may be easily extended by inclusion of external fields: the way how any arbitrary symmetry-breaking effect may be included within the model is also discussed in the text. Some comparison with experimental data is shown in the discussion of the main features of the model.

Based on the level scheme appropriate for the presented model, I developed a computer program that calculates the dynamics of the four-wave mixing response of semiconductors for arbitrary pulse durations, polarizations, mutual time delays and for arbitrary parameters of the material including the lattice symmetry. Results of the numerical calculations are then presented and discussed.

Since the main aim of the development of the model was to design an experiment in which the spin precession may be measured, I discuss possible methods of measurement of the spin precession in one of the chapters. Proposal of an experimental setup and simulations of the four-wave mixing spectra are also shown and discussed.

The thesis presents a novel approach to modeling of the four-wave mixing experiments on semiconductors and their nanostructures. As a result, I present a procedure for development of a set of differential equations appropriate for every particular situation. The model then may be depicted as an OBE-like scheme and interpreted in terms of level-to-level transitions. Its applicability to particular experimental situations and possible extensions are discussed in detail.

Modelování polarizace a dynamiky čtyřvlnového směšování v objemových polovodičích a polovodičových nanostrukturách

Polovodičové nanostruktury a spin elektronů jsou v současnosti jedny z nejintenzivněji zkoumaných oblastí fyziky. Vědci věří, že propojení těchto dvou oblastí povede k přímým aplikacím především v elektronice (spintronice) nebo informatice (kvantové počítače).

Jeden z výzkumných úkolů na tomto poli je vytvoření a praktické využití experimentálních metod, které umožní podrobné prozkoumání vlastností nových materiálů. Úkolem teoretického výzkumu je pak popsat experimentální metody, vytvořit model vhodný pro popis experimentu a přesně interpretovat naměřené hodnoty.

Změny stavů spinu elektronů a atomových jader v polovodičích jsou obvykle velmi rychlé v řádu stovek femtosekund. Proto jsou k výzkumu těchto změn potřeba experimentální metody ultrarychlé spektroskopie, tedy metody s vysokým časovým rozlišením. Optická spektroskopie s vysokým časovým rozlišením je od zhotovení prvních zdrojů světla produkujících ultrakrátké optické pulsy široce využívaná k výzkumu dynamiky opticky excitovaných nosičů v polovodičích.

Čtyřvlnové směšování je jedna z nelineárních metod ultrarychlé optické spektroskopie. Při použití této metody je vzorek excitován třemi koherentními optickými poli s dobře definovanými směry šíření. Pokud se omezíme pouze na procesy třetího řádu v amplitudě pole, optická pole se ve vzorku mísí a vytváří difraktované pole, které se šíří ve třech nových směrech: označíme–li vlnové vektory vstupních polí $\boldsymbol{K}_1$, $\boldsymbol{K}_2$ a $\boldsymbol{K}_3$, nová pole mají vlnové vektory $-\boldsymbol{K}_1+\boldsymbol{K}_2+\boldsymbol{K}_3$, $\boldsymbol{K}_1-\boldsymbol{K}_2+\boldsymbol{K}_3$ a $\boldsymbol{K}_1+\boldsymbol{K}_2-\boldsymbol{K}_3$. V atomárních systémech může být vlnové směšování chápáno jako vytvoření přechodné difrakční mřížky v interferenčním poli excitačních svazků. Saturace absorpce potom vede k difrakci posledního pole do výše popsaných difrakčních směrů. Tento model však selhává v polovodičích, a proto je třeba vytvořit jiný model.

Ve své dizertační práci představuji řešení teoretického úkolu z oboru ultrarychlé optické spektroskopie polovodičů a jejich nanostruktur. Představuji model, který byl vytvořen za účelem popisu a interpretace experimentů provedených na nepříměsových materiálech s využitím čtyřvlnového směšování jako metody. Zvláštní pozornost je věnována zejména polarizacím dopadajících a difraktovaných optických polí, a tedy spin elektronů a děr (a excitonů) jsou vzaty v úvahu po celou dobu uvažovaného vývoje excitovaného systému.

Ačkoliv v literatuře je mnoho již klasických teorií, které popisují čtyřvlnové interakce v polovodičích, představovaný model je založen na ojedinělém přístupu k problematice. Ostatní teorie mohou být obecně rozděleny na dvě skupiny: mikroskopické teorie a fenomenologické modely založené na optických Blochových rovnicích. První jmenované teorie jsou založeny na výpočtech rychlostních rovnic z mikroskopického hamiltoniánu elektronu v polovodiči, kdy je započítán spin elektronu, vícepásová struktura atd. Předpovědi těchto modelů se velmi dobře shodují s experimenty. Nevýhodou ovšem je, že dynamické rovnice mají poměrně složitou strukturu a proto musejí být řešeny numericky. Na druhé straně, optické Blochovy rovnice mají jednoduchou strukturu a mohou být přímo integrovány s uvážením excitace pomocí delta–pulsů. Původ těchto rovnic je ovšem fenomenologický. Stavy, které nejsou opticky aktivní, nejsou v modelech vůbec započítány a spin není zohledněn při popisu interakcí mezi částicemi. Účelem modelu odvozeného v této dizertační práci je proto spojit výhody dvou výše zmíněných druhů modelů: model by měl mít jednoduchou strukturu a dynamické rovnice z ní pocházející by měly být analyticky řešitelné (přímou integrací) a měl by správně popisovat dynamiku spinu nosičů v polovodiči.

Věřím, že model bude velice užitečný pro návrh experimentů. Standardní experimenty umožňují měření tlumení koherence nebo dynamiky nekoherentní relaxace populace nosičů. Aplikovatelnost čtyřvlnového směšování jako experimentální metody může být však mnohem širší a může být použito k měření koherentní dynamiky spinu elektronů a excitonů (precese spinu). Výsledky této práce tak mohou být využity k návrhu takového experimentu a k pochopení a interpretaci experimentálních dat.

Dizertační práce je uvedena souhrnem základů mnohačásticové fyziky a fyziky polovodičů. Poté následuje přehled v současnosti používaných modelů pro popis čtyřvlnového směšování v polovodičích včetně optických Blochových rovnic. Ty jsou aplikované na atomární systémy pro porovnání s experimentálními výsledky změřenými na polovodičích. Ve zvláštní kapitole jsou spočtena výběrová pravidla pro polarizaci difraktovaného svazku pro různé typy schémat hladin. Ukazuji, že tento model selhává při pokusu o aplikaci na polovodiče. V dalších kapitolách poté podrobně popisuji odvození nového modelu založeného na mikroskopickém hamiltoniánu. Dynamické rovnice jsou významně zjednodušeny a příslušné aproximace jsou popsány a diskutovány. V poslední kapitole práce prezentuji výsledky spočtené s využitím modelu a jejich diskusi.

Model byl vytvořen tak, aby byl univerzální pro libovolnou symetrii krystalové mřížky polovodiče. Základní excitace krystalu jsou popsány pomocí jejich úplné báze (vzhledem ke spinu) bozonizovaných excitonů; vlnové funkce jsou symetrizované vzhledem k symetrii krystalu. Model je použitelný pouze za předpokladu malé hustoty excitace (malé hustoty generovaných nosičů) kvůli bozonizaci základních excitací. Efektivní hamiltonián excitonů pak může být vypočten pomocí metody invariantů. Z tohoto hamiltoniánu je pak možné snadno identifikovat směr precese spinu excitonu.

V modelu beru v úvahu silnou exciton–fotonovou interakci, které způsobuje polaritonový jev. Signál ze čtyřvlnového směšování je pak popsán jako plně rezonantní jev v celé škále energií až po excitonovou rezonanci. Vliv elektron–děrového kontinua není v modelu zahrnut.

Jádro modelu leží v procesu vlnového směšování způsobeného polariton–polaritonovým rozptylem. V hamiltoniánu popisujícím rozptyl jsou zahrnuty všechny členy, přímé i výměnné, a proto je symetrie rozptylu vzhledem ke spinům polaritonů popsána správně. Rozptylové procesy, které nejsou rezonantní s biexcitony, jsou popsány poruchově v prvním řádu, protože jsou uvažovány jako slabé. Naopak procesy rezonantní s biexcitony jsou popsány přesně pomocí bipolaritonového modelu. Bipolaritonový model umožňuje mnohem lepší popis dynamiky kreace a rozpadu molekuly tvořené dvěma excitony a správně popisuje symetrii efektivního rozptylového procesu vzhledem ke spinům vstupních a výstupních polaritonů. Model pak bere v úvahu oba příspěvky od přímého (mimo rezonanci) a bipolaritonového kanálu (část rezonantní s biexcitony). Odezva pocházející z Pauliho blokování je také započítána mimo dvou výše uvedených příspěvků.

Možné modifikace modelu pro aplikaci na kvantové jámy nebo kvantové body jsou diskutované po odvození modelu pro objemové polovodiče. Diskutuji též možnost rozšíření o interakce s vnějšími poli: diskutuji obecný postup, jak do modelu zahrnout libovolný proces narušující symetrii systému. V diskusi modelu též prezentuji výpočty demonstrující hlavní charakteristiky modelu a ukazuji modelový výpočet a jeho porovnání s experimentem.

Na základě schématu hladin, které reprezentuje model, jsem vytvořil počítačový program, který počítá dynamiku odezvy čtyřvlnového směšování polovodičů pro libovolný tvar excitačních pulsů a libovolné materiálové parametry včetně symetrie krystalové mřížky. Výsledky numerických výpočtů jsou v dizertační práci uvedeny a diskutovány.

Jedním z důvodů pro vytvoření nového modelu byl požadavek na navržení experimentu, ve kterém by bylo možné změřit precesi spinu. Návrhy možných experimentálních uspořádání pro tento účel jsou proto diskutovány v závěrečné kapitole spolu se simulacemi spekter signálu čtyřvlnového směšování.

Dizertační práce představuje nový přístup k modelování čtyřvlnového směšování na polovodičích a jejich nanostrukturách. Představuji metodu k odvození diferenciálních rovnic, které popisují odezvu libovolného systému. Model může být reprezentován schématem hladin a interakcemi propojujícími tyto hladiny, podobně jako v případě optických Blochových rovnic. Velký prostor je věnován diskusi aplikací a možných rozšíření modelu.

Calcul modèle de polarisation et dynamique de mélange de quatre ondes sur des semi–conducteurs massifs et confinés.

Les études des nanostructures semi-conducteurs et de la dynamique de spin des électrons sont deux domaines sur lesquelles la recherche sest focalisée ces dernières années. On pense trouver à lintersection de ces deux domaines des applications intéressantes et directes en électronique de spin (spintronics) et en informatique quantique (quantum computers).

Changer létat de spin dun électron dans un semi-conducteur est un processus très rapide, de lordre dune centaine de femtosecondes. Afin de visualiser ces changements détat, on a besoin de méthodes expérimentales autorisant une grande résolution temporelle. Avec lapparition des sources laser ultra-rapides, une telle spectroscopie optique a pu tre réalisée.

Parmi dautres, le mélange de quatre ondes est une des techniques optiques non linéaires ultra-rapides qui permettent de déterminer la dynamique des porteurs photo-excités ainsi que leurs cohérences. Cette méthode utilise lexcitation dun échantillon par une séquence de trois impulsions cohérentes optiques qui possèdent des directions de propagation bien définies. Si lon se limite à des processus dordre trois, les champs électromagnétiques interagissent dans léchantillon et génèrent des champs diffractés dans trois nouvelles directions: si les champs incident ont les vecteurs donde $\boldsymbol{K}_1$, $\boldsymbol{K}_2$ et $\boldsymbol{K}_3$, les nouveaux champs possèdent les vecteurs donde $-\boldsymbol{K}_1+\boldsymbol{K}_2+\boldsymbol{K}_3$, $\boldsymbol{K}_1-\boldsymbol{K}_2+\boldsymbol{K}_3$ et $\boldsymbol{K}_1+\boldsymbol{K}_2-\boldsymbol{K}_3$.

Le processus de mélange dondes peut tre vu dans des systèmes atomiques en termes de création dun réseau de diffraction. Ceci est le résultat dun blanchiment de labsorption dans la figure dinterférence produit par deux champs optiques, suivis par la diffraction du troisième champ par le réseau ainsi induit. Ce modèle nest pas applicable aux semiconducteurs et a besoin dtre fortement adapté.

Dans cette thèse, je présente un travail théorique sur la spectroscopie optique ultrarapide des semi-conducteurs et de leurs nanostructures. Nous avons développé un modèle afin de décrire des expériences de mélange dondes menées sur des semi-conducteurs intrinsèques. Ce modèle met tout particulièrement laccent sur les effets liès aux polarisations des champs optiques incidents et émis et tient ainsi compte des spins des électrons et des trous (ainsi que des excitons) pendant toute lévolution temporelle du système.

Plusieurs théories sont capables de décrire des interactions à quatre ondes dans les semi-conducteurs. En général, ces théories peuvent tre divisées en deux classes: théories microscopiques qui considèrent le Hamiltonian des électrons dans les semi-conducteurs en tenant compte de leur spin, leur structure de bande etc. ainsi que théories phénomenologiques qui sinspirent des équations de Bloch Optiques (OBE). Les résultats des théories microscopiques sont en bon accord avec les expériences et ont eu beaucoup de succès. Leur désavantage est, par contre, que les équations dynamiques possèdent une structure complexe et on doit résoudre numériquement un système déquations différentielles couplé. Les OBE correspondent à des équations dynamiques simples, qui peuvent tre résolus analytiquement quand on utilise des impulsions dexcitation de forme de fonctions delta. Pourtant, de par leur nature phénoménologique, elles ne tient pas compte des états optiquement inactifs et les interactions entre particules ny dépendent pas du spin. Le but de notre étude est de rassembler les avantages de ces deux types de schémas dans un modèle qui possède une structure simple et dont les équations dynamiques peuvent tre résolues analytiquement par intégration directe. De plus, il doit décrire correctement lévolution du spin des porteurs dans le semi-conducteur considéré.

L'introduction de cette thèse donne un résumé des propriétés fondamentales de la physique à N-corps et des semi-conducteurs. Je discute ensuite des modèles récents, utilisés pour décrire des expériences de mélange à quatre ondes. Pour pouvoir les comparer, jinclus une descritption des OBE qui sont appliquées aux systèmes atomiques. Les règles de sélection des polarisations sont déterminées pour différents schémas de niveaux. On retrouve ainsi que les OBE peuvent se révélées inappropriées quand elles sont appliquées aux semi-conducteurs.

Je donne ensuite une description détaillée du développement de notre modèle. En partant dun Hamiltonien microscopique, toutes les approximations introduites afin de simplifier la structure complexe microscopique des équations sont discutées. La dernière partie de la thèse présente et discute les résultats obtenus avec ce modèle.

Notre modèle a été développé afin dtre appliqué à des semi-conducteurs qui possèdent une structure de réseau cristallin de symétrie arbitraire. Les excitations élémentaires électroniques dun cristal semi-conducteur sont décrites dans une base complète (par rapport au spin) des excitons qui sont considérés comme des Bosons. Leurs fonctions donde sont symétrisés en accord avec la symétrie du cristal. La procédure de T̈bosonisationẗ des excitons implique que notre modèle est valable uniquement dans les conditions dune excitation faible. Dans ce cas on peut établir des Hamiltoniens effectifs pour les excitons en utilisant la méthode des invariants et déterminer les directions de précession des spin électroniques.

Notre modèle prend en compte le fort couplage entre excitons et photons qui donne lieu à leffet *polariton*. Le signal du mélange de quatre ondes est considéré comme généré par des processus résonants dans toute la gamme dénergie en dessous de la résonance excitonique, le continuum électron-trou nétant pas inclus ici. Ce signal est induit par des collisions entre polaritons. Nous tenons compte des termes directs et déchange dans le Hamiltonian qui décrit ces collisions. Ainsi, la symétrie des processus de collisions est correctement décrite pour ce qui concerne les spins des polaritons. Les processus de collisions, qui ne sont pas résonants avec les biexcitons, sont supposés tre suffisamment faibles pour tre traités en théorie de perturbation au premier ordre. Les collisions dont les énergies sont résonantes avec les biexcitons sont, par contre, décrites dans le cadre du modèle de bipolariton qui les traitent intégralement. Comparé aux OBE, ce modèle donne une meilleure description de la dynamique de création et dannihilation des molécules à deux excitons. De plus, il possède la symétrie correcte en ce que concerne le spin des polaritons incidents et émergeant dune collision. Pour évaluer le signal total, nous additionnons les champs des deux canaux dans notre modèle et considérons en plus linfluence du *blocage de Pauli* sur la réponse du système. Je compare les propriétés de notre modèle avec quelques résultats expérimentaux.

Basé sur un schéma de niveaux approprié, jai développé un programme de calcul numérique qui permet de déterminer la dynamique de la réponse du mélange à quatre ondes dans des semi-conducteurs. Le signal obtenu dépend de la symétrie du réseau cristallin ainsi que des durés dimpulsions et de leurs polarisations, de leurs retards mutuels ainsi que dautres paramètres du matériau. Je présente et discute les résultats de ces calculs numériques. Notre modèle étant tout dabord développé pour des matériaux massifs, des modifications sont nécessaires si lon veut ladapter aux puits quantiques ou aux points quantiques. Il peut également, tre facilement étendu afin dinclure des champs externes et nous avons étudié comment des champs arbitraires qui brisent la symétrie du cristal peuvent tre traités. Je présente diverses méthodes expérimentales qui peuvent tre envisagées pour mesurer la précession de spin, ainsi que les expériences que nous avons proposées avec la simulation de leurs spectres de mélange de quatre ondes.

En résumé, la thèse présentée ici décrit une modélisation des expériences de mélange de quatre ondes dans des semi-conducteurs et de leur nanostructures. La procédure que nous avons obtenue permet de développer un jeu déquations différentielles appropriés à chaque situation expérimentale particulière. Le modèle peut tre considéré comme une approche similaire aux équations de OBE et les résultats peuvent tre interprété en termes de transitions état par état. Les applications du modèle à des situations particulières expérimentales et ses extensions possibles sont discutées en détail.